Resolution improvement in fluorescence and phase optical microscopy

Emeric Mudry

Thèse présentée à l'université Paul Cézanne Aix-Marseille III pour obtenir le grade de docteur en sciences

Resolution improvement in fluorescence and phase optical microscopy

Emeric Mudry

25 septembre 2012

Membres du jury :

Président	**Colin Sheppard**
Rapporteur	**Dominique Lesselier**
Rapporteur	**Rainer Heintzmann**
Examinateur	**Emmanuel Beaurepaire**
Examinateur	**Sylvain Gigan**
Directeur de thèse	**Anne Sentenac**
Codirecteur de thèse	**Patrick C. Chaumet**
Codirecteur de thèse	**Kamal Belkebir**

Discipline :	Optique, photonique et traitement d'image
Laboratoire d'accueil :	Institut Fresnel, équipe S. E. M. O.
École Doctorale :	352 – Physique et sciences de la matière

Remerciements

Je voudrais d'abord remercier chaleureusement Anne Sentenac, mon directeur de thèse, pour m'avoir permis de réaliser ce travail de doctorat sous sa direction, et pour avoir dirigé mes recherches avec sagesse, motivation, disponibilité et enthousiasme. Je la remercie aussi de tout l'effort qu'elle a mis dans la correction de ce texte. Nulle doute qu'il ne serait pas aussi bon sans son aide et je l'imagine soulagée de voir cela enfin fini.

Je voudrais maintenant remercier Patrick C. Chaumet et Kamal Belkebir mes co-directeurs de thèse: Patrick pour son encadrement rude et juste et pour m'avoir enseigné tous les secrets du calcul numérique; Kamal pour ses talents d'inverseur et parce que ses intuitions les plus surprenantes sont les plus efficaces.

Je dois aussi remercier tous les institutions qui ont permis à cette thèse d'avoir lieu, le ministère de la recherche pour l'avoir financée, l'école doctorale et feu l'université Paul Cézanne pour l'avoir supervisée, et surtout l'Institut Fresnel qui m'a permis d'accomplir ce travail dans un cadre agréable, simple et efficace.

Now, I would like to thank all the members of the jury of my defence. First Pr. Colin Sheppard who has accepted to come from abroad for presiding the jury.

Then, I would also like to thank Pr. Rainer Heintzmann for his careful review of my thesis and for his frequent encouragements and useful advices all along my PhD. I am also grateful that he came from so far away for the defence.

Je voudrais aussi remercier Dominique Lesselier pour avoir accepté de relire ma thèse en pleine été. Je le remercie de son rapport si détaillé et regrette qu'il n'ait pu venir à la soutenance.

Je remercie enfin Emmanuel Beaurepaire et Sylvain Gigan d'être descendus si loin en province pour ma soutenance.

Je voudrais maintenant remercier Jules Girard qui a fait sa thèse expérimentale en parallèle de la mienne, pour sa motivation, son franc-parler et pour m'avoir montré tous les fruits qu'apportent une collaboration étroite entre théoriciens et expérimentateurs.

Je voudrais aussi remercier toutes l'équipe SEMO, pour leur aide et pour l'excellent esprit qui y règne. Je remercie en particulier l'équipe des expérimentateurs, Hugo, Guillaume, Jules, Éric, Nicolas et Yi, toujours prêts à s'intéresser au diverses idées parfois maladroites que nous pouvions leur présenter, Slimane et David pour des conversations qui sortait parfois très loin de la physique, mais aussi le reste de l'équipe qui a toujours été là pour me conseiller.

Je dois aussi remercier tous les membres du troisième étage, pour leur disponibilité pour toutes questions scientifiques et pour la joyeuse animation qui règne dans la salle café, remercier aussi les membres de l'équipe d'administration sans qui bien peu serait possible, en particulier, Nelly, Frederic et Magali, remercier enfin tous les membres de l'institut Fresnel avec qui j'ai pu collaborer.

Je voudrais aussi remercier ma famille qui m’a élevé et éduqué, mon père pour m’avoir transmis son goût pour la science, et ma mère pour me montrer qu’il y a aussi une vie hors de la science.

Je remercie aussi mes amis qui m’ont aimés et soutenus durant ces trois ans, tout particulièrement pendant la période très tendue de la rédaction.

Non posso finire senza ringraziare Federica, la più bella donna del mondo chi ha accettato di divenire la mia sposa.

Contents

Résumé du travail de thèse en langue française **9**

1 Contexte et cadre d'étude 9

1.1 Principes de base d'un microscope optique 9

1.2 La microscopie de fluorescence 11

1.3 Microscopie Tomographique par Diffraction 12

2 Miroir et résolution axiale 13

2.1 Microscopie tomographique par diffraction au-dessus d'un miroir . . . 13

2.2 Microscopie de fluorescence au-dessus d'un miroir 15

3 Résolution transverse et éclairement structuré 16

3.1 Éclairement structuré en microscopie de fluorescence 16

3.2 Microscopie tomographique par diffraction d'objets à fort indice 18

4 Conclusion 18

Introduction **21**

Notations **23**

I Basics of fluorescence and tomographic phase microscopy **25**

1 Basics of microscopy **26**

1.1 Modelling of the imaging system 27

1.1.1 General law of imaging system 27

1.1.2 Sine condition 27

1.2 Quality criteria defining an optical microscope 29

1.2.1 Resolution 29

1.2.2 Contrast 29

1.2.3 Noise 30

1.3 Transfer function 31

1.4 'Super-resolution' techniques based on image treatment 32

1.5 The structured illumination approach . . . 33
1.5.1 Scanning microscopy . . . 33
1.5.2 Pattern projection . . . 34
1.6 Conclusion . . . 34

2 Basics of fluorescence microscopy 36
2.1 Fluorescence contrast mechanisms . . . 36
2.2 Image formation . . . 37
2.3 Point-spread-function modelling . . . 38
2.3.1 Two-dimensional PSF . . . 38
2.3.2 Full three-dimensional PSF . . . 40
2.4 Conclusion . . . 41

3 Tomographic Diffraction Microscopy 42
3.1 Diffraction process . . . 42
3.2 Evaluation of the field inside the sample . . . 45
3.2.1 Born approximation and linear reconstruction . . . 45
3.2.2 Renormalised Born approximation . . . 46
3.3 Experimental implementation of TDM . . . 47
3.3.1 Measurement techniques . . . 47
3.3.2 Transmission vs reflection configuration . . . 48
3.4 Conclusion . . . 48

II Mirror and axial resolution 51

4 Mirror-assisted Tomographic Diffraction Microscopy 52
4.1 Two-dimensional scalar configuration . . . 53
4.1.1 Illumination with s polarisation . . . 53
4.1.1.1 Modelling of the diffracted field . . . 53
4.1.1.2 Reconstruction of the sample permittivity . . . 55
4.1.2 Illumination with both p and s polarisation . . . 56
4.2 Three-dimensional vectorial configuration . . . 58
4.2.1 Modelling the diffracted field . . . 58
4.2.2 Reconstruction of the sample polarisability . . . 59
4.2.3 Numerical experiments . . . 60
4.3 Conclusion . . . 61

5 Isotropic Single-Objective microscopy 63

5.1 Principle . . . 63
5.2 ISO microscopy: Theory and Experiment . . . 64
5.2.1 Introduction . . . 64
5.2.2 Principles of ISO focusing and simulations . . . 65
5.2.2.1 Time-Reversal focusing theory . . . 65
5.2.2.2 Simulation of the Point Spread Function (PSF) of the ISO microscope . . . 66
5.2.2.3 Discussion on the phase pattern . . . 69
5.2.3 Experimental results . . . 70
5.2.3.1 Description of the set-up . . . 70
5.2.3.2 Global PSF of the ISO microscope . . . 71
5.2.3.3 Tuning an ISO microscope, cautions and preliminary studies 73
5.2.4 Conclusion . . . 78
5.3 Further works and experiments . . . 79
5.3.1 Radial polarisation . . . 79
5.3.2 Two-photon microscopy . . . 79
5.4 Conclusion . . . 81

III Transverse resolution and Structured Illumination 82

6 Structured illumination in fluorescence microscopy 83
6.1 Introduction . . . 83
6.2 Blind-SIM reconstruction method . . . 84
6.2.1 Principle of blind-SIM . . . 84
6.2.2 Description of the algorithm . . . 85
6.2.2.1 Positivity . . . 86
6.2.2.2 Boundary effects . . . 87
6.2.2.3 Initial estimates . . . 88
6.2.2.4 Computational effort . . . 88
6.2.3 Deconvolution of the wide-field images obtained under uniform illumination . . . 88
6.2.4 Regularisation and stopping criterion . . . 88
6.3 Application of blind-SIM to speckle and periodic illuminations . . . 89
6.3.1 Synthetic data . . . 90
6.3.1.1 Blind-SIM applied to random speckle patterns . . . 90
6.3.1.2 Blind-SIM applied to distorted periodic illumination patterns 91

6.3.1.3 Performance of blind-SIM versus noise and comparison with other techniques . . . 92
6.3.2 Experimental data . . . 96
6.3.2.1 Classical periodic SIM . . . 98
6.3.2.2 Speckle patterns . . . 100
6.3.3 Discussion . . . 100
6.4 Improving further the resolution using Grating assisted SIM . . . 102
6.4.1 Principle . . . 102
6.4.2 Model of intensity pattern . . . 104
6.4.3 Filtered blind-SIM . . . 105
6.5 Conclusion . . . 108

7 Tomographic Diffraction Microscopy for highly refracting samples 109
7.1 Modelling the diffracting field . . . 110
7.1.1 Analytical models . . . 110
7.1.2 Description of the simulation method . . . 112
7.2 Description of different reconstruction methods . . . 112
7.2.1 General principle of the Conjugate gradient algorithm . . . 113
7.2.2 Specificity of the reconstruction algorithms . . . 114
7.2.2.1 The linearised Conjugate Gradient Method (CGM) . . . 114
7.2.2.2 Hybrid Gradient Method (HM) . . . 115
7.2.2.3 Contrast Source Inversion (CS) . . . 116
7.2.3 *a priori* information in the expression of the unknowns . . . 117
7.3 Application to micro-wave data . . . 118
7.3.1 Two cubes along the z direction . . . 119
7.3.2 Two spheres in contact . . . 122
7.4 Application to optical data . . . 124
7.4.1 Configuration and experimental set-up . . . 124
7.4.2 Results . . . 125
7.5 Conclusion . . . 126

Conclusion 128

Appendices 131

A Demonstration of the results cited in Sec. 4.1.1.2 132

B Gradient calculation 136

B.1 Definition of a functional gradient and basic examples 136
B.1.1 Definition 136
B.1.2 First example 136
B.1.3 Second example, functional with an auxiliary function variable 137
B.2 Gradients for Chap. 6 138
B.2.1 Gradients for the blind-SIM algorithm without positivity 138
B.2.2 Gradients for the blind-SIM algorithm with positivity 140
B.2.3 Gradients for the filtered blind-SIM 141
B.3 Gradients for Chap. 7 142
B.3.1 Gradients for the Hybrid Gradient Method 142
B.3.2 Gradients for the Contrast Source Method 144

Bibliography **147**

Résumé du travail de thèse en langue française

Ce chapitre résume les travaux présentés dans ce mémoire. La liste des sections et sous-sections suit la liste des parties et chapitres du mémoire. Seuls les résultats principaux sont présentés. Le lecteur intéressé est invité à se référer au texte en anglais pour trouver développements et démonstrations.

1 Contexte et cadre d'étude

La microscopie optique est une technique essentielle pour de nombreuses disciplines des sciences expérimentales. Elle permet en effet d'étudier des détails microscopiques d'un échantillon de manière non-destructive, grâce à des outils peu encombrants et relativement peu coûteux. Malheureusement les techniques classiques de microscopie optique sont limitées à des résolutions de l'ordre du demi micron, ce qui ne suffit pas pour de nombreuses applications. L'amélioration de cette résolution est donc un défi majeur de la recherche en microscopie optique. Dans ce cadre, j'ai étudié deux types de microscopie, avec et sans marquage : La microscopie de fluorescence qui permet d'imager la densité de fluorescence dans un échantillon et la microscopie tomographique par diffraction qui permet d'obtenir des cartes quantitatives de l'indice optique. Le point clé de ces deux approches est que l'interaction entre la lumière et l'échantillon est très classique (pas de saturation ou de non-linéarité) et qu'elles peuvent donc être implémentées avec des fluorophores courants et des intensités lumineuses réduites. L'objectif de la thèse est de montrer qu'en utilisant de nouvelles configurations et des traitements numériques sophistiqués, les résolutions axiale et latérale de ces techniques peuvent être fortement améliorées.

1.1 Principes de base d'un microscope optique

Un microscope optique est constitué de trois parties : d'abord un système d'éclairement qui envoie la lumière dans la partie de l'échantillon que l'on souhaite étudier ; ensuite un instrument optique permettant de collecter la lumière qui sort de l'échantillon et d'en créer une image agrandie sur le troisième composant : un détecteur, placé dans le plan image de cet instrument optique (FIG. 1). Pour modéliser correctement ce système, on doit se placer dans le cadre général de l'électromagnétisme.

On montre [1, section 3.12] que le champ électrique émergeant de l'objet et obtenu au plan focal objet peut être représenté comme une somme d'ondes planes se propageant dans le sens

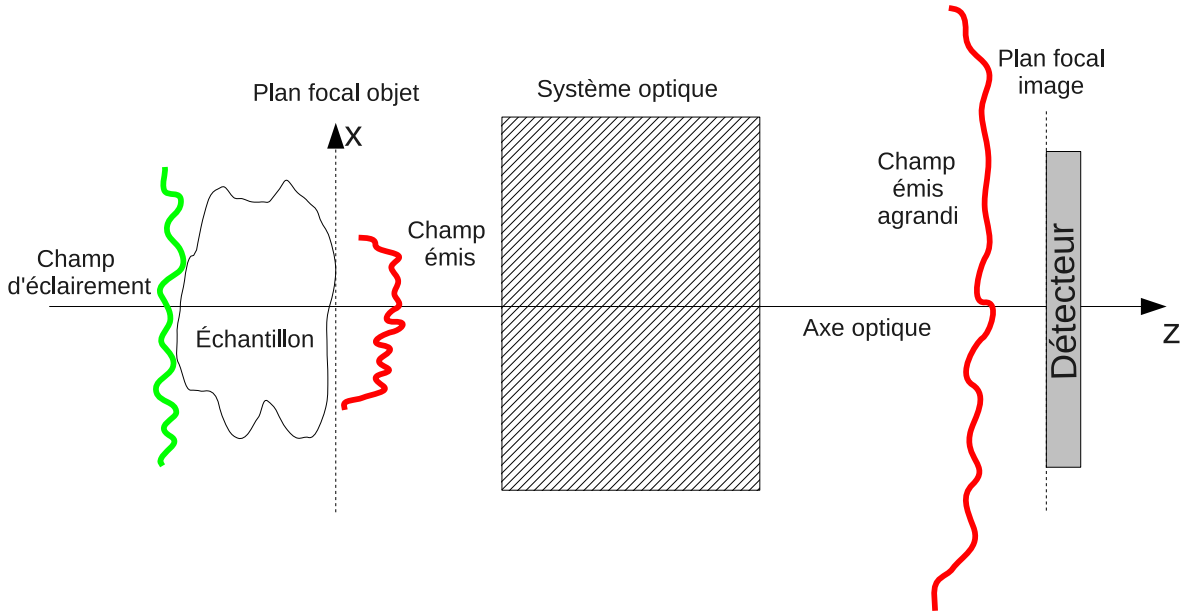

FIGURE 1 – Schéma de principe général de la microscopie optique

des z positifs :

$$\mathbf{E}(\mathbf{r}) = \int_{\mathbf{k}_\parallel \in \mathbb{R}^2} \mathbf{E}(\mathbf{k}_\parallel) \exp(i\mathbf{k}.\mathbf{r}) \mathrm{d}\mathbf{k}_\parallel \tag{1}$$

où $\mathbf{k}_\parallel = k_x\mathbf{x} + k_y\mathbf{y}$ est la projection sur le plan (x, y) de $\mathbf{k}$ le vecteur d'onde, vérifiant $\|\mathbf{k}\| = k_0 = 2\pi/\lambda$, et $\mathbf{E}(\mathbf{k}_\parallel)$ vérifie $\forall \mathbf{k}_\parallel, \mathbf{E}(\mathbf{k}_\parallel).\mathbf{k} = 0$.

Si l'axe **z** est orienté suivant l'axe optique (l'axe de symétrie de l'instrument d'optique) et si cet instrument optique (ordinairement constitué d'un objectif et d'un oculaire) a ses aberrations corrigées suivant les conditions de Sine-ABBE avec son plan focal objet à $z = 0$, les ondes planes telles que $\|\mathbf{k}_\parallel\| \leq k_0\mathrm{NA}$ sont collectées par cet instrument d'optique et produisent dans le plan image le champ [2, section 4.5] :

$$\mathbf{E}(\mathbf{r}) = \int_{\mathbf{k}_\parallel \in \mathcal{C}} \sqrt{\frac{k_z}{k_0}} \mathbf{E}(\mathbf{k}_\parallel) \exp(i\mathbf{k}'.\mathbf{r}) \mathrm{d}\mathbf{k}_\parallel \tag{2}$$

où $\mathcal{C}$ est le disque de centre **0** et de rayon $k_0\mathrm{NA}$, NA est l'ouverture numérique de l'instrument optique et $\mathbf{k}' = \left(k_x/\mathrm{MF}, k_y/\mathrm{MF}, \sqrt{k_0^2 - (k_x/\mathrm{MF})^2 - (k_y/\mathrm{MF})^2}\right)$, pour MF le grandissement du système optique.

Cette décomposition en ondes planes montre que les fréquences du champ supérieures à $k_0\mathrm{NA}$ ne sont pas collectées par le système optique. C'est cette perte d'information qui explique la limite de résolution *sur la mesure du champ*.

Cependant, en règle générale, les microscopistes ne sont pas intéressés par le champ sortant de l'échantillon mais plutôt par l'échantillon lui-même. Or, on peut montrer que, dans le cadre de la microscopie de fluorescence et de la microscopie tomographique de diffraction, les mesures M (qui sont reliées au champ) peuvent s'exprimer sous la forme $M = (OP) * h$ où O, la fonction objet, est la quantité d'intérêt de l'échantillon, P est la fonction sonde, une fonction du champ d'éclairement qui dépend du mécanisme de contraste utilisé et h est la fonction d'appareil qui découle du filtrage des hautes fréquences dans l'équation (2). C'est donc le produit OP qui est filtré et non O lui-même. L'idée est donc d'utiliser des fonctions sondes P

in-homogènes, donc contenant des hautes fréquences spatiales. La transformée de Fourier de M s'exprime, selon le théorème de convolution comme $\tilde{M} = (\tilde{0} * \tilde{P})\tilde{h}$, où $*$ est le produit de convolution. Ce produit de convolution va permettre aux hautes fréquences de O de contribuer aux mesures, malgré le filtrage par h. Il y a principalement deux façons d'appliquer cette approche de l'éclairement structuré :

- **la microscopie par balayage** la fonction sonde P est produite par un champ focalisé au point $\mathbf{r}_0$: $P(\mathbf{r}_0, \mathbf{r}) = P(\mathbf{r}_0 - \mathbf{r})$. Puis ce point $\mathbf{r}_0$ est balayé à travers tout l'échantillon. Ce principe est la base de la microscopie con-focale [3].

- **la projection de motifs** le principe est d'envoyer une succession de champs sondes P_n inhomogènes mais couvrant tout l'échantillon. Il n'y a donc pas besoin de balayage ce qui accélère l'acquisition des données. Par contre les images obtenues sont in-interprétables en-soi et de complexes algorithmes de reconstruction doivent être développés pour obtenir des images lisibles.

L'éclairement structuré a permis d'améliorer de manière significative la résolution des microscopes optiques « classiques », i. e. utilisant une interaction linéaire entre l'échantillon et la lumière. C'est cette approche que j'ai développée dans le cadre de la microscopie de fluorescence et la microscopie tomographique de diffraction dont les principes de base sont présentés ci-dessous.

1.2 La microscopie de fluorescence

Il existe des molécules, appelés fluorophores ou marqueurs fluorescents, capables d'absorber la lumière à une certaine longueur d'onde et de la ré-émettre ensuite à une autre longueur d'onde. Tant que l'intensité du champ d'éclairement n'est pas trop élevée, on peut considérer que l'on est dans le régime d'émission linéaire. Alors l'intensité I_{em} émise par l'échantillon est proportionnelle à $I_{\text{écl}}$, l'intensité du champ d'éclairement : $I_{\mathrm{em}} = \sigma I_{\text{écl}}$, où σ est le coefficient d'émission du fluorophore. D'ordinaire, la distance entre deux fluorophores voisins est très inférieure à la résolution que l'on peut obtenir. On peut donc traiter la répartition de fluorophores comme une fonction continue ρ de densité de fluorophores définie par : $\rho(\mathbf{r})\mathrm{d}\mathbf{r} = \sum_{l=1}^{L} \sigma_l$, où L est le nombre de fluorophores dans le petit volume $\mathrm{d}\mathbf{r}$ et σ_l est le coefficient d'émission du l^{e}fluorophore. Ceci permet d'obtenir des mesures suivant le modèle :

$$M = (\rho I_{\text{écl}}) * h \tag{3}$$

Ici, M est l'intensité du champ obtenu dans le plan focal image et la fonction sonde est l'intensité du champ électrique éclairant. Dans les microscopes à fluorescence classiques, $I_{\text{écl}}$ est homogène sur l'échantillon. L'équation (2) permet d'évaluer le support spectral de h. En effet cette intégrale peut être vue comme la transformée de Fourier d'une fonction dont le support est la surface que parcourt $\mathbf{k}'$ lorsque $\mathbf{k} \in \mathcal{C}$. Cette surface est la calotte de la sphère de centre $\mathbf{0}$ et de rayon k_0 représentée dans la FIG. 2 (a). On peut montrer que $\tilde{h}$ est l'auto-corrélation de cette surface, soit le tore ayant pour section le papillon représenté dans la FIG. 2 (b). Le filtrage par $\tilde{h}$ des fréquences spatiales de l'objet étant beaucoup plus sévère selon k_z que selon k_x et k_y, on constate que la résolution axiale est nettement inférieure à la résolution latérale.

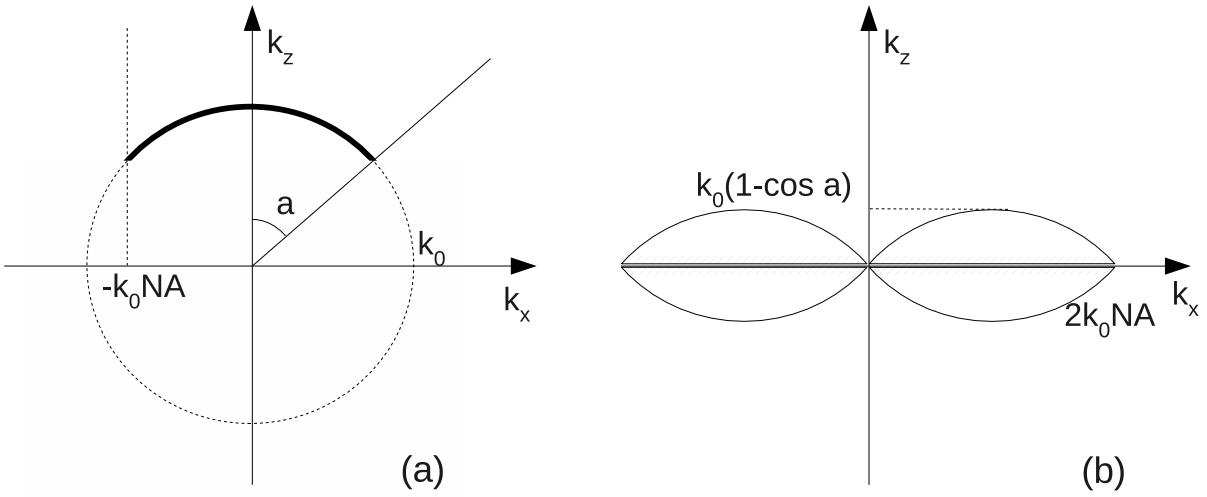

FIGURE 2 – Schéma de coupe (k_x, k_z) du support de la transformée de Fourier des fonctions E et I dans l'image d'un diffuseur ponctuel. (a) Support de la transformée de Fourier de la répartition du champ électrique E. a est l'angle maximal que peut collecter le système optique. Le cercle en pointillé est la coupe (k_x, k_z) de la sphère de centre $\mathbf{0}$ et de rayon k_0, appelée sphère d'EWALD. (b) Support de la transformée de Fourier de la répartition d'intensité I, auto-corrélation de (a) et fonction de transfert de la détection $\tilde{h}$.

1.3 Microscopie Tomographique par Diffraction

La Microscopie Tomographique par Diffraction (MTD) est une évolution de la microscopie de phase et de l'holographie digitale. On envoie grâce à un laser une onde plane sur un échantillon et on détecte en amplitude et en phase le champ qu'il a diffracté. L'effet de diffraction est dû aux variations locales de la permittivité relative ε de l'échantillon. On réalise cette mesure successivement pour différents angles d'incidence puis on reconstruit numériquement une carte en trois dimensions de ε.

Un calcul électromagnétique permet de montrer que le champ diffracté $\mathbf{E}_{\mathrm{d}}(\mathbf{k}_{\|})$ mesuré dans le plan focal arrière est égal à, pour $\mathbf{P} = \varepsilon_0 \chi \mathbf{E}$ et $\chi = \varepsilon - 1$:

$$\mathbf{E}_{\mathrm{d}}(\mathbf{k}) = k_0 \mathbf{k} \times \left(\mathbf{k} \times \frac{\tilde{\mathbf{P}}(\mathbf{k})}{\varepsilon_0} \right) \tag{4}$$

$$\mathbf{E}_{\mathrm{d}}(\mathbf{k}) = k_0 \mathbf{k} \times \left(\mathbf{k} \times \int_{\Omega} \exp(-i\mathbf{k}.\mathbf{r}) \chi(\mathbf{r}) \mathbf{E}(\mathbf{r}) \mathrm{d}\mathbf{r} \right). \tag{5}$$

où $\chi = \varepsilon - 1$, Ω est le domaine où l'échantillon est présent, $\mathbf{P} = \varepsilon_0 \chi \mathbf{E}$ et le champ total $\mathbf{E}$ est la somme du champ incident $\mathbf{E}_{\mathrm{inc}}$ et du champ diffracté par l'objet. Le champ $\mathbf{E}$ satisfait l'équation intégrale,

$$\mathbf{E}(\mathbf{r}) = \mathbf{E}_{\mathrm{inc}}(\mathbf{r}) + \int_{\Omega} \bar{\mathcal{G}}(\mathbf{r}, \mathbf{r}') k_0^2 \chi(\mathbf{r}') \mathbf{E}(\mathbf{r}') \mathrm{d}\mathbf{r}' \qquad \text{avec}$$

$$\bar{\mathcal{G}}(\mathbf{r}, \mathbf{r}')\mathbf{p} = -\frac{1}{4\pi k_0^2} \nabla \times \nabla \times \left(\frac{\exp(ik_0 \Delta r)}{\Delta r} \mathbf{p} \right) + \frac{1}{k_0^2} \mathbf{p} \delta(\mathbf{r} - \mathbf{r}'), \quad \text{pour tout vecteur } \mathbf{p} \tag{6}$$

Lorsque le contraste de permittivité $\chi = \varepsilon - 1$ est petit devant 1, il est possible d'appliquer l'approximation de Born : $\mathbf{E} \approx \mathbf{E}_{\mathrm{inc}}$. Cette approximation simplifie fortement les formules

précédentes. On peut alors prouver que pour un champ incident $\mathbf{E}_{\text{inc}} = \mathbf{E}_0 \exp(i\mathbf{k}_{\text{inc}}.\mathbf{r})$, on obtient

$$\mathbf{E}_{\text{d}}(\mathbf{k}, \mathbf{k}_{\text{inc}}) = k_0 \tilde{\chi}(\mathbf{k} - \mathbf{k}_{\text{inc}})\mathbf{k} \times (\mathbf{k} \times \mathbf{E}_0)\,. \tag{7}$$

Chaque point de mesure correspond donc à la valeur d'une composante spectrale de χ. Au cours de l'acquisition, on va récolter ces composantes spectrales puis obtenir la carte de permittivité par une simple transformée de Fourier inverse.

La résolution obtenue va dépendre de l'ensemble des points de l'espace de Fourier obtenus avec $\mathbf{k} - \mathbf{k}_{\text{inc}}$. Il y a deux configurations possibles :

- la configuration en transmission, où le champ incident est émis par un système optique faisant face à celui utilisé pour détecter le champ diffracté. L'ensemble des fréquences mesurables est le support de $\tilde{h}$ de la FIG. 2 (b). La résolution axiale est donc nettement inférieure à la résolution latérale.

- la configuration en réflexion, où le champ est émis et collecté par le même système optique. L'ensemble des fréquences mesurables est la portion $k_z \geq 2k_0 \cos a$ de la sphère de rayon $2k_0$ centrée en $\mathbf{0}$. Cet ensemble n'est pas symétrique par rapport à $\mathbf{0}$. L'image reconstruite par transformée de Fourier mélangera donc les parties réelle et imaginaire de ε.

Aucune de ces configurations n'amène à une résolution axiale équivalente à la résolution latérale.

2 Miroir et résolution axiale

Nous avons vu que la résolution axiale des microscopes optiques (avec ou sans marquage) n'est jamais aussi bonne que la résolution latérale. Cela provient du fait que la détection et l'illumination ne se font que d'un seul côté de l'objet ce qui limite l'étendue spectrale de $\tilde{h}$ selon k_z. Ce problème fondamental est particulièrement gênant pour les applications tri-dimensionnelles qui se développent fortement actuellement. Nous proposons dans la section suivante une configuration, utilisant un miroir, permettant de résoudre cette difficulté.

2.1 Microscopie tomographique par diffraction au-dessus d'un miroir

En déposant l'échantillon sur un miroir dans un Microscope Tomographique par Diffraction (MTD) en configuration de réflexion, on s'assure que l'illumination et la détection se feront des deux côtés à la fois. En effet, l'échantillon sera éclairé par le champ incident mais aussi par sa réflexion sur le miroir et on captera le champ diffracté directement vers l'objectif mais aussi le champ diffracté dans l'autre direction puis réfléchi par le miroir. De manière plus précise, sous l'approximation de Born, chaque mesure de champ correspond à la somme de quatre composantes de Fourier qui peuvent être assemblées deux par-deux en utilisant la transformée cosinus. On note

$$\tilde{\tilde{\chi}}(k_z, \mathbf{k}_{\|}) = \int_{\Omega} \chi(\mathbf{r}) \cos(k_z z) \exp(-i\mathbf{k}_{\|}.\mathbf{r}_{\|}) \mathrm{d}\mathbf{r}, \tag{8}$$

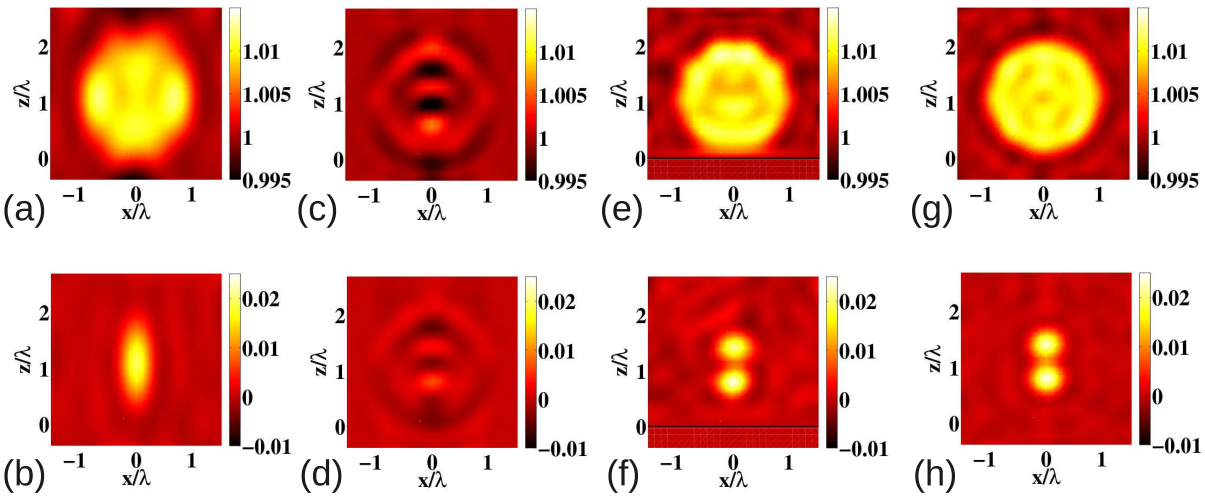

FIGURE 3 – Résultats de simulation numérique d'expériences de microscopie tomographique par diffraction. (a-b) parties réelle et imaginaire de la carte de permittivité reconstruite à partir d'une expérience de MTD en configuration en transmission. (c-d) *idem* avec une configuration en réflexion. (e-f) *idem* avec une configuration en réflexion au dessus d'un miroir. La ligne noir indique la position du miroir. (g-h) *idem* avec un système optique idéal, capable d'éclairer et de collecter la lumière dans toutes les directions autour de l'échantillon.

la transformée de Fourier suivant les axes $\mathbf{x}$ et $\mathbf{y}$ de la transformée cosinus suivant l'axe $\mathbf{z}$. Alors les mesures valent [4]

$$\mathbf{E}_{\mathrm{d}}(\mathbf{k}, \mathbf{k}_{\mathrm{inc}}) = \left(\mathbf{A} f^{-} + \mathbf{B} f^{+}\right) \tag{9}$$

$$\mathbf{A} = k_0 \mathbf{k} \times \left(\mathbf{k} \times \mathbf{E}_{0,\|}\right) \tag{10}$$

$$\mathbf{B} = E_{0,z} k_0 \mathbf{k} \times (\mathbf{k} \times \mathbf{z}) \tag{11}$$

$$f^{+} = \tilde{\tilde{\chi}}\left(|k_z + k_{\mathrm{inc},z}|, \mathbf{k}_{\|} - \mathbf{k}_{\mathrm{inc},\|}\right) + \tilde{\tilde{\chi}}\left(|k_z - k_{\mathrm{inc},z}|, \mathbf{k}_{\|} - \mathbf{k}_{\mathrm{inc},\|}\right) \tag{12}$$

$$f^{-} = \tilde{\tilde{\chi}}\left(|k_z + k_{\mathrm{inc},z}|, \mathbf{k}_{\|} - \mathbf{k}_{\mathrm{inc},\|}\right) - \tilde{\tilde{\chi}}\left(|k_z - k_{\mathrm{inc},z}|, \mathbf{k}_{\|} - \mathbf{k}_{\mathrm{inc},\|}\right) \tag{13}$$

En mesurant au moins deux composantes du champ vectoriel $\mathbf{E}_{\mathrm{d}}$, il est possible d'obtenir les valeurs de $\tilde{\tilde{\chi}}\left(|k_z + k_{\mathrm{inc},z}|, \mathbf{k}_{\|} - \mathbf{k}_{\mathrm{inc},\|}\right)$ et $\tilde{\tilde{\chi}}\left(|k_z - k_{\mathrm{inc},z}|, \mathbf{k}_{\|} - \mathbf{k}_{\mathrm{inc},\|}\right)$. Ensemble, ces deux composantes parcourent toute la demi-sphère $k_z \geq 0$ de centre $\mathbf{0}$ et de rayon $2k_0$. En inversant la transformée Fourier-cosinus, on obtient une carte de χ avec une résolution isotrope à $\lambda/2$. Le miroir permet donc bien de résoudre le problème de la résolution axiale. Cette étude a été validée par des tests numériques illustrés par la FIG. 3. Le miroir permet d'obtenir le même résultat que celui donné par un système idéal où l'illumination et la collection se font selon toutes les directions (comme dans un scanner).

Fort de ce succès, nous avons appliqué cette idée à la microscopie de fluorescence. Plus particulièrement, nous l'avons appliquée à la microscopie con-focale qui souffre d'une résolution axiale réduite car le motif d'intensité focalisé est plus étalé dans la direction axiale que dans les directions latérales.

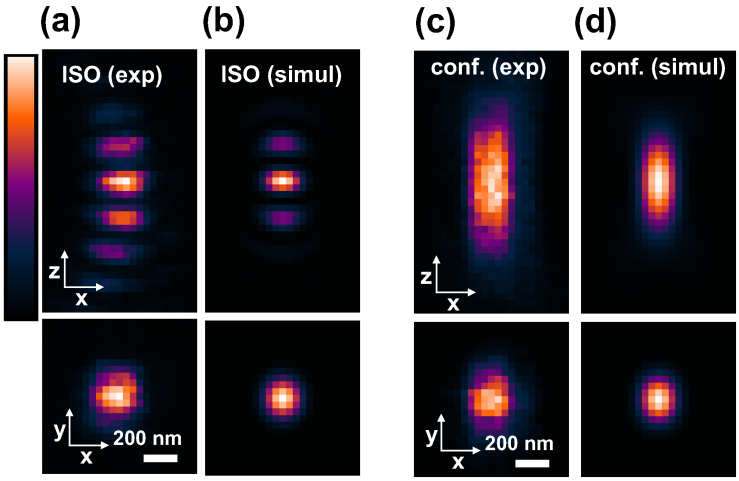

FIGURE 4 – (a-b) Coupe (x, z) et (x, y) de l'image d'une bille fluorescente de 100 nm en microscopie con-focale lorsque la focalisation est réalisée avec la technique ISO. (c-d) *idem* en microscopie con-focale classique.

2.2 Microscopie de fluorescence au-dessus d'un miroir

Le problème de la résolution axiale est dû au fait qu'on focalise la lumière par le système optique de manière asymétrique, avec uniquement des ondes se propageant selon les z positifs. Une solution, proposée par HELL *et al.* [5], consiste à placer en vis-à-vis deux objectifs de microscope et à focaliser de manière cohérente à travers ces deux systèmes optiques. Ce système, nommé microscopie 4Pi, donne de bons résultats, mais il impose un montage substantiellement plus compliqué et sensible aux vibrations qu'un microscope con-focal classique. C'est pourquoi nous avons proposé de remplacer un des objectifs par un miroir [6, 7, 8].

Le principal problème est bien sûr de savoir comment focaliser correctement au-dessus d'un miroir, en prenant en compte tous les effets d'interférence et de polarisation. Un outil très pratique est le renversement temporel virtuel [9, 6]. Nous calculons quel est le champ créé dans le plan focal arrière par un dipôle placé à la position $\mathbf{r}_0$. La théorie du renversement temporel prédit que si l'inverse temporel (ou le conjugué pour des ondes monochromatiques) de ce champ est envoyé dans ce plan focal arrière, il va se focaliser exactement à la position $\mathbf{r}_0$ [10]. En pratique, nous envoyons sur le plan focal arrière une onde plane créée par un laser et nous modulons le front d'onde par un modulateur spatial de lumière. Les plus simples de ces appareils modulent seulement la phase. Nous leur imposons donc, comme motif de phase, l'opposé de la phase du champ calculé.

De nombreuses simulations et expériences de cette technique, appelée ISO pour « Isotropic Single Objective » viennent soutenir cette théorie, comme le montre la FIG. 4. On obtient une tâche focale isotrope entourée de deux lobes. Cette tâche est exactement la même que celle obtenue en microscopie 4Pi, mais avec un montage beaucoup plus simple. La différence entre les mesures et les simulations sont dues aux imperfections des systèmes optiques réels. Ceux-ci atténuent plus fortement les ondes planes les plus éloignées de l'axe optique que ce que la théorie prévoit, et cet effet n'est pas tabulé.

3 Résolution transverse et éclairement structuré

Nous nous intéressons maintenant à l'amélioration de la résolution latérale grâce à l'éclairement structuré. Le point clé de cette approche repose sur l'algorithme d'inversion qui permet de reconstruire l'objet à partir des multiples images obtenues sous divers éclairements. Mon travail a essentiellement consisté à développer des algorithmes d'inversion pour la microscopie de fluorescence à éclairement structuré et la microscopie tomographique de diffraction. Leur originalité par rapport aux techniques existantes est que ces algorithmes permettent de reconstruire à la fois le paramètre d'intérêt de l'échantillon, la fonction objet O, ET les différents éclairements, les fonctions sonde P_n. Cela permet de simplifier le montage expérimental en microscopie de fluorescence et d'aborder l'imagerie d'objets fortement diffractants en microscopie tomographique de diffraction.

3.1 Éclairement structuré en microscopie de fluorescence

En microscopie de fluorescence classique, utilisant une intensité d'illumination homogène, les informations fréquentielles de l'objet supérieures à $k_c = 2k_0\mathrm{NA}$ sont perdues. Pour améliorer cela il a été proposé d'utiliser la technique de l'éclairement structuré [11, 12, 13] en champ large qui consiste à éclairer l'échantillon avec une intensité hétérogène, généralement sinusoidale et obtenue via l'interférence de deux faisceaux collimatés cohérents. Le mélange de fréquences entre l'éclairement et l'objet permet de mesurer des fréquences spatiales au-delà de cette limite.

Plus précisément, les mesures M_l de l'incidence l sont reliés à la densité de fluorophores ρ et à l'intensité du champ incident I_l par

$$M_l = (I_l \rho) * h$$

dont la transformée de Fourier donne, par le théorème de convolution

$$\tilde{M} = (\tilde{\rho} * \tilde{I_l})\tilde{h}.$$

Si les intensités d'éclairement I_l sont de la forme $I_l(\mathbf{r}) = 1 + \cos(\mathbf{K}.\mathbf{r} + \phi_l)$, on obtient

$$\tilde{M_l}(\mathbf{k}) = \left[\tilde{\rho}(\mathbf{k}) * \left(\delta(\mathbf{k}) + \frac{1}{2}\exp(i\phi_l)\delta(\mathbf{k}+\mathbf{K}) + \frac{1}{2}\exp(-i\phi_l)\delta(\mathbf{k}-\mathbf{K})\right)\right]\tilde{h}(\mathbf{k}) \quad (14)$$

$$= \left(\tilde{\rho}(\mathbf{k}) + \frac{1}{2}\exp(i\phi_l)\tilde{\rho}(\mathbf{k}+\mathbf{K}) + \frac{1}{2}\exp(-i\phi_l)\tilde{\rho}(\mathbf{k}-\mathbf{K})\right)\tilde{h}(\mathbf{k}) \quad (15)$$

$$= \tilde{M}^0(\mathbf{k}) + \exp(i\phi_l)\tilde{M}_l^+(\mathbf{k}) + \exp(-i\phi_l)\tilde{M}_l^-(\mathbf{k}). \quad (16)$$

M^0 est l'image qu'on aurait obtenue avec un éclairement homogène. Il ne comprend donc que les basses fréquences de l'objet. Par contre les $M_l^{\pm}$ contiennent les fréquences de l'objet sur les disques de rayon k_c autour de $\mathbf{K}$ et $-\mathbf{K}$. En utilisant trois mesures avec trois ϕ_l différents (obtenus en introduisant un déphasage sur un des faisceaux formant le motif d'interférence), on peut séparer ces trois termes et donc mesurer les fréquences de ρ sur un domaine de Fourier plus vaste qu'en microscopie de fluorescence classique.

Malheureusement, les images reconstruites par ce type de méthode qui nécessite une bonne connaissance de l'intensité éclairante sont très sensibles à de petites erreurs sur la valeur de ϕ_l ou sur la période et l'orientation de la grille de lumière. La plus petite variation expérimentale de

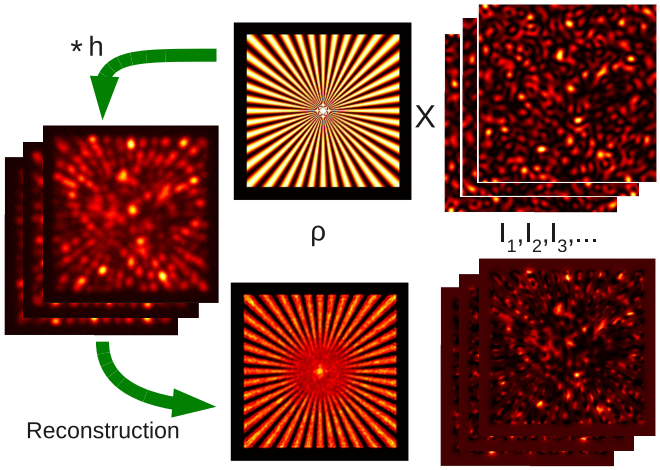

FIGURE 5 – Illustration des différentes étapes d'une expérience blind-SIM. 160 champs incidents d'intensité in-homogène I_l (en haut à droite) sont multipliés par la densité de fluorophore ρ (en haut au centre) puis filtrés par la fonction d'instrument h. Ces données, une fois bruitées, (à gauche) sont traitées par l'algorithme de reconstruction produisant une estimation haute résolution de ρ (en bas au centre) et 160 estimations pour les intensités des champs incidents I_l (en bas à droite).

l'intensité éclairante provoque de gros artefacts nuisant à l'interprétation de l'image produite. Cela limite fortement le champ d'application de cette technique. C'est pourquoi nous avons proposé de reconstruire en même temps l'intensité des champs incidents I_l et la densité de fluorophores ρ [14]. Comme nous n'imposons plus de connaissances *a priori* particulières sur l'intensité d'illumination, nous limitons les artefacts causés par une distorsion ou une variation de l'éclairement causées par une mauvaise stabilisation du montage ou par l'échantillon lui-même. De plus, comme aucune forme particulière n'est imposée à ces champs incidents, nous pouvons utiliser des intensités de speckle (tavelure), qui sont produites en plaçant un simple papier diffusant dans le chemin du laser d'éclairement, ce qui simplifie énormément le montage. La FIG. 5 illustre ce processus.

Notre algorithme, appelé blind-SIM, reconstruit à la fois l'échantillon et les différentes intensités d'illumination. Il cherche le minimum de la fonctionnelle

$$F(\rho, I_{l=1,\cdots,L-1}) = \sum_{l=1}^{L-1} \|M_l - (I_l\rho) * h\|^2 + \left\| M_L - \left[\left(LI_0 - \sum_{l=1}^{L-1} I_l \right) \rho \right] * h \right\|^2, \qquad (17)$$

grâce à un algorithme inspiré de la méthode du gradient conjugué [15][16, section 10.6]. Les résultats de simulation, comme celle de la FIG. 5, montrent que les estimations obtenues ont une très forte corrélation avec les fonctions à estimer. De plus les ρ obtenues comportent bien des fréquences spatiales supérieures à celles obtenues avec des données sans éclairement structuré. Cette étude a ensuite été validée par des résultats expérimentaux. La FIG. 6 compare des images de billes fluorescentes de 90 nm de diamètre obtenues avec et sans éclairement structuré. L'amélioration de résolution y est clairement visible.

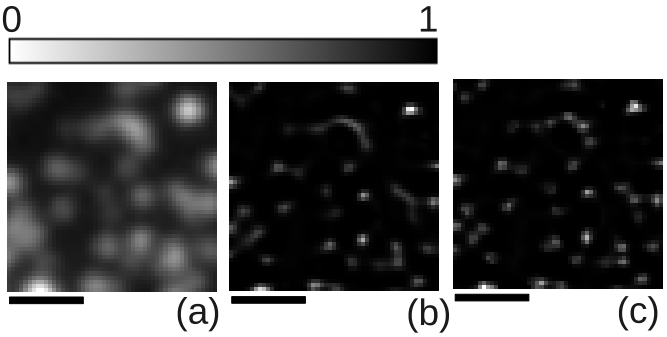

FIGURE 6 – (a) image de billes fluorescentes de 90 nm de diamètre obtenue en microscopie de fluorescence. (b) dé-convolution de l'image (a). (c) image obtenue en traitant 24 images d'éclairement structuré avec l'algorithme blind-SIM.

3.2 Microscopie tomographique par diffraction d'objets à fort indice

Lorsque l'échantillon observé par microscopie tomographique par diffraction est fortement diffractant, on ne peut plus appliquer l'approximation de Born. La reconstruction par transformée de Fourier citée dans la section 1.3 n'est plus applicable. Il faut en effet prendre en compte le fait que l'échantillon modifie le champ qui le sonde. Ainsi, l'algorithme de reconstruction devra à la fois estimer l'objet et le champ à l'intérieur de l'objet. Pour cela, des méthodes d'optimisation itératives non-linéaires ont été proposées. Ces méthodes itératives nécessitent en général de résoudre le problème de diffraction rigoureusement, *i. e.* de calculer $\mathbf{E}$ satisfaisant l'équation (6) pour chaque nouvelle estimée de la permittivité. Ces calculs numériques peuvent être très lourds, ce qui explique que la plupart des méthodes d'inversion permettant de retrouver des objets fortement diffractants ont été développées pour le cas simplifié 2D scalaire. L'augmentation de la rapidité des ordinateurs et de récents progrès algorithmiques [17, 18] permettent maintenant de passer à des échantillons réalistes, donc en trois dimensions. Mon travail a consisté à étendre à la troisième dimension, en prenant en compte l'aspect vectoriel des champs électromagnétiques, un algorithme prometteur, la méthode de gradient hybride [19] et à le comparer à une méthode de référence, l'inversion contraste source [20].

Nous avons montré sur des données expérimentales micro-ondes issues d'une base en libre accès [21], que notre algorithme a des résultats comparables à ceux de l'inversion contraste source, mais qu'il est beaucoup plus rapide, de plusieurs ordres de grandeur. Cette rapidité nous a permis de l'utiliser pour des ensembles de données importants (provenant par exemple d'une expérience comportant beaucoup de directions d'observation), comme ceux produits par des expériences de MTD. Cet algorithme a été utilisé avec succès [22] pour traiter des mesures expérimentales obtenues sur un microscope tomographique de diffraction pour l'échantillon-test présenté dans la FIG. 7.

4 Conclusion

Au cours de cette étude, nous avons étudié deux voies pour améliorer la résolution en microscopie optique. La première voie propose de placer un miroir derrière l'échantillon, ce qui permet d'améliorer fortement la résolution axiale. Cela a été montré pour les deux techniques de microscopie linéaire qui nous intéresse, la microscopie de fluorescence et la microscopie to-

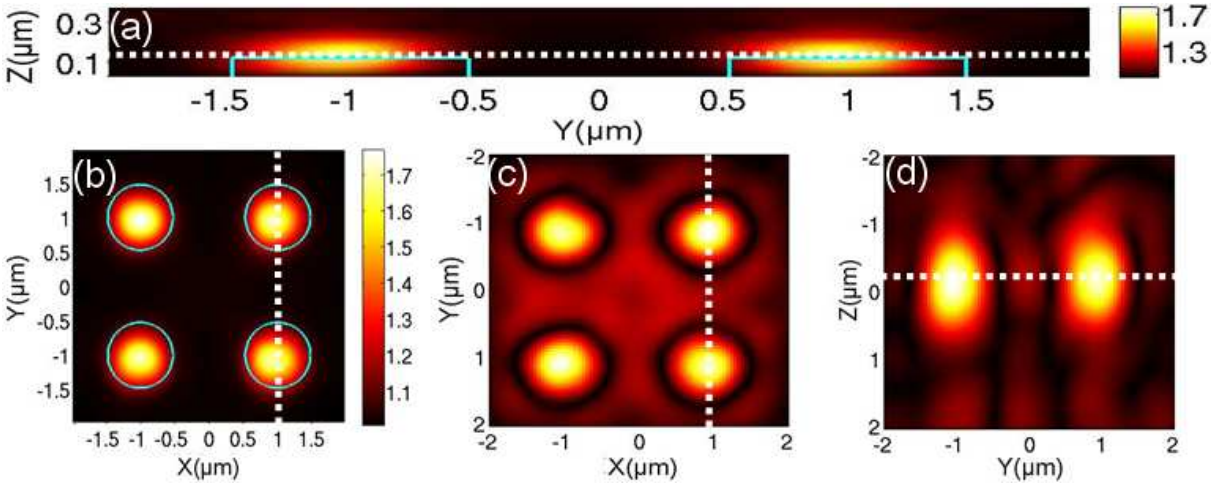

FIGURE 7 – Comparaison entre la carte de permittivité quantitative obtenue avec notre algorithme (a-b) et le module de la carte obtenue par la reconstruction linéaire par transformée de Fourier (c-d). La carte de permittivité quantitative (complexe) de cette dernière reconstruction est trop éloignée du véritable échantillon. C'est pourquoi nous en avons affiché seulement le module. (a) coupe longitudinale à $y = 1$ μm, (b) coupe transverse à $z = 125$ nm (ligne bleue continue : géométrie réelle de l'échantillon de permittivité $\varepsilon = 2$). (c) coupe transverse à $z = 53$ nm. (d) coupe longitudinale à $y = 1$ μm. Les coupes sont selon les lignes blanches en pointillés. Les échelles de couleurs représentent la permittivité relative.

mographique par diffraction. Le succès de cette approche pour ces deux techniques nous incite à penser qu'elle serait aussi valide pour d'autres techniques de microscopie où la résolution axiale est un problème.

Ensuite nous avons proposé des algorithmes de reconstruction itératifs estimant en même temps l'objet d'étude et le champ qui le sonde. Dans le cas de la microscopie de fluorescence, cela permet d'utiliser l'éclairement structuré sans avoir à contrôler très précisément le champ d'éclairement, ce qui simplifie drastiquement les procédés expérimentaux. Dans le cas de la microscopie tomographique par diffraction cela permet de prendre en compte la perturbation du champ sonde provoquée par la diffraction. Une possible extension serait de mélanger ces deux approches et d'opérer la MTD avec des champs aléatoires ou peu contrôlés, ce qui simplifierait là encore les procédés expérimentaux.

Introduction

Optical microscopy is an essential tool for various fields of science like biology, material science and medicine. Its main interest is the possibility to observe small details of a sample without disturbing it. Optical microscopes are also small and cheap enough to allow any laboratory to possess one.

One of the main limitations of optical microscopy is its resolution. Research and technology are constantly requiring systems to see smaller details. For long, improvements came mainly from the technological conception of objective lenses. Yet, modern objectives lenses are almost reaching the theoretical limit of resolution, called the diffraction limit, and one cannot hope significant resolution improvements in this way. It is now necessary to invent new imaging techniques using these objective lenses. This has been the aim of more than 30 years of research efforts.

Promising solutions use non-linearity in the light-matter interaction [23, 24, 25] or propose to scan a probe in the near-field of the sample [26, 27], reaching resolutions about several tens of nano-meters. They require, however, high power laser, special markers or a deep modification of the microscope set-up and will be out of the scope of this work. Here, we consider only classical light-sample interactions and study both fluorescence microscopy, that images specific chemical components of a sample thanks to a selective staining using fluorophores, and unstained microscopy that images the intrinsic optical contrast of the sample. In this general framework, we focus on two promising approaches, whose principles are very similar:

- Structured Illumination Fluorescence Microscopy, in which the sample is illuminated under different spatially inhomogeneous incident intensities. Confocal microscopy is one of the most famous example of structured illumination microscopy. The fluorescence density of the sample is reconstructed numerically (or analogically) from the different recorded data;

- Tomographic Diffraction Microscopy, in which several holograms of the object are recorded under different illuminations. This quite recent technique, which is an evolution of phase contrast microscopy and digital holography, is the most complete version of stainless microscopy as its data can be used to reproduce any microscopy type (dark-field, phase-microscopy, ...). The post-treatments of the holograms allows a quantitative reconstruction of the sample optical properties; its optical index and its absorption coefficient, summarised in the concept of complex relative permittivity.

The thesis is separated in three parts. The first one details the general concepts of optical microscopy and explains the basics of the two above microscopy approaches. The second part explains how one can improve the axial resolution by placing a mirror behind the sample. This

concept is presented for tomographic diffraction microscopy and fluorescence confocal microscopy in two different chapters. The third part is devoted to the inversion methods that are developed to reconstruct quantitatively the sample parameter of interest from the different recorded images for both the structured illumination fluorescence microscopy and tomographic diffraction microscopy.

Notations

In this work, one uses bold scripts for vectors $\mathbf{v}$, over-lined bold script for tensors $\bar{\mathbf{T}}$ and italic script for scalars s.

All positions and vectors are measured in the right-hand orthonormal coordinate system $(O, \mathbf{x}, \mathbf{y}, \mathbf{z})$. Vector $\mathbf{r} = (x, y, z)$ refers to the position in this coordinate system. $\mathbf{0}$ is the null vector. $\mathbf{u}$ and $\mathbf{v}$ being two vectors, $\mathbf{u}.\mathbf{v}$ is their dot (scalar) product and $\mathbf{u} \times \mathbf{v}$ is their cross (vector) product. $\|\mathbf{u}\|$ is the norm of $\mathbf{u}$ defined by $\|\mathbf{u}\|^2 = \mathbf{u}.\mathbf{u}$.

For each vector $\mathbf{v}$, one defines $v_z = \mathbf{v}.\mathbf{z}$ and $\mathbf{v}_{\|} = (\mathbf{v}.\mathbf{x})\mathbf{x} + (\mathbf{v}.\mathbf{y})\mathbf{y}$ the projection of $\mathbf{v}$ on the (x, y) plane.

$\mathbb{R}$ is the set of real numbers.
$\mathbb{C}$ is the set of complex numbers.
i is the imaginary unit $i^2 = -1$.
z being a complex number, z^* is its conjugate, $\Re e(z)$ its real part, $\Im m(z)$ its imaginary part and $|z|$ its absolute value.

In all this study, one assumes that light is monochromatic with wavelength in vacuum noted λ. For each electromagnetic field, one assumes a time dependence in $\exp(-i\omega t)$, t being the time of the referential and $\omega = 2\pi c/\lambda$ the angular velocity, with c the light velocity in vacuum. Electric $\mathbf{E}$ and magnetic $\mathbf{B}$ fields are given in SI units.

f being a function of space $\mathbb{R}^3$, $\tilde{f}$ is its Fourier transform, defined by

$$\tilde{f}(\mathbf{k}) = \int_{\mathbb{R}^3} \exp(-i\mathbf{k}\mathbf{r}) f(\mathbf{r}) \mathrm{d}\mathbf{r}.$$

Thus f is the inverse Fourier transform of $\tilde{f}$ obtained with the formula

$$f(\mathbf{r}) = \frac{1}{8\pi^3} \int_{\mathbb{R}^3} \exp(i\mathbf{k}\mathbf{r}) \tilde{f}(\mathbf{k}) \mathrm{d}\mathbf{k}.$$

$\mathbf{P}(\mathbf{r}) = P_x(\mathbf{r})\mathbf{x} + P_y(\mathbf{r})\mathbf{y} + P_z(\mathbf{r})\mathbf{z}$ being a vectorial function of space, $\tilde{\mathbf{P}}$ is its Fourier transform defined by

$$\tilde{\mathbf{P}}(\mathbf{k}) = \tilde{P}_x(\mathbf{k})\mathbf{x} + \tilde{P}_y(\mathbf{k})\mathbf{y} + \tilde{P}_z(\mathbf{k})\mathbf{z}.$$

Ω being a sub-set of $\mathbb{R}^n$, where n is a positive integer, $\langle f|g\rangle_\Omega$ is the inner product on Ω defined as

- given f and g two real functions of Ω

$$\langle f|g\rangle_\Omega = \int_\Omega f(\mathbf{r}) g(\mathbf{r}) \mathrm{d}\mathbf{r}.$$

- given f and g two complex functions of Ω,

$$\langle f|g\rangle_\Omega = \int_\Omega f^*(\mathbf{r})g(\mathbf{r})\mathrm{d}\mathbf{r}.$$

- given $\mathbf{u}$ and $\mathbf{v}$ two complex vectorial functions of Ω,

$$\langle \mathbf{u}|\mathbf{v}\rangle_\Omega = \int_\Omega \mathbf{u}^*(\mathbf{r}).\mathbf{v}(\mathbf{r})\mathrm{d}\mathbf{r}.$$

f being a function of Ω, $\|f\|_\Omega$ is the norm defined by $\|f\|_\Omega^2 = \langle f|f\rangle_\Omega$.

$\mathcal{B}$ being an operator transforming a function defined on Ω in a function defined on Γ, where Ω and Γ being two sub-sets of $\mathbb{R}^n$, $\mathcal{B}^\dagger$ is the adjoint operator of $\mathcal{B}$ defined by

$$\forall (f,g) \in \Gamma \times \Omega, \langle f|\mathcal{B}g\rangle_\Gamma = \langle \mathcal{B}^\dagger f|g\rangle_\Omega.$$

f and g being two functions defined on $\mathbb{R}^n$, $f * g$ is the convolution product of f and g defined by

$$(f * g)(\mathbf{r}) = \int_{\mathbb{R}^n} f(\mathbf{r}')g(\mathbf{r}-\mathbf{r}')\mathrm{d}\mathbf{r}'.$$

Part I

Basics of fluorescence and tomographic phase microscopy

Chapter 1

Basics of microscopy

A microscope is a tool providing images of a sample that are sufficiently enlarged to show details that were previously too small to be visible. An optical microscope is composed of three parts. First an illumination system that shines light through the sample. Then, an imaging system that collects and magnifies light emerging out of the sample and casts it on an image plane. Finally, a detector is placed on the image plane for recording this light intensity. Nowadays the detector is often an electronic camera allowing quantitative measurement of the received field intensity. These three parts are conceived such that the light intensity is modulated spatially on the detector and such that this modulation, called the detected image, bears a magnified information on the sample.

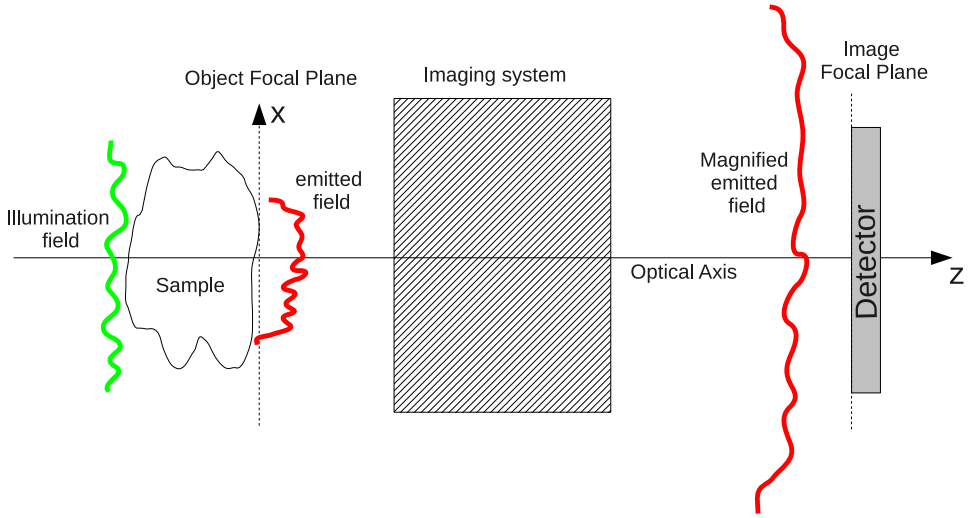

Light is an electromagnetic wave. Its propagation is described by the Maxwell equations and classical electrodynamics. In particular, it can be proven that any electric field propagating in the increasing z direction in an homogeneous media can be decomposed as a sum of plane waves [1, Sec. 3.12]

$$\mathbf{E}(\mathbf{r}) = \int_{\mathbf{k}_\parallel \in \mathbb{R}^2} \frac{k_0}{k_z} \mathbf{E}(\mathbf{k}_\parallel) \exp(i\mathbf{k}.\mathbf{r}) \mathrm{d}\mathbf{k}_\parallel, \tag{1.1}$$

where $\mathbf{k}_\parallel = k_x\mathbf{x} + k_y\mathbf{y}$ is the projection of $\mathbf{k}$ on the (x, y) plane, $\mathbf{k}$ is the wave vector, with the constraint $\|\mathbf{k}\| = k_0 = 2\pi/\lambda$ and $\mathbf{E}(\mathbf{k}_\parallel)$ verifies $\forall \mathbf{k}_\parallel, \mathbf{E}(\mathbf{k}_\parallel).\mathbf{k} = 0$. When $\|\mathbf{k}_\parallel\| \geq k_0$, k_z is a

complex number

$$k_z = i\sqrt{\|\mathbf{k}_\parallel\|^2 - k_0^2}$$

and $\mathbf{E}(\mathbf{k}_\parallel)\exp(i\mathbf{k}.\mathbf{r})$ is an evanescent plane wave.

This plane wave decomposition is particularly useful for modelling image formation in optical microscopes. It is indeed natural to apply this decomposition using as $\mathbf{z}$ axis, the axis of symmetry of the imaging system, called the optical axis. The imaging system can then be modelled as a filter that collects some of these plane waves and transforms them in other plane waves reaching the image plane.

1.1 Modelling of the imaging system

1.1.1 General law of imaging system

The first constraint on the imaging system design comes from the detector. Indeed each detector imposes a limit on the smallest detail it can distinguish. For example, the smallest detail visible by a bare eye has a size of some hundredths of millimetres, and a camera is limited by its pixel size of several micrometres. In order to image smaller details, the imaging system is designed to cast a magnified image of the object on the detector. One thus defines the **Magnifying Factor** MF as the ratio between image and object sizes.

Once this magnifying factor is chosen, the imaging system has to be stigmatic. This means that the image obtained on each point of the detector has to be sharp. There is indeed a large variety of aberrations that can blur, distort or mix the different parts of the image, and they become more and more severe as the field of view increases. In our plane wave modelling, one says that the imaging system is stigmatic at point P if all plane waves that have the same phase at P are transformed by the imaging system in plane waves that have the same phase at a point P', called the conjugate of P trough the imaging system.

There is now more than two centuries of studies on aberration. There is however a fundamental limit on their corrections. Maxwell has indeed shown [28][2, Sec. 4.2.1] that an optical system cannot be stigmatic on all points of space, unless its magnifying factor is equal to $\mathrm{MF} = n_i/n_d$, where n_i is the refraction index of the medium surrounding the sample, and n_d that of the medium surrounding the detector. In all other cases, the system can only be stigmatic on a plane [28, 2].

1.1.2 Sine condition

The most common way to design an optical system is to have it stigmatic on a plane perpendicular to the optical axis called the Object Focal Plane. This system has to produce a magnified image on the detector plane. Thus, each point P of the object focal plane has its conjugate P' on the image focal plane. This imposes a condition, called the Sine (or the Sine-Abbe condition) which can be described as follows: A plane wave with transverse wave vector $\mathbf{k}_\parallel$ is transformed by the imaging system into a plane wave with transverse wave vector $\mathbf{k}'_\parallel = -\mathbf{k}_\parallel/\mathrm{MF}$. In other term, the polar angle θ' of the plane wave direction obtained in the image focal domain satisfies $\sin\theta = \mathrm{MF}\sin\theta'$, where θ is the polar angle of the plane wave direction in the object focal

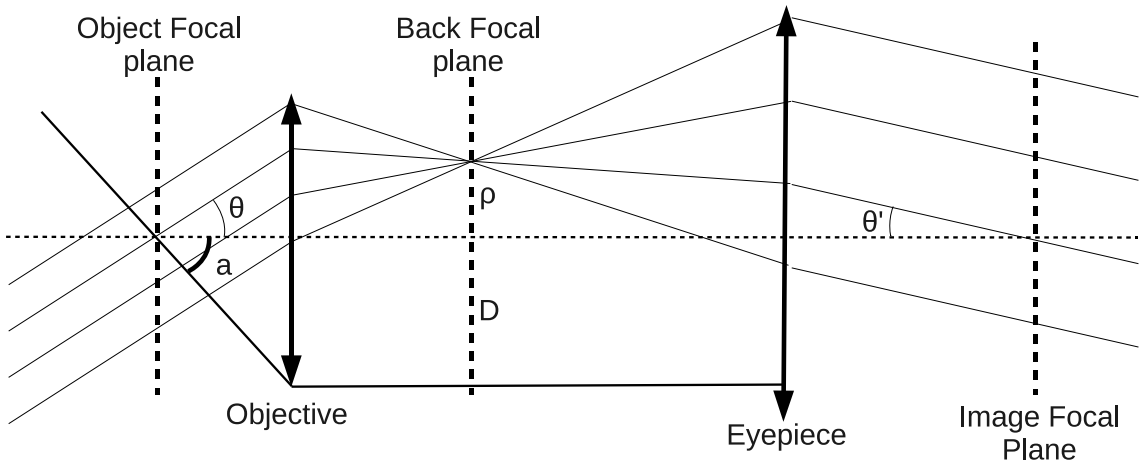

Figure 1.1: Sketch of an objective corrected under the Sine-Abbe condition. A plane wave passing through the sample whose direction make an angle θ with the optical axis is focussed by the objective to a point being in the back focal plane, on the plane containing the optical axis and the direction of the plane wave, at a distance $\rho = D\sin\theta/\sin a$, where a is the maximum angle of the plane wave collected by the objective and D is the diameter of the exit pupil. Then, this focussed beam becomes through the eyepiece a plane wave making an angle θ' with the optical axis, such that $\sin\theta = \mathrm{MF}\sin\theta'$.

domain ([2, Sec. 4.5] and references therein). In the plane wave decomposition modelling, the field defined by Eq. (1.1) is transformed by the objective into

$$\mathbf{E}(\mathbf{r}) = \int_{\mathbf{k}_\parallel \in \mathcal{C}} \sqrt{\frac{k_0}{k_z}}\mathbf{E}(\mathbf{k}_\parallel)\exp(i\mathbf{k}'.\mathbf{r})\mathrm{d}\mathbf{k}_\parallel \tag{1.2}$$

where $\mathcal{C}$ is the $k_0\mathrm{NA}$-radius disk centred in $\mathbf{0}$. NA is the Numerical Aperture, $\mathrm{NA} = n_i \sin a$, where a is the maximum polar angle of the plane waves collected by the objective and efficiently transformed by the imaging system. $\mathbf{k}'$, the wave vector in the image focal domain, is defined by

$$\mathbf{k}' = \left(\frac{k_x}{\mathrm{MF}}, \frac{k_y}{\mathrm{MF}}, \sqrt{k_0^2 - \left(\frac{k_x}{\mathrm{MF}}\right)^2 - \left(\frac{k_y}{\mathrm{MF}}\right)^2}\right).$$

The term $\dfrac{k_0}{k_z}$ has been multiplied by $\sqrt{\dfrac{k_z}{k_0}}$ that stands for the energy conservation [29, Chap. 4].

Classically, a microscope imaging system is composed of two lenses: an objective lens with a short focal length placed close to the sample and an eyepiece (or tube lens) with a longer focal length. There is a specific plane between these two lenses called the Back Focal Plane of the objective. If the objective lens is corrected with the Sine condition, it is performing a Fourier transform between fields on its object focal plane and its back focal planes [30, section 5.2]. Indeed each plane wave going through the object focal plane and the objective is transformed into a wave converging to a point in the back focal plane. Furthermore, each spherical wave emitted from a point on the object focal plane of the objective is transformed into a plane wave passing through the back focal plane. More precisely the field in the back focal plane of the objective is [31]

$$\mathbf{E}_{\mathrm{d,bfp}}\left(\frac{D}{k_0\mathrm{NA}}\mathbf{k}_\parallel\right) = C\sqrt{\frac{k_0}{k_z}}\mathbf{E}_{\mathrm{d}}(\mathbf{k}), \tag{1.3}$$

where C is a constant depending on the objective and D is the diameter of the exit pupil, the illuminated part of the back focal plane which depends on the Numerical Aperture of the objective.

This modelling neglects imperfections of the actual lenses that are not perfectly stigmatic on the whole object focal plane and that have a reduced transmission efficiency for high incident angle. However, since there is no precise data on these imperfections, we will keep this ideal description of the image formation process in the rest of this study.

1.2 Quality criteria defining an optical microscope

Three main criteria are usually studied to describe the quality of a microscope and evaluate its usefulness for a defined application: Resolution, Contrast and Noise.

1.2.1 Resolution

The first interesting criterion is the resolution. It is defined as the size of the smallest detail that can be observed by the microscope. A formal criterion is necessary for defining what means "observed by the microscope". Many criteria have been proposed [32] and the most common are discussed in Sec. 1.3.

Resolution in mainly limited by what is often called the limit of diffraction. Indeed all plane waves emerging from the sample that are either evanescent or whose $\mathbf{k}$ vector has a polar angle superior to a are lost. One defines the **Numerical Aperture** as $\mathrm{NA} = \mathrm{n_i} \sin \mathrm{a}$. In the plane wave decomposition Eq. (1.2), all plane waves whose $\|\mathbf{k}_{\|}\|$ is superior to $k_0\mathrm{NA}$ are lost. This means that the field frequencies above $k_0\mathrm{NA}$ cannot be retrieved. Research is still going on for obtaining higher NA objectives while keeping good aberration correction and to immerse the sample in higher index media (large n_i). For now the highest numerical aperture for commercialised objectives is about 1.5.

Resolution in the axial direction needs a specific attention. For long, the only way to obtain resolution in this direction was to cut the sample in slices, this process being called sectioning. Later were introduced several techniques allowing axial resolution of deep samples, like confocal microscope [3] and Apotome [33], for example. This axial selectivity was called **optical sectioning** or depth discrimination. In this work, we will talk about the axial resolution and compare it to the lateral or transverse resolution (in the (x, y) plane).

1.2.2 Contrast

The contrast of an image measures the possibility to distinguish the sample from the surrounding background. Different definitions of this criterion can be found in the literature. Here we use the one proposed by Michelson [34], that is sufficiently general for our use: $C = \dfrac{I_M - I_m}{I_M + I_m}$, where I_M is the maximum intensity and I_m is the minimum. Depending on the contrast techniques, I_M can be the signal intensity and I_m the background intensity or *vice versa*. Obviously, a value of C close to 1 describes a highly contrasted image while a value close to 0 measures a weakly contrasted image, probably useless for interpretation. However, this criterion actually depends

on the size and shape of the sample. A more quantitative tool is proposed in the next section.

The contrast mechanisms are the interactions between the illumination light and the sample that produces a contrasted intensity pattern on the detector. The first contrast mechanisms used historically were absorption and reflection. However a large part of the interesting samples are transparent or almost transparent. They provide weakly contrasted images when they are illuminated by light in a classical microscope. Thus two main ways have been developed along the years to improve the contrast.

- The first one consists in filling the sample with markers that produces a sufficient contrast in images. One of the main advantage of marking is the possibility to select markers that target chemically a specific component of the sample. It allows the observation of the repartition of this specific component. Further, by using different markers with different spectral behaviour, different chemical components can be imaged simultaneously in the same sample. If historical markers were absorbing colourant, the most widely used nowadays are fluorescent markers. They have the ability to absorb light at a wavelength and to emit at a different wavelength. By using spectral filters, it is possible to remove the illumination field, obtaining thus a contrast equal to 1, whatever the sample. Imaging process with fluorescent markers are described in details in Chap. 2 of this thesis.

- The second one consists in modifying the set-up for getting contrast from the refraction index variations [35, 36, 37]. This is called phase microscopy. It requires the use of interferences and thus specific set-up for illumination and detection of coherent light. This approach requires that the refraction index contrast be higher than the background fluctuations.

1.2.3 Noise

The third criterion is the noise strength. Noise deteriorates the image and prevents the observation of the finest details. The criterion ordinarily used to estimate this issue is the Signal-to-Noise Ratio $\mathrm{SNR} = \langle I \rangle / \sigma_b$, where $\langle I \rangle$ is the average signal and σ_b is the noise standard deviation. There are two types of noises. First a noise that does not depend on the sample. It has a constant statistic over the whole image. It is ordinary modelled as a white Gaussian process since it is the sum of several sources of noise (thermal signal, electronic amplification, data transmission between the camera and the computer, ...) that apply independently on each pixel of the camera. The second one is the shot-noise. It is due to the statistical nature of light emission by matter. For a certain intensity, the number of photons that reach a pixel camera follows a Poisson statistics. When the number of photons is larger than 10, a good approximation of this statistic is a Gaussian statistic whose standard deviation is $\sqrt{N}$, where N is the average number of photons. It is clear from this discussion that SNR is high for high intensity and low for low intensity. This is an important point to keep in mind while comparing contrast techniques. Indeed absorbing markers and phase contrast provide very bright images for moderate contrast, whereas fluorescent markers have a perfect contrast but a limited brightness. Noise is thus, in most cases, a limiting factor in fluorescence microscopy.

1.3 Transfer function

Analysis of the resolution, contrast and noise provides a useful description of the microscope performance. However one would prefer a general quantitative criterion. Now, when there is a linear relation between the sample function of interest O and the image, the **Transfer Function** appears to be an ideal tool. Indeed, in this case, the image M is the convolution of the function of interest O by a certain point-spread-function h

$$M = O * h.$$

Basically, h represents the image of a point object which is assumed to be same, whatever the position of the object.

The **Transfer Function** is the Fourier transform $\tilde{h}$ of this convolution function. The Fourier transform of M and O fullfills $\tilde{M} = \tilde{O}\,\tilde{h}$. $\tilde{h}$ is thus the filter applied to $\tilde{O}$ during the measurement process.

One of the main characteristic of a Transfer Function $\tilde{h}$ is its support, namely the region of the Fourier space where it is non-null. This defines the frequencies of O that are accessible in the measurements. In microscopy, $\tilde{h}$ is usually a low-pass filter and it is null beyond a bounded Fourier domain about the $\mathbf{0}$ frequency. All the object frequency information inside this Fourier domain is transmitted to the image M. All the frequency information that are outside this Fourier domain is lost. The radius of the support of the Transfer Tunction is called the frequency cut-off.

An important interpretation of the Transfer Function is the image contrast of sinusoidal patterns. Actually $\tilde{h}(\mathbf{k})$ is the image contrast of a sample whose quantity of interest is $1 + \cos(\mathbf{k}.\mathbf{r})$. This links the notion of Transfer Function with the more classical limit of resolution. The Rayleigh criterion is obtained when the minimum intensity I_m is $8/\pi^2$ of the maximum intensity I_M. This gives a contrast $C \approx 0.10$. Thus the resolution corresponding to the Rayleigh criterion is the period of the sinusoidal pattern whose image has a contrast of 0.10. The Sparrow criterion is when the contrast reaches 0. A resolution according to the Sparrow criterion is thus the inverse of the frequency cut-off. Actually the resolution, for each criterion, is often not the same in every directions. One thus defines a resolution along each principal axis.

The Transfer Function is a lot more complete than a simple limit of resolution since it provides a whole curve of contrast with respect to the spatial frequency. It allows for example the definition of a resolution criterion with respect to noise. A detail becomes detectable when its contrast is greater than the noise level. The resolution can then be defined as the period for which the contrast is equal to the inverse of the SNR [38].

As will be seen later, a Transfer Function linking the density of fluorescent markers and the intensity collected by the detector can be derived in fluorescence microscopy. Similarly, a transfer function linking the actual sample permittivity to the reconstructed permittivity can be obtained for Tomographic Diffraction Microscopy, under the single scattering approximation (weakly scattering sample). On the contrary, there is no linear relationship between the sample permittivity and the recorded image in ordinary incoherent illumination microscopy [39][2, Sec. 10.6], or in Tomographic Diffraction Microscopy in presence of multiple scattering. In these cases, defining a transfer function is not possible and only *ad-hoc* comparison between test samples can give a hint on the performances of the imaging systems.

1.4 'Super-resolution' techniques based on image treatment

In most modern techniques, images are produced by a computer. It is then natural to wonder if this computer can improve images. Indeed, there is a whole range of de-noising and deconvolution algorithms, using the experimental Transfer Function, which can improve the contrast or the SNR of the image. Yet, the frequency cut-off due to the bounded support of the Transfer Function remains. To improve the resolution, it is necessary to introduce *a priori* knowledge on the sample.

The simplest and most common *a priori* information on the sample is to assume that it is included in a box of finite size. In this case, it can be shown that the Fourier Transform of the object function is analytic. Now, the knowledge of this analytic function on a disk with radius the frequency cut-off is sufficient to extrapolate its value on all the Fourier space by analytic continuation. This means that one could, in principle, obtain a perfect reconstruction of the sample (see [30, Sec. 6.6] for a more formal demonstration and further discussion). This property is at the basis of many super-resolution theories that were mainly discussed in the 70's. Unfortunately, it appeared that the presence of noise prevented almost all practical implementations.

To explain the fundamental limit of all these numerical "superresolution" techniques, the notion of **Degree of Freedom** of an image has been derived for coherent absorption microscopy [40, 41] and then extended to other forms of microscopy [42, 43]. One decomposes the linear operator that links the object quantity of interest to the recorded images using a Singular Value Decomposition (SVD). Namely, one builds an orthogonal basis of functions in the sample domain (sample eigenvectors) whose images through the operator form an orthogonal basis of the image plane (image eigenvectors). With a correct normalisation, only a few of the image eigenvectors are above the noise level. The number of detectable sample eigenvectors yields the Degree Of Freedom of the imaging system. Whatever the numerical treatment applied to the image, sole the detectable sample eigenvectors can be recovered.

This point of view explains why the super-oscillating fields (see for example [44]) recently evoked to perform super-resolution imaging are likely to fail. This technique is based on the well known observation (basically that at the basis of Toraldo rings) that a suitable combination of propagative plane waves can generate a light spot much smaller than the diffraction limit, provided that most of the energy is pushed out of the chosen field-of-view. An SVD analysis between the space of the incident plane wave amplitudes and the space of the bounded observation domain shows that the tiny spot is obtained with singular eigenvectors that have very small singular values, as most of the eigenvectors energy is pushed out of the bounded observation domain [45]. Thus, even a very small amount of noise (such as scattering in the sample) is sufficient to prevent its formation.

A specific attention has now to be drawn to the use of positivity *a priori* information. Indeed, the values taken by the object function being often bounded, this *a priori* information is used in many deconvolution algorithms (and in particular in part III of this thesis). For example, the density of fluorescent markers is physically positive and the relative permittivity of dielectric media has its real part superior to 1 and its imaginary part positive. Including this *a priori* information improves clearly the visual aspect and the apparent resolution of the reconstructed image, but may lead to artefacts or disappearance of interesting details. Sementilli *et al.* [46] proposed a method to evaluate the frequency radius up to which the Fourier components of the sample are correctly retrieved using this *a priori* information. For large field-of-view and

common noise level there is almost no amelioration of the frequency cut-off.

Last, one may consider more stringent *a priori* information. For example, one can assume that the sample consists in lines or tubes or presents a high level of sparsity. In its most extreme version, the sample can be assumed to be constituted of isolated emitters. In this case, one can localise, detect and separate two of them even if they are a lot closer than the resolution limit [23, 47, 48]. However, whatever the *a priori* information information added, one cannot decompose the sample images on a set of components larger than the Degree of Freedom [40, 49, 50]. The key point for high-resolution imaging is thus the development of technical solutions insuring that only few of these components contribute to each of the measurements. Promising recent super-resolution microscopy approaches (PALM, STORM in particular) are based on this idea.

1.5 High spatial frequencies measurements: the structured illumination approach

Since one cannot rely on bare numerical treatments for improving resolution, one has to find a physical process to extract information on the sample high frequencies. A simple and widely spread technique, which can be applied to any contrast mechanism, is to use spatially inhomogeneous illuminations [11]. Noting P the illumination or probing function, (P depends on the chosen light-matter interaction, it corresponds to the incident field intensity in one-photon fluorescence microscopy and to the incident field in tomographic diffraction microscopy), and O the sample contrast distribution (which is either the fluorescence density or the relative permittivity respectively), the radiated signal is often proportional to the product OP. The imaging system does not act on the sample function O itself, but on this product, so that the recorded image is given by $M = (OP) * h$.

The convolution theorem states that the Fourier transform of a product is the convolution of the Fourier transforms,

$$\tilde{M} = (\tilde{O} * \tilde{P})\tilde{h}.$$

Using an inhomogeneous probing P, information on some of the high frequencies of O are moved inside the measurements M. To separate the contributions of O and P in the filtered product, one takes several measurements with several probing fields: $M_n = (OP_n) * h$. The sample contrast distribution O is then recovered from the many recorded images using a numerical treatment.

1.5.1 Scanning microscopy

The oldest method using this structured illumination approach is scanning microscopy. The inhomogeneous illumination is a light spot obtained by focusing a wave into the smallest possible volume. This spot is then moved all over the sample. Noting $P(\mathbf{r}_0, \mathbf{r}) = P(\mathbf{r}_0 - \mathbf{r})$, the illumination function produced in $\mathbf{r}$ when focussing on $\mathbf{r}_0$, the field in the image space is

$$M(\mathbf{r}_0, \mathbf{r}) = [O(\mathbf{r})P(\mathbf{r}_0 - \mathbf{r})] * h(\mathbf{r}). \tag{1.4}$$

One can easily show that

$$M(\mathbf{r}_0, \mathbf{r}_0) = O(\mathbf{r}_0) * (h(\mathbf{r}_0)P(\mathbf{r}_0)). \tag{1.5}$$

Equation (1.5) is the at the basis of confocal microscopy [3]. This microscopy technique proposes to focus a laser beam, thanks to a microscope objective, on a point $\mathbf{r}_0$ of the sample, and to detect through the same objective the light radiated by the same point. This technique exhibits an effective point-spread-function $h_{\text{eff}} = hP$ and an effective Transfer Function $\tilde{h}_{\text{eff}} = \tilde{h} * \tilde{P}$.

Further improvements can be obtained by collecting the whole light information of Eq. (1.4) [51, 52, 53, 54, 55, 56, 57] or by diminishing the size of the probing function P, in shaping the incident beam [58, 5, 59, 60], using non-linear contrast mechanisms [24, 25], or near-field evanescent waves at the surface of nano-structured substrates [9, 61, 62, 63, 48].

1.5.2 Pattern projection

In the second important implementation of the structured illumination principle, the inhomogeneous probing functions P_n stretch over all the sample. The sample is not scanned by a spot but illuminated successively under many different illumination patterns. This wide-field approach requires a complex numerical treatment of the different images to extract a correct estimation of O.

The most classical illumination pattern is sinusoidal [33, 13, 12]: $P_n(\mathbf{r}) = 1+\cos(\mathbf{K}.\mathbf{r}+\phi_n)$, where $\mathbf{K}$ is the vector of the sinusoidal pattern and ϕ_n is a phase that has to be different for each illumination. This pattern is usually obtained via the interference of two coherent collimated beams.

In this case, the Fourier transform of the images $M_n = (OP_n) * h$ fullfills

$$\tilde{M_n}(\mathbf{k}) = \left[\tilde{O}(\mathbf{k}) * \left(\delta(\mathbf{k}) + \frac{1}{2}\exp(i\phi_n)\delta(\mathbf{k}+\mathbf{K}) + \frac{1}{2}\exp(-i\phi_n)\delta(\mathbf{k}-\mathbf{K})\right)\right]\tilde{h}(\mathbf{k}) \quad (1.6)$$

$$= \left(\tilde{O}(\mathbf{k}) + \frac{1}{2}\exp(i\phi_n)\tilde{O}(\mathbf{k}+\mathbf{K}) + \frac{1}{2}\exp(-i\phi_n)\tilde{O}(\mathbf{k}-\mathbf{K})\right)\tilde{h}(\mathbf{k}) \quad (1.7)$$

$$= \tilde{M_n^0}(\mathbf{k}) + \exp(i\phi_n)\tilde{M_n^+}(\mathbf{k}) + \exp(-i\phi_n)\tilde{M_n^-}(\mathbf{k}). \quad (1.8)$$

It is clear that $\tilde{M_n^0}(\mathbf{k}) = \tilde{O}(\mathbf{k})\tilde{h}(\mathbf{k})$ is the image that would be obtained under an homogeneous illumination and contains only the low frequencies of the object. On the contrary $\tilde{M_n^\pm}(\mathbf{k}) = \tilde{O}(\mathbf{k} \pm \mathbf{K})\tilde{h}(\mathbf{k})$ contains frequencies of O around the $\pm\mathbf{K}$ frequency. Using three different ϕ_n it is possible to separate these three components and to reconstruct $\tilde{O}$ in a Fourier domain that is larger than the support of $\tilde{h}$. The resulting Transfer Function depends on h and on $\mathbf{K}$. The same process can be repeated for different orientations of $\mathbf{K}$ in order to get an isotropic improvement.

1.6 Conclusion

In this introductory chapter, we explain the basics of the image formation in a microscope, we describe the main criteria used for the analysis of the imaging system performances, in particular the notion of Transfer Function, and we discuss several means for ameliorating the resolution. In this framework, we insist on the concept of structured illumination as its two main forms, the scanning microscopy and the pattern projection, are at the basis of the work described in parts II and III. In the following two chapters, we present in more details the principle of fluorescence microscopy and that of Tomographic Diffraction Microscopy. In both

cases, we give the analytical expression of their Transfer Function in order to thoroughly model the functioning and performances of the imaging system.

Chapter 2

Basics of fluorescence microscopy

2.1 Fluorescence contrast mechanisms

Fluorescence is one of the leading contrast technique for biology since it allows selective imaging with a high contrast. A fluorescent marker is a molecule or a system that is able to absorb energy from an incident field at a certain wavelength and to re-emit it later on at another wavelength. This time delay implies that this emission is totally incoherent, *i.e.* the phase and direction of the emission is random and independent of the absorption. This time delay is about several ns, short enough to be neglected in the imaging process.

Since excitation and emission occur at different wavelengths, it is possible to filter out the excitation light which ensures a nearly perfect contrast. Moreover, it is possible to fix these markers to specific targets and thus to image a specific chemical component of the sample.

When the excitation intensity received by the fluorescent marker is low, the emitted intensity is proportional to the excitation intensity surrounding it [64]: $I_{\mathrm{out}} = \sigma I_{\mathrm{ext}}$, where I_{out} is the intensity emitted by the marker and I_{ext} is the intensity of the field at the absorption wavelength and at the position of the marker. The coefficient σ expresses the efficiency of the marker. In this study, we assume that the fluorescence process follows this linear regime.

Ordinary fluorescent markers are a lot smaller than the resolution reachable in optical microscopy. It is generally possible to consider a collection of markers diluted in a sample as a continuous density. One defines the function ρ of the space position $\mathbf{r}$ such that $\rho(\mathbf{r})\mathrm{d}\mathbf{r} = \sum_{l=1}^{L} \sigma_l$, where L is the number of markers in the small volume $\mathrm{d}\mathbf{r}$ and σ_l is the emission coefficient of the l-th fluorophore. However this modelling neglects three issues,

- Bleaching: The coefficient σ actually decreases with time. More precisely, its decay is proportional to its emitted energy I_{out} [65].

- Blinking: Besides this decay, there is a quick fluctuation of σ versus time. This fluctuation is useful for techniques like PALM and STORM [23] and is at the basis of SOFI [66]. Here, we assume that the integration time is long enough to average this variation.

- Near-Field interactions: The coefficient σ of a fluorophore is actually influenced by its surroundings [67, 68]. For example, the emission of a single marker close to a mirror depends on its position with respect to the mirror.

In the theoretical study developed in this work, these effects are neglected and they constitute the main sources of error of the model.

2.2 Image formation

The model of image formation in fluorescence microscopy assumes the total independence and incoherence of the light emitted by each fluorescent marker. The intensity measured by the detector is the sum of the intensity emitted by each fluorophores.

$$M = (\rho I_{\text{ext}}) * h, \tag{2.1}$$

where h is the intensity distribution created on the detector by a single dipole emitter placed in the centre of the coordinate system with total emitted intensity 1. The measurements are performed on a planar detector placed at the image focal plane of the microscope. As discussed in Sec. 1.1.2, it is the only plane were the imaging system is stigmatic. Thus, the recorded intensity at (x, y) on the detector can be modelled as,

$$\begin{aligned} M(x,y) &= [(\rho I_{\text{ext}}) * h]_{z=0} && (2.2)\\ &= \int_{\mathbb{R}^3} \rho(x',y',z') I_{\text{ext}}(x',y',z') h(x-x', y-y', 0-z') \mathrm{d}x'\mathrm{d}y'\mathrm{d}z'. && (2.3) \end{aligned}$$

For obtaining a three-dimensional image, it is not possible to scan the detector through the image space. Indeed images are aberrated for all planes but that at $(z = 0)$. Instead, the sample is scanned vertically through the focal plane. Defining $M(x, y, z_0)$ the image recorded when the sample has been drifted vertically by $-z_0$, one gets,

$$M(x,y,z_0) = \int_{\mathbb{R}^3} \rho(x',y',z'+z_0) I_{\text{ext}}(x',y',z') h(x-x', y-y', -z') \mathrm{d}x'\mathrm{d}y'\mathrm{d}z'. \tag{2.4}$$

This equation is the fundamental relation that describes the image formation in three-dimensional fluorescence microscopy.

In the particular and widely spread case where the illumination is homogeneous over the sample, $I_{\text{ext}} = constant$, one obtains,

$$M(x,y,z_0) = I_{\text{ext}} \int_{\mathbb{R}^3} \rho(x',y',z'+z_0) h(x-x', y-y', -z') \mathrm{d}x'\mathrm{d}y'\mathrm{d}z'. \tag{2.5}$$

Noting $z'' = z' + z_0$ yields to,

$$M(x,y,z_0) = I_{\text{ext}} \int_{\mathbb{R}^3} \rho(x',y',z'') h(x-x', y-y', z_0-z'') \mathrm{d}x'\mathrm{d}y'\mathrm{d}z''. \tag{2.6}$$

This result can be summarized by the compact formula,

$$M = I_{\text{ext}}(\rho * h), \tag{2.7}$$

where $I_{\text{ext}}h$ is the effective point-spread-function of the wide-field fluorescence microscopy.

In structured illumination techniques I_{ext} is spatially in-homogeneous over the sample. The link between ρ and the measurement depends on the variations of the illumination intensity patterns with respect to the vertical scanning. In cases where I_{ext} is invariant along the **z** direction, one deduces from Eq. (2.4) that

$$M = (\rho I_{\text{ext}}) * h. \tag{2.8}$$

2.3 Point-spread-function modelling

Modelling accurately the Point-Spread Function h (PSF) is generally not possible since the latter depends on optical components (objective, ocular) that are not well known. Yet, one can derive a simple approximated expression which is enough to give useful information. By definition, h is the intensity distribution radiated on the detector by a single dipole emitter, placed at the crossing between the optical axis and the object focal plane, with total emitted intensity 1. Strictly speaking, the actual PSF h depends on the orientation of the emitter. Yet, in most cases, in the small volume $\mathrm{d}\mathbf{r}$, there are several emitters each oriented in a different direction and they are spinning during each measurements. For this reason, one assumes that the "model" fluorescent marker emits a perfectly spherical scalar field, this scalar field representing the average of the radiated vectorial field components over all polarisations.

The spherical scalar field can be decomposed as a sum of plane waves emerging from the emitter, all of them having a zero phase at the marker position $P = (0, 0, 0)$. From ref. [2, Sec. 13. 2] this spherical scalar field can be written under the Weyl decomposition as,

$$E(\mathbf{r}) = \frac{\exp(ik_0 r)}{4\pi r} = \frac{i}{8\pi^2} \int_{\mathbf{k}_\parallel \in \mathbb{R}^2} \frac{1}{k_z} \exp(i\mathbf{k}.\mathbf{r}) \mathrm{d}\mathbf{k}_\parallel, \tag{2.9}$$

where $\mathbf{k}_\parallel = k_x\mathbf{x} + k_y\mathbf{y}$ is the projection of $\mathbf{k}$ on the (x, y) plane, and

$$k_z = \begin{cases} \sqrt{k_0^2 - \|\mathbf{k}_\parallel\|^2} & \text{if} \|\mathbf{k}_\parallel\| \leq k_0, \\ i\sqrt{\|\mathbf{k}_\parallel\|^2 - k_0^2} & \text{if} \|\mathbf{k}_\parallel\| \geq k_0. \end{cases} \tag{2.10}$$

As explained in Sec. 1.1.2, all plane waves that are either evanescent ($\|\mathbf{k}_\parallel\| \geq k_0$) or whose polar angle with respect to the optical axis θ is superior to the maximum angle a are lost. The others are collected by the objective. In the spherical coordinates basis where $k_x = k_0 \sin\theta\cos\phi$, $k_y = k_0 \sin\theta\sin\phi$, $k_z = k_0\cos\theta$, the collected field reads,

$$\begin{aligned} E_{\text{collected}}(\mathbf{r}) &= \frac{i}{8\pi^2} \int_{\theta\in[0,a]} \int_{\phi\in[0,2\pi]} \frac{1}{k_0\cos\theta} \exp(i\mathbf{k}.\mathbf{r}) k_0^2 \sin\theta\cos\theta \mathrm{d}\theta\mathrm{d}\phi \\ &= \frac{i}{8\pi^2} \int_{\theta\in[0,a]} \int_{\phi\in[0,2\pi]} \exp(i\mathbf{k}.\mathbf{r}) k_0 \sin\theta \mathrm{d}\theta\mathrm{d}\phi. \end{aligned} \tag{2.11}$$

2.3.1 Two-dimensional PSF

In this paragraph, one assumes that the sample thickness is small in comparison to the wavelength λ. It is thus unnecessary to scan the sample vertically and the measurements are linked to the two-dimensional surface density of fluorophores by a two-dimensional PSF. This restrictive model, which is appropriate for samples that have been physically sectioned in thin slices, is interesting because it leads to an analytical formula for the PSF. It will be used throughout all the work of Chap. 6.

One notes $\mathbf{r}' = (x', y')$ an orthogonal coordinate system centred at the crossing between the optical axis and the image focal plane and $(x, y) = (x'/\mathrm{MF}, y'/\mathrm{MF})$ a coordinate system that reduces all dimensions to fit the actual dimensions of the sample.

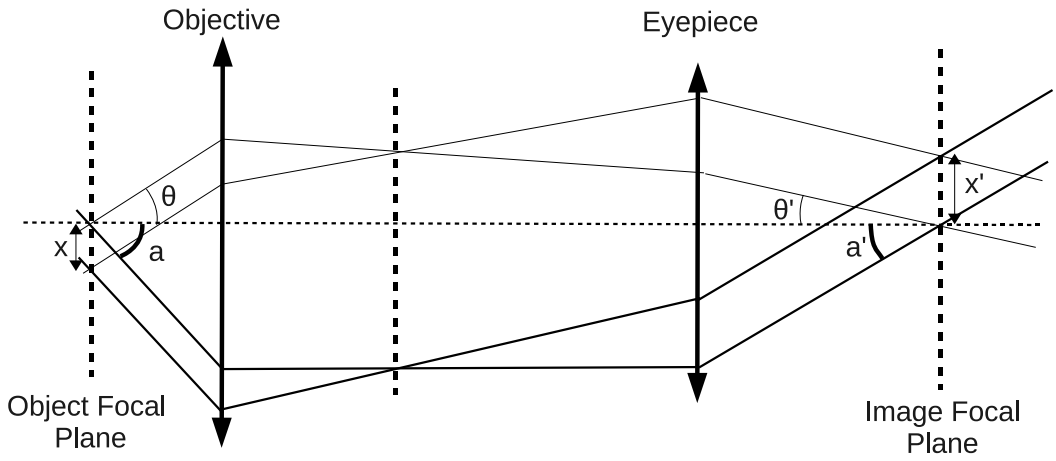

Figure 2.1: Sketch of the geometrical notations used for the point-spread-function modelling.

Under the Sine-Abbe condition, each plane wave, with wave vector $\mathbf{k} = (k_0, \theta, \phi)$ radiated by the emitter placed at P in the object focal plane is transformed into a plane wave with wave vector $\mathbf{k}' = (k_0, \theta', \phi)$, such that $\sin\theta = \mathrm{MF}\sin\theta'$ at the image focal plane and a complex amplitude dimmed by the $\sqrt{\cos\theta}$ factor. All the plane waves in the image domain interfere constructively at $P' = (0, 0)$, the conjugate point of P through the whole imaging system. Noting a', $\sin a = \mathrm{MF}\sin a'$, the maximum angle of the plane waves reaching the detector plane (Figure 2.1 illustrates the notations) the field obtained at the image focal plane reads [29, Chap. 4],

$$\begin{aligned} E(x', y') &= \frac{i}{8\pi^2}\int_{\theta'\in[0,a']}\int_{\phi\in[0,2\pi]} \exp(i\mathbf{k}'.\mathbf{r}')\sqrt{\cos\theta}k_0\sin\theta'\mathrm{d}\theta'\mathrm{d}\phi \qquad (2.12)\\ &= \frac{i}{8\pi^2}\int_{\theta'\in[0,a']}\int_{\phi\in[0,2\pi]} \exp\left[ik_0\sin\theta'(x'\sin\phi + y'\cos\phi)\right]\sqrt{\cos\theta}k_0\sin\theta'\mathrm{d}\theta'\mathrm{d}\phi. \end{aligned}$$

Expressing this field in terms of the coordinate $(x, y) = (x'/\mathrm{MF}, y'/\mathrm{MF})$ and using $\sin\theta = \mathrm{MF}\sin\theta'$ and $\mathrm{d}\theta' = \cos\theta/\sqrt{\mathrm{MF}^2 - \sin^2\theta}\mathrm{d}\theta$, leads to,

$$\begin{aligned} E(x, y) &= \frac{i}{8\pi^2}\int_{\theta\in[0,a]}\int_{\phi\in[0,2\pi]} \exp\left[ik_0\sin\theta(x\sin\phi + y\cos\phi)\right]\\ &\times \frac{k_0}{\mathrm{MF}^2}\frac{\sqrt{\cos\theta}}{\sqrt{1-\sin^2\theta/\mathrm{MF}^2}}\sin\theta\cos\theta\mathrm{d}\theta\mathrm{d}\phi \qquad (2.13)\\ &= \frac{ik_0}{\mathrm{MF}^2 4\pi}\int_{\theta\in[0,a]} J_0(k_0 r\sin\theta)\frac{\sqrt{\cos\theta}}{\sqrt{1-\sin^2\theta/\mathrm{MF}^2}}\sin\theta\cos\theta\mathrm{d}\theta, \qquad (2.14) \end{aligned}$$

where $r = \sqrt{x^2 + y^2}$.

Neglecting the $\sqrt{\cos\theta}/\sqrt{1-\sin\theta^2/\mathrm{MF}^2}$ factor, that is about 1 for low numerical aperture, one gets for the scalar field E and the intensity per surface unit $I = |E|^2$ ([2, Sec. 8.5.2],

$$\begin{aligned} E(\mathbf{r}) &= \frac{ik_0\mathrm{NA}^2}{\mathrm{MF}^2 4\pi}\frac{J_1(k_0\mathrm{NA}r)}{k_0\mathrm{NA}r} \qquad (2.15)\\ I(\mathbf{r}) &= \left(\frac{k_0\mathrm{NA}^2}{\mathrm{MF}^2 4\pi}\right)^2\left(\frac{J_1(k_0\mathrm{NA}r)}{k_0\mathrm{NA}r}\right)^2. \qquad (2.16) \end{aligned}$$

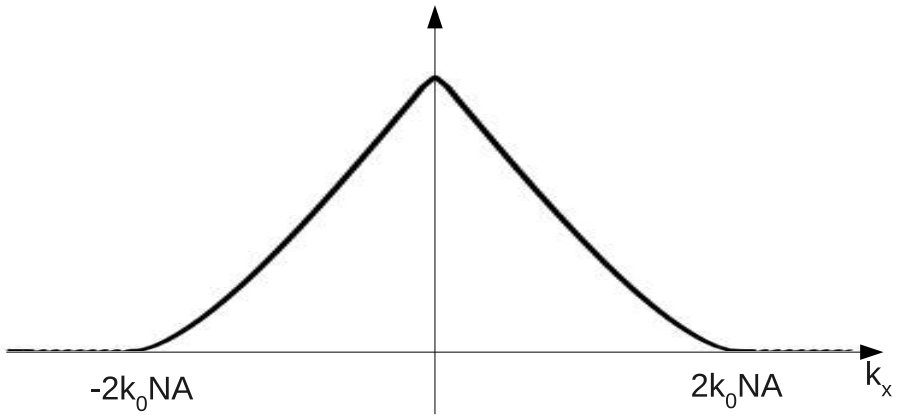

Figure 2.2: Radial cut of the Transfer Function of a fluorescent microscope imaging a 2D sample.

The expression Eq. (2.16) is approximative but it presents the main characteristics of the actual experimental PSF. Note that it can be seen as a Fourier transform operating on the 2D support function of a disk centred at **0** with radius $k_0\mathrm{NA}$. Thus, the detected field $E(\mathbf{r})$ does not contain frequencies beyond $k_0\mathrm{NA}$ and $I(\mathbf{r}) = |E(\mathbf{r})|^2$ does not contain frequencies beyond $k_c = 2k_0\mathrm{NA}$. Equation (2.16) gives a resolution of $0.61\lambda/\mathrm{NA}$ for the Rayleigh criterion. The Fourier transform of Eq. (2.16) is the Transfer Function of the imaging system and can be seen as a low-pass filter. Its radial cut is plotted in Fig. 2.2. It decays continuously as the spatial frequency increases and exhibits a non derivable peak at zero frequency.

2.3.2 Full three-dimensional PSF

To model the actual three-dimensional PSF, one has to consider the contribution of fluorophores that are out of the object focal plane. The intensity map on the detector depends on their axial position. We define the 3D PSF as the 3D image created by scanning a single emitter along the optical axis. Let's consider an emitter placed at the axial position $-z$ from the focal plane. It emits a spherical field which can be decomposed as a sum of plane waves with constant amplitude and zero phase at the emitter position, leading to a phase accumulation of $k_0 z\cos\theta$ at the focal plane [31]. Using Eq. (2.13) the field generated in the image plane is [29, Chap. 4],

$$\begin{aligned} E(x,y,z) &= \frac{ik_0}{\mathrm{MF}^2 8\pi^2}\int_{\theta\in[0,a]}\int_{\phi\in[0,2\pi]} \exp\left[ik_0\sin\theta(x\sin\phi + y\cos\phi) + ik_0 z\cos\theta\right] \\ &\times \frac{\sqrt{\cos\theta}}{\sqrt{1-\sin^2\theta/\mathrm{MF}^2}}\sin\theta\cos\theta\mathrm{d}\theta\mathrm{d}\phi. \end{aligned} \tag{2.17}$$

This expression can be seen as a Fourier transform operated on a finite part of 3D spatial frequency space: the part of the sphere of radius k_0 centred in **0**, whose inclination angle with respect to the optical axis verifies $\theta \leq a$ (see Fig. 2.3 (a)). Then, the intensity $I(x,y,y) = |E(x,y,z)|^2$ is the inverse Fourier transform of the autocorrelation of a function defined on this cap of sphere. Hence, the frequencies of I are contained in the eye-shaped torus whose (x,z) cut is represented in Fig. 2.3 (b).

Note that the $(k_z = 0)$ cut of the 3D support of the Transfer Function is exactly that of the 2D Transfer Function. One observes that the k_z extension of the 3D support when $(k_x = 0, k_y = 0)$

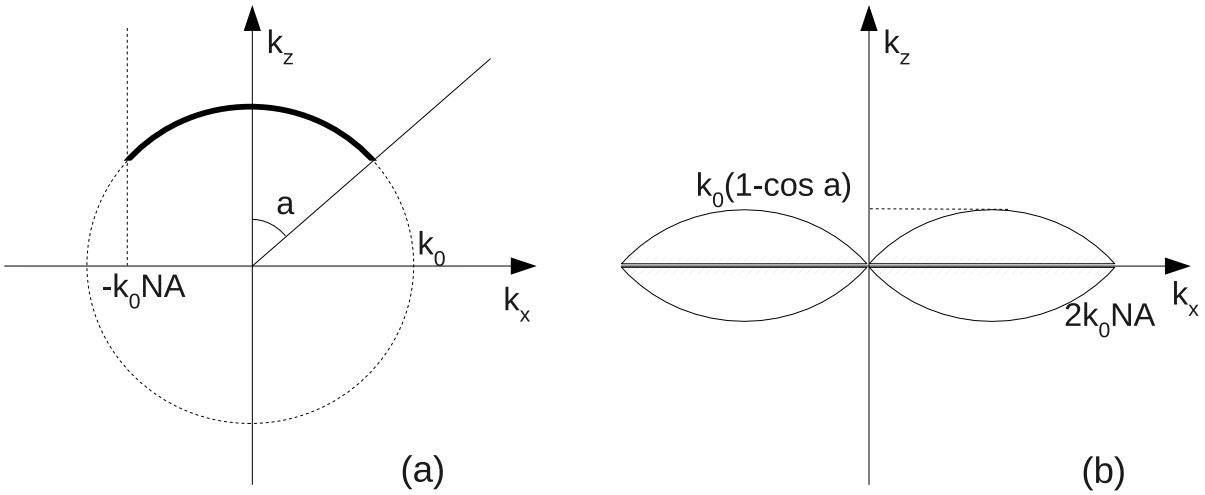

Figure 2.3: Sketch of the (k_x, k_z) cut of the support of the Fourier Transform of the 3D PSF. (a) Support of the Fourier Transform of the electric field repartition E. a is the maximum angle accessible through the objective. The dotted circle is the (k_x, k_z) cut of the k_0-radius sphere called the Ewald Sphere. (b) Support of the Fourier Transform of the intensity repartition I, autocorrelation of (a) and transfer function of the detection.

is infinitely small. This last property implies that, whatever the z position of an emitting plane, its average light-intensity arrives unattenuated on the detector. In practical situations, this out-of-focus contribution dramatically dims the image contrast. Moreover, the global extension along the k_z direction of the Transfer Function is much smaller than that obtained along the k_x and k_y directions, see Fig. 2.3. Thus, the axial resolution is expected to be much worse than the lateral resolution.

2.4 Conclusion

In this chapter, a model describing the three-dimensional image formation in a classical fluorescence microscope is derived. The expression of the Transfer Function is given in the two-dimensional and three-dimensional configuration. This study stresses the need for sectioning techniques for improving the axial resolution. Imaging of deep three-dimensional samples is indeed almost impossible in a classical wide-field fluorescence microscopy.

This chapter is an introduction to the two studies we led on fluorescence microscopy. The first one, presented in Chap. 5, proposes an improvement of confocal fluorescence microscopy by placing a mirror behind the sample. The second one, presented in Chap. 6, is devoted to structured illumination fluorescence microscopy.

Chapter 3

Tomographic Diffraction Microscopy

Tomographic Diffraction Microscopy (TDM) is a technique that has been described 40 years ago [69][2, section 13.2] but that has waited until recent years to see experimental realisations in optics. It consists in recording the field (amplitude and phase) diffracted by a sample for many different illuminations and to reconstruct numerically the sample relative permittivity from the stack of complex data. This method is an extension of digital holography in which the sample is illuminated by a collimated coherent beam (a plane wave), and an interferometric mounting is used to record an hologram of the diffracted field. In Tomographic Diffraction Microscopy, the angles of illumination are varied and several holograms are recorded.

In this chapter, the relationship between the sample relative permittivity and the diffracted field is derived in the electromagnetism framework. Then, the existence of a Transfer Function under the Born approximation is discussed. Finally, several experimental implementations of TDM are presented and compared.

3.1 Diffraction process

The field surrounding an object placed in vacuum and illuminated by an incident monochromatic electromagnetic wave satisfies the Maxwell equations,

$$\nabla . \mathbf{D} = 0, \tag{3.1}$$

$$\nabla . \mathbf{B} = 0, \tag{3.2}$$

$$\nabla \times \mathbf{B} = \mu_0(\mathbf{J} - i\omega\mathbf{D}), \tag{3.3}$$

$$\nabla \times \mathbf{E} - i\omega\mathbf{B} = \mathbf{0}, \tag{3.4}$$

where $\mathbf{J}$ is the source current that generates the incident electromagnetic wave, $\mathbf{E}$ is the electric field, $\mathbf{B}$ is the magnetic field, μ_0 is the vacuum magnetic permeability. The displacement field $\mathbf{D}$ is linked to $\mathbf{E}$ by

$$\mathbf{D} = \varepsilon_0\mathbf{E} + \mathbf{P}, \tag{3.5}$$

where $\mathbf{P}$ is the polarisation vector field and ε_0 is the vacuum permittivity. Inserting Eqs. (3.3) and (3.5) in $\nabla\times$(3.4), one obtains

$$\nabla \times (\nabla \times \mathbf{E}) - k_0^2\mathbf{E} = i\omega\mu_0\mathbf{J} + \omega^2\mu_0\mathbf{P}, \tag{3.6}$$

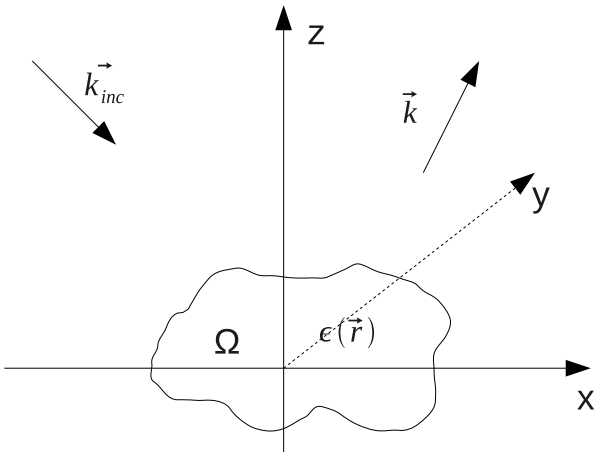

Figure 3.1: Sketch of the general principle of Tomographic Diffraction Microscopy. The sample contained in the volume Ω with a space-dependent relative permittivity $\varepsilon(\mathbf{r})$ is illuminated successively with plane waves with wave vector $\mathbf{k}_{\text{inc}}$. For each incident plane wave, one measures the diffracted field for many $\mathbf{k}$ directions.

where $k_0 = \omega/c$ for $c = 1/\sqrt{\varepsilon_0\mu_0}$. $\mathbf{P}$ models the light-matter interaction and governs the interaction between the object and the incident wave. For a linear interaction, $\mathbf{P} = \varepsilon_0\chi\mathbf{E}$, where χ is the space dependent linear susceptibility of the object. The linear susceptibility is also called the permittivity contrast as $\chi = \varepsilon - 1$, where $\varepsilon(\mathbf{r})$ is the relative permittivity, *i. e.* the square of the complex refractive index of the object.

To pursue further our analysis, we now assume that the object, described by its complex relative permittivity $\varepsilon(\mathbf{r})$ and contained in the finite volume Ω is illuminated by an incident field $\mathbf{E}_{\text{inc}}$. $\mathbf{E}_{\text{inc}}$ is the field created by the current $\mathbf{J}$ that would exist in absence of the sample, *i. e.* when $\mathbf{P} = \mathbf{0}$. The incident field satisfies the equation,

$$\nabla \times (\nabla \times \mathbf{E}_{\text{inc}}) - k_0^2\mathbf{E}_{\text{inc}} = i\omega\mu_0\mathbf{J}. \tag{3.7}$$

One defines the diffracted field $\mathbf{E}_{\text{d}}$ as the difference between the total field $\mathbf{E}$ and the incident field, $\mathbf{E}_{\text{d}} = \mathbf{E} - \mathbf{E}_{\text{inc}}$. Subtracting Eq. (3.7) from Eq. (3.6) one gets,

$$\nabla \times (\nabla \times \mathbf{E}_{\text{d}}) - k_0^2\mathbf{E}_{\text{d}} = \omega^2\mu_0\mathbf{P}, \tag{3.8}$$

with $\mathbf{P} = \varepsilon_0\chi\mathbf{E}$. This equation allows the computation of the diffracted field from the knowledge of the polarisation field $\mathbf{P}$. As it is a linear equation, we can solve it using the Green's function technique.

The Green's tensor $\bar{\mathcal{G}}$ of Eq. (3.8) is defined such that $\bar{\mathcal{G}}(\mathbf{r}, \mathbf{r}')\mathbf{p}$ is the field created at $\mathbf{r}'$ by an infinitely small dipole emitter $\mathbf{p}$ placed at $\mathbf{r}$. Thus, $\bar{\mathcal{G}}(\mathbf{r}, \mathbf{r}')\mathbf{p}$ is solution of

$$\nabla \times \Big(\nabla \times \bar{\mathcal{G}}(\mathbf{r}, \mathbf{r}')\mathbf{p}\Big) - k_0^2\bar{\mathcal{G}}(\mathbf{r}, \mathbf{r}')\mathbf{p} = \delta(\mathbf{r} - \mathbf{r}')\mathbf{p}. \tag{3.9}$$

The outgoing solution for the Green's function is [1, section 9.2]

$$\bar{\mathcal{G}}(\mathbf{r}, \mathbf{r}')\mathbf{p} = -\frac{1}{4\pi k_0^2}\nabla \times \nabla \times \left(\frac{\exp(ik_0\Delta r)}{\Delta r}\mathbf{p}\right) + \frac{1}{k_0^2}\mathbf{p}\delta(\mathbf{r} - \mathbf{r}'), \tag{3.10}$$

where $\Delta r = \|\mathbf{r} - \mathbf{r}'\|$, that can be decomposed using the Weyl decomposition in [2, Sec. 13. 2] and assuming $z \geq z'$

$$\bar{\mathcal{G}}(\mathbf{r}, \mathbf{r}')\mathbf{p} = \frac{i}{8\pi^2 k_0^2} \int_{\mathbf{k}_\parallel \in \mathbb{R}^2} \frac{1}{k_z} \exp\big(i\mathbf{k}.(\mathbf{r} - \mathbf{r}')\big)\mathbf{k} \times (\mathbf{k} \times \mathbf{p})\, \mathrm{d}\mathbf{k}_\parallel + \frac{1}{k_0^2}\mathbf{p}\delta(\mathbf{r} - \mathbf{r}'), \tag{3.11}$$

with

$$k_z = \begin{cases} \sqrt{k_0^2 - \|\mathbf{k}_\parallel\|^2} & \text{if } \|\mathbf{k}_\parallel\| \leq k_0, \\ i\sqrt{\|\mathbf{k}_\parallel\|^2 - k_0^2} & \text{if } \|\mathbf{k}_\parallel\| \geq k_0. \end{cases} \tag{3.12}$$

The solution of Eq. (3.8) can be expressed as

$$\begin{aligned} \mathbf{E}_\mathrm{d}(\mathbf{r}) &= \int_\Omega \bar{\mathcal{G}}(\mathbf{r}, \mathbf{r}')\omega^2\mu_0\mathbf{P}(\mathbf{r}')\mathrm{d}\mathbf{r}' && (3.13) \\ &= \frac{i\omega^2\mu_0}{8\pi^2 k_0^2} \int_\Omega \int_{\mathbf{k}_\parallel \in \mathbb{R}^2} \frac{1}{k_z} \exp\big(i\mathbf{k}.(\mathbf{r} - \mathbf{r}')\big)\mathbf{k} \times (\mathbf{k} \times \mathbf{P}(\mathbf{r}'))\, \mathrm{d}\mathbf{k}_\parallel \mathrm{d}\mathbf{r}' + \frac{\omega^2\mu_0}{k_0^2}\mathbf{P}(\mathbf{r}) \\ &= \frac{i\omega^2\mu_0}{8\pi^2 k_0^2} \int_{\mathbf{k}_\parallel \in \mathbb{R}^2} \frac{1}{k_z} \exp(i\mathbf{k}.\mathbf{r})\mathbf{k} \times \left(\mathbf{k} \times \int_\Omega \exp(-i\mathbf{k}.\mathbf{r}')\mathbf{P}(\mathbf{r}')\mathrm{d}\mathbf{r}'\right) \mathrm{d}\mathbf{k}_\parallel + \frac{\omega^2\mu_0}{k_0^2}\mathbf{P}(\mathbf{r}) \\ &= \frac{i\omega^2\mu_0}{8\pi^2 k_0^2} \int_{\mathbf{k}_\parallel \in \mathbb{R}^2} \frac{1}{k_z} \exp(i\mathbf{k}.\mathbf{r})\mathbf{k} \times \left(\mathbf{k} \times \tilde{\mathbf{P}}(\mathbf{k})\right) \mathrm{d}\mathbf{k}_\parallel + \frac{\omega^2\mu_0}{k_0^2}\mathbf{P}(\mathbf{r}) && (3.14) \end{aligned}$$

Noting that $(\omega^2\mu_0)/k_0^2 = 1/\varepsilon_0$ as $k_0 = \omega/c = \omega/\sqrt{\varepsilon_0\mu_0}$, the expression of the diffracted field reads

$$\mathbf{E}_\mathrm{d}(\mathbf{r}) = \frac{i}{8\pi^2} \int_{\mathbf{k}_\parallel \in \mathbb{R}^2} \frac{1}{k_z} \exp(i\mathbf{k}.\mathbf{r})\mathbf{k} \times \left(\mathbf{k} \times \frac{\tilde{\mathbf{P}}(\mathbf{k})}{\varepsilon_0}\right) \mathrm{d}\mathbf{k}_\parallel + \frac{\mathbf{P}(\mathbf{r})}{\varepsilon_0}. \tag{3.15}$$

This relation shows that the diffracted field is a sum of plane waves, each proportional to a Fourier component of $\mathbf{P}$. As explained in Sec. 1.1.2, the plane waves such that $\|\mathbf{k}_\parallel\| \leq k_0\mathrm{NA}$ are collected by the microscope objective and focussed on a point of the back focal plane. More precisely, if the field diffracted by the sample towards the objective is written as

$$\mathbf{E}_\mathrm{d}(\mathbf{r}) = \frac{i}{8\pi^2 k_0} \int_{\mathbf{k}_\parallel \in \mathbb{R}^2} \frac{1}{k_z}\mathbf{E}_\mathrm{d}(\mathbf{k}) \exp(i\mathbf{k}.\mathbf{r})\mathrm{d}\mathbf{k}_\parallel, \tag{3.16}$$

the diffracted field at the back focal plane of the objective reads

$$\mathbf{E}_{\mathrm{d,bfp}}\left(\frac{D}{k_0\mathrm{NA}}\mathbf{k}_\parallel\right) = C\frac{i}{8\pi^2}\sqrt{\frac{k_0}{k_z}}\mathbf{E}_\mathrm{d}(\mathbf{k}), \tag{3.17}$$

where C is a constant depending on the objective and D is the diameter of the exit pupil, the illuminated part of the back focal plane. Eq. (3.17) shows that part of the plane wave decomposition of $\mathbf{E}_\mathrm{d}(\mathbf{k})$ can be measured directly at the back focal plane of the objective. Detail on how this can be done experimentally is described in Sec. 3.3. Using Eqs. (3.15) and (3.16), the plane wave amplitude of the diffracted field, $\mathbf{E}_\mathrm{d}(\mathbf{k})$, can be expressed as the Fourier transform of the product $\chi\mathbf{E}$ of the linear susceptibility and the total field inside the sample

$$\mathbf{E}_\mathrm{d}(\mathbf{k}) = k_0\mathbf{k} \times \left(\mathbf{k} \times \frac{\tilde{\mathbf{P}}(\mathbf{k})}{\varepsilon_0}\right) \tag{3.18}$$

$$\mathbf{E}_\mathrm{d}(\mathbf{k}) = k_0\mathbf{k} \times \left(\mathbf{k} \times \int_\Omega \exp(-i\mathbf{k}.\mathbf{r})\chi(\mathbf{r})\mathbf{E}(\mathbf{r})\mathrm{d}\mathbf{r}\right). \tag{3.19}$$

Eq. (3.19) is the fundamental relationship of Tomographic Diffraction Microscopy explaining how the measurements of the diffracted field can be used to retrieve quantitatively the shape and nature of the sample (namely, the map of χ). For one given illumination, the Fourier transform of $\chi\mathbf{E}$ is known on a cap of sphere of radius k_0 corresponding to the extremity of the wave-vectors collected by the objective, see Fig. 2.3 (a). As expected, the far-field measurement of the microscope filters out the diffracted field transverse spatial frequencies over $k_0\mathrm{NA}$.

However, because of the frequency mixing between χ and $\mathbf{E}$, the accessible spatial frequencies of χ are not limited by this fundamental limit. The accessible frequencies of χ that can be retrieved from the diffracted field measurement depends on the spatial frequencies of $\mathbf{E}$, the field inside the sample and can be found beyond the $k_0\mathrm{NA}$ domain. The field inside the sample changing with the illumination, each novel measurement yields a different accessible Fourier domain for χ. Hence, we see that Tomographic Diffraction Microscopy is a perfect example of Structured Illumination Microscopy as presented in Sec. 1.5. The performance of TDM and the ability to reconstruct easily the map of χ depends on the field $\mathbf{E}$ probing the sample.

3.2 Evaluation of the field inside the sample

The field inside the sample is equal to the sum of the incident and diffracted fields, $\mathbf{E} = \mathbf{E}_{\mathrm{inc}} + \mathbf{E}_{\mathrm{d}}$. Using Eq. (3.13), this leads to

$$\mathbf{E}(\mathbf{r}) = \mathbf{E}_{\mathrm{inc}}(\mathbf{r}) + \int_{\Omega} \bar{\mathcal{G}}(\mathbf{r},\mathbf{r}')\omega^2\mu_0\mathbf{P}(\mathbf{r}')\mathrm{d}\mathbf{r}' \tag{3.20}$$

$$\mathbf{E}(\mathbf{r}) = \mathbf{E}_{\mathrm{inc}}(\mathbf{r}) + \int_{\Omega} \bar{\mathcal{G}}(\mathbf{r},\mathbf{r}')k_0^2\chi(\mathbf{r}')\mathbf{E}(\mathbf{r}')\mathrm{d}\mathbf{r}'. \tag{3.21}$$

This integral equation allows the computation of $\mathbf{E}$ knowing the incident field $\mathbf{E}_{\mathrm{inc}}$ and the sample permittivity contrast χ. We observe that $\mathbf{E}$, the field inside the sample, depends on χ, *i. e.* on the sample itself. As a result, the diffracted field, which is related to the Fourier transform of $\chi\mathbf{E}$ is not linearly linked to χ. Thus, Tomographic Diffraction Microscopy and, more generally, all unstained microscopy techniques are NOT linear imaging tools and cannot be described by a Transfer Function. However, under certain important assumptions, Eq. (3.21) can be simplified, leading to a linear dependence of the diffracted field with the sample parameter of interest. Most of the microscopy theories are developed under these assumptions.

3.2.1 Born approximation and linear reconstruction

In cases where $\chi \ll 1$ and the volume Ω is small in comparison to λ^3, one can apply the **Born approximation** [70]. The field diffracted by the sample is assumed to be negligible compared to the incident field, leading to $\mathbf{E} \approx \mathbf{E}_{\mathrm{inc}}$ in Ω, so that Eq. (3.19) can be rewritten as

$$\mathbf{E}_{\mathrm{d}}(\mathbf{k}) \approx k_0\mathbf{k} \times \left(\mathbf{k} \times \int_{\Omega} \exp(-i\mathbf{k}.\mathbf{r})\chi(\mathbf{r})\mathbf{E}_{\mathrm{inc}}(\mathbf{r})\mathrm{d}\mathbf{r}\right) \tag{3.22}$$

If the incident field is a plane wave $\mathbf{E}_{\mathrm{inc}} = \mathbf{E}_0 \exp(i\mathbf{k}_{\mathrm{inc}}.\mathbf{r})$, where $\mathbf{E}_0$ is the incident vector

amplitude, Eq. (3.22) is cast in the form

$$\begin{aligned}\mathbf{E}_{\mathrm{d}}(\mathbf{k},\mathbf{k}_{\mathrm{inc}}) &= k_0\int_\Omega \exp(-i\mathbf{k}.\mathbf{r})\chi(\mathbf{r})\exp(i\mathbf{k}_{\mathrm{inc}}.\mathbf{r})\mathbf{k}\times(\mathbf{k}\times\mathbf{E}_0)\,\mathrm{d}\mathbf{r} &(3.23)\\ &= k_0\tilde{\chi}(\mathbf{k}-\mathbf{k}_{\mathrm{inc}})\mathbf{k}\times(\mathbf{k}\times\mathbf{E}_0)\,, &(3.24)\end{aligned}$$

where $\tilde{\chi}$ is the Fourier Transform of the permittivity contrast χ.

Thus, under the Born approximation, each measurement is proportional to a Fourier component of χ. Reconstruction can be simply done using an inverse Fourier transform. The obtained image is thus linear in the permittivity contrast. The transfer function is equal to 1 in the volume of the Fourier space reached by $\mathbf{k}-\mathbf{k}_{\mathrm{inc}}$ and 0 everywhere else.

3.2.2 Renormalised Born approximation

If we cannot assume the Born approximation, one has to solve Eq. (3.21) to know the field inside the sample. Solving it presents a mathematical difficulty because the tensor $\bar{\mathcal{G}}$ given by Eq. (3.10) has a non-integrable singularity. The classical way to solve this issue is to separate the integral appearing at the right hand side of Eq. (3.21) in two: First the integral in a small ball with radius d around $\mathbf{r}$, then the rest of Ω. When d tends toward 0, the first part becomes a linear tensor of the value at $\mathbf{r}$, and the second a Cauchy principal value [71],

$$\int_\Omega \bar{\mathcal{G}}(\mathbf{r},\mathbf{r}')\mathbf{P}(\mathbf{r}')d\mathbf{r}' = \bar{\mathbf{L}}\mathbf{P}(\mathbf{r}) + \mathrm{PV}\int_\Omega \bar{\mathcal{G}}(\mathbf{r},\mathbf{r}')\mathbf{P}(\mathbf{r}')\mathrm{d}\mathbf{r}', \tag{3.25}$$

where $\bar{\mathbf{L}} = -\bar{\mathbf{I}}/3k_0^2$ for $\bar{\mathbf{I}}$ the identity tensor on $\mathbb{C}^3$. Of course $\bar{\mathbf{L}}$ and the principal value change depending on the geometry of the exclusion volume [71].

Thus Eq. (3.21) becomes:

$$\mathbf{E}(\mathbf{r}) = \mathbf{E}_{\mathrm{inc}}(\mathbf{r}) - \frac{\varepsilon(\mathbf{r})-1}{3}\mathbf{E}(\mathbf{r}) + \mathrm{PV}\int_\Omega \bar{\mathcal{G}}(\mathbf{r},\mathbf{r}')[\varepsilon(\mathbf{r}')-1]\mathbf{E}(\mathbf{r}')k_0^2\mathrm{d}\mathbf{r}', \tag{3.26}$$

Noting $\mathbf{E}_{\mathrm{local}}(\mathbf{r}) = \mathbf{E}(\mathbf{r})[\varepsilon(\mathbf{r})+2]/3$ and $\alpha(\mathbf{r}) = 3[\varepsilon(\mathbf{r})-1]/[\varepsilon(\mathbf{r})+2]$ one obtains

$$\begin{aligned}\mathbf{E}_{\mathrm{local}}(\mathbf{r}) &= \mathbf{E}_{\mathrm{inc}}(\mathbf{r}) + \mathrm{PV}\int_\Omega \bar{\mathcal{G}}(\mathbf{r},\mathbf{r}')3\frac{\varepsilon(\mathbf{r}')-1}{\varepsilon(\mathbf{r}')+2}\mathbf{E}_{\mathrm{local}}(\mathbf{r}')k_0^2\mathrm{d}\mathbf{r}' &(3.27)\\ &= \mathbf{E}_{\mathrm{inc}}(\mathbf{r}) + \mathrm{PV}\int_\Omega \bar{\mathcal{G}}(\mathbf{r},\mathbf{r}')\alpha(\mathbf{r}')\mathbf{E}_{\mathrm{local}}(\mathbf{r}')k_0^2\mathrm{d}\mathbf{r}'. &(3.28)\end{aligned}$$

By analogy with concepts issued from the theory of macroscopic field in dense dielectric material [1, Sec. 4.5], α is called the bulk **polarisability** and $\mathbf{E}_{\mathrm{local}}$ the local field. Looking at Eq. (3.28) and remembering the Born approximation, one can formulate the **renormalised Born approximation** [72] by $\mathbf{E}_{\mathrm{local}}(\mathbf{r}) \approx \mathbf{E}_{\mathrm{inc}}(\mathbf{r})$. Under this approximation, one obtains again a simple formula for the diffracted field

$$\mathbf{E}_{\mathrm{d}}(\mathbf{k},\mathbf{k}_{\mathrm{inc}}) = k_0\tilde{\alpha}(\mathbf{k}-\mathbf{k}_{\mathrm{inc}})\mathbf{k}\times(\mathbf{k}\times\mathbf{E}_0)\,, \tag{3.29}$$

where $\tilde{\alpha}$ is the Fourier Transform of α. An inverse Fourier transform of the measured field, yields a map of α from which one can deduce a map of ε. Under the renormalised Born approximation, the recorded data are linearly linked to the sample polarisability. The renormalised

Born approximation can be applied to higher permittivity contrast than that required for the usual Born approximation. Yet, there remain cases where none are valid (for example, the manufactured nano-structured components of the micro-electronic domains). In these cases, the field inside the sample is given by Eq. (3.28). The image formation is no more linear in α and the reconstruction requires specific algorithms (see Chap. 7).

3.3 Experimental implementation of TDM

We now turn to a rapid description of the different implementations of TDM.

3.3.1 Measurement techniques

In most existing configurations [73, 74, 75], the sample is illuminated by a collimated laser beam, the direction of which is controlled by a tilting mirror, and a microscope objective is used to collect the diffracted field. The incident and observation directions are limited by the numerical aperture NA of the objective. The plane wave amplitudes of the diffracted field $\mathbf{E}_{\mathrm{d}}(\mathbf{k})$ can be measured directly on a plane conjugated to the back focal plane of the objective. Alternatively, one measures the diffracted field on a plane conjugated with the sample one [76] and the plane wave amplitude are recovered by a numerical Fourier transform.

The main difficulty of TDM is to record the phase and amplitude of the diffracted field for various illuminations. That means having in parallel with the ordinary intensity map, a phase map of the received optical field on the detector. Many techniques can be used to measure the phase of the field,

- One can use a classical interferometric method in which the phase is retrieved from several interferences of the diffracted field with a reference beam whose phase is rotated [77, 78].
- One can use off-axis interferometry in which the reference beam is tilted. This produces a periodic pattern that is perturbed by the phase and amplitude modulation of the diffracted field. From a single measurement it is possible by a treatment in the Fourier space to retrieve both amplitude and phase of the diffracted field [79, 80].
- One can use the Transport-of-Intensity Equation which allows, from measurements of the diffracted intensity in two parallel planes, thus without the need of a reference beam, to recover the phase and amplitude in one of those planes [81].
- Last, one can use quadri-wave lateral shearing interferometry in which the field map produced by a diffraction grating placed at some distance before the camera allows via a numerical treatment in the Fourier space to recover the amplitude and the phase gradient [82, 83].

Moreover, this task requires the finding of a reference phase, via the reflected or the transmitted specular values, for getting rid of the uncontrolled phase of the incident beam [73]. These various approaches have been used for two main geometries, the transmission and the reflection configurations [75].

3.3.2 Transmission vs reflection configuration

In the transmission configuration, the illumination and the observation are performed from two different sides of the sample (using a condenser and an objective facing each other). In the reflection configuration, one illuminates and observes the sample from the same side with the same objective.

In the transmission configuration, assuming that the condenser and the objective have the same maximum angle a, $\mathbf{k}$ and $\mathbf{k}_{\text{inc}}$ are both contained in the part of the Ewald sphere where the polar angle is inferior to a (see Fig. 2.3 (a)). Thus the volume of the Fourier space that is accessible by $\mathbf{k} - \mathbf{k}_{\text{inc}}$ is the eye-shape torus volume shown in Fig. 3.2 (a). As seen in Figs. 3.2 (a) and 2.3 (b) the support of Transfer Function for a transmission TDM in the same as the one in fluorescence microscopy. However the Transfer Function in TDM is always 1 in its support, which is not the case in fluorescence microscopy. The point-spread-function, obtained by inverse Fourier transforming the transfer function is shown in Fig. 3.2 (c). The radial resolution is now $\lambda/(2\text{NA})$, according to the Rayleigh criterion defined in Sec. 1.3, and the axial one is at best $\lambda/(1-\cos a)$. Note that in TDM the Rayleigh and Sparrow criterion give the same resolution. Indeed the transfer function is always equal to 1 (and then superior to 0.10) as long as the frequency is below the frequency cut-off.

In the reflection configuration, $\mathbf{k}_{\text{inc}}$ is now reversed. It is contained in the part of the Ewald sphere where the polar angle is superior to $\pi - a$. Thus the volume of the Fourier space that is accessible by $\mathbf{k} - \mathbf{k}_{\text{inc}}$ is the volume delimited by the part of the $2k_0$-radius sphere with polar angle inferior to a and the plane $(k_z = 2k_0 \cos a)$ (shown in Fig. 3.2 (b)). Figure 3.2 (b) shows that the Transfer Function of TDM in the reflection configuration is not symmetrical about zero. Thus, its inverse Fourier transform is not real. In Fig. 3.2 (d) and (e) we plot the real and imaginary part of the Point-Spread-Function. While the real part shows an almost spherical shape, the imaginary part is of the same order as the real part and antisymmetric. If the sample α has both a real and imaginary part, their images are mixed by this convolution function. The reflection configuration is thus limited to pure phase samples. For pure phase samples the resolution is almost isotropic, being equal to $\lambda/(2\text{NA})$ in the lateral direction and $\lambda/2$ in the axial one. An example of sample reconstruction can be found in Sec. 4.2.3

Note that this analysis assumes an infinitely low noise level. Indeed the Fourier components of α are measured several times in the measurement process. For the same $\mathbf{k}_{\text{mes}}$, several pairs $(\mathbf{k}, \mathbf{k}_{\text{inc}})$ verify $\mathbf{k}_{\text{mes}} = \mathbf{k} - \mathbf{k}_{\text{inc}}$. Noise can thus be reduced by averaging redundant measurements of $\tilde{\alpha}(\mathbf{k}_{\text{mes}})$. However, this averaging has not the same strength on the whole support of the transfer function [84]. Of course the precise value of this noise averaging function depends on the chosen set of illumination directions.

3.4 Conclusion

This chapter explains the principles of Tomographic Diffraction Microscopy. Inhomogeneity in the sample permittivity causes diffraction of the incident field. Measurement of the diffracted field in the back focal plane of the objective allows the measurement of Fourier components of $\chi\mathbf{E}$, the product of the linear susceptibility and the field inside the sample. Usually, the probing field $\mathbf{E}$ depends also on the sample susceptibility. Thus, in general, the recorded data are non-linearly linked to the sample parameter of interest and requires non-linear reconstruc-

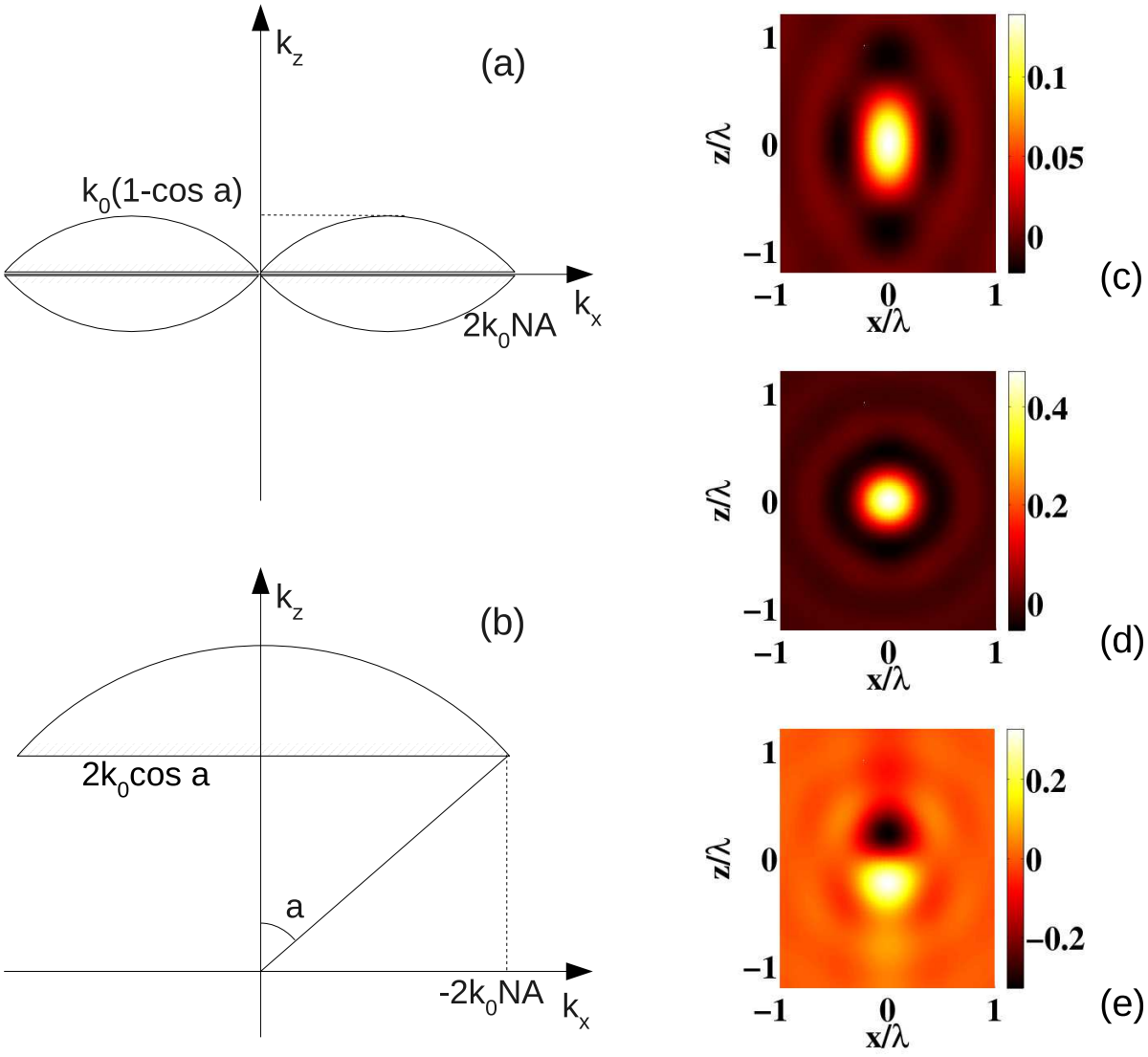

Figure 3.2: Transfer Function and Point-Spread-Function of the transmission and reflection configuration in TDM. (a) Transfer Function for the transmission configuration. The Transfer Function is 1 in the hatched region and 0 elsewhere. (b) Transfer Function for the reflection configuration. (c) Point-Spread-Function for the transmission configuration. (d) and (e) real and imaginary part of the Point-Spread-Function for the reflection configuration. In (c-e) one assume that the maximum angle accessible trough the objective is $a = 70°$, which corresponds to a numerical aperture NA=0.95.

tion schemes for retrieving the sample. A study on these sophisticated inversion techniques is presented in Chap. 7.

Yet, assuming the Born approximation, or better the renormalised Born approximation, a linear link between the diffracted field and the Fourier components of χ can be derived. In this case, a simple linear reconstruction of the sample permittivity map is possible and one can derive Transfer and point-spread-functions for various configurations such as transmission and reflection set-ups. We observe that, in transmission, the axial resolution is much worse than the lateral one. In reflection, the axial resolution is comparable to the lateral one, but the point-spread-function mixes the real and imaginary parts of the permittivity leading to uninterpretable images when the samples are not pure phase objects. We show in the next chapter how one can improve the TDM implementation so as to obtain an isotropic resolution without mixing the real and imaginary parts of the estimated permittivity maps. The main idea is to combine both the transmission and reflection configurations by placing the sample on a mirror.

Part II

Mirror and axial resolution

Chapter 4

Mirror-assisted Tomographic Diffraction Microscopy

Like most optical microscopy techniques, the axial resolution of Tomographic Diffraction Microscopy (TDM) in transmission configuration is several times poorer than the lateral one. This comes from the fact that the illumination and observation is performed from one side only of the sample (through the objective and condenser). In an ideal configuration where the sample could be observed and illuminated from all possible directions, TDM would yield (under the Born approximation) the permittivity map of the sample with an isotropic resolution $\lambda/2$. The microscope asymmetry and the lack of angular coverage can be partially compensated by rotating the sample [74, 85] or by imposing the positivity of the sought dielectric contrast in the inversion procedure [86]. Yet, these approaches are limited to certain types of samples and the image resolution remains generally below that which would be obtained with a complete isotropic tomography configuration where the sample is illuminated and observed from every possible angles. Hence, the best solution is to illuminate and observe the sample from both sides, for example by placing the sample between two opposing objectives as in a 4Pi microscope set-up. Unfortunately, although 4Pi TDM is easier to implement than 4Pi fluorescence microscopy, as it does not require any precise alignment and stabilisation of the objectives, this approach is quite time-consuming and requires a complex set-up.

To simplify the data recording and the experimental implementation, we propose, in this chapter, to take advantage of the versatility of the numerical reconstruction process for considering a configuration in which the sample is deposited onto a mirror [4] and introduced in a classical TDM set-up in reflection. Thanks to the reflection on the mirror, the sample is illuminated and observed from both sides, and thanks to the numerical reconstruction, the entangled top and back views of the sample can be unravelled. This mirror approach, which is new to our knowledge in optics, has had precursors in the mechanical [87, 88], radar [89] and acoustic [90] waves domains, mostly in the two-dimensional simplified case.

In the first section of this chapter, we provide an analysis of the mirror-assisted TDM in the two-dimensional (2D) scalar configuration. This study allows interesting insights on the information content of the measurements and underlines the role of polarisation. In the second section, the full three-dimensional (3D) model is derived and results are supported by simulations.

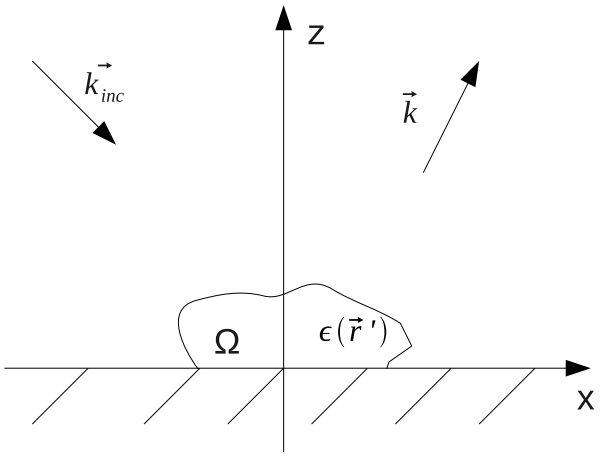

Figure 4.1: Sketch of the mirror-assisted Tomographic Diffraction Microscopy. The sample is illuminated successively by several incident plane waves with wave vectors $\mathbf{k}_{\text{inc}}$. For each incident plane wave, the diffracted field is measured for all $\mathbf{k}$ directions that are accessible through the objective.

4.1 Mirror-assisted Tomographic Diffraction Microscopy in the two-dimensional scalar configuration

Let $(O, \mathbf{x}, \mathbf{y}, \mathbf{z})$ be the right-handed Cartesian coordinate frame such that the mirror is on the plane $(z = 0)$ and $\mathbf{z}$ is the optical axis. The sample is placed in the half-space $z \geq 0$ over the mirror (see Fig. 4.1). The sample is supposed to be invariant along the $\mathbf{y}$ direction so that its permittivity depends only on the x and z variables $\varepsilon(\mathbf{r}) = \varepsilon(x, z)$. Illuminations and observations are done only in the (x, z) plane. To simplify the formulation, the x and z Cartesian coordinates of the incident and detected wave vectors are denoted as β and γ. Thus, the incident and detected wave vectors reads respectively $\mathbf{k}_{\text{inc}} = \beta_{\text{inc}}\mathbf{x} - \gamma_{\text{inc}}\mathbf{z}$ and $\mathbf{k} = \beta\mathbf{x} + \gamma\mathbf{z}$. The mirror is assumed to be perfectly conductor, so that the reflection coefficient is equal to -1 for s-polarisation (the electric field $\mathbf{E}$ is directed along the $\mathbf{y}$ axis) and 1 for p-polarisation (the magnetic field $\mathbf{H}$ is directed along the $\mathbf{y}$ axis).

4.1.1 Illumination with *s* polarisation

We first study the s-polarisation configuration in which the incident electrical field is perpendicular to (x, z), $\mathbf{E}^{\text{s}}_{\text{inc}} = E_0 \exp(i\beta_{\text{inc}}x + i\gamma_{\text{inc}}z)\mathbf{y}$. Symmetry considerations show that the diffracted field is also s-polarised: $\mathbf{E}^{\text{s}}_{\text{d}} = E^{\text{s}}_{\text{d}}(x, z)\mathbf{y}$.

4.1.1.1 Modelling of the diffracted field

The reference field, which is the field that would exist without the sample, $\mathbf{E}^{\text{s}}_{\text{ref}}$ is the sum of the incident field and the field reflected by the mirror

$$\mathbf{E}^{\text{s}}_{\text{ref}} = E^{\text{s}}_{\text{ref}}\mathbf{y} = E_0 \left[\exp(i\beta_{\text{inc}}x + i\gamma_{\text{inc}}z) - \exp(i\beta_{\text{inc}}x - i\gamma_{\text{inc}}z)\right]\mathbf{y}. \tag{4.1}$$

Following the derivation of Sec. 3, we know that the field measured in the back focal plane of the objective is proportional to $E^{\text{s}}_{\text{d}}(\mathbf{k})$ the plane wave decomposition of the diffracted field

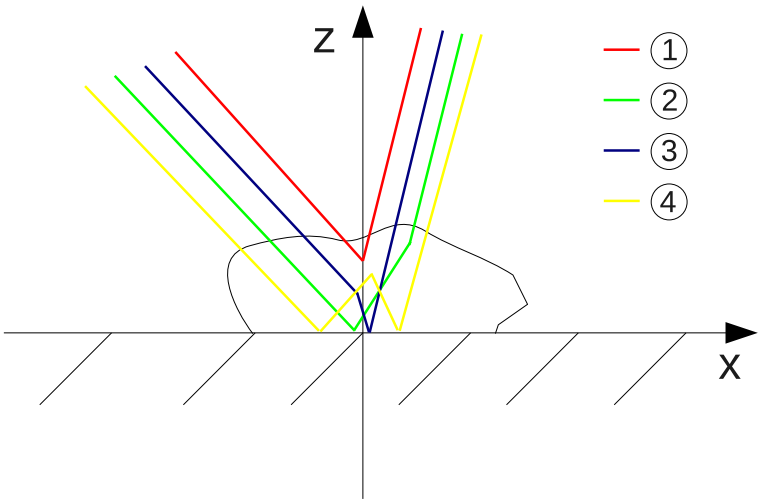

Figure 4.2: Sketch of the 4 contributions appearing in Eq. (4.4). (1) contribution of waves directly diffracted by the sample. (2) contribution of waves reflected by the mirror and then diffracted by the sample. (3) contribution of waves diffracted by the sample and then reflected by the mirror. (4) contribution of waves reflected by the mirror, diffracted by the sample and reflected again by the mirror.

which in 2D reads [91]

$$E_{\mathrm{d}}^{\mathrm{s}}(x,y) = -\frac{i}{4\pi}\int_{\beta\in\mathbb{R}} \frac{1}{\gamma} E_{\mathrm{d}}^{\mathrm{s}}(\mathbf{k}) \exp(i\mathbf{k}.\mathbf{r})\mathrm{d}\beta. \tag{4.2}$$

To calculate $E_{\mathrm{d}}^{\mathrm{s}}(\mathbf{k})$, we calculate $\bar{\mathcal{G}}^{\mathrm{s}}_{\mathrm{mirror}}\mathbf{p}$ the field radiated by a line-source $\mathbf{p} = p_y\mathbf{y}$ placed at (x,z) in presence of the mirror. By virtue of the method of images, this field is equal to the field radiated in free space by the line-source plus the field radiated in free-space by its image through the mirror. The image of the line-source $\mathbf{p}$ at (x,z) is another line-source $\mathbf{p}' = -p_y\mathbf{y}$ placed at $(x,-z)$. The expression of $\bar{\mathcal{G}}^{\mathrm{s}}_{\mathrm{mirror}}\mathbf{p}$ is thus, ref. [91]

$$\begin{aligned}\bar{\mathcal{G}}^{\mathrm{s}}_{\mathrm{mirror}}(\mathbf{r},\mathbf{r}')p_y\mathbf{y} = -\frac{i}{4\pi}\int_{\beta\in\mathbb{R}} \frac{1}{\gamma} \big[&\exp\big(-i\beta(x-x') - i\gamma|z-z'|\big) \\ &- \exp\big(-i\beta(x-x') + i\gamma(z+z')\big)\big]\, p_y\mathbf{y}\mathrm{d}\beta.\end{aligned} \tag{4.3}$$

Using the Born approximation $\mathbf{P} \approx \chi\mathbf{E}^{\mathrm{s}}_{\mathrm{ref}}$, and inserting Eqs. (4.1) and (4.3) in Eq. (3.13), one gets for $E_{\mathrm{d}}^{\mathrm{s}}$ defined in Eq. (4.2)

$$\begin{aligned}E_{\mathrm{d}}^{\mathrm{s}}(\mathbf{k},\mathbf{k}_{\mathrm{inc}}) = E_0 k_0^2 \big[&\tilde{\chi}(\beta_{\mathrm{inc}}-\beta,\gamma_{\mathrm{inc}}-\gamma) - \tilde{\chi}(\beta_{\mathrm{inc}}-\beta,\gamma_{\mathrm{inc}}+\gamma) \\ &- \tilde{\chi}(\beta_{\mathrm{inc}}-\beta,-\gamma_{\mathrm{inc}}-\gamma) + \tilde{\chi}(\beta_{\mathrm{inc}}-\beta,-\gamma_{\mathrm{inc}}+\gamma)\big].\end{aligned} \tag{4.4}$$

The first term of Eq. (4.4) represents contributions corresponding to an illumination and an observation without any interaction with the mirror, Fig. 4.2 (1). It is thus equivalent to the unique term of Eq. (3.24), obtained in the configuration without the mirror. The second term of Eq. (4.4) represents contributions in which the sample is illuminated by the reflection of the incident beam onto the mirror and the diffracted waves are directly collected by the objective, Fig. 4.2 (2). The third one represents contributions in which the sample is directly illuminated by the incident beam and the observation is done after reflection of the diffracted waves onto the mirror, Fig. 4.2 (3). The last term corresponds to contributions where the sample is illuminated

by the reflection of the incident beam and the diffracted waves are collected after reflection onto the mirror, Fig. 4.2 (4).

We see in Equation (4.4) that each measurement depends on four Fourier components of the linear susceptibility of the sample. To reconstruct the sample permittivity map, it is thus necessary to separate those terms. To address this issue, Mora [87] and Hutt *et al.* [88] used *a priori* information on the sample. Nolan *et al.* [89] proposed a configuration where each contribution are separated geometrically by using two perpendicular mirrors instead of one. This cannot be done easily in optics since it would require a positioning of the corner between the two mirrors more precise than the available stages. To simplify the problem, Natterer [90] noticed that these four contributions can be paired by introducing $\tilde{\tilde{\chi}}$, the Fourier transform along the $\mathbf{x}$ axis of the cosine transform along the $\mathbf{z}$ axis of χ

$$\begin{aligned}\tilde{\chi}(\beta,\gamma)+\tilde{\chi}(\beta,-\gamma) &= \int_\Omega \chi(x,z)\exp(-i\beta x - i\gamma z)+\exp(-i\beta x + i\gamma z)\mathrm{d}x\mathrm{d}z \\ &= 2\int_\Omega \chi(x,z)\exp(-i\beta x)\cos(|\gamma| z)\mathrm{d}x\mathrm{d}z \qquad (4.5)\\ &= 2\tilde{\tilde{\chi}}(\beta,|\gamma|). \qquad (4.6)\end{aligned}$$

From the knowledge of $\tilde{\tilde{\chi}}(\beta,\gamma)$ for $\gamma \geq 0$, it is possible to obtain $\chi(x,z)$ for $z \geq 0$ by inverse Fourier and cosine transforms. From Eqs. (4.4) and (4.6), the scattered field may be rewritten as

$$E_{\mathrm{d}}^{\mathrm{s}}(\mathbf{k},\mathbf{k}_{\mathrm{inc}}) = 2E_0 k_0^2\left[\tilde{\tilde{\chi}}(\beta_{\mathrm{inc}}-\beta,|\gamma_{\mathrm{inc}}-\gamma|)-\tilde{\tilde{\chi}}(\beta_{\mathrm{inc}}-\beta,|\gamma_{\mathrm{inc}}+\gamma|)\right]. \qquad (4.7)$$

To reconstruct χ, it is necessary to find a procedure for separating the two Fourier components $\tilde{\tilde{\chi}}$ appearing in the right hand side of Eq. (4.7).

4.1.1.2 Reconstruction of the sample permittivity

The problem can be stated as follows. Is it possible to infer from a set of measurements of $E_{\mathrm{d}}^{\mathrm{s}}(\mathbf{k},\mathbf{k}_{\mathrm{inc}})$ the value of $\tilde{\tilde{\chi}}$ on a certain domain of the Fourier space? To answer this question, one notes (A,B) the spatial frequencies of the first term of Eq. (4.7) $(\beta_{\mathrm{inc}}-\beta,|\gamma_{\mathrm{inc}}-\gamma|)$, and (C,D) that of the second term of Eq. (4.7) $(\beta_{\mathrm{inc}}-\beta,|\gamma_{\mathrm{inc}}+\gamma|)$ that are accessible with one measurement of the diffracted field for the illumination-observation pair $(\mathbf{k}_{\mathrm{inc}},\mathbf{k})$. The frequencies (A,B,C,D) must verify the system

$$\beta_{\mathrm{inc}}-\beta = A \qquad (4.8)$$
$$|\gamma_{\mathrm{inc}}-\gamma| = B \qquad (4.9)$$
$$\beta_{\mathrm{inc}}-\beta = C \qquad (4.10)$$
$$|\gamma_{\mathrm{inc}}+\gamma| = D \qquad (4.11)$$

It is possible to prove (demonstration is in Appendix A) that this system has a solution only if $A=C$ and $D=|A|\sqrt{\frac{4k_0^2}{A^2+B^2}-1}$. Moreover, the frequency vector (C,D) is located inside the k_0-radius half-disks centred at $(k_0,0)$ and $(-k_0,0)$ of the Fourier space, which corresponds to the zone (2) of Fig. 4.3. Zone (2) is the Fourier domain of the permittivity that is accessible in the transmission configuration of TDM. On the other hand, the vector (A,B) is located in zone (1) which corresponds to the $2k_0$-radius half-disk centred at $\mathbf{0}$ excluding zone (2). Zone (1) is

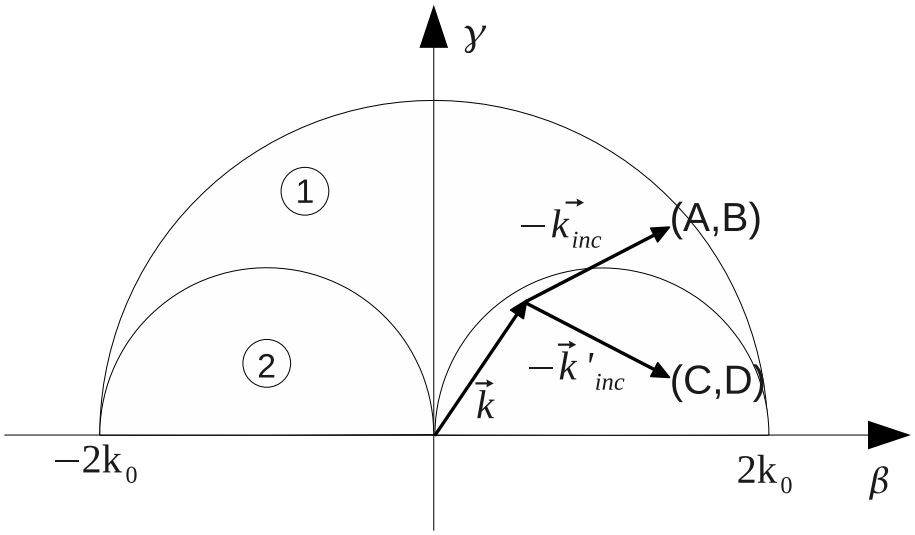

Figure 4.3: Zone (1) et (2) in the Ewald Sphere. Zone (1) is accessible through the term $(A, B) = \mathbf{k} - \mathbf{k}_{\rm inc}$ and zone (2) through the term $(C, D) = \mathbf{k} - \mathbf{k}'_{\rm inc}$, $\mathbf{k}'_{\rm inc}$ being the symmetric of $\mathbf{k}_{\rm inc}$ with respect to the mirror.

the Fourier domain that is accessible in the reflection configuration[1]. Finally, Eq. (4.7) rewritten as

$$E_{\rm d}^{\rm s}(\mathbf{k}, \mathbf{k}_{\rm inc}) = E_0 \left[\tilde{\tilde{\chi}}(A, B) - \tilde{\tilde{\chi}}(C, D)\right] \tag{4.12}$$

shows that each measurement is proportional to the difference of a Fourier component in zone (1) and a Fourier component in zone (2). Changing the illumination-observation pairs, within the possibility of the objective, allows the simultaneous scan of zone (1) and zone (2), i.e. the whole $2k_0$-radius half-ball $\gamma \geq 0$. Unfortunately, because of this simultaneous scanning, there is no way to extract the value of $\tilde{\tilde{\chi}}$ at a given frequency (A, B) from the set of measurements. For any arbitrary value of $\tilde{\tilde{\chi}}(A, B)$ in zone (1), there is a value of $\tilde{\tilde{\chi}}(C, D)$ in zone (2) that produces $E_{\rm d}^{\rm s}(\mathbf{k}, \mathbf{k}_{\rm inc})$. It appears that the data stack, obtained with only one polarisation, is not complete enough for imaging. We have thus decided to consider also the diffracted field obtained with a p-polarised incident field.

4.1.2 Illumination with both *p* and *s* polarisation

For the p-polarisation, *i. e.* with a magnetic field perpendicular to the incident plan $\mathbf{H} = H(x, z)\mathbf{y}$, the reference field reads,

$$\mathbf{E}_{\rm ref}^{\rm p} = E_0 \left[\exp(i\beta_{\rm inc}x + i\gamma_{\rm inc}z)\frac{\mathbf{y} \times \mathbf{k}_{\rm inc}}{k_0} + \exp(i\beta_{\rm inc}x - i\gamma_{\rm inc}z)\frac{\mathbf{y} \times \mathbf{k}'_{\rm inc}}{k_0}\right], \tag{4.13}$$

where $\mathbf{k}'_{\rm inc} = \beta_{\rm inc}\mathbf{x} - \gamma_{\rm inc}\mathbf{z}$ is the symmetric of $\mathbf{k}_{\rm inc}$ with respect to the mirror. Note that in this case the reflection coefficient is equal to $+1$. Using $\bar{\mathcal{G}}_{\rm mirror}^{\rm p}$ in ref. [92], the method of images

[1] For the sake of simplicity, one assumes in this chapter that the maximum angle accessible through the objective is $a = \pi/2$. Simulations in Sec. 4.2.3 considers a more realistic case.

and Eq. (3.13), one obtains after some tedious but straight-forward calculations

$$\begin{aligned}\mathbf{E}_{\mathrm{d}}^{\mathrm{p}}(\mathbf{k},\mathbf{k}_{\mathrm{inc}}) &= 2E_0\left[\mathbf{k}.\mathbf{k}_{\mathrm{inc}}\tilde{\tilde{\chi}}(\beta_{\mathrm{inc}}-\beta,|\gamma_{\mathrm{inc}}-\gamma|)\right.\\ &+ \left.\mathbf{k}.\mathbf{k'}_{\mathrm{inc}}\tilde{\tilde{\chi}}(\beta_{\mathrm{inc}}-\beta,|\gamma_{\mathrm{inc}}+\gamma|)\right]\frac{\mathbf{y}\times\mathbf{k}}{k_0}. \end{aligned} \tag{4.14}$$

Of course, using the sole p-polarisation measurements shows the same indetermination as using the s-polarization measurements. On the other hand, combining both sets of measurements allows the retrieving of $\tilde{\tilde{\chi}}$ on all the $2k_0$-radius half-ball. Indeed, with the linear system defined by Eqs. (4.7) and (4.14), one can separate the contribution of $\tilde{\tilde{\chi}}(\beta_{\mathrm{inc}}-\beta,|\gamma_{\mathrm{inc}}+\gamma|)$ and $\tilde{\tilde{\chi}}(\beta_{\mathrm{inc}}-\beta,|\gamma_{\mathrm{inc}}-\gamma|)$ provided that the determinant of the system, $4\beta_{\mathrm{inc}}\beta E_0 k_0^2$, is non-null. In this case, one gets

$$\tilde{\tilde{\chi}}(\beta_{\mathrm{inc}}-\beta,|\gamma_{\mathrm{inc}}-\gamma|) = \frac{E_{\mathrm{d}}^{\mathrm{p}}(\mathbf{k},\mathbf{k}_{\mathrm{inc}})+\dfrac{\mathbf{k}.\mathbf{k'}_{\mathrm{inc}}}{k_0^2}E_{\mathrm{d}}^{\mathrm{s}}(\mathbf{k},\mathbf{k}_{\mathrm{inc}})}{4\beta_{\mathrm{inc}}\beta E_0} \tag{4.15}$$

$$\tilde{\tilde{\chi}}(\beta_{\mathrm{inc}}-\beta,|\gamma_{\mathrm{inc}}+\gamma|) = \frac{E_{\mathrm{d}}^{\mathrm{p}}(\mathbf{k},\mathbf{k}_{\mathrm{inc}})-\dfrac{\mathbf{k}.\mathbf{k}_{\mathrm{inc}}}{k_0^2}E_{\mathrm{d}}^{\mathrm{s}}(\mathbf{k},\mathbf{k}_{\mathrm{inc}})}{4\beta_{\mathrm{inc}}\beta E_0}. \tag{4.16}$$

Noting θ_{inc} the angle between $-\mathbf{k}_{\mathrm{inc}}$ and $\mathbf{z}$ and θ the angle between $\mathbf{k}$ and $\mathbf{z}$, one obtains the simplified formulae

$$\tilde{\tilde{\chi}}(\beta_{\mathrm{inc}}-\beta,|\gamma_{\mathrm{inc}}-\gamma|) = \frac{E_{\mathrm{d}}^{\mathrm{p}}(\mathbf{k},\mathbf{k}_{\mathrm{inc}})-\cos(\theta+\theta_{\mathrm{inc}})E_{\mathrm{d}}^{\mathrm{s}}(\mathbf{k},\mathbf{k}_{\mathrm{inc}})}{4\sin\theta\sin\theta_{\mathrm{inc}}E_0} \tag{4.17}$$

$$\tilde{\tilde{\chi}}(\beta_{\mathrm{inc}}-\beta,|\gamma_{\mathrm{inc}}+\gamma|) = \frac{E_{\mathrm{d}}^{\mathrm{p}}(\mathbf{k},\mathbf{k}_{\mathrm{inc}})-\cos(\theta-\theta_{\mathrm{inc}})E_{\mathrm{d}}^{\mathrm{s}}(\mathbf{k},\mathbf{k}_{\mathrm{inc}})}{4\sin\theta\sin\theta_{\mathrm{inc}}E_0}. \tag{4.18}$$

During measurements, for all possible directions of $\mathbf{k}$ and $\mathbf{k}_{\mathrm{inc}}$, Eq. (4.17) fills the area of zone (1), while Eq. (4.18) fills the area of zone (2). We thus have the value of $\tilde{\tilde{\chi}}$ on the $2k_0$-radius half disk $\gamma \geq 0$. By an inverse Fourier transform along the $\mathbf{x}$ axis and an inverse cosine transform along the $\mathbf{z}$ axis of the measured value of $\tilde{\tilde{\chi}}$, one obtains the polarisability map χ_{mes}. The resulting point-spread-function h, which is the inverse Fourier transform of the Transfer Function, *i. e.* the disk of radius $2k_0$ [75] centred in $\mathbf{0}$, is then given by

$$h(x,z) = \frac{J_1\left(2k_0 r\right)}{2\lambda r}, \tag{4.19}$$

where J_1 is the Bessel function of the first kind and of order 1 and $r = \sqrt{x^2+z^2}$. Actually, the reconstructed χ_{mes} is not really χ convolved by h. Indeed, the cosine transform reconstructs the even part of functions. Thus, the inverse cosine transform creates a χ_{mes} that is symmetric about the mirror. More exactly, the reconstructed χ_{mes} is the sum of the actual χ convolved by h plus the symmetric of χ with respect to the mirror convolved by h.

We have seen in this section the principle of mirror-assisted tomography in a simplified 2D scalar configuration. We have stressed the interest of using the two incident polarisations in order to distinguish the different Fourier components of the susceptibility that appear in the expression of the diffracted field. We will now apply the same technique to the complete three-dimensional configuration.

4.2 Mirror-assisted Tomographic Diffraction Microscopy in the three-dimensional vectorial configuration

In the 3D configuration, the sample permittivity varies along the 3 directions of space. We assume, that, in an ideal configuration, the sample can be illuminated by a plane wave with any downward directed wave-vector $\mathbf{k}_{\rm inc}$ and observed along any upward direction $\mathbf{k}$ (Fig. 4.1).

4.2.1 Modelling the diffracted field

We first establish the expression of the field diffracted along any direction $\mathbf{k}$ by a sample deposited on a mirror and illuminated by a plane wave along any direction $\mathbf{k}_{\rm inc}$. It is recalled that, for an incident field $\mathbf{E}_{\rm inc}(\mathbf{r}) = \mathbf{E}_0 \exp(i\mathbf{k}_{\rm inc}.\mathbf{r})$, the reference field existing above the mirror without the sample reads

$$\mathbf{E}_{\rm ref}(\mathbf{r}) = (\mathbf{E}_{0,\parallel} + E_{0,z}\mathbf{z}) \exp(i\mathbf{k}_{{\rm inc},\parallel}.\mathbf{r}_\parallel + k_{{\rm inc},z} z) + (-\mathbf{E}_{0,\parallel} + E_{0,z}\mathbf{z}) \exp(i\mathbf{k}_{{\rm inc},\parallel}.\mathbf{r}_\parallel - k_{{\rm inc},z} z) \tag{4.20}$$

where $E_{0,\parallel}$ is the projection of $\mathbf{E}_0$ on the mirror plane. Moreover, the field diffracted by a dipole placed above the mirror is equal, by virtue of the method of images, to the field radiated in free space by the dipole plus the field radiated by its image through the mirror. If the mirror is perfectly conducting, the image of the dipole $\mathbf{p} = \mathbf{p}_\parallel + p_z\mathbf{z}$ placed at $(\mathbf{r}_\parallel, z)$ is the dipole $\mathbf{p}' = -\mathbf{p}_\parallel + p_z\mathbf{z}$ placed at $(\mathbf{r}_\parallel, -z)$. Then, using Eq. (3.11) the field radiated by a dipole placed above a mirror can be written as, for z and z' positive,

$$\begin{aligned}\bar{\mathcal{G}}_{\rm mirror}(\mathbf{r},\mathbf{r}')\mathbf{p} = \frac{i}{8\pi^2 k_0^2} \int_{\mathbf{k}_\parallel \in \mathbb{R}^2} \frac{1}{k_z} \Big[&\exp\big(-i\mathbf{k}_\parallel.(\mathbf{r}_\parallel - \mathbf{r}'_\parallel) - k_z|z-z'|\big)\mathbf{k} \times \big(\mathbf{k} \times (\mathbf{p}_\parallel + p_z\mathbf{z})\big) \\ &+ \exp\big(-i\mathbf{k}_\parallel.(\mathbf{r}_\parallel - \mathbf{r}'_\parallel) - k_z(z+z')\big)\mathbf{k} \times \big(\mathbf{k} \times (-\mathbf{p}_\parallel + p_z\mathbf{z})\big)\Big] \, {\rm d}\mathbf{k}_\parallel \\ &+ \frac{1}{k_0^2}\mathbf{p}\delta(\mathbf{r}-\mathbf{r}').\end{aligned} \tag{4.21}$$

Inserting Eqs (4.20) and (4.21) in Eq. (3.13), one gets the expression of $\mathbf{E}_{\rm d}(\mathbf{k})$ defined by Eq. (3.16), under the renormalised Born approximation ($\mathbf{P} \approx \alpha \mathbf{E}_{\rm ref}$)

$$\begin{aligned}\mathbf{E}_{\rm d}(\mathbf{k},\mathbf{k}_{\rm inc}) = k_0 \int_\Omega &\exp[-i(\mathbf{k}_\parallel - \mathbf{k}_{{\rm inc},\parallel}).\mathbf{r}_\parallel] \cos[|k_{{\rm inc},z} - k_z|z]\alpha(\mathbf{r})\mathbf{k} \times \big(\mathbf{k} \times (\mathbf{E}_{0,\parallel} + E_{0,z}\mathbf{z})\big) \\ &+ \exp[-i(\mathbf{k}_\parallel - \mathbf{k}_{{\rm inc},\parallel}).\mathbf{r}_\parallel] \cos[|k_{{\rm inc},z} + k_z|z]\alpha(\mathbf{r})\mathbf{k} \times \big(\mathbf{k} \times (-\mathbf{E}_{0,\parallel} + E_{0,z}\mathbf{z})\big) {\rm d}\mathbf{r}.\end{aligned} \tag{4.22}$$

Following the approach developed in the 2D case, we define $\tilde{\tilde{\alpha}}$ as the Fourier transform in the $\mathbf{x}$ and $\mathbf{y}$ directions of the cosine transform along the $\mathbf{z}$ direction of α,

$$\tilde{\tilde{\alpha}}(k_z, \mathbf{k}_\parallel) = \int_\Omega \alpha(\mathbf{r}) \cos(k_z z) \exp(-i\mathbf{k}_\parallel.\mathbf{r}_\parallel) {\rm d}\mathbf{r}. \tag{4.23}$$

Then, introducing $\mathbf{A} = k_0 \mathbf{k} \times \big(\mathbf{k} \times \mathbf{E}_{0,\parallel}\big)$ and $\mathbf{B} = E_{0,z} k_0 \mathbf{k} \times (\mathbf{k} \times \mathbf{z})$, one obtains,

$$\mathbf{E}_{\rm d}(\mathbf{k},\mathbf{k}_{\rm inc}) = \big(\mathbf{A} f^- + \mathbf{B} f^+\big) \tag{4.24}$$

$$f^+ = \tilde{\tilde{\alpha}}\left(\mathbf{k}_\parallel - \mathbf{k}_{{\rm inc},\parallel}, |k_z + k_{{\rm inc},z}|, \right) + \tilde{\tilde{\alpha}}\left(\mathbf{k}_\parallel - \mathbf{k}_{\rm inc\parallel}, |k_z - k_{{\rm inc},z}|\right) \tag{4.25}$$

$$f^- = \tilde{\tilde{\alpha}}\left(\mathbf{k}_\parallel - \mathbf{k}_{{\rm inc},\parallel}, |k_z + k_{{\rm inc},z}|\right) - \tilde{\tilde{\alpha}}\left(\mathbf{k}_\parallel - \mathbf{k}_{{\rm inc},\parallel}, |k_z - k_{{\rm inc},z}|\right), \tag{4.26}$$

which gives the expression of the diffracted field with respect to the sample polarisability (under the renormalised Born approximation).

4.2.2 Reconstruction of the sample polarisability

We observe from Eq. (4.24) that the diffracted field depends on two values of $\tilde{\tilde{\alpha}}$, taken at two different spatial frequencies. Yet, these two terms can be easily separated if the vectorial diffracted field (*i. e.* the s and p components) is measured (provided that $\mathbf{A}$ and $\mathbf{B}$ are not collinear). Alternatively, the two terms can be separated if one measures only one component of $\mathbf{E}_{\mathrm{d}}$ for two different incident polarisations $\mathbf{E}_0$, as in the previous section.

Once $\tilde{\tilde{\alpha}}$ is retrieved, α_{mes} is reconstructed by an inverse Fourier transform along the $\mathbf{x}$ and $\mathbf{y}$ axis and an inverse cosine transform along the $\mathbf{z}$ axis. If measurements were possible along all possible angles, one would get the value of $\tilde{\tilde{\alpha}}$ in the $2k_0$-radius half ball $k_z \geq 0$. The point spread function of this imaging system, h, is the Fourier Transform of the support function of a ball of radius $2k_0$ centred in $\mathbf{0}$ [75],

$$h(r) \;=\; \frac{1}{2\pi^2 r^3}\left[\sin(2k_0 r) - 2k_0 r\cos(2k_0 r)\right] = \frac{J_{\frac{3}{2}}(2k_0 r)}{(\lambda r/2)^{\frac{3}{2}}}. \tag{4.27}$$

More precisely, the reconstructed polarisability, α_{mes}, is the sum of the actual α convolved by h and plus the symmetric of α with respect to the mirror convolved by h [75]. For example, the reconstructed image of a point-object placed at $(0,0,z_0)$ above the mirror is

$$h_{\mathrm{mirror}}(\mathbf{r}_{\parallel}, z) \;=\; h\left(\sqrt{\|\mathbf{r}_{\parallel}\|^2 + (z-z_0)^2}\right) + h\left(\sqrt{\|\mathbf{r}_{\parallel}\|^2 + (z+z_0)^2}\right). \tag{4.28}$$

The influence of the symmetric object on the reconstructed polarisability is usually not an issue, as one knows that there is no sample below the mirror. Actually, if the object is placed about one λ away from the mirror, the mirror image does not modify the reconstruction. In this case, the resolution is isotropic with a resolution of $\lambda/2$ according to the Rayleigh criterion. For objects closer to the mirror, the influence of the image trough the mirror is noticeable and enlarges the resolution.

We have seen that by measuring two components of the diffracted field for any $(\mathbf{k}, \mathbf{k}_{\mathrm{inc}})$ observation-illumination pairs, or measuring one component of $\mathbf{E}_{\mathrm{d}}$ for two incident polarisations, one can analogically extract $\tilde{\tilde{\alpha}}$ and retrieve the sample polarisability. Practically, obtaining this set of data requires two successive recording of the diffracted field for each incident direction and may not be very convenient. Now, we will show in the following that, contrary to the 2D configuration, it is also possible to retrieve α from the measure of only one component of $\mathbf{E}_{\mathrm{d}}$ for only one incident polarisation.

In the three-dimensional configuration, there are several illumination-observation pairs pinpointing on the same spatial frequencies for $\tilde{\tilde{\alpha}}$. This redundancy stems from the skew-rays for which $\mathbf{k}$, $\mathbf{k}_{\mathrm{inc}}$ and $\mathbf{z}$ are not coplanar. It permits to build a linear combination of $\mathbf{E}_{\mathrm{d}}$ for extracting $\tilde{\tilde{\alpha}}$ at a given vector frequency. More precisely, introducing (A,B,C) and (D,E,F) the polarisability vector frequencies that appear in $\mathbf{E}_{\mathrm{d}}$ for a given $(\mathbf{k}_{\mathrm{inc}}, \mathbf{k})$, one gets

$$(A,B,C) \;=\; (k_x - k_{\mathrm{inc},x}, k_y - k_{\mathrm{inc},y}, |k_z - k_{\mathrm{inc},z}|) \tag{4.29}$$

$$(D,E,F) \;=\; (k_x - k_{\mathrm{inc},x}, k_y - k_{\mathrm{inc},y}, |k_z + k_{\mathrm{inc},z}|). \tag{4.30}$$

This system has a solution if and only if $A = D$, $B = E$, (D, E, F) is in the zone (2) of Fig. 4.3 (assuming cylindrical symmetry around the $\mathbf{z}$ axis) and (A, B, C) belong to the whole $2k_0$ half-ball radius [73]. There is, however, no defined link between C and F. Indeed for every point (A, B, C) of zone (2), it is possible (with a reasoning similar to that of Appendix A), to find a pair $(\mathbf{k}, \mathbf{k}_{\rm inc})$ such that $(D, E, F) = (A, B, F)$ with F being any value of $[0, \sqrt{2k_0 - A^2 - B^2}]$. In particular, for any $\boldsymbol{\nu} = A\mathbf{x} + B\mathbf{y}$ and C such that $(\boldsymbol{\nu}, C)$ belong to the half-ball of radius $2k_0$, one can find an observation-pair $(\mathbf{k}, \mathbf{k}_{\rm inc})$ such that $F = 0$

$$\mathbf{k} = \frac{1}{2}\boldsymbol{\nu} \pm \sqrt{k_0^2 - \frac{\|\boldsymbol{\nu}\|^2 + C^2}{4}}\boldsymbol{\nu}_\perp + \frac{1}{2}C\mathbf{z} \tag{4.31}$$

$$\mathbf{k}_{\rm inc} = \frac{1}{2}\boldsymbol{\nu} \mp \sqrt{k_0^2 - \frac{\|\boldsymbol{\nu}\|^2 + C^2}{4}}\boldsymbol{\nu}_\perp - \frac{1}{2}C\mathbf{z} \tag{4.32}$$

$$\boldsymbol{\nu}_\perp = \frac{\mathbf{z} \times \boldsymbol{\nu}}{|\boldsymbol{\nu}|} \tag{4.33}$$

These two solutions correspond to the inversion of the role of the incident and diffraction directions. The Reciprocity Theorem [93] states indeed that $\mathbf{E}_{\rm d}(\mathbf{k}, \mathbf{k}_{\rm inc}) = \mathbf{E}_{\rm d}(\mathbf{k}_{\rm inc}, \mathbf{k})$ for all $\mathbf{k}$ and $\mathbf{k}_{\rm inc}$. Measurements obtained with these specific illumination-observation pairs are proportional to $\tilde{\tilde{\alpha}}(\boldsymbol{\nu}, 0) - \tilde{\tilde{\alpha}}(\boldsymbol{\nu}, C)$. Inverse cosine-Fourier transforming this set of data, yields the same $\alpha_{\rm mes}$ map plus a Dirac contribution at $z = 0$ plane that can be discarded.

This procedure shows that there is enough information for reconstructing $\alpha_{\rm mes}$ in a set of data consisting of only one incident polarization and one component of the diffracted field. However, the proposed solution, seems impractical as it requires to select the proper illumination-observation pair for each vector frequency $(\boldsymbol{\nu}, C)$ of $\tilde{\tilde{\alpha}}$. Usually the set of measurement never contains exactly the proper pair $(\mathbf{k}, \mathbf{k}_{\rm inc})$. This is why we preferred to used the iterative inversion algorithm described in the next section.

4.2.3 Numerical experiments

To show the interest of the mirror-assisted TDM concept, we performed numerical simulations of the experiment and developed an iterative inversion procedure to reconstruct $\alpha_{\rm mes}$. The calculations were done thanks to a Fortran code provided by Patrick C. Chaumet [72].

We consider a sample consisting in a non-absorbing dielectric sphere with relative permittivity $\varepsilon = 1.01$ containing two absorbing spherical inclusions with permittivity $\varepsilon = 1.01 + 0.02i$ separated vertically by 0.6λ centre-to-centre (see Fig. 4.4). The far-field diffracted by the sample placed in free-space or on a mirror is calculated rigorously with the Coupled Dipole Method (*cf.* Sec. 7.1) and corrupted with noise (5%) [72]. The incident (respectively diffracted) waves are sent (respectively detected) in a cone with half-angle 70° corresponding to $\mathrm{NA} = 0.95$. We use 64 incident plane waves and 121 observation directions regularly spaced within the incident and observation cones. All the incident plane waves are s-polarised and only one component of the diffracted field is measured (which simplifies greatly the experimental set-up).

We study four different TDM configurations: the transmission case where incident and observation cones are opposite; the reflection case, where the incident and observation directions are done from the same side; the ideal 4Pi case, where incidences and observations fill both

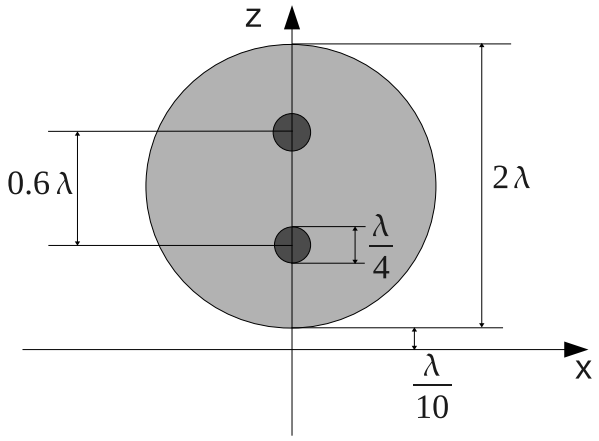

Figure 4.4: Sketch of the test sample used to compare the different TDM configurations. The 2λ-diameter sphere has a relative permittivity $\varepsilon = 1.01$ and contains two absorbing inclusions with relative permittivity $\varepsilon = 1.01 + 0.02i$. These permittivity values are low enough for the renormalised Born approximation to be valid.

cones above and under the sample; the mirror assisted case, where the illumination and observation are done from the same side and the sample is placed in the vicinity of a mirror.

To retrieve the permittivity map from the diffracted far-field, an inversion procedure based on the linearised conjugate gradient algorithm described in Sec. 7.2.2.1 is used. Under the renormalised Born approximation, the field inside the sample is assumed to be equal to the reference field, *i. e.* the field that would exist without the sample. This approximation permits to diminish dramatically the computational burden.

Results are presented in Fig. 4.5. The transmission configuration gives a correct image of the sphere but does not resolve the two inclusions. The map obtained from the reflection configuration is impossible to interpret because the real and imaginary parts of the sample permittivity are mixed (see Sec. 3.3 and Figs. 3.2 (d) and (e)). The mirror-assisted and the complete configuration give comparable images. The sphere is well reconstructed and the two small inclusions are resolved. This illustrates clearly the interest of the mirror-assisted TDM. The mirror configuration brings about a resolution equivalent to the ideal 4Pi one, with a set-up no more complex than that used for the reflection configuration. The resolution is almost isotropic, being equal to $\lambda/(2\mathrm{NA})$ in the lateral direction and $\lambda/2$ in the axial one.

4.3 Conclusion

In this chapter we have shown the interest of placing the sample in the vicinity of a mirror for improving the axial resolution of Tomographic Diffraction Microscopy. We have observed that, in the specific two-dimensional scalar configuration where the sample is invariant along one axis and the illumination and observation are performed within one plane, it is necessary to measure sequentially the diffracted field for two different polarisations of the illumination field for reconstructing properly the sample permittivity. In the vectorial three-dimensional configuration, the measurement of one component of the diffracted field for one incident polarisation for illumination-observation pairs scanning the objective accessible cone is sufficient for retrieving the sample permittivity map. One obtains the same resolution as an ideal set-up

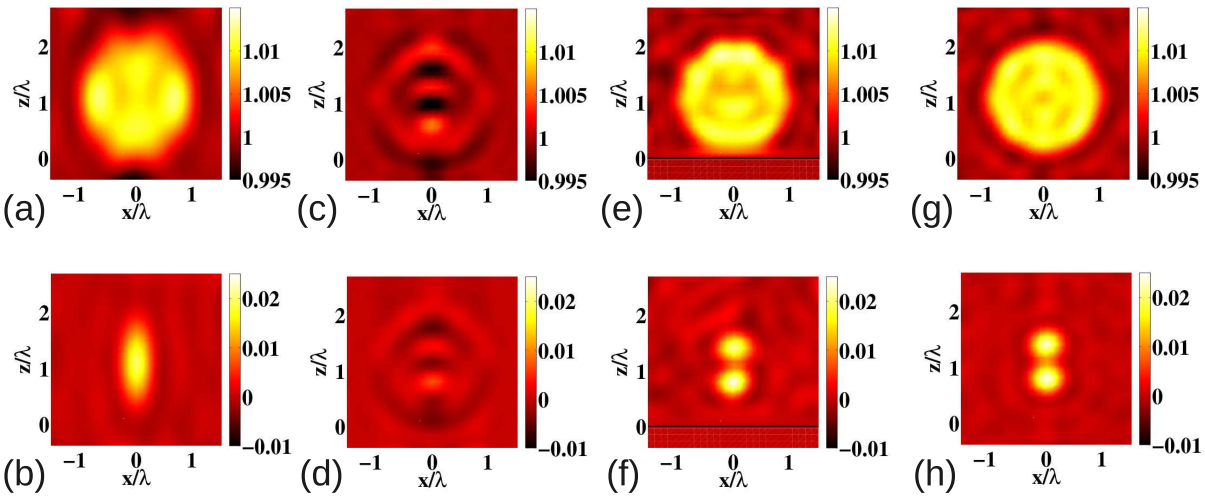

Figure 4.5: Reconstructed permittivity maps obtained for different configurations of TDM. The sample is described in Fig. 4.4. The maximum angle defined by the objective numerical aperture is $70°$. (a) and (b) real and imaginary part of the permittivity map reconstructed from a transmission TDM experiment. (c) and (d) real and imaginary part of the permittivity map reconstructed from a reflection TDM experiment. (e) and (f) real and imaginary part of the permittivity map reconstructed from a mirror-assisted TDM experiment. The black line indicates the mirror position. (g) and (h) real and imaginary part of the permittivity map reconstructed from an ideal TDM experiment where illumination and observation are performed from both sides of the sample.

where the sample is illuminated and observed from all possible directions (as can be done with two opposing objectives). The improvement brought about by the mirror and the simplicity of its practical implementation suggests that it could also be useful for other types of microscopy techniques. Indeed there is also a lack of axial resolution in confocal microscopy as in all types of technique that requires focussing of a laser beam. In the following chapter, we propose to use a mirror in a confocal microscopy set-up for improving the axial resolution.

Chapter 5

Isotropic Single-Objective microscopy: a mirror-assisted confocal fluorescence microscopy

5.1 Principle

In this chapter, we adapt the mirror approach to confocal microscopy in order to ameliorate the axial resolution [6]. Indeed, similarly to Tomographic Diffraction Microscopy, the axial resolution of confocal microscopes is several times larger than the transverse one because of the asymmetry of the illumination and observation (see Sec. 2.3.2). To address this problem, it has been proposed by Hell *et al.* [5] to create a quasi-isotropic illumination spot by sending the laser beam trough two opposing objectives. The interference between the counter-propagative beams allows the reduction of the spot size along the optical axis. However this approach requires a long-arm interferometric set-up that is difficult to tune and stabilise. We propose here to replace one of the objective by a mirror.

Focusing a laser beam before or after a mirror, by itself, cannot bring any improvement of the spot geometry simply because the incident and the reflected fields do not participate together to the spot formation. It is also necessary to shape the incident beam so that both incident and reflected fields converge toward the same point. Electromagnetic time reversal theory recently provides a proper framework for this goal [9, 6, 94]. The theory states that by sending in time reversed order (or with phase conjugation), the field radiated by a point source in an arbitrary environment, one forms an optimal light spot at the source location [10]. Hence, to focus light into an isotropic spot before the mirror, one needs to shape the beam reaching the back focal plane of the objective so that it resembles the conjugated of the field radiated by a dipole placed at the focussing position. Our approach consists in first simulating, at the back focal plane of the objective, the field radiated by an emitter placed at z_0 above the mirror. Then, we use a Spatial Light Modulator (SLM) to impose the required phase variation on the collimated laser beam reaching the back focal plane. This phase has to be the opposite of the simulated field phase (phase conjugation). With this proper wave-front the beam focus at the desired position with an optimal isotropic shape.

The next section gives all the theoretical and practical details on the mirror-assisted ISO fluorescence microscopy. The text corresponds essentially to the article by E. Le Moal, E.

Mudry, P. C. Chaumet, P. Ferrand, and A. Sentenac, *Isotropic single-objective microscopy: theory and experiment*, J. Opt. Soc. Am. A **28**, 1586–1594 (2011) [7]. Additional work on radial polarisation and two-photon microscopy is also presented at the end of the chapter.

5.2 Isotropic Single Objective (ISO) microscopy: Theory and Experiment[1]

5.2.1 Introduction

Sharp focusing of light beams is the keystone of numerous applications in crucial technological fields including far-field optical microscopy [95], optical writing and reading for high-density data storage [96, 97], and trapping and manipulation of nano-particles [98, 99, 100]. Objective lenses of high numerical aperture with high-order aberration corrections have been developed to reduce the dimensions of the focal spot down to the diffraction limit. Still, optical focusing systems based on a single-lens geometry cannot focus light into ideally spherical volumes because the illumination comes only from one side of the focal point. As a result, the focal spot is elongated along the lens optical axis, with an axial dimension about threefold larger than the transverse ones, at best. Such a pronounced anisotropy constitutes a serious drawback for any three-dimensional (3D) application in the above-mentioned fields of technology. This fundamental issue has motivated the study of many different approaches, among which are notably the use of pupil filters to control the amplitude and/or the phase distribution of the input field [58, 101, 102, 103, 104, 60] and (or together with) the use of peculiar polarisation modes [59, 105, 106]. These approaches allow to engineer, to a certain extent, the spatial field distribution at the focus; however, they bring about only modest improvement concerning the axial dimension of the focal spot [107].

In the specific field of 3D fluorescence imaging in biology, the resolution issue has been addressed through sophisticated approaches resorting on non-linear excitation processes and optical focusing systems based on a multiple-lens geometry [108, 109]. In 4Pi microscopy, the sample is sandwiched between two opposing lenses having the same optical axes and front focal planes. Focusing light through both lenses in a coherent way, yields an interference pattern that exhibits a quasi-spherical intensity peak surrounded by some side lobes [5, 110, 111]. The 4Pi focusing (and detection) scheme has brought about a spectacular improvement in the axial resolution of 3D fluorescence imaging but it requires a careful alignment of the lenses and turns out to be quite sensitive to mechanical drifts.

In this work, we demonstrate that light can be focused into a quasi-spherical spot thanks to one microscope objective lens, a mirror and a specially shaped incident beam [6]. In a naive view, the ISO focusing set-up is equivalent to the 4Pi set-up in which the role of the second lens is played by the image of the first one in a mirror.

We first detail the concept of ISO microscopy and describe the numerical technique that permits to simulate with the least possible approximations the point spread function of a realistic

[1]This section was originally published in E. Le Moal, E. Mudry, P. C. Chaumet, P. Ferrand, and A. Sentenac, *Isotropic single-objective microscopy: theory and experiment*, J. Opt. Soc. Am. A **28**, 1586–1594 (2011) [7]. Theory and simulations were made by Patrick C. Chaumet, Anne Sentenac and myself with the advices of Pr. Colin Sheppard; Experiments were made by Eric le-Moal and Patrick Ferrand with the advices of Pr. Rainer Heintzmann.

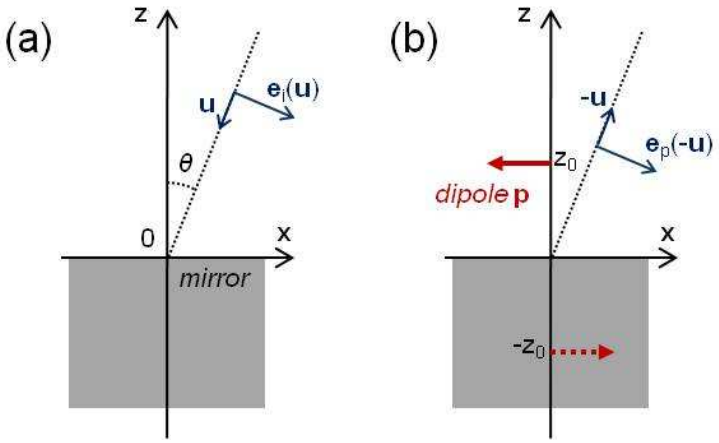

Figure 5.1: Illustration of the ISO focusing concept, based on the time reversal theory. (a) The incident field is made of a sum of plane waves propagating along $\mathbf{u}$ with complex vector amplitude $\mathbf{e}_i(\mathbf{u})$. (b) the field radiated by a dipole placed at $z_0\mathbf{z}$ before the mirror can be decomposed as a sum of plane waves propagating along $-\mathbf{u}$ with complex vector amplitude $\mathbf{e}_p(-\mathbf{u})$. To focus at point $z_0\mathbf{z}$, the time reversal focusing theory states that $\mathbf{e}_i(\mathbf{u})$ should ideally be equal to the conjugate of $\mathbf{e}_p(-\mathbf{u})$.

ISO fluorescence microscope. Then, we show how an ISO fluorescence microscope can be built out of a conventional confocal microscope and display experimental point-spread-functions. We point out the main features that can hamper the performances of the microscope and give some hints to overcome them.

5.2.2 Principles of ISO focusing and simulations

5.2.2.1 Time-Reversal focusing theory

To focus light into a spherical spot, the illumination should ideally reach the focal point from every possible direction. To approach this spherical illumination with a single objective lens, we place a mirror nearby the focal plane and engineer the incident wave front so that part of the incident and mirror-reflected fields converge towards the focal point.

Hereafter, the sample space (after the objective lens) is described by a Cartesian set of coordinates (x, y, z) with the origin placed at the focal point of the lens and the $\mathbf{z}$ axis corresponding to its optical axis. In this part, for simplicity, the mirror plane is set at the $z = 0$ plane which corresponds to the focal plane. To describe the incident beam, it is convenient to introduce the polar and azimuthal angles (θ, ϕ) associated to the unit vectors $\mathbf{u}$ defined by $\mathbf{u} = \cos\theta\mathbf{z} + \sin\theta\cos\phi\mathbf{x} + \sin\theta\sin\phi\mathbf{y}$, $\mathbf{u}_\phi = \mathbf{z} \times \mathbf{u}$ and $\mathbf{u}_\theta = \mathbf{u} \times \mathbf{u}_\phi$. The incident field on the mirror is cast as a sum of monochromatic plane waves [see Fig. 5.1(a)], propagating in the $\mathbf{u}$ direction with complex amplitude vector $\mathbf{e}(\mathbf{u})$,

$$\mathbf{E}_{\text{inc}}(\mathbf{r}) = \int_{\phi\in[0,2\pi]} \int_{\theta\in[-\theta_{\max},\theta_{\max}]} \sin\theta \mathbf{e}_i(\mathbf{u}) \exp(ik_0\mathbf{u}\cdot\mathbf{r}) \mathrm{d}\theta\mathrm{d}\phi \tag{5.1}$$

where $k_0 = 2\pi/\lambda$ is the wave number in the sample space, and $\theta_{\max}$ is the maximum angle that can be reached in the sample space with the chosen numerical aperture of the objective. Because of the transverse nature of the plane waves, $\mathbf{e}_i(\mathbf{u})$, can be decomposed on the $(\mathbf{u}_\theta, \mathbf{u}_\phi)$

basis. Assuming the mirror to be perfectly conducting, the reflected beam reads,

$$\mathbf{E}_{\text{refl}}(\mathbf{r}) = \int_{\phi\in[0,2\pi]} \int_{\theta\in[-\theta_{\max},\theta_{\max}]} \sin\theta \mathbf{e}_r(\mathbf{u}) e^{ik_0[\mathbf{u}-2(\mathbf{u}\cdot\mathbf{z})\mathbf{z}]\cdot\mathbf{r}} \mathrm{d}\theta\mathrm{d}\phi \tag{5.2}$$

with $\mathbf{e}_r(\mathbf{u}) = -\mathbf{e}_i(\mathbf{u}) + 2[\mathbf{e}_i(\mathbf{u})\cdot\mathbf{z}]\mathbf{z}$.

The shaping of the incident beam is performed following the time reversal focusing theory depicted in Ref. [10] and illustrated in Fig. 5.1. To focus light at the point $\mathbf{r}_0 = z_0\mathbf{z}$, $\mathbf{e}_i(\mathbf{u})$ should ideally be equal to the complex conjugate of $\mathbf{e}_p(-\mathbf{u})$, the complex amplitude vector of the plane wave emitted in the $-\mathbf{u}$ direction by a dipole-source $\mathbf{p}$ placed at $\mathbf{r}_0$. The radiation of the dipole in front of the mirror is equivalent to that of two dipoles in free space, symmetrically positioned with respect to the mirror plane at z_0 and $-z_0$, with same z-component and opposite (x, y) components. As a result, one finds for $\mathbf{p}$ parallel to the mirror,

$$\mathbf{e}_i^{\text{ideal}}(\mathbf{u}) \propto \sin(z_0 k_0 \cos\theta)[\mathbf{p} - (\mathbf{p}\cdot\mathbf{u})\mathbf{p}], \tag{5.3}$$

and the same expression with $\sin(z_0 k_0 \cos\theta)$ replaced by $\cos(z_0 k_0 \cos\theta)$ for a dipole normal to the mirror. Note that the incident beam $\mathbf{E}_{\text{inc}}$ defined by Eq. (5.1) with $\mathbf{e}_i$ given by Eq. (5.3) focuses at two points along the optical axis, at z_0 and $-z_0$.The shape of the two spots is elongated along the optical axis in the same way as that of the standard spot obtained by focusing a plane wave through one objective lens. The quasi-isotropic spot is obtained through the interference between the incident and the mirror-reflected beams.

More precisely, if $\theta_{\max} = \pi/2$, the time-reversal theory states that the total field, $\mathbf{E}_{\text{tot}}(\mathbf{r}, \mathbf{r}_0) = \mathbf{E}_{\text{inc}}(\mathbf{r}, \mathbf{r}_0) + \mathbf{E}_{\text{refl}}(\mathbf{r}, \mathbf{r}_0)$ with $\mathbf{e}_i$ satisfying Eq. (5.3) is proportional to the imaginary part of the electric field radiated by the dipole placed at $\mathbf{r}_0$ before the mirror [10]. Now, because of the rapid decay of the reflected field (namely the field emitted by the image dipole), the field radiated by the dipole before the mirror is quite similar to the field radiated by the same dipole in free-space. Its intensity distribution has a quasi-spherical shape with radius at half-maximum about $\lambda/2$. Hence, the time-reversal beam shaping appears as a very efficient way for obtaining an isotropic light spot that can be moved with respect to the mirror, without distortion, just by changing z_0 in Eq. (5.3).

5.2.2.2 Simulation of the Point Spread Function (PSF) of the ISO microscope

Considering a realistic objective lens, $\theta_{\max}$ is inevitably smaller than $\pi/2$. Moreover, it is generally difficult to shape simultaneously the phase, amplitude and polarisation of the incident waves to obtain a field satisfying Eq. (5.3). Hence, to investigate the achievable performances of the ISO focusing and imaging concept, we have performed simulations of the illumination and global PSF of the ISO microscope accounting for these constraints.

In our experimental configuration, a Spatial Light Modulator (SLM) that only modifies the phase of the field is placed at (or conjugated to) the rear focal plane of a microscope objective lens. The first difficulty is to relate the field leaving the SLM plane to the plane waves that illuminate the mirror.

To indicate points and vectors in the (x, y) SLM plane, we introduce the cylindrical set of coordinates (ρ, ψ) associated to the local basis

$$\mathbf{u}_\rho = \cos\psi\mathbf{x} + \sin\psi\mathbf{y}$$
$$\mathbf{u}_\psi = -\sin\psi\mathbf{x} + \cos\psi\mathbf{y}.$$

Under Abbe's sine condition, a point (ρ, ψ) of the rear focal plane (where the SLM is placed) corresponds to a plane wave propagating in the sample space along the $\mathbf{u}$ direction defined by the polar and azimuthal angles (θ, ϕ) which satisfy, ϕ equal to ψ and

$$\sin\theta = (\sin\theta_{\max})\rho/R, \tag{5.4}$$

where R is the radius of the aperture at the rear side of the objective lens. More precisely, provided that we can neglect the various reflections on the optical components, the electric field $\mathbf{E}(\rho,\psi)$ collinear to $\mathbf{u}_\phi$ [$\mathbf{u}_\rho$] leaving the SLM plane at point (ρ,ψ) is transformed into a plane wave propagating along $\mathbf{u}$ that is polarised along $\mathbf{u}_\psi$ [$-\mathbf{u}_\theta$] with a damped modulus $E(\rho,\psi)\sqrt{\cos\theta}$, where $\sqrt{\cos\theta}$ is the so-called aplanatic factor. Hence, the complex amplitude vectors of the incident plane waves in the sample space that are generated by any field $\mathbf{E}(\rho,\psi)$ leaving the SLM reads,

$$\mathbf{e}_i(\mathbf{u}) = \sqrt{\cos\theta}\Big([\mathbf{E}(\rho,\psi)\cdot\mathbf{u}_\phi]\mathbf{u}_\psi - [\mathbf{E}(\rho,\psi)\cdot\mathbf{u}_\rho]\mathbf{u}_\theta\Big). \tag{5.5}$$

Eq. (5.5) gives the field in an aberration-free system satisfying the sine condition. Other apodisation factors could be used (to account, for example, for the Fresnel transmission coefficients of the lens), but they were shown to have a limited impact on the size of the point spread function [112]. The field leaving the SLM $\mathbf{E}(\rho,\psi)$, can be written as $\mathbf{E}(\rho,\psi) = \mathbf{E}_0(\rho,\psi)\exp[if(\rho,\psi)]$, where $\mathbf{E}_0(\rho,\psi)$ is the incident field on the SLM and $f(\rho,\psi)$ is the phase modulation applied by the SLM. In our set-up, the SLM is illuminated by a collimated beam that is linearly polarised along the x axis which corresponds to the working axis of the SLM. Hence, $\mathbf{E}_0$ is a constant. The pattern displayed on the SLM is given by the phase of Eq. (5.3)

$$f(\rho,\psi) = \frac{\pi}{2}\mathrm{sign}[\sin(z_0 k_0\cos\theta)], \tag{5.6}$$

where θ is related to ρ through Eq. (5.4). Introducing Eq. (5.6) into Eq. (5.5) and comparing the latter to Eq. (5.3) with $\mathbf{p} = \mathbf{x}$, one observes that the phase of $\mathbf{e}_i$ coincides with that obtained for $\mathbf{e}_i^{\mathrm{ideal}}$. On the other hand, the modulus and polarisation differ, especially for large θ and for propagation directions outside the (x,z) or (y,z) planes, but the consequences on the focusing are negligible [113].

Once the complex vector amplitudes of the plane waves forming the incident beam are well defined, we calculate the reflected beam with Eq. (5.2). The total field

$$\mathbf{E}_{\mathrm{tot}}(\mathbf{r},\mathbf{r}_0) = \mathbf{E}_{\mathrm{inc}}(\mathbf{r},\mathbf{r}_0) + \mathbf{E}_{\mathrm{refl}}(\mathbf{r},\mathbf{r}_0)$$

depends on the chosen focal point $\mathbf{r}_0$ via the phase pattern displayed on the SLM, Eq. (5.6). Yet, we have checked numerically that, except when $\mathbf{r}_0$ is close to the mirror (typically for distances smaller than half the wavelength), the spot shape does not vary when $\mathbf{r}_0$ is changed. In other words, the illumination PSF, $\mathrm{PSF}_{\mathrm{ill}}(\mathbf{r}-\mathbf{r}_0) \propto |\mathbf{E}_{\mathrm{tot}}(\mathbf{r},\mathbf{r_0})|^2$ can be assumed to be homogeneous within the sample space.

Now, to perform a complete modelling of the experiment, one needs to simulate the image of a point-like fluorescent source placed at $\mathbf{r}$ in the sample space. In our set-up, we use a confocal detection scheme. The fluorescence light is modified by the SLM and polarised along the x axis in the same way as the incident light before being sent, through a pinhole, onto a detector. We assume that the intensity recorded by the detector is proportional to $\int_S |\mathbf{E}(\mathbf{v}).\mathbf{x}|^2 \mathrm{d}\mathbf{v}$ where S is the pinhole transmission area and $\mathbf{E}(\mathbf{v})$ is the field radiated at point $\mathbf{v}$ by the fluorescent dipole $\mathbf{p}_{\mathrm{fluo}}$ placed at $\mathbf{r}$ in the sample space for a given focal point $\mathbf{r}_0$ set on the SLM.

The calculation of $\mathbf{E}(\mathbf{v}) \cdot \mathbf{x}$ is easily done by invoking the reciprocity theorem [93]. We consider a virtual monochromatic dipole $\mathbf{p}_{\text{virtual}}$, oriented along the $\mathbf{x}$ axis, placed at the centre of the pinhole and radiating at the same wavelength as the fluorescent dipole, λ', which is slightly different from the wavelength of the illumination λ. It generates a plane wave normal to the SLM plane, and creates, in the sample space, the field $\mathbf{E}^{\lambda'}_{\text{tot}}(\mathbf{r}, \mathbf{r_0})$. If $\mathbf{p}_{\text{virtual}}$ is shifted by $\mathbf{v}$ in the pinhole plane, it creates the field $\mathbf{E}^{\lambda'}_{\text{tot}}(\mathbf{r}, \mathbf{r}_0 + \mathbf{v})$ in the sample space (for simplicity, we overlook the magnification factors between the pinhole and the sample space). The reciprocity theorem states that $\mathbf{E}(\mathbf{v}).\mathbf{p}_{\text{virtual}} = \mathbf{p}_{\text{fluo}}.\mathbf{E}^{\lambda'}_{\text{tot}}(\mathbf{r}, \mathbf{r}_0 + \mathbf{v})$. Now, the fluorescent dipole amplitude is proportional to the field at point $\mathbf{r}$ created by the incident laser field $\mathbf{E}^{\lambda}_{\text{tot}}(\mathbf{r}, \mathbf{r}_0)$. Finally, the intensity recorded by the detector can be written as,

$$I(\mathbf{r}, \mathbf{r}_0) \propto \text{PSF}^{\lambda}_{\text{ill}}(\mathbf{r} - \mathbf{r}_0)\text{PSF}^{\lambda'}_{\text{det}}(\mathbf{r} - \mathbf{r}_0), \tag{5.7}$$

where $\text{PSF}^{\lambda'}_{\text{det}}(\mathbf{r} - \mathbf{r}_0) = \int_S \text{PSF}^{\lambda'}_{\text{ill}}(\mathbf{r} - \mathbf{r}_0 - \mathbf{v})\text{d}\mathbf{v}$. We note that $I(\mathbf{r}, \mathbf{r}_0)$ depends solely on $\mathbf{r} - \mathbf{r}_0$. We then introduce the global PSF of the microscope, $\text{PSF}(\mathbf{r} - \mathbf{r}_0) \propto I(\mathbf{r}, \mathbf{r}_0)$ which, in the ideal case of a point detector and a perfectly coherent fluorescent source emitting at the same wavelength as the excitation light is equal to $\text{PSF}^2_{\text{ill}}$. This ideal configuration is equivalent to a 4Pi microscope of type C with a point detector [114]. Unfortunately, the fluorophore emits at a longer wavelength than the excitation wavelength and, more important, the coherence length of the emitted light is about 3 μm which is generally smaller than the distance between the fluorescent source and the mirror. As a result, the fluorescent light directly emitted towards the objective lens does not interfere with the emitted light that is reflected by the mirror before being collected. In this case,

$$|\mathbf{E}^{\lambda'}_{\text{tot}}(\mathbf{r}, \mathbf{r}_0)|^2 = |\mathbf{E}^{\lambda'}_{\text{inc}}(\mathbf{r}, \mathbf{r}_0)|^2 + |\mathbf{E}^{\lambda'}_{\text{refl}}(\mathbf{r}, \mathbf{r}_0)|^2$$

and the detection PSF is very similar to that of a conventional confocal microscope. This configuration corresponds to a 4Pi A type microscope [114]. Note that by placing a filter (with typically a 10 nm bandpass) in front of the pinhole, one could increase the coherence length of the fluorescence light so that the direct and reflected beams interfere. In this case, the detection PSF would be similar to the illumination PSF and the configuration would correspond to a 4Pi-C microscope.

Figure 5.2 shows the global PSF of the ISO microscope, calculated for a quasi-ideal objective with $\sin\theta_{\max} = 0.99$ and a more realistic one with $\sin\theta_{\max} = 0.80$. In these calculations, we use the parameters of the experimental set-up: wavelength $\lambda = 491$ nm and pinhole diameter in the focal plane 1.22λ. Light is focused in vacuum and the objective lens is assumed to be ideally un-aberrated. The validity of our numerical technique was checked by comparing its results for a standard confocal microscope to the semi-analytical expressions given in [29, Chapter 6]. The SLM is modelled as a 1000×1000 pixel array, with a constant phase value on each pixel. To account for possible errors stemming from the SLM pixellation, the propagation directions of the plane waves forming the incident beam are not discretised in the Cartesian SLM basis but in the spherical basis (θ, ϕ), 500 in θ and 180 in ϕ. The SLM pattern is tuned to focus light at $z_0 = 20\lambda$ from the mirror and the incident polarisation is collinear to the $\mathbf{x}$ axis. The fact that the emission wavelength differs from the excitation one is not taken into account for these simulations.

The global PSF obtained for $\text{NA} = 0.99$ is quasi-isotropic with diameter about $\lambda/3$. For $\text{NA} = 0.8$, the central peak of the PSF is also quasi-isotropic but it is plagued by side lobes of higher relative intensity (60% to 80% of the main lobe) than that observed for $\text{NA} = 0.99$ (about 20%).

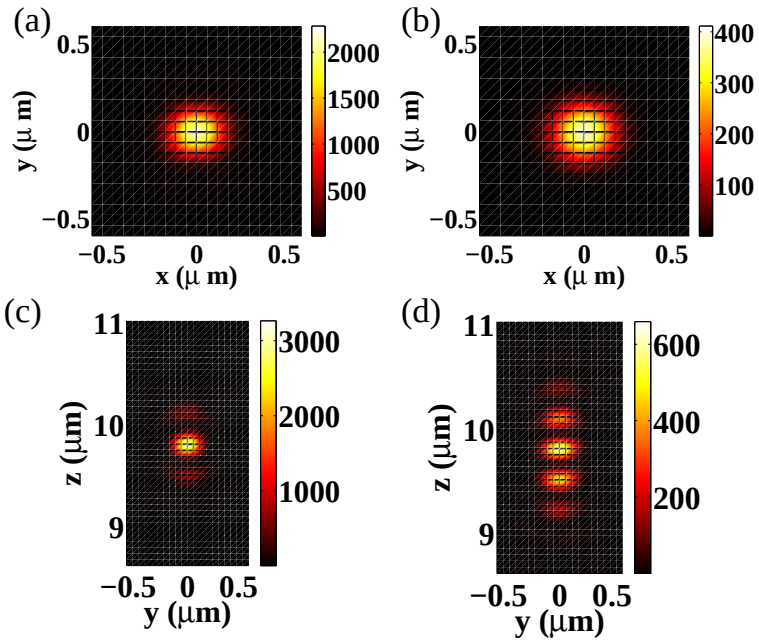

Figure 5.2: Global PSF of an ISO microscope, simulated for two different objectives in air: (a) and (c) ideal objective with $\mathrm{NA} = \sin\theta_{\max} = 0.99$. (b) and (d) realistic objective, $\mathrm{NA} = \sin\theta_{\max} = 0.80$. These images corresponds to slices taken (a,b) in the transverse and (c,d) axial planes.

Remarkably, we observe that, along the optical axis, the global $\mathrm{PSF}_{\mathrm{tot}}$ of the ISO microscope is perfectly fitted by the global $\mathrm{PSF}_{\mathrm{tot}}$ of the conventional confocal microscope (with same numerical aperture) times $\cos^2[\beta k_0(z - z_0)]$. The parameter β depends on the numerical aperture of the objective (0.70 for $\mathrm{NA} = 0.99$ and 1.02 for $\mathrm{NA} = 0.80$), see Fig. 5.3. This behaviour is easily understood if one approximates the ISO spot by the interference of two counter propagative Gaussian beams with superimposed waists. The parameter β indicates that, along the optical axis, the phase of the field forming the beams does not vary along z as $k_0 z$. Indeed, there exists a phase delay, known as the Gouy phase (which depends on the beam waist and thus on the numerical aperture of the objective), that modifies the period of the interference pattern. This property gives an interesting self-consistent way to verify that the ISO microscope is correctly tuned as it relates the ISO point spread function to the standard confocal one obtained with the same objective. In the following we will use this approach rather than a direct comparison between theory and experiment to assess the accuracy of our mounting. Indeed, we noticed that comparing theoretical results to experimental ones was particularly difficult as the claimed numerical aperture and apodisation functions of the objective were not that observed experimentally [115].

5.2.2.3 Discussion on the phase pattern

In the absence of the mirror, the incident beam described in Eqs. (5.1) and (5.3) focuses at two points, located at z_0 and $-z_0$ along the optical axis. Therefore, an alternative approach to time reversal focusing could consist in splitting the SLM in two and displaying two Fresnel lenses focusing at different points. The phase pattern of each Fresnel lens is then, $f(\rho, \psi) = k_0 z_0 \cos\theta$ for the first one, and $f(\rho, \psi) = -k_0 z_0 \cos\theta - \pi$ for the second one. The $-\pi$ added to this second

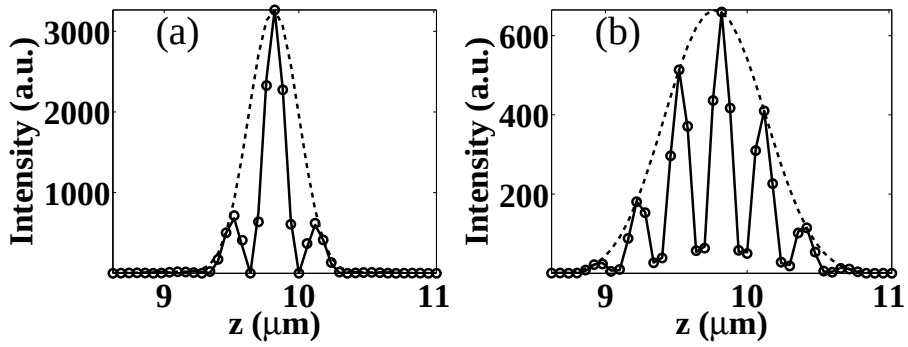

Figure 5.3: Axial profiles taken from the PSF of a ISO microscope (solid line) and a conventional confocal microscope (dashed line), simulated for different NA in vacuum. (a) $\mathrm{NA} = 0.99$. (b) $\mathrm{NA} = 0.80$. For comparison purpose, the PSF of the conventional confocal microscope has been plotted after modulation by $\cos^2[\beta k_0(z - z_0)]$ (circle markers). The observed asymmetry stems from the phase mask discretisation induced by the SLM.

formula is necessary to obtain the right phase match between these two focuses. The advantage of the Fresnel lens mask is that it can generate spots that are as close to each other as possible whereas the time-reversal mask becomes very approximate when z_0 decreases below a given value. In fact, as z_0 tends to 0, the number of sign changes in the function $\sin(z_0 k_0 n \cos\theta)$ tends to 0 too and, therefore, the phase modulation becomes increasingly less efficient to substitute for an ideal amplitude modulation in the time-reversal approach. The disadvantage of the Fresnel lens mask is that it requires to split the SLM in two areas so that only part of the $\mathbf{u}$ directions focus at z_0 ($-z_0$).

In Fig. 5.4 we give an example of the phase masks that are displayed on the SLM following the time reversal technique or the Fresnel lens approach with different templates for splitting the SLM. All three masks shown in Fig. 5.4 were designed for focusing light at $z_0 = 1$ μm (with $\lambda = 491$ nm). The simulations of the global PSF obtained with these different masks were very similar (not shown).

We now turn to the experimental measurement of the global PSF of the ISO microscope. In our experimental set-up, we have used both the time-reversal and Fresnel lenses techniques for engineering the incident beam.

5.2.3 Experimental results

5.2.3.1 Description of the set-up

The experimental configuration of the microscope exhibits the same features as that presented in the theoretical and numerical section. Basically, the ISO microscope consists in a conventional home-built confocal microscope that has been modified to allow the wave front shaping of the incident and detected light, see Fig. 5.5. More precisely, a phase-only SLM (PlutoVIS, Holoeye) functioning in reflection was introduced between a dichroic mirror (z488/633, Chroma) and a water immersion objective lens (Plan Apo VC $60\times$, $\mathrm{NA} = 1.2$, Nikon). The SLM plane was optically conjugated to the rear focal plane of the lens using a telescope. Hence, each pixel of the SLM corresponded to one direction in the observation region as assumed in the first section. Excitation was supplied by a continuous wave 491 nm laser. The fluorescence

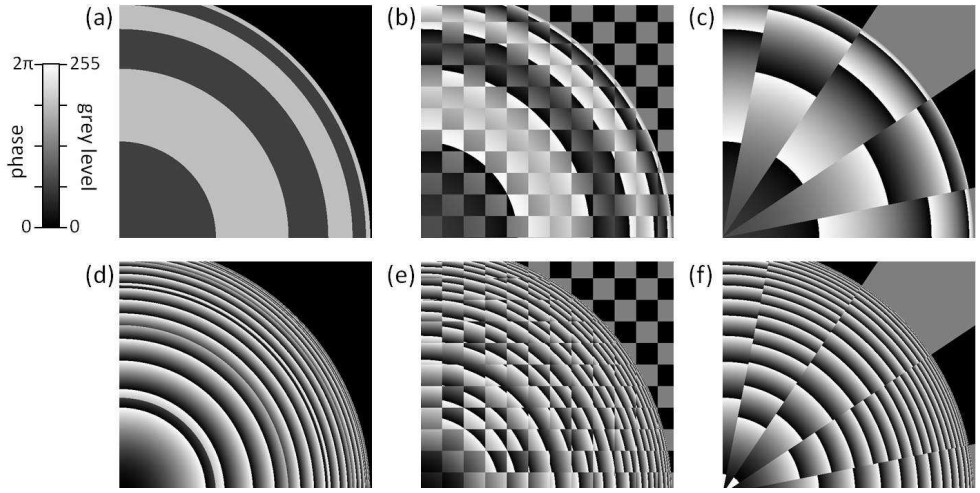

Figure 5.4: Examples of phase masks for ISO focusing. For symmetry reasons, only the top right quarter of the masks are shown (bottom left corner is the centre of symmetry). Mask designs are based on (a,d) the principle of time reversal focusing and (b,c,e,f) combinations of Fresnel phase plates following (b,e) a checker board of 50×50 pixel^2-wide squares and (c,f) a pie chart of 16 slices. These masks were generated for two different configurations in which the mirror is placed (a-c) in the genuine focal plane of the objective lens and (d-f) at $d = 6$ μm above it. In the latter case, the term $k_0 d \cos\theta$ has been added to all the phase patterns given in the text.

light collected in epi-geometry was "de-scanned" by the SLM, in order to keep the optical conjugation between the pinhole and the probed region. It was spectrally filtered (FF01-525/39-25, Semrock; centre wavelength: 525 nm; band width: 39 nm at 90% transmittance, 45 nm at 50% transmittance, corresponding to a coherence length of about 3 μm in vacuum) and spatially filtered with a 30 μm pinhole (*i.e.* 1 Airy diameter) placed in front of a photon counter (PD1C0C, Micro Photon Devices). Both excitation and fluorescence lights were horizontally polarised (along the $\mathbf{x}$ axis) so as to be parallel to the working axis of the SLM. Typical excitation power and acquisition dwell time were 10 μW and 1 ms/pixel, respectively.

The sample consisted in a suspension of isolated 100 nm spheres (Fluospheres Yellow/green, Invitrogen) in a $1\%wt$ agarose gel film (typical thickness of 5 to 10 μm) and was sandwiched between a Ag coated mirror and a conventional 150 μm cover slip. The mirror, was placed a few microns away from the focal plane of the microscope objective lens on a nano-positioning stage (NanoLP100, Mad City Labs). In our configuration, axial scanning was performed by changing the SLM pattern while transverse scanning was done by translating the mirror in the (x, y) plane with the stage.

5.2.3.2 Global PSF of the ISO microscope

To estimate the global PSF of the ISO microscope, we measured three-dimensional images of isolated beads in the sample and assumed that the latter were small enough to be considered point-like sources. Although a more precise assessment of the PSF would require 3D-deconvolution of the image by the bead volume, we found by numerical simulations that the actual bead size (100 nm) only slightly affects the fringe contrast. Different patterns were displayed on the SLM to engineer the wave front. The best results were obtained for the time-

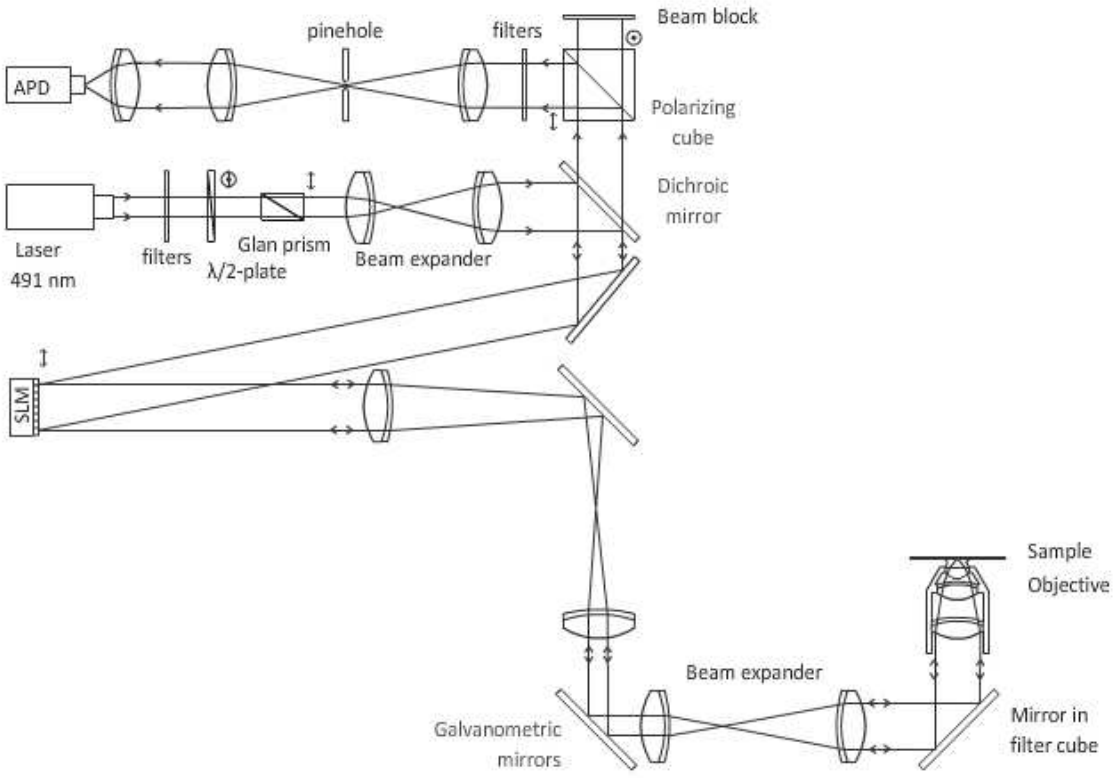

Figure 5.5: Schematic of the microscope set-up. Captions: avalanche photo-diode (APD); half-wave plate (HWP); phase-only spatial light modulator (SLM); rear focal plane (*rfp*). Lenses are achromatic doublets. See details in text.

reversal mask [see Fig. 5.6 (a)] and the Fresnel mask with a 16 slices pie-chart template [see Fig. 5.6 (b)]. We observed that the performance of the checker board templates decreased with the square size (from 50×50 pixel^2 to 1×1 pixel^2). The influence of the templates on the experimental image, which is not retrieved with the simulations, points out the practical limits of the SLM and, in particular, its failure to generate important phase changes at high spatial frequency, see Sec. 5.2.3.3 for more details.

To check the performance of the ISO set-up, we compared the image of a bead obtained in the ISO configuration to that of a bead measured in the conventional confocal geometry (*i.e.* without the mirror and the SLM), see Fig. 5.6 (a). Similarly to the simulated PSF shown in the first section, we observed that the experimental ISO PSF is close to the experimental PSF of the conventional confocal microscope, modulated by $\cos^2[\beta k_0(z - z_0)]$. We thus obtain a quasi-isotropic central peak, flanked by high side lobes that reflect the less than perfect focusing achievement of the conventional confocal microscope.

We then checked the homogeneity of the global PSF, by studying the images of beads located at various distances from the mirror, Fig. 5.7. We observed that, as expected, the profiles exhibit the same features whatever the distance of the bead to the mirror and the positions of the fringes change with the location of the beads.

These experimental results suggest that we have achieved the finest ISO point spread function possible with such a confocal microscope. It is worth noting that even for experiments requiring 15 to 20 minute-long measurements, we observed no drift of the set-up; namely the ISO PSF was preserved all along. We now describe the preliminary studies that were necessary to tune properly the ISO set-up and obtain these results.

5.2.3.3 Tuning an ISO microscope, cautions and preliminary studies

Basically, the ISO set-up requires to check three important steps, the confocal detection, the engineering of the wave front and the mirror positioning.

Confocal detection We have seen in the first section that ISO microscopy requires that both incident excitation light and collected fluorescence light be treated by the SLM; otherwise, it would not be compatible with a confocal detection scheme. Now, fluorescence light has a slightly longer wavelength than that of the excitation light, for which the phase masks were designed. Due to this chromaticism issue, we expect the optimal position of the pinhole to slightly change when going through the phase mask series. Therefore, we evaluated the detection efficiency of the microscope for each of the phase masks, by focusing light in a droplet of fluorescent dye solution (Rhodamine 6G, 10^{-6} mol L^{-1}), as schematised in Fig. 5.8. The position of the pinhole was optimised while focusing light 6 μm before the focal plane. We observed that the detection efficiency decays slowly as the focus is moved away by displaying different masks on the SLM. Loss of efficiency is observed down to about 20% at the extremes. Unsurprisingly, we found that the decay depends on the size of the pinhole; larger pinholes yield smaller losses. A pinhole of diameter 30 μm, (*i.e.* one Airy diameter), appeared to be a fair trade-off between the optical sectioning and a relatively constant efficiency of detection over a sufficiently wide scanning range along the optical axis.

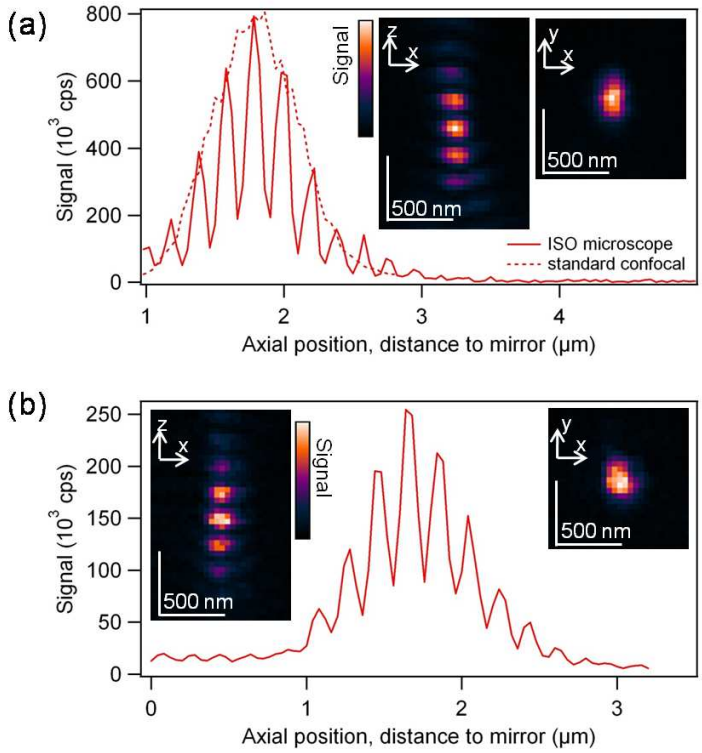

Figure 5.6: Profile intensity along the z axis of the images of isolated 100 nm fluorescent beads, measured by ISO microscopy. Vertical and horizontal slices of these images are shown in insets. Phase mask designs were based on (a) time reversal and (b) combinations of Fresnel phase plates with respect to a pie chart of 16 slices, see Fig. 5.4. Note that the image of the bead was recorded by transverse scanning with the nano-positioning stage and axial scanning of the sample with the SLM.

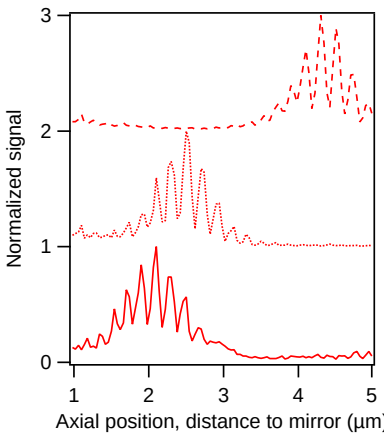

Figure 5.7: Intensity profiles taken along the axial direction of 3D images of 100 nm fluorescent beads, measured by ISO microscopy using time-reversal phase masks. Bead-to-mirror distances are estimated, on the basis of the position of the brightest fringe in the interference patterns, to 2.1 μm (–), 2.5 μm (...) and 4.3 μm (- -).

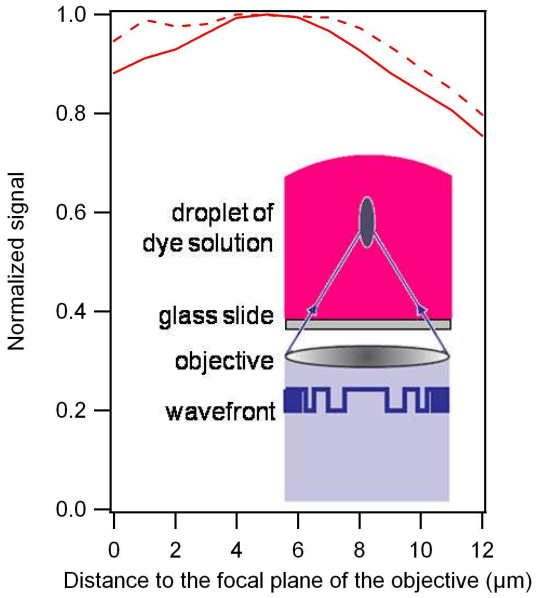

Figure 5.8: Relative variation of the fluorescent signal as a function of the phase masks displayed on the SLM, measured by focusing light in a droplet of fluorescent dye solution (Rhodamine 6G). Fresnel-lens phase masks were used to focus light in a single spot 0 to 12 μm before the genuine focal plane of the objective lens. Spatial filtering at detection was performed with pinholes of diameter 30 μm ($-$) and 50 μm (- -). These curves reveal the dependence of the detection sensitivity on the SLM display.

Engineering the wave front of the incident beam In a naive view, ISO focusing consists in forming two spots along the optical axis, one at the focal position and the other at its virtual image behind the mirror. Hence, at least one of them forms out of the genuine focal plane of the objective lens. Now, for achieving an interference pattern of optimal contrast, the two spots should have a similar field distribution and be accurately positioned. Hence, it is necessary to check that focusing out of the focal plane does not deteriorate the spots. We tested the ability of our water-immersion microscope objective to focus light up to 12 μm before its focal plane by displaying a Fresnel lens with varying focal length on the SLM. This was done by recording images of beads scattered in an agarose gel film deposited on a standard glass slide. Axial slices of these images are shown in Figs. 5.9 (a-b). Spot radii at $1/e^2$ [see Fig. 5.9] were then evaluated by fitting axial and transverse profiles taken from the image with a Gaussian function. Axial and transverse widths were found almost constant (to within 0.03 μm), which indicates that focusing out of the focal plane by wave front shaping with simple Fresnel phase masks introduces only negligible aberrations, within 12 μm (at least) before the focal plane of the objective.

We decided to place the mirror at $d = 6$ μm before the genuine focal plane of the objective in order to minimise the influence of the incident light that is unaffected by the SLM which then focuses behind the mirror. The phase masks were then designed to generate two spots at equidistant locations with respect to a plane that lays at $d = 6$ μm before the genuine focal plane, see Fig. 5.4, and their axial range was limited to 6 μm above and below this plane to remain within the checked aberration-free domain. Hence, in all the experiments, the samples were axially scanned over a layer of 6 μm before the mirror only.

The phase mask building required also some cautions. In order to apply the time reversal formulae or to arrange a combination of Fresnel lenses in a mask, one needs to associate the

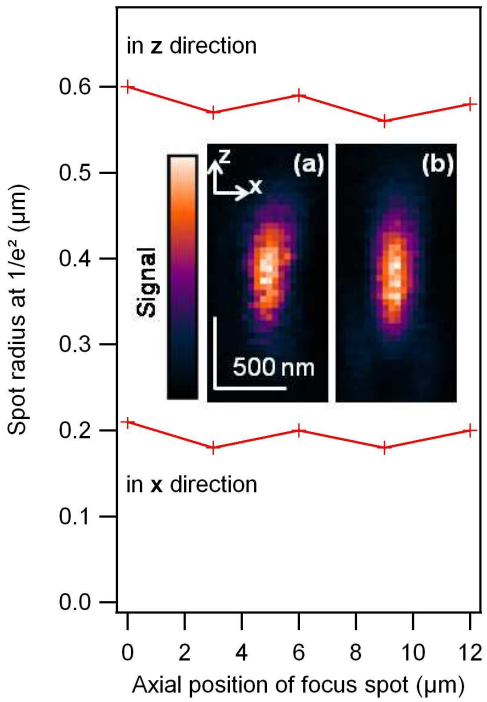

Figure 5.9: Spot radii at $1/e^2$, evaluated by fitting (with a Gaussian curve) axial and transverse profiles taken from fluorescence images of a 100 nm bead, measured while controlling the actual plane where light focuses using the SLM. Insert: Axial slices of two of these images, measured while focusing (a) in the genuine focal plane of the lens and (b) in a plane located 12 μm before it.

pixels of the SLM [defined by their coordinates (ρ, ψ)] to the propagation directions $\mathbf{u}$ after the objective lens. The main difficulty is to determine the radius R of the pupil image on the SLM as introduced in Eq. (5.4). First, an approximate value of R can be calculated from the specifications of the objective lens (numerical aperture and radius of the pupil) and the magnification ratio brought by the telescope between the SLM and the objective lens. Then, this value of R can be refined through a simple calibration method that consists in measuring the 3D image of a fluorescent bead (in absence of the mirror) while displaying on the SLM a phase mask for ISO focusing. In that case axial scanning is performed with the stage. The phase mask is designed to generate a spot at a given distance z_0 to the mirror and yields two spots separated by $2z_0$ along the optical axis in the absence of the mirror. The image reveal the positions of the two spots and the radius R is optimised until the distance between the two spots actually corresponded to two times the targeted z_0. Figures 5.10 (b-c) show vertical slices in an axial plane of the bead image, measured with phase masks designed with the time-reversal approach for z_0 = 1 and 2 μm. After calibration, the image reveals pairs of spots that are separated by $2z_0$ =2 and 4 μm along the optical axis, as expected.

Placing the mirror Once the two twin spots are created, we axially scan the mirror through focus and measure the detected signal strength. This technique permits one to localise the two spots with accuracy. The mirror is then placed at equidistance of the spots with the stage. A slight tilt of the mirror, if any, can be very accurately corrected by translating the centre of the phase mask on the SLM. Namely, its translation by one pixel in either the x or y directions (*i.e.* by 8 μm) equates in first approximation to a tilt correction by about $0.1°$. The accurate

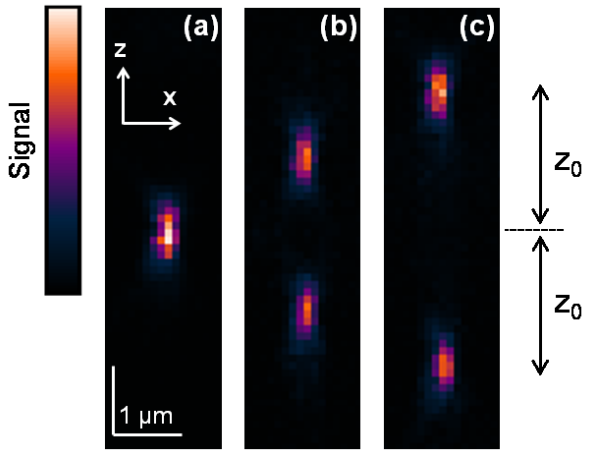

Figure 5.10: Fluorescence images (axial slices) of a 100 nm bead, measured with time-reversal phase masks that yield pairs of spots separated by (a) 0, (b) 2 and (c) 4 μm along the optical axis in the absence of the mirror.

positioning of the mirror is crucial as it governs the overlapping of the spots.

To investigate the sensitivity of the ISO PSF to possible mispositioning or drifts of the mirror, we measured the image of a bead for different positions of the mirror. As shown in Fig. 5.11, the alteration of the PSF is obvious for shifts of 0.10 μm or larger. Thus, mechanical drifts above 100 nm are expected to deteriorate significantly the PSF. Now, we found that, although we did not used any additional stabilising system, 15 to 20-minutes long measurements could be conducted without seeing any deterioration of the PSF. Hence, we believe that the stability of the mirror position within 100 nm over the experiment time is not an issue.

Correction and calibration of the spatial light modulator The technology of our SLM (liquid crystals on silicon chip) has the disadvantage that it makes displays of relatively poor surface flatness, which may degrade the incident wave front and alter the ability of the microscope to focus light. Therefore we did a complete diagnosis of these aberrations by analysing the reflection of coherent light by the SLM using a wave front sensor (SID-4 HR, Phasics) mounted on the microscope at the position of the rear focal plane of the objective lens. We found that the curvature of the SLM mainly introduced defocus and astigmatism, as well as spherical aberrations to a lower extent. We compensated for defocus and astigmatism by finely adjusting the axial and lateral positions of the lenses in the set-up. This was achieved while keeping all optical planes conjugated and it allowed us to reach wave front RMS flatness lower than 0.1 times the wavelength of light. The remaining spherical aberrations were minimised by finely adjusting the objective correction collar while monitoring the aspect of the focal spot on a reflective interface of the sample. As an alternative to compensate for the SLM curvature, we also exploited the wave front analysis to calculate a ”correction map” that can be added to any phase mask on the SLM. However, the first option (*i.e.* handling the ”physical” lenses of the set-up) has the advantage over the second one that the confocal microscope can still be operated in conventional mode (*i.e.* without wave front shaping) simply by switching off the SLM.

We configured the SLM to have a linear relationship between the signal sent to its driving unit and the phase shift actually experienced by the reflected light. For this purpose, we measured the phase characteristic of the SLM in an interferometric set-up. Then we inverted it to obtain a new data look-up table for the driving unit, in order to have a linear phase response

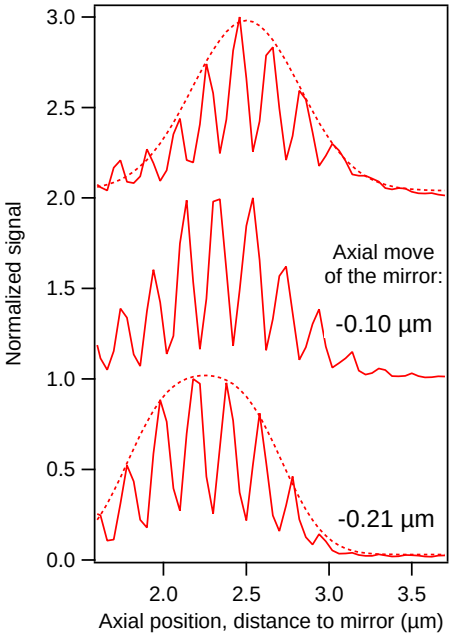

Figure 5.11: Three intensity profiles, taken in the axial direction from fluorescence images of a single 100 nm bead, for different positions of the mirror. In the middle and bottom profiles, the mirror position differs by 0.10 μm and 0.21 μm from that of the top profile, respectively. Top and bottom profiles are fitted with envelope curves (dashed line) corresponding to (top) a Gaussian function of radius 0.65 μm at $1/e^2$ and (bottom) a sum of two identical Gaussian functions of same radius 0.65 μm but of different centres.

within a well-defined $0 - 2\pi$ phase range at the wavelength of our excitation source (491 nm). We also modified the addressing scheme of the SLM. This addressing is digital, which means that the phase levels are created by pulse width modulation. Due to low addressing rate and limited viscosity of the LC molecules, the actual phase levels exhibit a certain flicker that is reminiscent from the addressing sequences. Nevertheless, the flicker can be reduced by shortening the pulse sequences and addressing them more often within one frame. Therefore we switched from the default configuration, designed for 1216 different phase levels, to a custom one with 192 phase levels. This naturally reduces the number of distinguishable phase levels that can be created, which might not suit all applications.

5.2.4 Conclusion

We have presented in this section the simulations and the experimental implementation of a novel epifluorescence confocal microscopy technique, called ISO microscopy (for Isotropic Single Objective), in which the sample is laid on a mirror and scanned by a quasi-isotropic spot that is formed through the interference of the direct and mirror-reflected field of a specially shaped illumination beam. We have shown theoretically and experimentally that the point spread function of this system is similar to that of a 4Pi-A microscope. It displays a quasi-isotropic spot of diameter about $\lambda/2$ surrounded by high side lobes. Reducing the side-lobes is the key point for further improvements of the technique. It should be obtained by using a microscope objective with an acceptance solid-angle about $65°$ [116]. The development of an 4Pi-C equivalent ISO scheme could also be a solution. We have also investigated in the following

section the interest of radial polarisation and two photons illumination.

5.3 Further works and experiments

Reducing the side-lobes is the key point for further improvements of the technique. To this aim, we have investigated the interest of radial polarisation and two photons illumination.

5.3.1 Radial polarisation

In a standard confocal microscope, the spot size can be ameliorated by illuminating the back focal plane of an objective by a radially polarised beam [59]. Now, the radially polarised beam at the back focal plane corresponds to the field radiated by a dipole oriented along the optical axis. It is thus natural to think that using this polarisation could further improve ISO microscopy, particularly in reducing the side lobes. We have thus calculated the field radiated by a dipole oriented perpendicularly to the mirror, see section 5.2.2.1. One obtains,

$$\mathbf{e}_i^{\text{ideal}}(\mathbf{u}) \propto \cos(z_0 k_0 \cos\theta)[\mathbf{p} - (\mathbf{p}\cdot\mathbf{u})\mathbf{p}], \tag{5.8}$$

We have simulated the field intensity obtained before the mirror when focusing a radially polarized beam with its wave-front shaped accordingly to the phase of Eq. (5.8). All the numerical parameters are the same as that in Sec. 5.2.2.2. The results are plotted in Fig. 5.12. We observe that the PSF obtained with the radial polarisation has smaller vertical side lobes but higher transverse side lobes than the PSF obtained with linear polarisation. It is thus unclear which is the best for imaging.

5.3.2 Two-photon microscopy

We also applied ISO microscopy concepts to two-photon fluorescence microscopy [8]. Some fluorescent markers can absorb photons presenting a wavelength twice larger than their absorption wavelength [29, Chap. 2]. The absorbed energy is then proportional to the square of the intensity at the fluorophore position $I_{\text{out}} = \sigma_{2\text{ph}} I_{\text{ext}}^2$. While largely less efficient than the usual fluorescence, this process has many applications in microscopy [29, Chap. 2]. Indeed, as the total intensity emitted by a fluorescent marker is proportional to the square of the incident intensity one can expect focusing deeper in diffusive tissue and obtaining a better axial resolution. Generally, in scanning two-photon microscopy, light is focussed into the sample but the detection is performed on a large detector, without a confocal set-up. We checked the performance of the ISO-scheme in this specific configuration. Figure 5.13 shows images of fluorescent beads illuminated with a pulsed laser source (Nd-YVO4, Amplitude) emitting 6 ps pulses at 1064 nm with a repetition rate of 34.5 MHz. A SLM compatible with infra-red light (X8267-15, Hamamatsu) was used to shape the beam wave-front. Light emitted by the sample was collected in epi-configuration and detected without spatial filtering by an avalanche photo-diode. We observed a significant reduction of the side-lobes as compared to one photon fluorescence set-up, even though the latter was coupled to a confocal detection scheme. Further improvement of the ISO-two-photons fluorescence microscope would be to use also a confocal scheme. As the illumination and observation wavelengths are very different, a second SLM would be necessary to

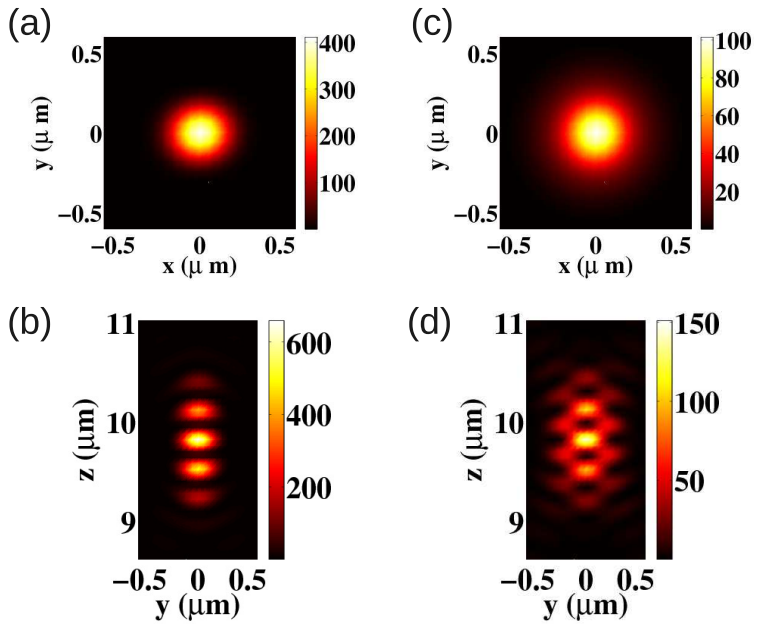

Figure 5.12: Comparison of ISO PSF for linear and radial polarisation. (a) and (b) $(z = 0)$ and $(x = 0)$ cut of simulated ISO PSF with a field in the back focal plane polarised along direction **x** (see Fig. 5.2). (c) and (d) $(z = 0)$ and $(x = 0)$ cut of simulated ISO PSF with a field in the back focal plane polarised radially.

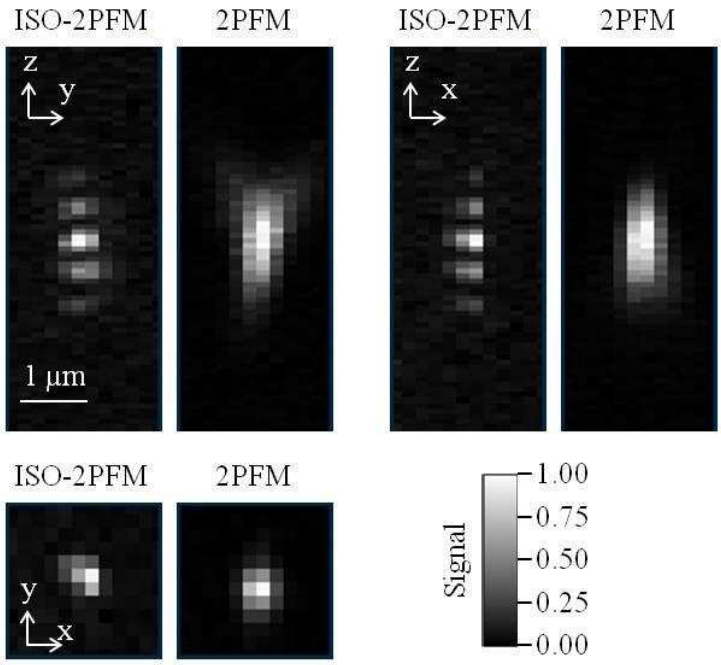

Figure 5.13: Axial (y, z) and (x, z), and transverse (x, y) cuts taken from three-dimensional fluorescence images of 200 nm beads, experimentally measured by two-photon fluorescence ISO microscopy and standard two-photon fluorescence microscopy. Both techniques are based on non-confocal detection. Fluorescence signal is displayed with a linear grey-level scale. (Courtesy E. Le Moal)

process the light emitted by the markers. Indeed, the masks defined by Eq. (5.3) are inherently wavelength dependent.

5.4 Conclusion

We have presented in this section the simulations and the experimental implementation of a novel epi-fluorescence confocal microscopy technique, called ISO microscopy (for Isotropic Single Objective) in which the sample is laid on a mirror and scanned by a quasi-isotropic spot that is formed through the interference of the direct and mirror-reflected field of a specially shaped illumination beam. We have shown theoretically and experimentally that the point spread function of this system is similar to that of a 4Pi-A microscope. It displays a quasi-isotropic spot of diameter about $\lambda/2$ surrounded by high side lobes. Reducing the side-lobes is the key point for further improvements of the technique. We have investigated the interest of radial polarization and two photons illumination for this purpose Additional improvements could be obtained by using a microscope objective with an acceptance solid-angle about $65°$ [116] and by developing a 4Pi-C equivalent ISO scheme.

This chapter concludes my work devoted to the amelioration of the axial resolution via the use of a mirror. In the following chapters, I consider the amelioration of the lateral resolution via structured illumination and the development of reconstruction algorithms.

Part III

Transverse resolution and Structured Illumination

Chapter 6

Structured illumination in fluorescence microscopy[1]

6.1 Introduction

In classical wide-field fluorescence microscopy, the sample fluorescence is excited by a uniform light intensity and the emitted fluorescence is detected at the image plane of a microscope objective. In the linear regime, the recorded intensity M can be modelled as the convolution of the fluorescence density of the sample ρ with the microscope detection point-spread-function h. The image resolution is limited by the spectral band pass of h whose cut-off is fixed by $\nu_{\mathsf{max}} = 2\mathrm{NA}/\lambda_{\mathrm{em}}$ where λ_{em} is the emitted wavelength and NA is the numerical aperture of the microscope objective. To improve the frequency content of the image, a widely spread solution consists in illuminating the sample with a non-uniform light pattern. In this case, the recorded intensity reads, as seen in Chap. 2,

$$M = (I\rho) * h, \tag{6.1}$$

where $*$ stands for the convolution product and I is the spatially varying illumination intensity.

Now, if the illumination largest spatial frequency allowed by the excitation band-pass is ν_i, the convolution theorem shows that M depends on the spatial frequencies of ρ up to $\nu_{\mathsf{max}} + \nu_i$. Thus, the recorded intensity map contains sample information that is beyond the detection band-pass. Many imaging approaches exhibiting a resolution better than that of classical wide-field microscopy, like Structured Illumination fluorescence Microscopy (SIM) with periodic excitation patterns [12, 13, 11], near-field hot spots [48, 117], translating speckles [118, 119] and even confocal or related microscopies with focused excitation spots [56, 57], rest on this principle.

However, although these approaches exhibit resolutions up to two-fold better than that of the wide-field microscope [120, 121], they are still seldom used in the microscopy community. The main reason is that they all rely on reconstruction algorithms that require a precise knowledge of the illumination patterns, small errors on the latter yielding artefacts in the final high resolution

[1] Most of the text of this section was originally published in E. Mudry, K. Belkebir, J. Girard, J. Savatier, E. Le Moal, C. Nicoletti, M. Allain and A. Sentenac, Nature Photonics, **6** 312–315 (May 2012), and its supplementary material [14]. Theory and simulations were made by Kamal Belkebir, Marc Allain, Anne Sentenac and myself; experiments and data pre-treatments were led by Jules Girard and Eric Le Moal; samples were prepared by Cendrine Nicoletti and Julien Savatier.

image. This important constraint can be met only if the illumination distortion induced by the sample or the objective aberrations is negligible and if the set-ups are carefully calibrated and stabilised to control the illumination. It limits the application domain to weakly scattering samples and make the experimental implementation very technical. Hence, a major step forward to extend the potential of Structured Illumination Microscopy techniques is to develop a method, hereafter named blind-SIM, that is able to retrieve the sample fluorescence density without *a priori* information on the illumination patterns.

The first section of this chapter describes the principle of blind-SIM algorithm. The second section presents simulations and experiments of the blind-SIM algorithm applied to classical periodic structured illumination and to speckle illumination data. The third and last section presents our attempts to modify the blind-SIM algorithm for treating measurements with high frequency illumination patterns produced in the near-field of a periodic nano-structure.

6.2 Blind-SIM reconstruction method

6.2.1 Principle of blind-SIM

We consider an experimental configuration in which a two-dimensional fluorescent sample is successively illuminated by L different light patterns $I_{l=1,\dots,L}$. The fluorescence density ρ is linked to the L images $M_{l=1,\dots,L}$ through

$$M_l = (I_l \rho) * h. \tag{6.2}$$

Given the L images, we seek to reconstruct both the fluorescence density and the L incident intensities, *i. e.* $L+1$ unknowns. The system is thus highly under-determined. To avoid this problem, we introduce the constraint that the sum of all the incident intensities be roughly homogeneous over the sample plane. This condition assumes that the sample is uniformly illuminated on average. It reads

$$\sum_{l=1}^{L} I_l \;\approx\; L I_0, \tag{6.3}$$

where I_0 is constant over the sample plane. We use this constraint for reducing the number of unknowns. The last intensity I_L is assumed to be equal to

$$I_L = L I_0 - \sum_{l=1}^{L-1} I_l, \tag{6.4}$$

so that the L^{th} equation of (6.2) can be expressed as

$$M_L = \left[\left(L I_0 - \sum_{l=1}^{L-1} I_l \right) \rho \right] * h, \tag{6.5}$$

where I_L is now absent.

The fluorescence density and the $L-1$ first illuminations are then jointly estimated in an iterative way so as to minimise the cost functional,

$$F(\rho, I_{l=1,\dots,L-1}) = \sum_{l=1}^{L-1} \|M_l - (I_l \rho) * h\|^2 + \left\| M_L - \left[\left(L I_0 - \sum_{l=1}^{L-1} I_l \right) \rho \right] * h \right\|^2,$$

where $\|.\|$ is an euclidean norm over the image space. As the illumination functions I_l are jointly estimated, one need no more assumption on their value than the approximate homogeneity of their sum. Note that with this approach, the residual inhomogeneity of the illumination average will be transferred to the reconstructed fluorescence density.

There are various means for finding the minimum of a functional. We have chosen an approach based on a non-linear conjugate gradient algorithm.

6.2.2 Description of the algorithm

The aim of blind-SIM algorithm is to determine the density of fluorophores ρ and the L illuminations $\{I_l\}$ from the knowledge of the measured intensities M_l. One notes Ω the sub-set of $\mathbb{R}^2$ where ρ and $\{I_l\}$ are reconstructed and Γ the sub-set of $\mathbb{R}^2$ where M_l is measured.

For a given density of fluorophores ρ and excitations I_l, one defines the residual error r_l on Eq. (6.2) as follows

$$r_l = M_l - (\rho I_l) * h. \tag{6.6}$$

The basic idea of the blind-SIM minimisation is to build up two sequences related to the density of fluorophores and illuminations $\{\rho_n\}$ and $\{I_{l,n}\}$, respectively, so as to minimise

$$\begin{aligned} F\Big(\rho, (I_l)_{l=1,\dots,L-1}\Big) &= W \sum_{l=1}^{L} ||r_l||_\Gamma^2 \\ &= W \sum_{l=1}^{L-1} ||M_l - (\rho I_l) * h||_\Gamma^2 + W \left\| M_L - \left[\rho\left(L I_0 - \sum_{l=1}^{L-1} I_l\right)\right] * h \right\|_\Gamma^2, \end{aligned} \tag{6.7}$$

where W is the normalisation factor

$$W = \frac{1}{\sum_{l=1}^{L} \|M_l\|_\Gamma^2}. \tag{6.8}$$

Subscripts Ω and Γ are included in the norm $||\cdot||$ and later in the inner product $\langle\cdot|\cdot\rangle$ to indicate the domain of integration.

The minimisation of Eq. (6.7) provides a maximum likelihood estimation under the assumption that the residual (6.6) is an uncorrelated Gaussian noise and, as such, does not account properly for the Poisson nature of the data. Its main advantage is that it does not require to tune any noise-related parameter. Thus, it can be used readily on any experiment. Of course, in cases where the noise has been thoroughly analysed, it may be worth deriving specially adapted algorithms [122, 123].

Series $\{\rho_n\}$ and $\{I_{l,n}\}$ are updated at each iteration according to the following recursive relations

$$\begin{aligned} \rho_n &= \rho_{n-1} + \alpha_n d_{n;\rho}, \\ I_{l,n} &= I_{l,n-1} + \beta_{l,n} d_{l,n;I}, \end{aligned} \tag{6.9}$$

where $d_{n;\rho}$ and $d_{l,n;I}$ are updating directions with respect to the density of fluorophores ρ and illuminations $\{I_l\}$, respectively. Scalar coefficients α_n and $\beta_{l,n}$ are weights that are chosen at each iteration step such that they minimise

$$f\big(\alpha_n, (\beta_{l,n})_{l=1,\dots,L-1}\big) = F(\rho_{n-1} + \alpha_n d_{n;\rho}, (I_{l,n-1} + \beta_{l,n} d_{l,n;I})_{l=1,\dots,L-1}).$$

This choice for α_n and $\beta_{l,n}$ ensures that $\mathcal{F}\big(\rho_n, (I_{l,n})\big)$ is reduced at every step. Calculation of the function f leads to a polynomial of variables α_n and $\beta_{l,n}$ for which the minimum is obtained thanks to a Conjugate Gradient method [16, p 413][15].

The updating directions $d_{n;\rho}$ and $d_{l,n;I}$ are based on the gradient of the cost functional $\mathcal{F}(\rho, I_l)$: g_ρ is the gradient of the cost functional $\mathcal{F}(\rho, I_l)$ with respect to ρ assuming that the intensities I_l do not change within the domain Ω; while $g_{l,I}$ is the gradient of $\mathcal{F}(\rho, I_l)$ with respect to the l-th intensity, I_l, assuming that the density of fluorophores, and the $L-1$ other intensities do not change inside the domain Ω. The derivation of these gradients is reported in the Appendix B and their expressions read as

$$g_{n,\rho} = -2W \sum_{l=1}^{L} I_{l,n-1} r_{l,n-1} * h, \tag{6.10}$$

$$g_{l,n,I} = -2W\rho\Big((r_{l,n-1} - r_{L,n-1}) * h\Big). \tag{6.11}$$

Using gradients as updating direction being generally inefficient, one prefers to use a conjugation algorithm [15]. We choose the Polak-Ribière conjugate gradient formula [124], known as one of the most efficient ones

$$\begin{aligned} d_{n;\rho} &= g_{n;\rho} + \gamma_{n;\rho} d_{n-1;\rho} \\ &\text{with} \quad \gamma_{n;\rho} = \frac{\langle g_{n;\rho} | g_{n;\rho} - g_{n-1;\rho} \rangle_\Omega}{||g_{n-1;\rho}||^2_\Omega}, \end{aligned} \tag{6.12}$$

$$\begin{aligned} d_{n,l;I} &= g_{l,n;I} + \gamma_{n,I} d_{l,n-1;I} \\ &\text{with} \quad \gamma_{n;I} = \frac{\langle g_{l,n;I} | g_{l,n;I} - g_{l,n-1;I} \rangle_\Omega}{||g_{l,n-1;I}||^2_\Omega}. \end{aligned} \tag{6.13}$$

6.2.2.1 Positivity

In many cases, the use of *a priori* information ameliorates the stability of solution with respect to noise. In our problem, the sought density of fluorophores ρ and intensities I_l are both real and positive. To incorporate this information in the reconstruction algorithm, ρ and the $L-1$ first illuminations $\{I_l\}$ are written as the square of auxiliary functions ξ and $\{i_l\}$ such that

$$\begin{aligned} I_l &= i_l^2, \\ \rho &= \xi^2. \end{aligned} \tag{6.14}$$

The cost functional to be minimised depends now on these auxiliary functions as,

$$F(\xi, (i_l)_{l=1,\dots,L-1}) = W \sum_{l=1}^{L-1} \left\| M_l - \left(\xi^2 i_l^2\right) * h \right\|^2_\Gamma + W \left\| M_L - \left[\xi^2 I_L\right] * h \right\|^2_\Gamma, \tag{6.15}$$

with $I_L = LI_0 - \sum_{l=1}^{L-1} i_l^2$. As previously, one can define the derivatives of this functional with respect to ξ and i_l and perform a minimisation through a gradient type algorithm. The final

estimated values for ρ and I_l are then the square of the final estimates of ξ and i_l. In this case, the iterative scheme remains unchanged although the updating directions d_ρ and $d_{l,I}$ reported in Eqs. (6.9) to (6.12) are rewritten with respect to ξ and i_l instead of ρ and I_l, respectively

$$\begin{aligned} d_{n;\xi} &= g_{n;\xi} + \gamma_{n;\xi} d_{n-1;\xi} \\ &\text{with} \quad \gamma_{n;\xi} = \frac{\langle g_{n;\xi} | g_{n;\xi} - g_{n-1;\xi} \rangle_\Omega}{||g_{n-1;\xi}||^2_\Omega}, \\ d_{n,l;i} &= g_{l,n;i} + \gamma_{n,i} d_{l,n-1;i} \\ &\text{with} \quad \gamma_{n;i} = \frac{\langle g_{l,n;i} | g_{l,n;i} - g_{l,n-1;i} \rangle_\Omega}{||g_{l,n-1;i}||^2_\Omega}, \end{aligned} \tag{6.16}$$

where g_ξ and g_i denote the gradients of the cost functional $\mathcal{F}$ with respect to ξ and i, respectively

$$\begin{aligned} g_{n,\xi} &= -4W \sum_{l=1}^{L-1} i^2_{l,n-1} \xi_{n-1} (r_{l,n-1} * h) - 2W I_{L,n-1} \xi_{n-1} (r_{L,n-1} * h) \\ g_{l,n,i} &= -4W \xi^2_{n-1} i_{l,n-1} \Big((r_{l,n-1} - r_{L,n-1}) * h \Big). \end{aligned} \tag{6.17}$$

6.2.2.2 Boundary effects

An important issue of the reconstruction procedure is the boundary effects. Indeed, the image on the camera of each emitting fluorophore is as large as the point spread function. Thus, fluorophores that are outside Γ and close to the borders may contribute to the measurements. In the same way, images of fluorophores inside Γ and close to the borders may be truncated. Neglecting these effects leads to strong artefacts that hinders the image interpretation.

To circumvent these boundary effects, we apply a commonly used method in astronomy [125, 126]. The domain Ω in which the fluorescence density and incident intensities are sought is taken larger than the image area Γ. As seen in Fig. 6.1, one adds on the four sides of Γ a large edge of width equal to that of the point spread function h. During the reconstruction procedure, the fluorescence density ρ_n and the incident intensities $I_{l,n}$ can vary freely on Ω but the measurements M_l and the residual errors $r_{l,n}$ are only evaluated on Γ.

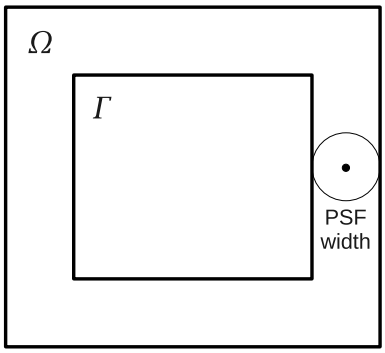

Figure 6.1: Schematic of the interlocking of Ω, the domain of reconstruction around Γ, the domain of measurement.

Generally, the reconstructed density and illuminations over these edges are false (as there is no measurement to constrain them), but they constitute the proper boundary condition for

obtaining a good evaluation of I_l and ρ in the subset of Ω that corresponds to Γ. All the reconstructed density and illuminations presented in the main part of the paper are obtained with these additional edges. This technique is very efficient to remove the boundary effects except at the very borders of the image.

6.2.2.3 Initial estimates

The initial estimate of the auxiliary function corresponding to the fluorescence density, ξ_0, is taken constant equal to 1. For the periodic SIM data, the initial estimates of the L auxiliary functions corresponding to the illumination patterns $i_{l,0}$ are homogeneous over Ω and equal to $\sqrt{I_0}$. In the speckle case, better initial estimates of the illumination patterns are obtained by keeping ξ_0 constant, (imposing $d_{n;\xi} = 0$) during the first 10 iterations.

6.2.2.4 Computational effort

The dominant operation in the blind-SIM algorithm is the convolution product, $*h$. This operation, which has to be done several times for each illumination is made using Fast Fourier Transforms (FFT). Thus, at each iteration n, the computational effort is in $\mathcal{O}(LN\log(N))$, where N is the number of pixels in Ω and L is the number of illuminations. Typical computation times are presented together with the experimental results.

6.2.3 Deconvolution of the wide-field images obtained under uniform illumination

It is well known that the positivity *a priori* information included in any inversion algorithm permits the recovery of sample high spatial frequencies that are not accessible with the imaging procedure (and not always present in the sample) [46, 47]. Hence, it is necessary to check that the resolution amelioration that we observed in the reconstructed fluorescence maps comes from the physical process of combining different structured illuminations and not only from the inversion procedure. We thus adapted our algorithm in order to estimate the fluorescence density from one single image of the same sample obtained under uniform illumination. The fluorescence density ξ^2 is estimated by minimising the functional,

$$F(\xi) \quad = \quad W\|M - (I_0\xi^2) * h\|^2_\Gamma, \tag{6.18}$$

where M is the image obtained with the uniform illumination I_0, with a conjugate gradient technique. Our approach amounts to deconvolving the image with a positivity constraint. We then compared the reconstructed fluorescence map obtained from the single image with uniform illumination to the one obtained by processing the L SIM images. As the two experiments should exhibit the same signal to noise ratio to provide a fair comparison, the single image with uniform illumination is always generated by summing the L images of the structured illumination experiment.

6.2.4 Regularisation and stopping criterion

As it stands, both blind-SIM and deconvolution algorithms are not well regularised. They converge towards meaningless images in which the noise is amplified. To circumvent this often

encountered issue, a Tikhonov [127] or a Total variation regularisation term is usually added to the cost functional. The weight of the additional regularised term is optimised by forming many reconstructions of the same sample with different parameters and eventually choosing the ”most appropriate” one (for instance, by the mean of the L-Curve [128], GCV [129], or even ’by eye’). To bypass this rather long procedure (that must be repeated as soon as the experimental conditions are modified), we have chosen an algorithm-dependent regularisation which consists in stopping the reconstruction before convergence.

Indeed, the specificity of gradient-type algorithms is that the spatial frequency content of the reconstructions increases with the iteration number. At the beginning of the iterative process, the introduced spatial frequencies stem from meaningful information contained in the data. Then, after a certain number of iterations, they correspond essentially to high-frequency noise. Early-stopping of the iterative process is known as a simple (but efficient) regularisation technique [130, Chap. 5] that basically acts as a Tikhonov regularisation. Furthermore, because the iteration number controls the regularity of the solution, the practitioner can choose ”by eye” the solution with the best trade-off between resolution and noise amplification. The stopping point depends essentially on the signal-to-noise ratio and on the theoretically accessible spatial frequencies of the imaging system. Practically, appearance of noise-induced features in the reconstruction is easily seen, being independent for each pixel.

As we are using the same gradient-type algorithm in the blind-SIM and the deconvolution methods, this algorithm-dependent regularisation procedure acts in a similar way for all our data processes. We stopped the iterations at the appearance of some pixel-size structures (for the synthetic data) or for a given level of background noise (for the experimental data). Using this criterion, inversions were stopped at different iteration steps depending on the experiments.

6.3 Application of blind-SIM to simulated and experimental data obtained with speckle and periodic illuminations

In this section, blind-SIM algorithm is applied to data sets obtained with different illumination patters, classical periodic ones or random speckle ones. Periodic sinusoidal patterns belong to the classical illumination schemes used in SIM fluorescence microscopy [12, 13, 121]. It is usually obtained via the interference of two coherent collimated beams (stemming from a diffraction grating for example) onto the sample. Several images of the sample are recorded for different positions and rotations of the pattern.

Speckle patterns have also been used in SIM fluorescence microscopy [118, 119], but classical reconstruction techniques require their measurement before imaging the sample. With blind-SIM is it now possible to use random speckle patterns. They are produced when random phases are applied to different points of a coherent beam. They can be obtained easily by moving a diffusive paper through the laser beam before the objective. In the following, we show the performances of blind-SIM on simulated and experimental data and we discuss the limits of the algorithm.

6.3.1 Synthetic data

To analyse the resolution gain brought about by blind-SIM, we considered a flat two-dimensional fluorescent sample whose fluorescence density is given by

$$\rho(r,\theta) \propto [1+\cos(40\theta)] \tag{6.19}$$

where (r,θ) are the polar coordinates of $\mathbf{r}$ in the sample plane. This radial sample is particularly convenient for studying the resolution of imaging techniques. Indeed, its radial features dwindle as one moves closer to the image centre and there is always a limit radius under which they are not recovered.

The sample is placed at the object focal plane of a microscope objective of numerical aperture $\mathrm{NA} = 1.49$. It is imaged with the detection point-spread-function

$$h(r,\theta) = \left(J_1(\mathrm{NAk_0r})/\mathrm{k_0r}\right)^2 \mathrm{k_0^2}/\pi, \tag{6.20}$$

where J_1 is the first order Bessel function of the first kind and k_0 is the wave-number in vacuum. This equation is the normalised version of Eq. (2.16) calculated in Chap. 2. In the various simulated experiments, the same sample is illuminated by different illumination patterns, classical periodic patterns, distorted periodic patterns and random speckle patterns. In all cases, the excitation wavelength is assumed to be equal to the observation wavelength.

The synthetic images are obtained following Eq. (6.2) and corrupted with Poisson noise and an additional Gaussian noise corresponding to the read noise. The image pixel size is $\lambda/20$. Except said otherwise, the photon budget, *i. e.* the *total* amount of photons detected by one pixel for all the measurements is 20,000 on average. The Gaussian noise standard deviation corresponds to 7 photons per pixel and per measurement. We first investigate the performances of the blind-SIM algorithm on data obtained with random speckle illuminations then we point out the interest of blind-SIM for classical periodic SIM (especially if the patterns are distorted), last we analyse quantitatively the resolution gain for different patterns illuminations and different levels of noise.

6.3.1.1 Blind-SIM applied to random speckle patterns

Since blind-SIM does not assume any particular shape for the illumination pattern, we are free to use any inhomogeneous patterns and in particular random highly contrasted patterns such as speckles. Speckles are interesting for structured illumination microscopy because they bare high spatial frequencies and their statistical average intensity is homogeneous [131, Chap. 3] (provided enough illuminations are taken) as required by the blind-SIM algorithm. Moreover, from a practical point of view, they are easy to form and their statistical properties are very robust.

In this first simulated experiment, 160 different fully developed speckles are used. They are calculated as a sum of plane waves with equal amplitudes and random phases uniformly distributed in $[0, 2\pi]$ whose wave-vector transverse projections are taken on a disk of radius $\mathrm{NA_{eff}}k_0$. Fig. 6.2 illustrates the image formation process and the reconstruction. We observe that the blind-SIM estimations of the fluorescence density and of the first speckle patterns are in good agreement with the actual values.

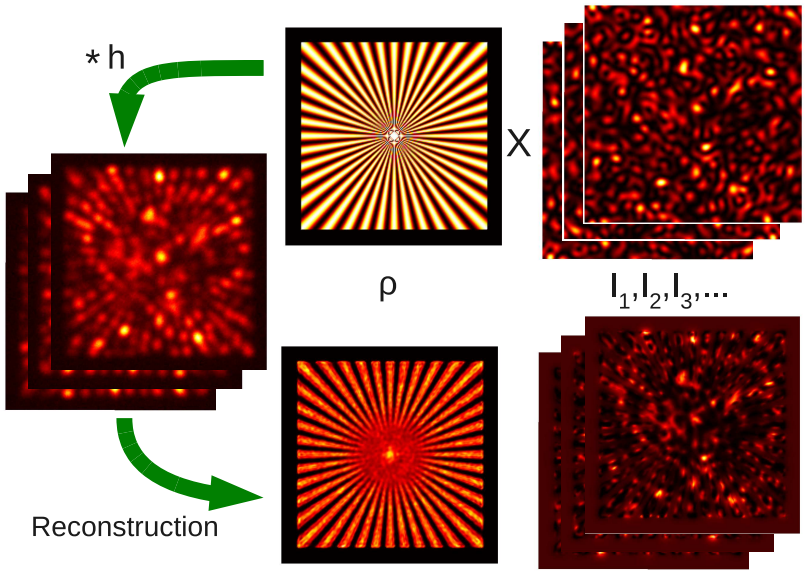

Figure 6.2: Illustration of the different steps of a simulated speckle blind-SIM experiment. 160 different speckle patterns with $\mathrm{NA}_{\mathrm{eff}} = \mathrm{NA}$ (upper right panel) are multiplied by the sample fluorophore density pattern (upper centre) and convolved by the microscope detection point spread function. The data are corrupted by Poisson and electronic noise to yield 160 low resolution images (left panel). The reconstruction algorithm estimates simultaneously the image of the fluorescence density (lower centre panel) and the 160 speckle patterns (lower right panel). The side of each square image is 10λ.

To verify that the frequency mixing between the illumination and the object is at the core of the blind-SIM resolution improvement, we considered a numerical experiment in which the same sample is illuminated by speckles with different spectra. In Fig. 6.3 (d,e,f) the reconstructed fluorescence densities obtained from $L = 160$ speckle images are displayed for $\mathrm{NA}_{\mathrm{eff}} = 0.5\mathrm{NA}$, $\mathrm{NA}_{\mathrm{eff}} = \mathrm{NA}$ and $\mathrm{NA}_{\mathrm{eff}} = 1.5\mathrm{NA}$, respectively and compared to the true fluorescence density of the sample, the wide-field image of the sample and the deconvolution of the wide-field image, Fig. 6.3 (a,b,c), respectively. As expected, the resolution of the blind-SIM images is always better than that of the deconvolved image and clearly improves with increasing $\mathrm{NA}_{\mathrm{eff}}$.

We now point out the interest of blind-SIM even for classical periodic SIM experiments.

6.3.1.2 Blind-SIM applied to distorted periodic illumination patterns

One drawback of the usual SIM reconstruction methods, such as the one described in Sec. 1.5.2, is its sensitivity to pattern distortion. Indeed, most of these algorithms assume that the pattern is a perfectly sinusoidal. Small variations on the contrast or on the position of the grid along the image yields strong artefacts [132, 133]. Now, unfortunately, patterns distortions are frequently present in experimental implementations due to the objective aberrations or to refraction inside the sample. In this case, it is interesting to compare the blind-SIM reconstruction results to that obtained with a classical inversion scheme.

I have thus simulated a SIM experiment in which the periodic illuminations are strongly distorted. The sample is illuminated by a periodic light grid with period $d \approx \lambda/(1.4\mathrm{NA})$ which

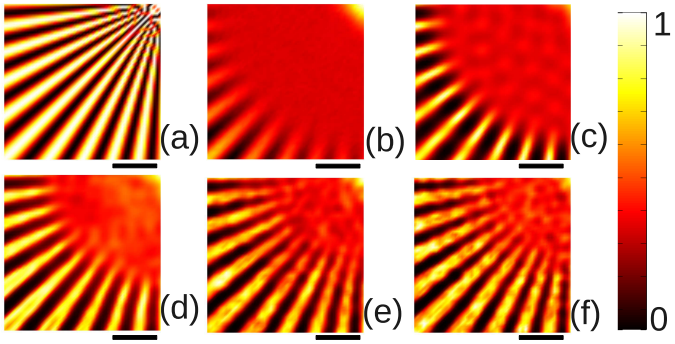

Figure 6.3: Numerical study of the resolution of the reconstructed sample using speckle blind-SIM versus the excitation pattern spectrum. (a) Fluorescence density of the object. (b) Image of the object obtained with a uniform illumination and an oil objective microscope $\mathrm{NA} = 1.49$. (c) Deconvolution of the wide-field image shown in (b). (d) Fluorescence density reconstructed by blind-SIM from $L = 160$ images obtained with speckle illuminations. The random speckles are generated with an effective numerical aperture that is half that of the detection $\mathrm{NA}_{\text{eff}} = 0.5\mathrm{NA}$. (e) Same as (d) but $\mathrm{NA}_{\text{eff}} = \mathrm{NA}$. (f) Same as (d) but $\mathrm{NA}_{\text{eff}} = 1.5\mathrm{NA}$. The black bar corresponds to the incident and emitted wavelength λ. The colour scale represents the normalised fluorophore density. For a fair comparison, the experiments have the same photon budget and the deconvolution procedure includes the same regularisation terms as blind-SIM.

is translated by $n(d/4)$, $n = 0, 1, 2, 3$ and rotated by $m(2\pi/3)$, $m = 0, 1, 2$. For each simulated image, the periodic illumination pattern is distorted with a different aberration.

Blind-SIM is compared to a reconstruction algorithm assuming that the illumination is sinusoidal and perfectly known. In this last case, the inversion method is similar to blind-SIM except that the $\{I_l\}$ are fixed to perfectly periodic patterns and the iterative search is performed only on the fluorescence density [134]. The perfectly periodic patterns are chosen such that they match the distorted patterns in the centre of the sample.

The results of this simulated experiment are displayed in Figure 6.4. We observe that blind-SIM is able to retrieve accurately the distorted periodic illuminations and reconstruct the sample without any visible artefacts. On the contrary the classical reconstruction method yields a sample image that contains strong artefacts (the converging rays of the radial sample are misplaced), especially far from the sample centre, where the distortion is the most important. This study demonstrates the robustness of blind-SIM against pattern distortions. Indeed, the illumination patterns being estimated correctly by the algorithm, one can obtain high resolution images without artefacts.

6.3.1.3 Performance of blind-SIM versus noise and comparison with other techniques

In this paragraph, we analyse the resolution gain achieved by blind-SIM versus the photon budget of the experiment. We study three different excitation patterns, the standard homogeneous illumination, the speckle illumination and the periodic (non distorted) illumination. For the speckle configuration, 80 images are simulated with different speckle patterns generated with $\mathrm{NA}_{\text{eff}} = \mathrm{NA}$. For the periodic configuration, 9 images are simulated using a periodic light grid with period $d \approx \lambda/(1.4\mathrm{NA})$ which is translated by $n(d/3)$, $n = 0, 1, 2$ and rotated by $m(2\pi/3)$, $m = 0, 1, 2$. The one-shot homogeneous illumination, the 9-shot periodic illuminations and the

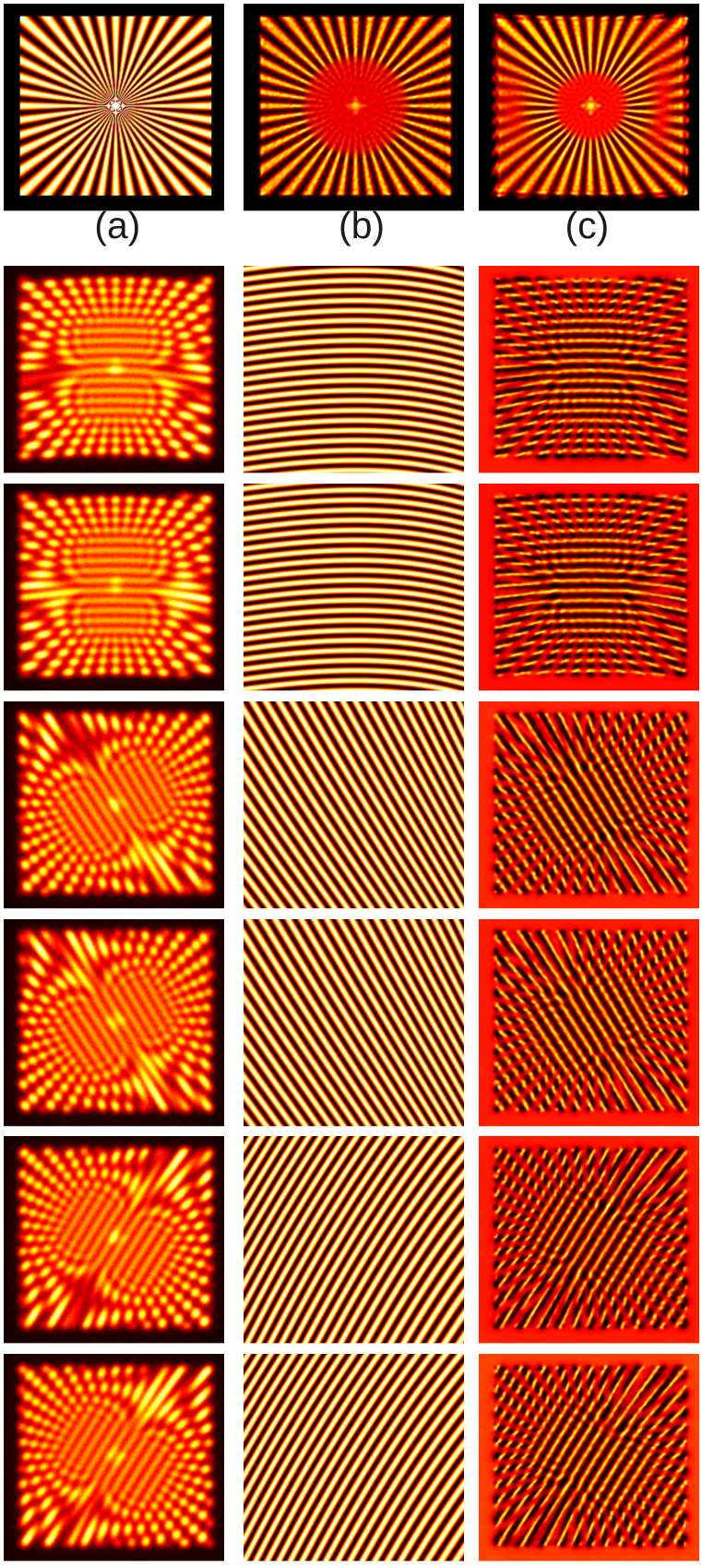

Figure 6.4: Reconstructed fluorescence density of the 'star-like' sample and reconstructed illumination patterns given by blind-SIM for a distorted periodic SIM experiment. (a) is the actual fluorophore density of the 'star-like' sample. (b) is the fluorophore density reconstructed using blind-SIM. (c) is the fluorophore density reconstructed using an inversion method assuming the illumination as periodic and known [134].
The first column of 6 images below the (a,b,c) figures corresponds to 6 of the 12 simulated measurements; the second column shows the actual illumination patterns that were used to create the simulated measurements; the third column shows the reconstructed illumination patterns using blind-SIM.

80-shot speckle illuminations are simulated with the same total amount of detected photons per pixel (on average).

The reconstructed images obtained under periodic and speckle illumination using blind-SIM (Periodic blind-SIM and Speckle blind-SIM) are compared to the wide-field image (Wide-Field), its deconvolution (Deconvolution) obtained with the non-linear algorithm described in Sec. 6.2.3, and the reconstruction of the periodic SIM data obtained by assuming that the excitation patterns are perfectly known (Periodic SIM). In this last case, the inversion process is similar to blind-SIM except that the $\{I_l\}$ are fixed to their actual values and the iterative search is performed only on the fluorescence density [134]. The fact that all the reconstruction procedures include the same regularisation technique permits a fair comparison between the different imaging techniques and allows one to focus on the role of the (known or unknown) excitation patterns.

We consider a realistic experiment in which the total photon budget detected on average on one Nyquist pixel (*i. e.* with size $\lambda/(4\mathrm{NA}) \approx \lambda/6$) is about $10,000$ and the read noise standard deviation corresponds to 6 photons per Nyquist pixel and per measurement. In this case, the photon noise is dominant and reaches 1% which is typical of most structured illumination experiments. We plot in Fig. 6.5 the Wide-field, Deconvolution, Speckle blind-SIM, Periodic blind SIM and periodic-SIM images together with one example of the speckle data. We observe that Periodic SIM, Speckle blind-SIM and Periodic blind-SIM allow a better reconstruction of the radial periodic pattern than the Deconvolution or Wide-field. The reconstructed pattern is more contrasted in the periodic SIM image than in the periodic and speckle blind-SIM images but the limit radius under which the modulation disappears is roughly the same for the three techniques.

To support this assertion quantitatively, we analysed specifically the values of the reconstructed fluorescence density along centred circles of various radius. The sample fluorescence density taken on a circle of radius R reads $f_R(s) \propto 1+\cos\big(2\pi s/L(R)\big)$ where s is the arc-length along the circle and $L(R) = 2\pi R/40$ is the period of the pattern, which decreases as R tends to zero. To estimate the ability of the reconstruction procedures to retrieve this oscillating pattern as a function of R, we calculated the modulation contrast $C(R) = 2\tilde{f}_R\big(1/L(R)\big)/\tilde{f}_R(0)$ where $\tilde{f}_R$ is the one-dimensional Fourier transform of $f_R(s)$. For the actual sinusoidal fluorescence density of the sample, $C(R) = [\max(f_R) - \min(f_R)]/[\max(f_R) + \min(f_R)] = 1$ whatever R.

We display in Fig. 6.6 the modulation contrasts obtained for the Wide-field, Deconvolution, Periodic blind-SIM, Speckle blind-SIM and periodic SIM images as a function of the period, $L(R)$. This plot shows that the deconvolution procedure permits to increase significantly the modulation contrast for periods bigger than the Rayleigh criterion $L_0 = 0.6\lambda/\mathrm{NA} \approx 0.4\lambda$ (namely it corrects the triangular low-pass detection filter), but marginally enhances the modulation contrast for periods smaller than L_0. On the other hand, speckle blind-SIM, periodic blind-SIM and periodic SIM recover the sample periodic pattern down to periods about $L_0/2$. To mimic the Rayleigh criterion, we defined the resolution of the reconstructed image as the period for which the contrast is about 0.10 [38], *i. e.* the modulation is still 'eye-visible'. With this definition, the resolution of the blind-SIM techniques is similar to that of periodic-SIM. Yet, the modulation contrast being better enhanced by periodic SIM than by blind-SIM, the periodic-SIM image remain visually more satisfactory than the blind-SIM images, see Fig. 6.5.

We perform the same analysis on many other simulated data with total photon budget detected on one Nyquist pixel ranging from $40,000$ to 600 (on average), see Fig. 6.7. Except for the 600 photon-budget experiment for which the read noise has a one photon standard devi-

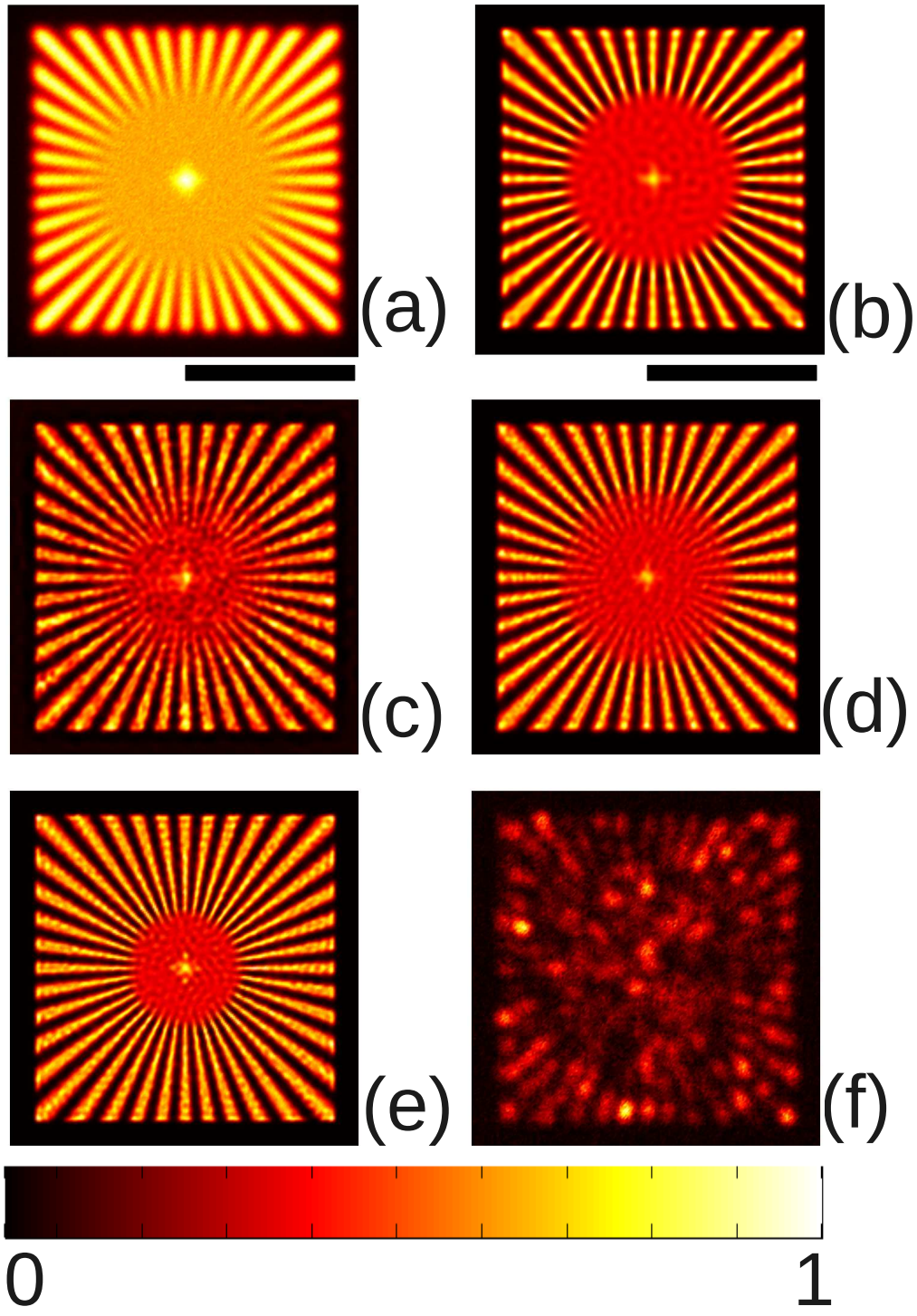

Figure 6.5: Reconstructed fluorescence density of the 'star-like' sample using various imaging techniques. Simulated data are obtained with a total photon budget detected on average on one Nyquist pixel of $10,000$ and 6 electrons read-noise per Nyquist pixel per measurement. (a) Wide-Field. (b) Deconvolution of (a). (c) Speckle blind-SIM. (d) Periodic blind-SIM. (e) Periodic-SIM (with known illumination patterns). (f) One example of the 80 measurements used for the Speckle blind-SIM reconstruction in (c). The black bars are 5λ-long. The colour scale represents the normalised density of fluorophores (normalised intensity for (f)).

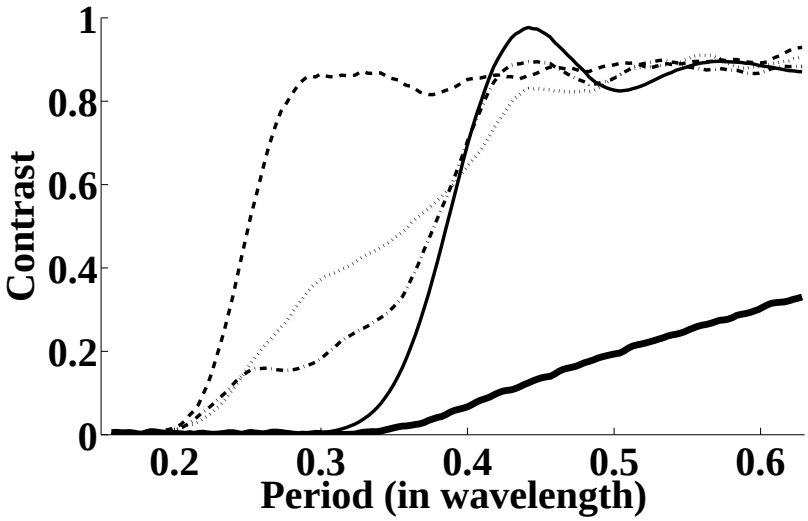

Figure 6.6: Contrast of the recovered fluorescence periodic density as a function of the period extracted from the images displayed in Fig. 6.5. Thick solid line: Wide-Field. Thin solid line: Deconvolution. Dotted line: Speckle blind-SIM. Dash-dotted line: Periodic blind-SIM. Dashed line: Periodic SIM (with known illumination patterns).

ation (which corresponded roughly to that of an Electron Multiplying Charge Coupled Device camera), we introduce a standard read noise of 6 photons per pixel and per measurement for modelling the camera performance. These values encompass a wide variety of experiments from the imaging of isolated fluorophores to that of continuous samples with high fluorescence density such as those presented in Sec. 6.3.2. In all these examples, the modulation contrast curves with respect to $L(R)$ obtained by the blind-SIM techniques resemble that depicted in Fig. 6.6. They are below the periodic-SIM curve, but remain above 0.1 for periods close to $L_0/2$, even with very noisy data, see Table 6.1. Actually, increasing the signal-to-noise ratio permits essentially to ameliorate the modulation contrast for the intermediary periods, between L_0 and $L_0/2$ as seen in Fig. 6.7.

This analysis demonstrates the ability of blind-SIM to recover sample high spatial frequencies beyond the detection cut-off even with noisy data and points out the interest of speckle illumination. Note that the granular aspect of the speckle blind-SIM image stems from the residual inhomogeneity of the average illumination, which is performed over 80 different speckles only, and could be reduced by taking more images. Moreover, we believe that there is still room for algorithmic improvements for enhancing the modulation contrast of the intermediary periods.

6.3.2 Experimental data

Blind-SIM was then validated on experimental images stemming from a wide-field microscope tuned for structured illumination experiments. The data were obtained using a home-built Structured Illumination Microscope with a high numerical aperture objective (NA=1.45, 100X, CFI Plan Apochromat, Nikon) in the Epi-illumination mode. The illumination was performed with a laser beam (He-Ne, 633 nm). The fluorescence light was separated from the laser reflection with a dichroic mirror and a filter, and finally imaged on an EMCCD camera (Andor iXon 897) with pixel size about 100 nm (after magnification) corresponding roughly to the Nyquist criterion,

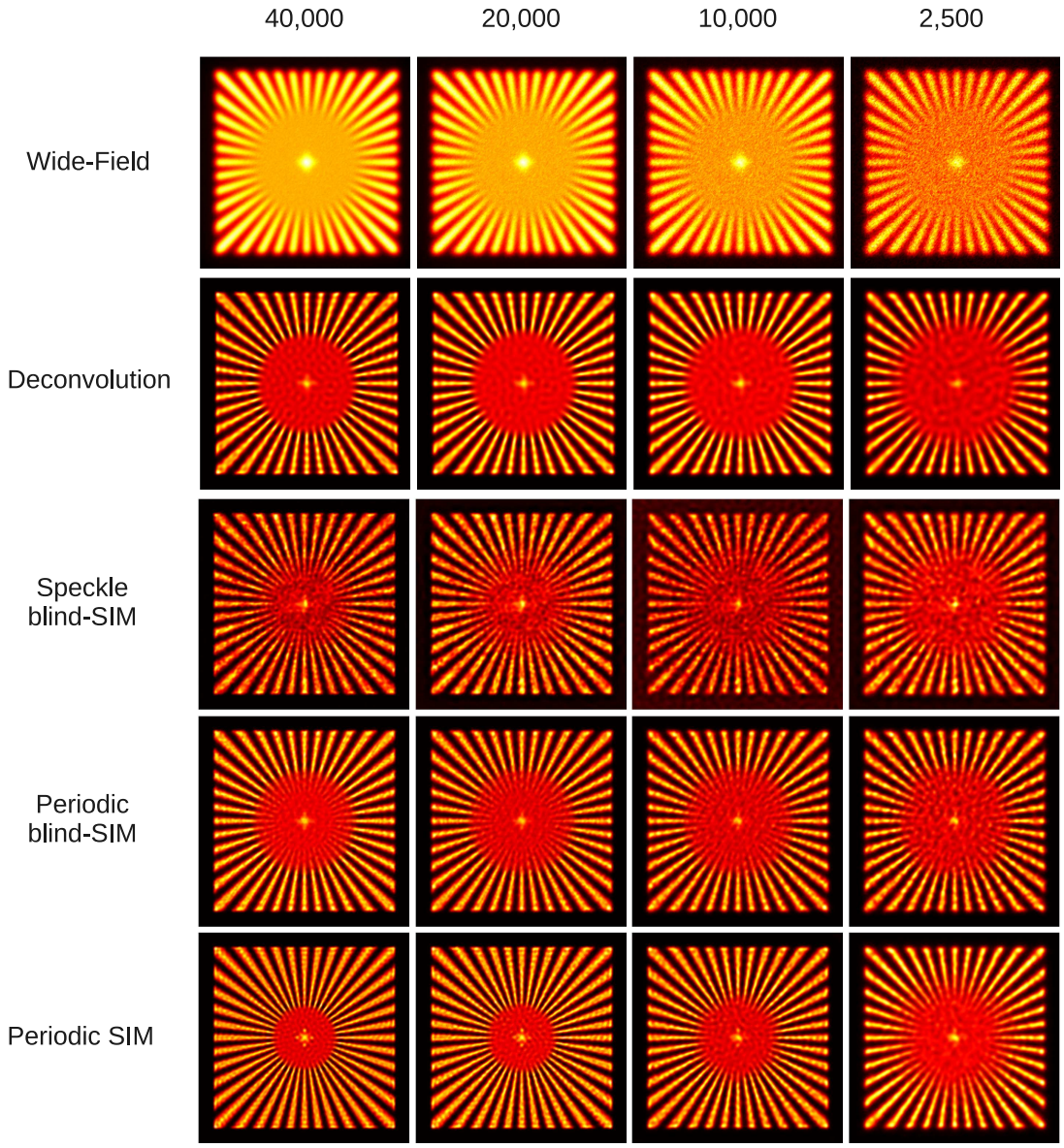

Figure 6.7: Reconstructed fluorescence density of the 'star-like' sample using different imaging techniques for various levels of photon noise. The first row corresponds to the reconstructions obtained with Wide-Field, the second row corresponds to the Wide-Field image deconvolution, the third row to Speckle blind-SIM using 80 speckle images, the fourth row to Periodic Blind-SIM using 9 periodic SIM images and the fifth row to periodic SIM (with known illumination patterns) using the same 9 periodic SIM images. The first, second and third columns correspond to data corrupted with 6 electrons read-noise per Nyquist pixel and per measurement and simulated with a total average number of photons per Nyquist pixel of 40,000, 10,000 and 2,500 respectively. The fourth column corresponds to data corrupted with 1 electron read-noise per Nyquist pixel and per measurement and simulated with a total average number of 600 photons per Nyquist pixel. See text for details. Whatever the level of noise, blind-SIM is always better than Deconvolution and its resolution is close to that of periodic SIM though with less contrasted periodic patterns. The granular aspect of Speckle blind-SIM is due to the residual inhomogeneity of the average illumination which is performed over 80 speckles only. The side of each square image is 10λ. The colour scale is the same as Fig. 6.5.

	40,000	10,000	2,500	600
Wide-Field	0.43	0.43	0.43	0.43
Deconvolution	0.33	0.35	0.36	0.36
Speckle blind-SIM	0.22	0.23	0.26	0.32
Periodic blind-SIM	0.23	0.23	0.25	0.29
Periodic SIM	0.21	0.22	0.24	0.29

Table 6.1: Resolution in λ unit of the reconstructed fluorescence density of the 'star-like' sample obtained with different imaging techniques versus the total amount of photons detected on average on one Nyquist pixel. The Rayleigh criterion is $L_0 = 0.6\lambda/\mathrm{NA} \approx 0.4\lambda$. With our definition, blind-SIM resolution is comparable to classical periodic-SIM except at very low signal to noise ratio. Yet, periodic-SIM yields images which are visually more satisfying than blind-SIM, as seen in Fig. 6.7, because the contrast of the periodic patterns are better enhanced.

$\lambda/(4\mathrm{NA})$. Before using the reconstruction procedure, the image pixel was reduced by a factor of two by interpolating the measurements using zero padding in the Fourier space. Provided that the Nyquist criterion is satisfied initially, this procedure does not create artefacts [135, pp. 59–79].

The unavoidable small experimental drift was corrected by registration of the images with sub-pixel accuracy [136]. For each experiment, we estimated accurately the detection point-spread-function by averaging the fluorescence density of registrated isolated fluorophores. Note that we did not correct for the photo-bleaching effect or the intensity fluctuations since they can be included in the intensity reconstruction.

6.3.2.1 Classical periodic SIM

Blind-SIM was first validated on experimental images of a beads sample illuminated by periodic excitation patterns. The sample consisted of 90 nm diameter fluorescent beads (Spherotech, SPHERO, Sky Blue) spread on a cover-slip and then immersed in glycerol. The sinusoidal light patterns (with period about 230 nm) were formed on the sample by imaging a glass transmission grating (holographic, 80 lines/mm) placed in a secondary image plane of the microscope. The orientation and position of the light pattern were modified by translating and rotating the transmission grating. Sole the ± 1 grating diffracted orders were used, the others being blocked with a diaphragm and a central stop. The grating was translated eight times for three different orientations (0, 60 and 120°), yielding a total of 24 recorded images. The translation step, corresponding to a quarter of the pattern period, was calibrated through the analysis of the laser reflection on the cover-slip surface. For ensuring the same photon budget, the wide-field image was obtained by summing the 24 structured illumination measurements.

An example of the recorded images and the blind-SIM reconstructed fluorescence density are displayed in Fig. (6.8). We observe that, although the excitation peaks are not visible on the Fourier transform of the raw images, Fig. 6.8 (a,b), blind-SIM retrieves accurately the light patterns, Fig. 6.8 (c,d). In this experiment where the measured width of the detection point-spread-function is about 360 nm, the resolution of the blind-SIM image, Fig. 6.8 (g) is as good as that given by an up-to-date SIM algorithm assuming the periodicity of the light pattern and reaches 160 nm. It is much better than that of the deconvolved wide-field image, Fig. 6.8 (f) which is about 250 nm.

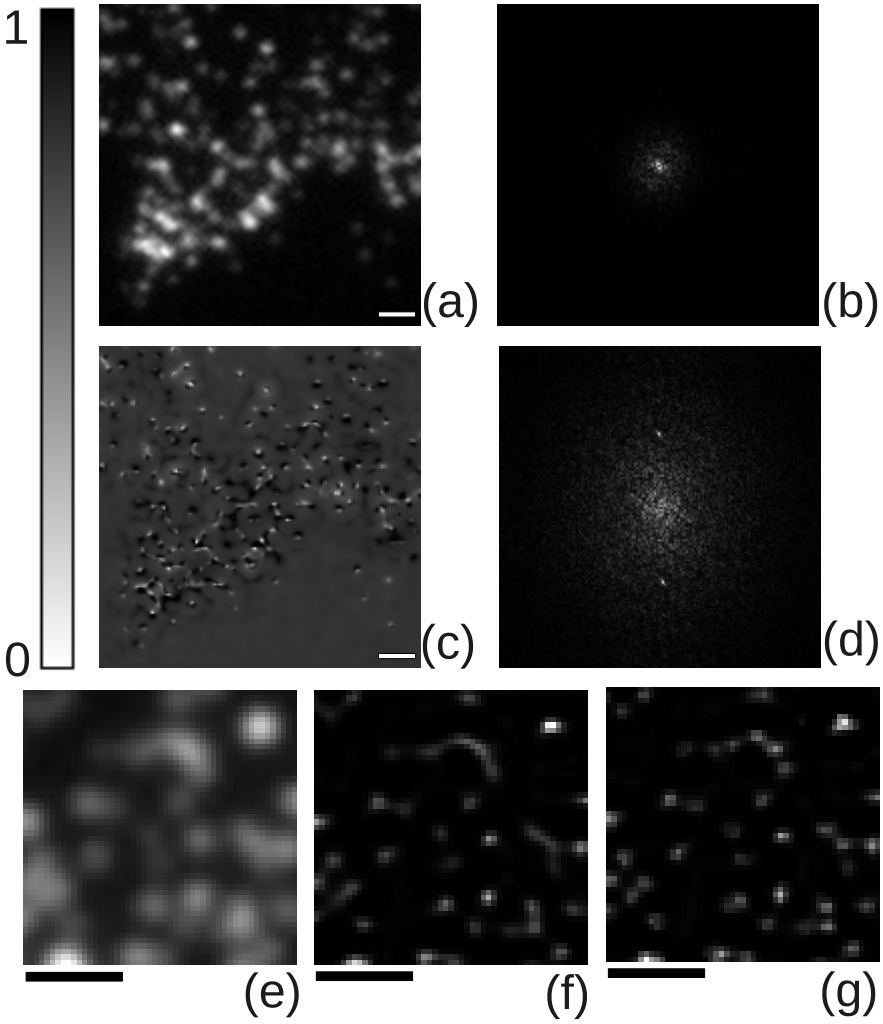

Figure 6.8: Experimental periodical SIM data processed by blind-SIM. Fluorescent beads with diameter 90 nm are illuminated by 24 different standing waves with period $d \approx 230$ nm through an oil objective with $\mathrm{NA} = 1.45$ at $\lambda_{exc} = 633$ nm. (a) One of the 24 recorded images. (b) Absolute value of the Fourier Transform of (a) (after subtracting the mean). The peaks of the light grid are not visible. (c) Blind-SIM reconstructed excitation pattern of the image displayed in (a). The pattern is reconstructed only where the reconstructed fluorescence density is non-zero. (d) Absolute value of the Fourier Transform of (c) (after subtracting the mean). The peaks of the light grid are clearly visible among noisy-like features which indicate the support of the pattern reconstruction. (e) Zoom of the sample image obtained under wide-field illumination. (f) Deconvolution of (e), closely located beads are unresolved. (g) Blind-SIM reconstructed fluorescent density obtained from the 24 structured illumination measurements, closely located beads are now well resolved. The white and black bars indicate 1 μm. The grey scale represents the normalised fluorescent density. About 10000 photons per bead are detected during the measurement process.

6.3.2.2 Speckle patterns

Last, blind-SIM was applied to the experimental microscope images of a biological sample illuminated by 150 different speckles. The speckles were obtained by moving a diffuser through the laser path prior the microscope objective. The sample was an ultra thin (80 nm) slice of rabbit jejunum with glycoproteins marked with Cy5 fluorescent dye. The wide-field image of the sample, the deconvolution of the wide-field image and the blind-SIM density of fluorescence are shown in Fig. 6.9 (a,b,c) respectively.

The set-up is the same as that described in the previous section except that the transmission grating was replaced by a diffuser (a grained sheet protector). Its position did not matter, as long as the back focal plane of the objective was filled with scattered light and as the diffuser was not directly imaged on the sample. 150 different speckle illuminations were obtained by translating the diffuser between each image recording. For ensuring the same photon budget, the wide-field image was obtained by summing the 150 speckle images.

The sample consisted in an ultra-thin (80 nm) Epon-embedded sections of rabbit jejunum deposited on a cover-slip, whose glycoproteins were marked with Cy5 fluorescent dye. More precisely, the tissue was fixed by immersion in 2,5% glutaraldehyde in phosphate buffer at pH 7,4 (PBS) 1H followed by 2% osmium tetroxide in PBS 1H. The specimens were dehydrated by passage through a graded series of ethanol (70, 90, 100%) and embedded in Epon 812. Ultra-thin sections (80 nm) were obtained with a microtome, and finally labelled with Cl 3.3 monoclonal antibody (1/100) and Cy5-conjugated goat anti mouse (1/200, Bethyl laboratories corporation).

We observe a significant improvement of the resolution achieved by blind-SIM. Note that taking the standard variation of the speckle images (as in the Dynamic Speckle Illumination approach [137]), while useful for removing out of focus fluorescence, did not yield any resolution improvement.

6.3.3 Discussion

In conclusion, we have developed a method (blind-SIM) that circumvents the major issue of the control and *a priori* knowledge of the excitation patterns in microscopy using non-uniform illumination. Using blind-SIM, images with a resolution about twice better than that of wide-field microscopy can be obtained by simply illuminating samples with random light speckles. Moreover the algorithm can process measurements with poorly controlled or even distorted periodic SIM illuminations. However, this technique is still in its infancy and there is still a lot of work to do.

First the mathematical proof of convergence is an open question. Preliminary studies tend to show that the implicit regularisation (see Sec. 6.2.4) plays a large role in the reconstruction success.

For now, this method has been developed for imaging thin two-dimensional samples only. It would be interesting to extend it to three-dimensional objects. The algorithm itself can be straight-forwardly extended to the third dimension. However, it requires measurements defined by the same model

$$M_l = (I_l \rho) * h,$$

with h, the three-dimensional PSF, and I_l and ρ three-dimensional illumination and fluoro-

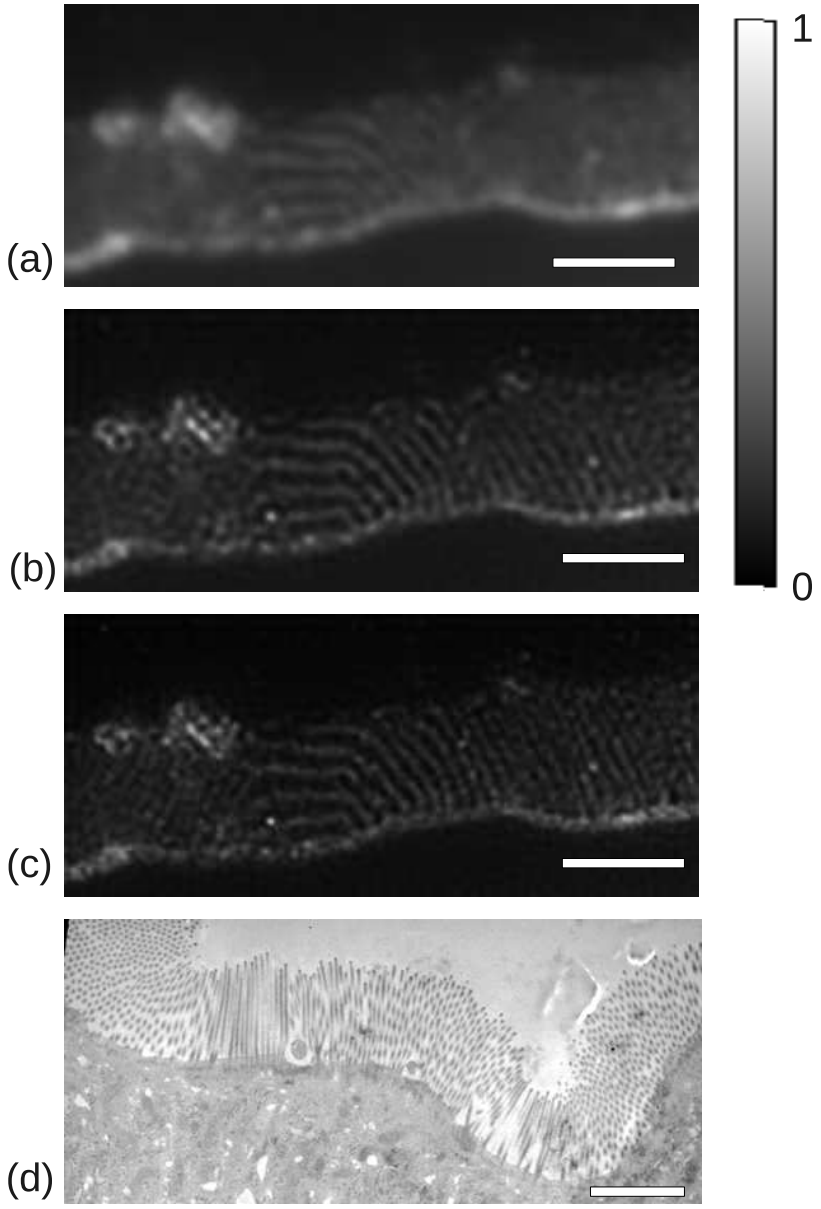

Figure 6.9: Experimental speckle data processed by blind-SIM. The sample is an ultra-thin (80 nm) Epon-embedded section of rabbit jejunum with glycoproteins marked with Cy5 fluorescent dye. It is illuminated by 150 uncontrolled different speckles through an oil objective ($\mathrm{NA} = 1.45$) at $\lambda_{exc} = 633$ nm. (a) Wide-field image of the sample. (b) Deconvolution of the wide-field image shown in (a).(c) Blind-SIM fluorescence density obtained from the 150 speckle images. (d) Image of a similar sample, using a transmission electronic microscope. The white bar indicates 3 μm. The grey scale is the normalised fluorophore density. The total number of photons per pixel, averaged over the marked micro-villi region, is about 20000. Note that the wavy lines observed in the centre of (a-c) are not an artefact. Similar lines made of dark points are visible on the TEM image, (d). They are due to the fact that the microtome cuts the micro-villi at an angle.

phore density fields. This means that one has to measure a three-dimensional image of $I_l\rho$ without modification of I_l which can be difficult experimentally. Another solution would be to use illumination patterns I_l that are vertically invariant like, for example, speckle Bessel beams [138, 139, 140], but the axial resolution would not be improved. Nonetheless, we believe that a suitable algorithm modification could lead to better solutions [141].

Finally, we have observed that sole the frequencies of I_l that are below the detection cut-off contributes to the improved resolution. If the sample is illuminated by a periodic pattern with a period smaller than the diffraction limit, blind-SIM is not able to retrieve the pattern, except in areas where the sample bares only low frequency information. As a consequence, these high frequencies illumination pattern do not ameliorate the image resolution. This hinders the use of blind-SIM for super-resolution configurations in which the sample is illuminated by sub-diffraction light patterns or in which the fluorescence mechanism is saturated [142, 143, 24, 25, 144, 117, 134]. Yet, we believe that modifications of this algorithm could solve this issue. Our attempts for breaking this limitation are presented in the next section.

6.4 Improving further the resolution using Grating assisted SIM

6.4.1 Principle

Grating-assisted SIM is based on the Total Internal Reflection Fluorescence Microscopy (TIRFM) [145]. In TIRFM, the sample is deposited on a substrate with a high index of refraction n_i. The sample is illuminated via the substrate by a collimated beam impinging at an angle high enough to obtain total internal reflection. The excitation field is thus evanescent and decays exponentially as one moves away from the substrate surface. As only a thin slice (one hundred of nanometres) of the sample is illuminated, one obtains a natural sectioning in the direction perpendicular to the substrate surface. TIRFM is popular in biology laboratories because of this sectioning property.

To combine this advantage with a high lateral resolution, SIM-TIRFM [13, 12, 146] has also been developed. In this case, two beams instead of one are sent towards the substrate interface. The interferences create a light pattern that is sinusoidal in the (x, y) plane and exponentially decaying in the axial, $\mathbf{z}$, direction (see Fig. 6.10 (a)). In this configuration, one can model the sample as a flat two-dimensional object (as only a thin slice fluoresces) and the intensity pattern as

$$I_l = 1 + \cos(\mathbf{K}.\mathbf{r}_{\|} + \phi_l),$$

where $\mathbf{K} = 2\mathbf{k}_{\mathrm{inc},\|}$ is a vector of the (x, y) plane. The SIM-TIRFM principle is similar to that of SIM as described in Sec. 1.5.2. Assuming that the observation is done via the substrate, one recorded image

$$M_l = (\rho I_l) * h$$

depends on the spatial frequencies of ρ contained in the union of the three $k_c = k_0\mathsf{NA}$-radius circles centred on $\mathbf{0}$, $\mathbf{K}$ and $-\mathbf{K}$. Using several (at least three) illuminations with different ϕ_n we can separate these three terms [13]. Repeating the same process by rotation of $\mathbf{K}$ in diverse directions of the plane, one can retrieve the frequencies of ρ in the circle of radius $k_c + \|\mathbf{K}\|$, as seen in Fig. 6.10 (b) and thus improve the lateral resolution of the image.

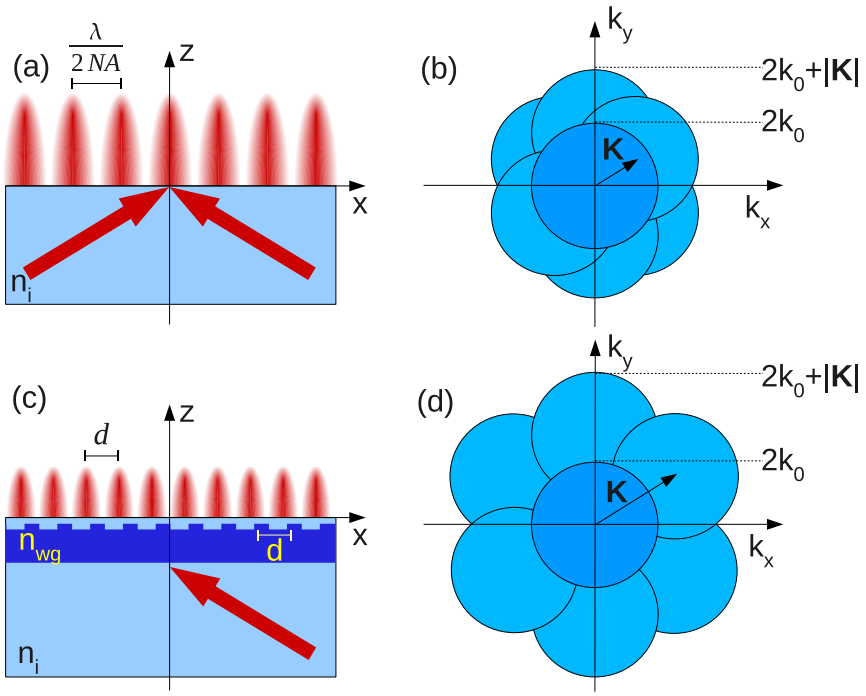

Figure 6.10: (a) Sketch of a SIM-TIRFM experiment. Two plane waves are sent via the substrate with optical index n_i towards the sample. (b) Union of the k_c radius circle in which the Fourier components of ρ are measured in SIM-TIRFM. (c) Sketch of a GA-SIM experiment. A plane wave is shaded on a resonant grating with period d, creating a sinusoidal intensity pattern with period d. n_{wg} is the optical index of the core of the wave guide. (d) Union of the k_c radius circle in which the Fourier components of ρ are measured in GA-SIM.

However in SIM-TIRFM, the maximum possible norm of $\mathbf{K}$ is obtained when the two illumination beams are parallel to the substrate interface. In this case,

$$\|\mathbf{K}\| = 2k_0 n_i \sin a = 2k_0 \mathrm{NA} = \mathrm{k_c},$$

where a is the maximum angle reachable with the lens used for projecting the beams. The cut-off of this technique is then limited to $2k_c$. To improve further the resolution, one has to find a way to create a sinusoidal pattern with a higher frequency.

One possible solution is the Grating Assisted SIM (GA-SIM) [117, 134]. This approach uses the fact that the light intensity existing at the surface of a grating is periodic with the grating frequency. If the grating is manufactured with a sub-100 nm period, the light intensity just above it will exhibit a sub-100 nm period whatever the illumination wavelength. Of course, as one moves away from the grating, one will retrieve a diffraction limited intensity pattern. The near-field intensity pattern is not diffraction limited because it is created by the interference of all the diffracted orders which contain high frequency evanescent waves. The problem is that, in general, the high frequency evanescent orders have a very low amplitude and are thus negligible in the sum. The near-field intensity pattern is then only weakly modulated.

To address this issue, it has been proposed [117] to use resonant gratings as substrate for the TIRFM experiment. A resonant grating is schematically a sub-diffraction periodically structured wave guide [147] (See Fig. 6.10 (c)). The period and illumination angle are chosen such that one order of the grating has the same wave-vector as a guided mode (at the excitation

wavelength). When the temporal and spatial frequencies of the electromagnetic field matches that of a mode of the structure, there is a resonance phenomenon. The amplitude of the corresponding grating order is then greatly enhanced. Through a correct optimisation [134][148, Chap IV], the field above the sample can then be approximated by the sum of the specularly transmitted wave and the resonant diffracted wave [117]. The resulting illumination pattern exhibits a lateral sinusoidal pattern $I_l = 1 + \cos(\mathbf{K}.\mathbf{r} + \phi_l)$, where $\|\mathbf{K}\| = 2\pi/d$, d is the grating period, and ϕ_l is a phase depending on the grating geometry and the illumination direction. Using silicon structured wave-guides that support guided modes with high spatial frequency [134], it is possible to obtain $\|\mathbf{K}\| \approx 3k_0\mathrm{NA}$. If the grating has a triangular mesh, one can define 6 possible resonant directions and thus expect the measurement of $\tilde{\rho}$ on a $(5/2)k_c$-radius circle (See Fig. 6.10 (d)).

Another possibility proposed in ref. [134] is to illuminate the grating with a standing wave pattern formed by the interference of two plane waves, as in a classical SIM experiment. In this case, the intensity pattern is the sum of four periodic patterns [148, Sec IV.2]: the grid with wave-vector $\mathbf{K}$ stemming from the interference between the transmitted and diffracted waves for each of incident plane wave; the grid produced by the two transmitted waves (with wave-vector $2\mathbf{k}_{\mathrm{inc},\|}$); the grid produced by the transmitted wave of one of the incident plane wave with the diffracted wave of the other incident plane wave (wave-vector $\mathbf{K} - 2\mathbf{k}_{\mathrm{inc},\|}$) and the grid produced by interferences between both diffracted waves (wave-vector $2\mathbf{K} - 2\mathbf{k}_{\mathrm{inc},\|}$). This configuration, hereafter called the Moiré configuration has two main advantages. First, the third grid has its wave-vector norm about half of k_c. It is thus visible is the measurement, allowing verification of the correct behaviour of the resonant grating [148, Sec IV.4.2]. Then, the wave vector of the fourth grid has for norm $\|2\mathbf{K} - 2\mathbf{k}_{\mathrm{inc},\|}\| \approx 4k_0\mathrm{NA}$, allowing measurement of $\tilde{\rho}$ on a $3k_c$-radius circle.

The grating-assisted SIM seems to be a promising technique for sub-diffraction resolution surface imaging. However, it suffers from a strong drawback. In its present state, the reconstruction algorithm [134] requires the precise knowledge of the illumination patterns. Now, experimentally, these patterns are always slightly modified by small errors in calibration, aberrations of the objectives or fabrication misprints. Moreover the precise position of the grating cannot be seen since its period is under the microscope resolution. The smallest error on this grating position leads to strong artefacts that hinders all image interpretation.

As noted in the previous section the blind-SIM algorithm does not work for illumination frequencies that are beyond the detection cut-off. In the following, two research avenues aiming at solving this issue are presented.

6.4.2 Model of intensity pattern

In blind-SIM, the only *a priori* information on the illumination patterns is the homogeneity of their sum $\sum_{l=1}^{L} I_l \approx LI_0$. In grating-assisted SIM, we have a lot of information on the intensity behaviour which stems from the sum of two (or four in the Moiré configuration) plane waves. Thus, we can try to build a simple parametric model for the illumination patterns as is done in many classical SIM reconstruction algorithms. The idea is to express I_l as functions of a defined series of parameters $(\mathbf{r}_0, A_0, A_1, \theta)$ where $\mathbf{r}_0$ is the grating position, A_0 is the transmission coefficient of the grating, A_1 is the amplitude of the enhanced diffracted order and θ is the angular misplacement of the grating. We keep the positivity *a priori* for the density function ρ which is written as the square of an auxiliary function ξ. Then we implement an

optimization algorithm where ξ and the parameter series are jointly estimated so as to minimise the functional

$$F(\xi, \mathbf{r}_0, A_0, A_1, \theta) \quad = \quad W \sum_{l=1}^{L} \|M_l - (\xi^2 I_l(\mathbf{r}_0, A_0, A_1, \theta)) * h\|^2.. \tag{6.21}$$

Unfortunately, numerical experiments showed that this algorithm was strongly sensitive to the initial guess for $\mathbf{r}_0$. As the latter is generally unknown, this algorithm can not be used to process experimental data.

To improve the parametric approach, and inspired by the reconstruction techniques available in classical SIM [54, 132, 133], I proposed to change the functional in order to introduce the autocorrelation of $\tilde{\rho}$ at $\mathbf{K}$. Indeed, defining

$$C_{\mathbf{K}}(\rho) = \left| \int_{\Omega} \tilde{\rho}(\mathbf{k}) \tilde{\rho}(\mathbf{k} - \mathbf{K}) \mathrm{d}\mathbf{k} \right|^2, \tag{6.22}$$

we observe that C is weak for the actual ρ^{true} and high for ρ estimated from wrong parameters. Thus, C is a good indicator of the accuracy of the estimated parameters. Using Parseval's theorem one shows that

$$\begin{aligned} C_{\mathbf{K}}(\xi) &= \left| \int_{\Omega} \rho^2(\mathbf{r}) \exp(i\mathbf{K}\mathbf{r}) \mathrm{d}\mathbf{r} \right|^2 \\ &= \left| \int_{\Omega} \xi^4(\mathbf{r}) \exp(i\mathbf{K}\mathbf{r}) \mathrm{d}\mathbf{r} \right|^2. \end{aligned} \tag{6.23}$$

The new functional is then defined as,

$$F(\xi, \mathbf{r}_0, A_0, A_1, \theta) = W \sum_{l=1}^{L} \left\| M_l - (\xi^2 I_l(\mathbf{r}_0, A_0, A_1, \theta)) * h \right\|^2 + \nu C_{\mathbf{K}}(\xi), \tag{6.24}$$

where ν is a parameter that has to be optimised. Joint optimisation with Eq. (6.24) gives good results with simulated data but failed with experimental ones. My opinion is that there is not enough parameters to fit properly the illumination patterns and the experimental variations. Moreover this approach requires to change the pattern model for each modification of the illumination series, involving substantial changes in the algorithm. For example switching from the one beam grating-assisted SIM to the Moiré grating-assisted SIM requires a deep modification of the reconstruction program.

This is why another approach is proposed in the following section. While imposing less constraints on the illumination pattern, it is easily tuned for diverse illumination series and less sensitive to experimental variations.

6.4.3 Filtered blind-SIM

To take into account all the possible experimental variations, we assume that $\tilde{I}_l$ is no more a simple collection of dirac-like peaks, as in theory, but that it can take non-zero values over small areas about the peaks location. One thus defines $\mathcal{S}$, the support of $\tilde{I}_l$, as a sub-set of the two-dimensional Fourier space. For example, one can define $\mathcal{S}$ as a series of small disks around

the theoretical positions of the different pattern frequencies. Then one notes $\tilde{\mathcal{S}}$ the set of real functions with value in Ω whose Fourier transform has its support included in $\mathcal{S}$. The principle of the filtered blind-SIM is to find the minimum of the functional Eq. (6.7), for I_l belonging to $\tilde{\mathcal{S}}$.

More precisely, the filtered blind-SIM algorithm consists in jointly estimating ρ and I_l so as to minimize the functional

$$F(\rho,(I_l)_{l=1,\dots,L-1}) = W\sum_{l=1}^{L-1}\|M_l-(\rho I_l)*h\|^2 + W\left\|M_L-\left[\rho\left(LI_0-\sum_{l=1}^{L-1}I_l\right)\right]*h\right\|^2, \tag{6.25}$$

for $\rho \in \Omega$ and $\forall l \in [1, L-1], I_l \in \tilde{\mathcal{S}}$. In other words, we minimise the same functional, but in a different space. As $\tilde{\mathcal{S}}$ is a sub-space of Ω, gradient-like algorithms are still efficient. The functional is minimised using the blind-SIM algorithm described in Sec. 6.2. The only modification are the gradients $g_{l,n;I}$ that are now (see Appendix B)

$$g_{l,n;I} = -2W\left[\rho\Big((r_{l,n-1}-r_{L,n-1})*h\Big)\right]*f, \tag{6.26}$$

where f is the function whose Fourier transform is 1 in $\mathcal{S}$ and 0 elsewhere. Practically, one filters all frequencies of $g_{l,n;I}$ that are out of $\mathcal{S}$ so that $g_{l,n;I} \in \tilde{\mathcal{S}}$. The initial guess $I_{l,0}$ is taken equal to I_0, as constant functions are members of $\tilde{\mathcal{S}}$. The series of $I_{l,n}$ remains thus in $\tilde{\mathcal{S}}$.

Note that this approach does not allows the use of the positivity constraint for I_l. Indeed finding the frequency content of the auxiliary functions i_l knowing the frequency content of $i_l^2 = I_l$ is a difficult task. In most cases there is no simple solutions. One solution is the use of the field amplitude E_l as auxiliary function, with $I_l = |E_l|^2$. Its frequency content is indeed easily evaluated. However all the phase information of E_l is lost in the fluorescence process. Admittedly, algorithms like the Fienup one [149] can recover the phase of a complex function from measurements of its modulus. However, they assume that there is no contribution of fluorophores out of the field of view and this assumption cannot be made with most of the experimental samples.

Numerical experiments have shown that this approach leads to correct reconstructions for classical periodic SIM, even when the norm of $\mathbf{K}$ is larger than the detection cut-off k_c. The Fourier support of I_l, $\mathcal{S}$, is, in this case, the union of the $k_0/2$-radius disks centred in $\mathbf{0}$ and in the six possible positions of $\mathbf{K}$ and $-\mathbf{K}$. We thus believe that this algorithm could be useful for treating experimental data obtained with saturated structured illumination microscopy, where high $\mathbf{K}$ are obtained using non-linearity in the emission coefficient σ [142, 143, 144].

Filtered blind-SIM has then be tested on simulated grating Moiré data. In this case, $\mathcal{S}$ is composed of small disks around each of the expected intensity frequencies for the three directions of illumination. We first considered the grating with period 170 nm that was designed in ref. [134]. We observe in Fig. (6.11) that the reconstructed fluorophore density and illumination patterns are close to the actual ones. The remaining difference is due to the inhomogeneity of the sum of illumination patterns. A further treatment is thus necessary to obtain a suitable image. For example, one could evaluate the residual inhomogeneity from the reconstructed ρ and rerun the algorithm using this information. We were unfortunately unable to reconstruct high frequency images from experimental data. We believe that the intensity at the surface of the manufactured 170 nm grating is too weak for a proper excitation of the fluorescence. The signal-to-noise ratio is then too small for measuring high-frequencies of ρ.

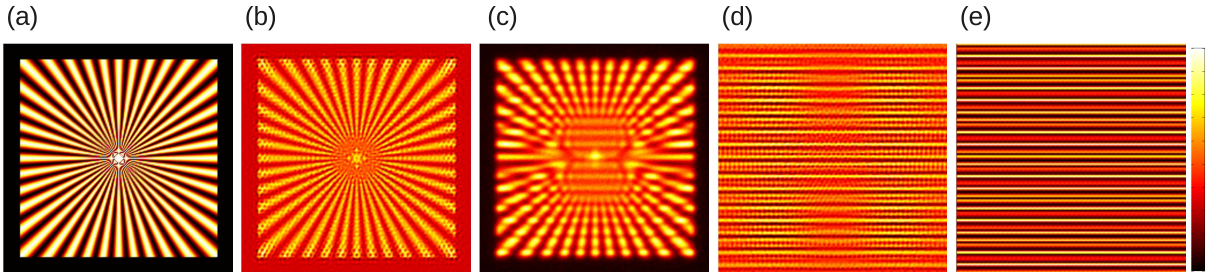

Figure 6.11: Example of numerical Moiré GA-SIM with a grating with period 170 nm. The star-like fluorescence density of the sample (a) is multiplied by 24 Moiré illumination patterns (I_1 shown in (e)). The product is convolved with the point-spread-function h and corrupted with noise (M_1 shown in (c)). Then, the filtered blind-SIM reconstructs a fluorophore density estimate (b) and 24 illumination pattern estimates (estimate of I_1 shown in (d)). The colour scale represents the normalised fluorophore density (respectively normalised intensity).

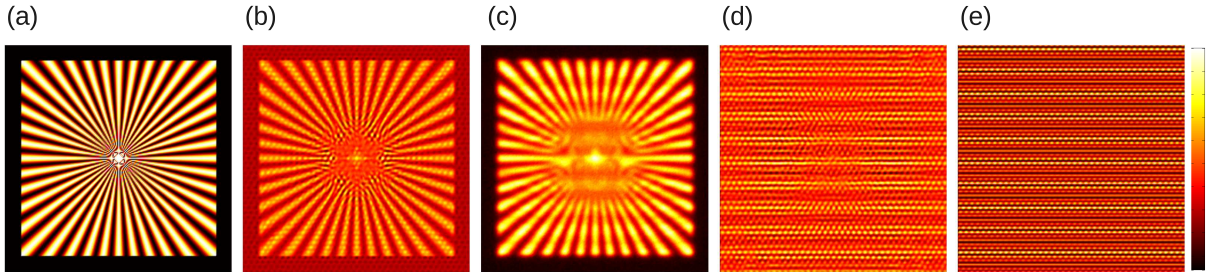

Figure 6.12: Example of numerical Moiré GA-SIM with the 210 nm grating. A star-like density of fluorophores (a) is multiplied to 24 Moiré illumination patterns (I_1 shown in (e)). Their products are convolved with the point-spread-function h and corrupted with noise (M_1 shown in (c)). Then the filtered blind-SIM reconstructs a fluorophore density estimate (b) and 24 illumination pattern estimates (estimate of I_1 shown in (d)). The colour scale represents the normalised fluorophore density (respectively normalised intensity). Artefacts appearing in the centre of (b) demonstrate that filtered blind-SIM is not efficient for all possible nano-structure for GA-SIM.

Then, we considered a grating with period 210 nm, as described in ref. [148, Sec. IV.1.3], which provides a higher intensity at the grating surface (thanks to a better excitation of the guided mode). Surprisingly, in this case, the filtered blind-SIM algorithm did not provide satisfactory reconstructions, see Fig. (6.12). We observed that sole the spatial frequencies that can be measured with a homogeneous illumination are well reconstructed but all high-frequency are false. We tried different Fourier supports and even defined a different $\mathcal{S}_l$ for each illumination without any positive outcome. A theoretical understanding of the convergence of the joint estimation is needed for explaining why filtered blind-SIM treats successfully data for certain illumination sets and not for others. Nonetheless, we believe that a suitable algorithm modification could lead to better results.

6.5 Conclusion

This chapter presents my work on algorithm development for image reconstruction in structured illumination fluorescence microscopy. The originality of the blind-SIM algorithm is to jointly estimate the object function and the probing illumination patterns. This algorithm is applied to simulated and experimental data. It is shown that blind-SIM retrieves correctly both the fluorophores density and the illumination patterns, provided that the illumination frequencies are contained in the detection transfer function. This algorithm can be used for classical SIM experiment using periodic light patterns, and, as there is no assumption on the illumination patterns except the homogeneity of their sum, using random speckle pattern. Thus blind-SIM is a promising solution for simplifying deeply experimental set-ups for SIM microscopy.

To address the challenge of sub-diffraction resolution with 'beyond the cut-off' illumination patterns, a modification of the blind-SIM algorithm has also been proposed. The filtered blind-SIM algorithm seems to be a promising solution although a theoretical understanding of its limits and an experimental demonstration are still missing.

Last, it is worth noting that the idea of jointly estimating object and probing functions is commonly used in micro-wave imaging and its optical counter part, non-linear Tomographic Diffraction Microscopy. Indeed, when the permittivity contrast is high, the field inside the sample is modified by the sample itself. In this case, one needs to update the probing field together with the permittivity contrast. Blind-SIM is actually directly inspired by the algorithms developed for non-linear electromagnetic imaging. In the following chapter, I will present an algorithmic improvement adapted to Tomographic Diffraction Microscopy data which is quite related to blind-SIM.

Chapter 7

Tomographic Diffraction Microscopy for highly refracting samples

As explained in Chap. 3, Tomographic Diffraction Tomography (TDM) is an optical stainless microscopy technique aiming at reconstructing a three-dimensional map of the sample permittivity. The sample, defined by its relative permittivity ε is illuminated successively by several incident plane waves $\mathbf{E}_{\mathrm{inc},l}$. For each illumination, the diffracted field $\mathbf{E}_{\mathrm{d},l}$ is measured in amplitude and phase along different directions of observation. The aim of TDM is to retrieve a quantitative three-dimensional map of the sample permittivity from the diffracted field measurements. In Chaps. 3 and 4 we have presented a linear reconstruction technique based on the Born (or renormalised Born) approximation which assumes that the field inside the sample is not modified by the sample itself. This assumption is valid when the permittivity contrast of the sample with respect to the background medium is weak. When the permittivity contrast is high, this approximation is no more valid and the linear reconstruction techniques do not lead to satisfying images of the sample permittivity. In this case, one cannot neglect the modification induced by the sample on the probing field. As the relation between the sample and the reconstructed image is no more linear, one cannot define a transfer function and the very notion of resolution becomes problematic. Indeed, it can be shown that, in the multiple scattering regime, all the Fourier components of the sample permittivity contribute to the far-field measurements [150]. Hence, it is theoretically possible to retrieve information on ε that are far beyond the diffraction limit. Examples of such super-resolved reconstructed permittivity maps have already been obtained in the simplified two-dimensional scalar configuration [151, 152].

The inverse problem in the multiple scattering regime is non-linear and ill-posed in the sense of Hadamard. Hadamard defines a well-posed inverse problem as respecting three conditions [153]

- Solutions exist for all possible set of data.
- There is only one solution for each set of data.
- The solution is continuous with respect to the data.

The inverse problems studied in this chapter and in the previous one fail to respect the last condition, requiring a technique of regularisation (see Sec. 6.2.4). However non-linear TDM also fails to respect the second condition. Two different permittivity maps can indeed have the same diffracted field for all illuminations [154, Annexe G].

Most of the non-linear inversion algorithms are iterative. Starting from an initial guess of the permittivity map, they improve at each iteration the estimation of the permittivity map by comparing the measured fields to the field that would be obtained with the estimate. These algorithms often use an accurate and efficient numerical tool for simulating the diffracted field from the permittivity map estimates. The non-linear inversion methods require generally a lot of computation resources, which explains that most of the existing algorithms for electromagnetic imaging were developed for two-dimensional samples. Thanks to the increasing computer performances and algorithmic improvements, it is now possible to consider more realistic samples. This chapter presents my work on the adaptation of a non-linear reconstruction algorithm to the vectorial three-dimensional configuration.

The first section introduces the model used for simulating the diffracted field and presents its numerical implementation. The second section describes the reconstruction algorithm. In the third section the algorithm is applied to experimental data, obtained with a microwave imager. The fourth section presents the results obtained from optical experimental data provided by a Tomographic Diffraction Microscope.

7.1 Modelling the diffracting field

The basics of electromagnetic modelling have been presented in Chap. 3. Here, we recall its main results and write them in a more convenient way for introduction the inverse problem.

7.1.1 Analytical models

As there is a large variety of possible imaging configurations, we use symbolic notations for stating the problem. The sample is assumed to be contained in the finite volume Ω and the measurements are taken on the surface Γ. The field $\mathbf{E}_l$ inside the sample is the solution on Ω of the linear equation (See Chap. 3)

$$\mathbf{E}_l = \mathbf{E}_{\mathrm{inc},l} + \bar{\mathbf{A}}\chi\mathbf{E}_l, \tag{7.1}$$

where $\bar{\mathbf{A}}$ is a linear tensor operator and $\chi = \varepsilon - \varepsilon_b$, for ε_b the permittivity of the medium surrounding the sample. The diffracted field measured on Γ is given by,

$$\mathbf{E}_{\mathrm{d},l} = \bar{\mathbf{B}}\chi\mathbf{E}_l, \tag{7.2}$$

where $\bar{\mathbf{B}}$ is a linear tensor operator.

The integral operators $\bar{\mathbf{A}}$ and $\bar{\mathbf{B}}$ depend on the studied configuration. Using the Green's function theory, $\bar{\mathbf{A}}$ can be expressed as

$$\bar{\mathbf{A}}\mathbf{V} = \int_\Omega \bar{\mathcal{G}}(\mathbf{r},\mathbf{r}')\mathbf{V}(\mathbf{r}')k_0^2\mathrm{d}\mathbf{r}', \tag{7.3}$$

for any vector field $\mathbf{V}$, $\bar{\mathcal{G}}$ is the Green's tensor that depends on the surrounding of the sample.

We now introduce the three configurations that have been used for this work. The first one is the classical configuration for TDM (as in Chap. 3), the sample is assumed to be in free space and its diffracted field is collected by a microscope objective; the second one is a TDM configuration with a reflecting substrate (as in Chap. 4). The last one is a free-space configuration with measurement in the Fresnel-zone, as in done in most microwave imaging set-ups. They are sketched in Fig. 7.1 and described hereafter.

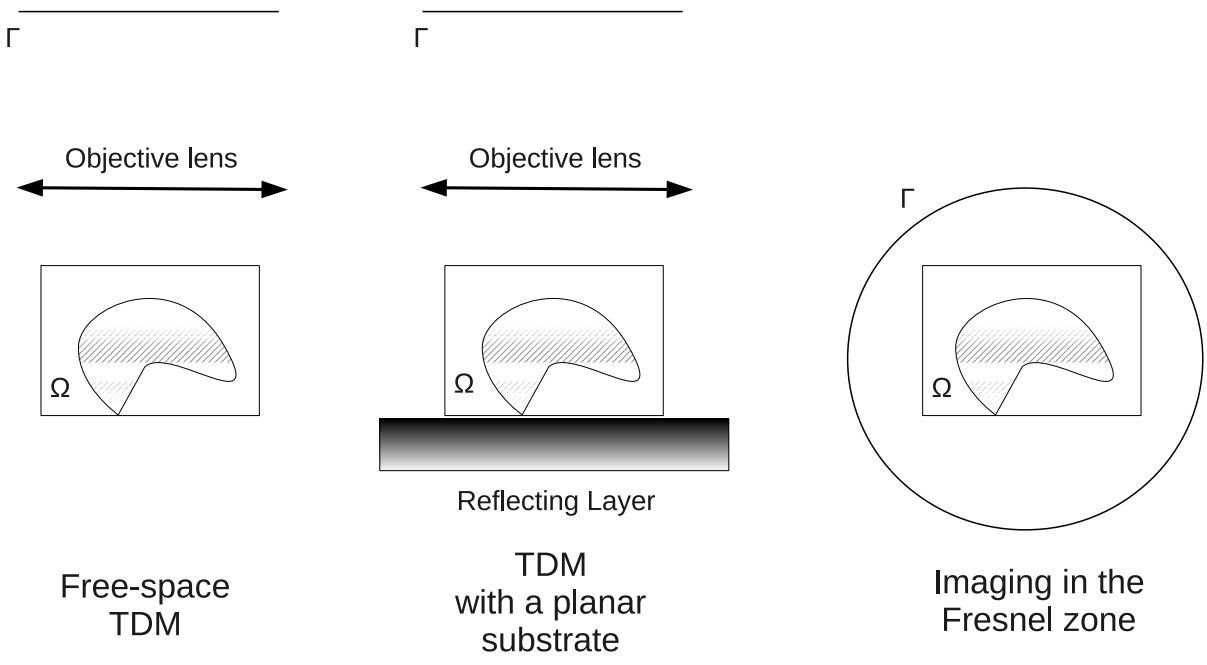

Figure 7.1: Sketch of the three configurations appearing in this chapter

Free-space Tomographic Diffraction Microscopy The sample is in free space, and the detection is done by a microscope objective. This configuration corresponds to that described in Chap. 3. Demonstrations therein shows that

$$\bar{\mathcal{G}}(\mathbf{r},\mathbf{r}')\mathbf{p} = -\frac{1}{4\pi k_0^2}\nabla\times\nabla\times\left(\frac{\exp(ik_0\Delta r)}{\Delta r}\mathbf{p}\right) + \frac{1}{k_0^2}\mathbf{p}\delta(\mathbf{r}-\mathbf{r}'), \tag{7.4}$$

for any vector $\mathbf{p}$, with $\Delta r = \|\mathbf{r}-\mathbf{r}'\|$.

Γ is the set of $\mathbf{k}$ directions such that $\mathbf{k}_\parallel \leq k_0\mathrm{NA}$ and $\bar{\mathbf{B}}$ is defined by

$$\bar{\mathbf{B}}\mathbf{V}(\mathbf{k}) = k_0\mathbf{k}\times\left(\mathbf{k}\times\tilde{\mathbf{V}}(\mathbf{k})\right), \tag{7.5}$$

for any vector field $\mathbf{V}$.

Tomographic Diffraction Microscopy with a planar substrate The sample is deposited on a planar substrate with a relative permittivity ε_1 and the detection is done by a microscope objective. This configuration corresponds to a generalisation of the mirror-assisted TDM studied in Chap. 4. One can prove that [72],

$$\begin{aligned}\bar{\mathcal{G}}(\mathbf{r},\mathbf{r}')\mathbf{p} = \frac{i}{8\pi^2 k_0^2}\int_{\mathbf{k}_\parallel\in\mathbb{R}^2}\frac{1}{k_z}\Big[&\exp\big(-i\mathbf{k}_\parallel.(\mathbf{r}_\parallel-\mathbf{r}'_\parallel)-k_z|z-z'|\big)\mathbf{k}\times\big(\mathbf{k}\times(\mathbf{p}_\parallel+p_z\mathbf{z})\big)\\ &+\bar{\mathbf{r}}(\mathbf{k})\exp\big(-i\mathbf{k}_\parallel.(\mathbf{r}_\parallel-\mathbf{r}'_\parallel)-k_z(z+z')\big)\mathbf{k}\times\big(\mathbf{k}\times(-\mathbf{p}_\parallel+p_z\mathbf{z})\big)\Big]\,\mathrm{d}\mathbf{k}_\parallel\\ &+\frac{1}{k_0^2}\mathbf{p}\delta(\mathbf{r}-\mathbf{r}'),\end{aligned} \tag{7.6}$$

where $\bar{\mathbf{r}}(\mathbf{k})$ is the Fresnel reflection tensor defined by

$$\bar{\mathbf{r}}(\mathbf{k})\mathbf{E}_0 = \frac{\sqrt{\varepsilon_1 k_0^2-|\mathbf{k}_\parallel|^2}-\sqrt{k_0^2-|\mathbf{k}_\parallel|^2}}{\sqrt{\varepsilon_1 k_0^2-|\mathbf{k}_\parallel|^2}+\sqrt{k_0^2-|\mathbf{k}_\parallel|^2}}\mathbf{E}_\mathrm{s} + \frac{\sqrt{\varepsilon_1 k_0^2-|\mathbf{k}_\parallel|^2}-\varepsilon_1\sqrt{k_0^2-|\mathbf{k}_\parallel|^2}}{\sqrt{\varepsilon_1 k_0^2-|\mathbf{k}_\parallel|^2}+\varepsilon_1\sqrt{k_0^2-|\mathbf{k}_\parallel|^2}}\mathbf{E}_\mathrm{p}, \tag{7.7}$$

with $\mathbf{E}_\mathrm{s} = (\mathbf{E}_0.\mathbf{u}_\mathrm{s})\mathbf{u}_\mathrm{s}$ and $\mathbf{E}_\mathrm{p} = (\mathbf{E}_0.\mathbf{u}_\mathrm{p})\mathbf{u}_\mathrm{p}$, for $\mathbf{u}_\mathrm{s} = \mathbf{z} \times \mathbf{k}/k_0$ and $\mathbf{u}_\mathrm{p} = \mathbf{z} \times \mathbf{u}_\mathrm{s}$. $\bar{\mathbf{B}}$ is defined by

$$\bar{\mathbf{B}}\mathbf{V}(\mathbf{k}) = k_0\mathbf{k} \times \left(\mathbf{k} \times \tilde{\mathbf{V}}(\mathbf{k})\right) + k_0\bar{\mathbf{r}}(\mathbf{k})\mathbf{k} \times \left(\mathbf{k} \times \tilde{\mathbf{V}}(\mathbf{k}')\right), \tag{7.8}$$

with $\mathbf{k}' = \mathbf{k}_\parallel - k_z\mathbf{z}$.

Imaging in the Fresnel-zone The sample is in free space and the detection is performed on a surface Γ surrounding the sample. In this case, $\bar{\mathcal{G}}$ is given by Eq. (7.4) and $\bar{\mathbf{B}}$ by

$$\bar{\mathbf{B}}\mathbf{V}(\mathbf{r}) = \int_\Omega \bar{\mathcal{G}}(\mathbf{r}, \mathbf{r}')\mathbf{V}(\mathbf{r}')k_0^2 \mathrm{d}\mathbf{r}'. \tag{7.9}$$

7.1.2 Description of the simulation method

To compute numerically $\mathbf{E}_{\mathrm{d},l}$, from a given $\chi(\mathbf{r})$, the first step is to solve Eq. (7.1). One discretises Ω in I subunits Ω_i arranged on a cubic lattice and one assumes the fields $\mathbf{E}_{\mathrm{inc},l}$ and $\mathbf{E}_l$ and the permittivity contrast χ to be constant over each subunit. Equation (7.1)

$$\begin{aligned}\mathbf{E}_l(\mathbf{r}) &= \mathbf{E}_{\mathrm{inc},l}(\mathbf{r}) + \bar{\mathbf{A}}\chi\mathbf{E}_l \\ &= \mathbf{E}_{\mathrm{inc},l}(\mathbf{r}) + \int_\Omega \bar{\mathcal{G}}(\mathbf{r}, \mathbf{r}')\chi(\mathbf{r}')\mathbf{E}_l(\mathbf{r}')k_0^2 \mathrm{d}\mathbf{r}'\end{aligned}$$

can be rewritten under this approximation as [155]

$$\mathbf{E}_l(\mathbf{r}_i) \approx \mathbf{E}_l^\mathrm{inc}(\mathbf{r}_i) + \sum_{j=1}^{I} \bar{\mathbf{G}}(\mathbf{r}_i, \mathbf{r}_j)\chi(\mathbf{r}_j)\mathbf{E}_l(\mathbf{r}_j)k_0^2 d^3, \tag{7.10}$$

where d is the edge length of the lattice, $\mathbf{r}_i$ is the centre of Ω_i and

$$\bar{\mathbf{G}}(\mathbf{r}_i, \mathbf{r}_j) = \frac{1}{d^3}\int_{\Omega_j} \bar{\mathcal{G}}(\mathbf{r}_i, \mathbf{r}')\mathrm{d}\mathbf{r}' \tag{7.11}$$

is the propagator between the subunit i and the subunit j. This method converges if $d \ll \lambda$ [156].

Usually an additional approximation is made. The Green function $\bar{\mathcal{G}}$ is also assumed to be constant over each subunit, leading to $\bar{\mathbf{G}}(\mathbf{r}_i, \mathbf{r}_j) \approx \bar{\mathcal{G}}(\mathbf{r}_i, \mathbf{r}_j)$. As long as the permittivity contrast is not too high, this discretisation allows a correct computation of the field inside the sample [156]. For strongly diffracting samples, however, a better approximation is necessary [157, 158, 156].

Equation (7.10) is a linear system. It is solved numerically thanks to a bi-conjugate type method [159, 160], that is proved to have the best convergence for electromagnetic fields [18]. Then, the diffracted fields $\mathbf{E}_{\mathrm{d},l}$ are obtained using Eq. (7.2) and the field $\mathbf{E}_l$ previously calculated.

7.2 Description of different reconstruction methods

This section introduces three reconstruction algorithms that can be found in the literature (for two-dimensional configurations essentially). First, the linearised Conjugate Gradient method

(CGM), a linearised inversion algorithm that has the advantage of speed but is unstable for highly refracting samples [161, 72]. Then the Hybrid gradient Method (HM), proposed as Modified^2 Gradient Method in ref. [19], combining advantages of speed and stability. Finally the Contrast Source Inversion (CSI) [20] known as one of the most stable one, used as reference for stability [162, 163]. All these techniques are iterative and inspired by the Conjugate Gradient algorithm. That is why a general presentation of this algorithm is expounded in the following subsection.

7.2.1 General principle of the Conjugate gradient algorithm

The Conjugate Gradient [15] is an iterative algorithm for finding the minimum of a functional $F(\chi)$. Starting from an initial guess χ_0, one builds a series $(\chi_n)_{n=1,\dots,\infty}$ converging towards the minimum of a functional F. More precisely, one chooses for each n a χ_{n+1} such that $F(\chi_{n+1}) \leq F(\chi_n)$. If χ_{n+1} is properly chosen, this series converges to the minimum of F. The gradient algorithm (or Steepest Descent algorithm) is a way to choose an update χ_{n+1} from χ_n. The first step is to compute $g_{n;\chi}$ the gradient of F at the point χ_n. The gradient of F is the direction where F varies the most. A formal definition and calculation rules of a functional gradient can be found in Appendix B. Then, the update χ_{n+1} is defined as,

$$\chi_{n+1} = \chi_n + \beta_n g_{n;\chi}, \tag{7.12}$$

where β_n minimises

$$f(\beta_n) = F(\chi_n + \beta_n g_{n;\chi}). \tag{7.13}$$

This is a crucial step. One indeed searches for the minimum of F on the line passing through χ_n with vector $g_{n;\chi}$. This insures that $F(\chi_{n+1}) \leq F(\chi_n)$. The value of β_n has to be computed at each iteration. In some cases there is an analytical formula, but most of the time β_n has to be estimated iteratively [16, part 10.5].

This method insures that $F(\chi_{n+1}) \leq F(\chi_n)$ and, if F is convex, it converges towards the minimum [16, part 10.6]. However, the convergence is very slow. One need a really high number of iterations for obtaining a good estimate of the minimum. To accelerate this convergence, one can use the Conjugate Gradient algorithm [15]. The main idea is to modify χ_{n+1} so that it depends on $g_{n;\chi}$, but also on all $(g_{i;\chi})_{i=1,\dots,n-1}$. More precisely, one defines the update as

$$\chi_{n+1} = \chi_n + \beta_n d_{n;\chi} \tag{7.14}$$

with

$$d_{n;\chi} = g_{n;\chi} + \gamma_n d_{n-1;\chi}. \tag{7.15}$$

One calls $d_{n;\chi}$ the descent direction. The line minimisation is performed along the line parallel to it $f(\beta_n) = F(\chi_n + \beta_n d_{n;\chi})$. The conjugation factor γ_n is chosen following to the Polak-Ribière conjugation suggestion [124] (which is known as one of the most efficient),

$$\gamma_n = \frac{\langle g_{n;\chi} | g_{n;\chi} - g_{n-1;\chi} \rangle}{\|g_{n-1;\chi}\|^2}. \tag{7.16}$$

Two points still need to be specified before running the algorithm. The first one is the initial guess χ_0. It has to be easy to compute and as close as possible to the minimum. A good initial guess reduces indeed the number of iterations. The second one is the stopping criterion. For our

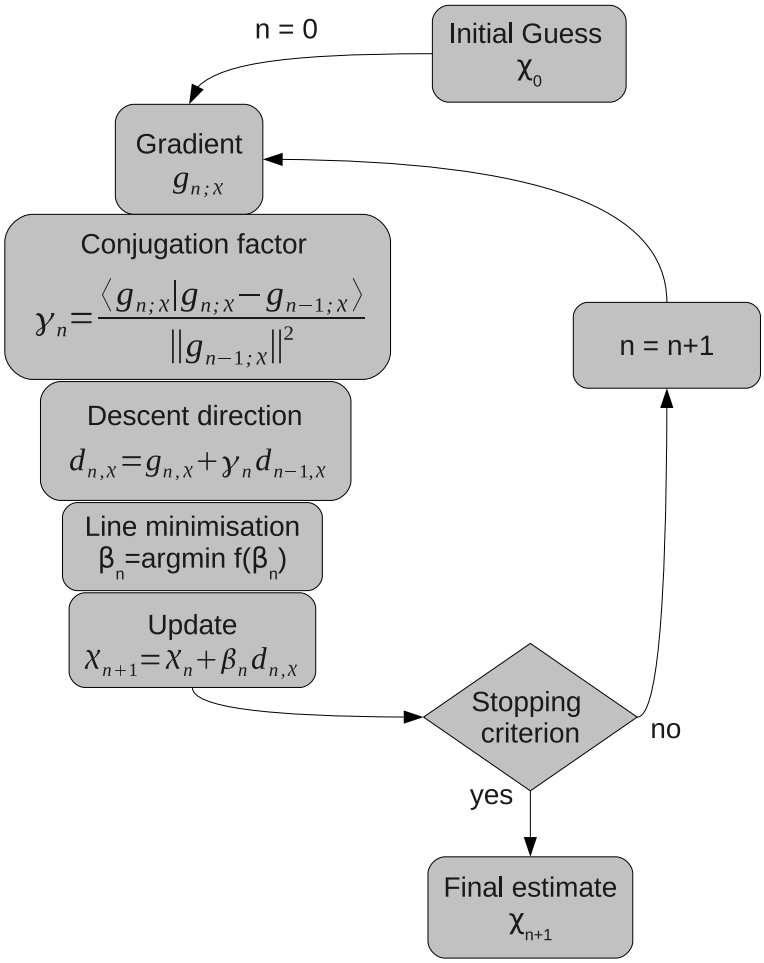

Figure 7.2: Flow-chart of the conjugate gradient algorithm.

ill-posed problems, this stopping criterion is used as a regularisation technique. As discussed in Sec. 6.2.4, one registers χ_n for a set of iterations n and the practitioner chooses the one that has the best trade-off between resolution and noise. A flow-chart summarising the successive steps of this algorithm is plotted in Fig. 7.2.

7.2.2 Specificity of the reconstruction algorithms

We now describe the three different reconstructions methods that were studied in this work. They are all iterative and they all rely on the gradient conjugate algorithm. They essentially differ by the functional they minimise and by the minimisation strategy. Yet, in all cases, the functionals are built in such a way that the measured fields are compared to the fields that would be produced by the estimates χ and $\mathbf{E}_l$.

7.2.2.1 The linearised Conjugate Gradient Method (CGM)

In the linearised conjugate gradient method (CGM) [161, 72], fields $\mathbf{E}_{l,n}$ are assumed constant during each minimisation step n. The functional that we minimise depends only on the variable

χ but changes for each iteration

$$F_n(\chi) = W_\Gamma \sum_{l=1}^{L} \|\mathbf{E}_{\mathrm{d},l} - \bar{\mathbf{B}}\chi\mathbf{E}_{l,n}\|_\Gamma^2, \tag{7.17}$$

where W_Γ is the normalisation factor

$$W_\Gamma = \frac{1}{\sum_{l=1}^{L} \|\mathbf{E}_{\mathrm{d},l}\|_\Gamma^2}.$$

χ_{n+1} is computed from χ_n using the conjugate gradient descent direction

$$\chi_{n+1} = \chi_n + \beta_n d_{n;\chi},$$

where $d_{n;\chi}$ is the conjugate descent direction computed from the gradient $g_{n;\chi}$ and the previous descent directions. β_n is the complex value minimising

$$f(\beta_n) = F(\chi_n + \beta_n d_{n;\chi}).$$

Once χ_{n+1} is computed, $\mathbf{E}_{l,n+1}$ is obtained solving the near-field equation (7.1)

$$\mathbf{E}_{l,n+1} \quad = \quad \mathbf{E}_{\mathrm{inc},l} + \bar{\mathbf{A}}\chi_{n+1}\mathbf{E}_{l,n+1}.$$

As long as the permittivity contrast is not too high, this algorithm converges to an acceptable reconstruction in less than a hundred of iteration. However, since the minimisation of F at each iteration is not ensured, it becomes unstable for high permittivity samples.

7.2.2.2 Hybrid Gradient Method (HM)

The Hybrid gradient Method (HM) is an hybrid between the linearised Conjugate Gradient Method and the Modified Gradient Method. This method is quite original and, before this thesis, it had been developed only for two-dimensional scalar configurations.

The Modified Gradient Method The Modified gradient Method [164, 165] proposes the minimisation of a functional built from both Eqs. (7.2) and (7.1)

$$F_n(\chi, (\mathbf{E}_l)_{l=1,\dots,L}) = W_\Gamma \sum_{l=1}^{L} \|\mathbf{E}_{\mathrm{d},l} - \bar{\mathbf{B}}\chi\mathbf{E}_l\|_\Gamma^2 + W_\Omega \sum_{l=1}^{L} \|\mathbf{E}_l - \mathbf{E}_{\mathrm{inc},l} - \bar{\mathbf{A}}\chi\mathbf{E}_l\|_\Omega^2, \tag{7.18}$$

where W_Ω is the normalisation factor

$$W_\Omega = \frac{1}{\sum_{l=1}^{L} \|\mathbf{E}_{\mathrm{inc},l}\|_\Gamma^2}.$$

Then, the L+1 variables $(\chi, (\mathbf{E}_l)_{l=1,\dots,L})$ are jointly updated so as to minimise F using the gradient conjugate algorithm. This algorithm insures the minimisation of F at each iteration. It is thus far more stable that the CGM method. However it requires a large number of iterations, implying a long computation time.

Hybridisation The Linearised Conjugate Gradient is time efficient but fails to reconstruct highly diffracting samples. On the contrary, Modified Gradient Method is time consuming but succeeds in reconstructing (to a certain extent) highly diffracted samples. The Hybrid gradient Method [19, 166] is a combination of both approaches. It consists in minimising the Modified Gradient functional Eq. (7.18). One computes the gradient of F along all its variable $g_{n;\chi}$ and $\mathbf{g}_{l,n;\mathbf{E}}$, which, through the Polak-Ribiére conjugation, leads to two descent directions $d_{n;\chi}$ and $\mathbf{v}_{l,n}$. Then, following the Linearised Conjugate Gradient approach, another descent direction $\mathbf{w}_{l,n}$ is introduced, based on the solution of the near-field equation Eq. (7.1). We define $\mathbf{w}_{l,n} = \mathbf{E'}_{l,n} - \mathbf{E}_{l,n}$ where $\mathbf{E'}_{l,n}$ is the solution of

$$\mathbf{E'}_{l,n} = \mathbf{E}_{\text{inc},l} + \bar{\mathbf{A}}\chi_n \mathbf{E'}_{l,n}.$$

The estimate $(\chi_n, (\mathbf{E}_{l,n})_{l=1,\dots,L})$ is then updated using the iteration relation,

$$\chi_{n+1} = \chi_n + \beta_n d_{n;\chi} \tag{7.19}$$
$$\mathbf{E}_{l,n+1} = \mathbf{E}_{l,n} + \alpha^v_{l,n}\mathbf{v}_{l,n} + \alpha^w_{l,n}\mathbf{w}_{l,n} \tag{7.20}$$

The crucial point is the choice of the parameters $\alpha^v_{l,n}$ and $\alpha^w_{l,n}$. It is clear that if $\forall l, \alpha^v_{l,n} = 0$ and $\alpha^w_{l,n} = 1$, one obtains the same update as in the linearised Conjugate Gradient Method. Conversely, if $\forall l, \alpha^w_{l,n} = 0$, we are using a variant of the Modified Gradient Method. The Hybrid gradient Method proposes the use of $(\beta_n, (\alpha^v_{l,n})_{l=1,\dots,L}, (\alpha^w_{l,n})_{l=1,\dots,L})$ that minimises

$$f\Big(\beta_n, (\alpha^v_{l,n})_{l=1,\dots,L}, (\alpha^w_{l,n})_{l=1,\dots,L}\Big) = F\Big(\chi_n + \beta_n d_{n;\chi}, (\mathbf{E}_{l,n} + \alpha^v_{l,n}\mathbf{v}_{l,n} + \alpha^w_{l,n}\mathbf{w}_{l,n})_{l=1,\dots,L}\Big). \tag{7.21}$$

This way, one chooses for each incidence l the best compromise between the two descent directions for the electric field $\mathbf{E}_{l,n}$.

7.2.2.3 Contrast Source Inversion (CS)

The Contrast Source Inversion [20] (CSI) is a modification of the Modified Gradient Method. It rewrites Eqs. (7.1) and (7.2) in terms of the source density $\mathbf{P}_l = \chi\mathbf{E}_l$ [167]

$$\mathbf{E}^{\text{d}}_l = \bar{\mathbf{B}}\mathbf{P}_l \tag{7.22}$$
$$\mathbf{P}_l = \chi\mathbf{E}_{\text{inc},l} + \chi\bar{\mathbf{A}}\mathbf{P}_l. \tag{7.23}$$

This leads to the functional

$$F_n\Big(\chi, (\mathbf{P}_l)_{l=1,\dots,L}\Big) = W_\Gamma \sum_{l=1}^{L} \|\mathbf{E}_{\text{d},l} - \bar{\mathbf{B}}\mathbf{P}_l\|^2_\Gamma + W'_\Omega \sum_{l=1}^{L} \|\mathbf{P}_l - \mathbf{E}_{\text{inc},l} - \chi\bar{\mathbf{A}}\mathbf{P}_l\|^2_\Omega, \tag{7.24}$$

where

$$W'_\Omega = \frac{1}{\sum_{l=1}^{L} \|\chi_n \mathbf{E}_{\text{inc},l}\|^2_\Gamma}$$

Diverse iterative schemes have been proposed to find the minimum of this functional. Our proposal is to use the iterative relations

$$\chi_{n+1} = \chi_n + \beta_n d_{n;\chi} \tag{7.25}$$
$$\mathbf{P}_{l,n+1} = \mathbf{P}_{l,n} + \alpha_{l,n}\mathbf{d}_{l,n;\mathbf{P}} \tag{7.26}$$

with $d_{n;\chi}$ and $\mathbf{d}_{l,n;\mathbf{P}}$ the descent directions according to the gradient conjugate method, and $(\beta_n, (\alpha_{l,n})_{l=1,\dots,L})$ minimising

$$f\Big(\beta_n, (\alpha_{l,n})_{l=1,\dots,L}\Big) = F\Big(\chi_n + \beta_n d_{n;\chi}, (\mathbf{P}_{l,n} + \alpha_{l,n}\mathbf{d}_{l,n;\mathbf{P}})_{l=1,\dots,L}\Big). \tag{7.27}$$

The Contrast Source Inversion is known as one of the most stable inversion method [162, 163]. We use it as a reference for testing the stability of the HM method. However it requires a very large number of iterations, leading to computation time too long for practical use.

7.2.3 *a priori* information in the expression of the unknowns

Physical considerations impose constraints on the values of the permittivity ε. Indeed, since its imaginary part is proportional to the absorption coefficient, it cannot be negative for usual materials. Moreover for dielectric materials, the real part of the relative permittivity is always superior to 1. Adding this information can help the resolution of the inverse problem [46]. Algorithms that use positivity constraints are indeed more robust to noise [168]. Our way to impose this constraint is the expression of the complex χ in term of two real auxiliary functions ξ and η [169]

$$\chi = 1 + \xi^2 + i\eta^2 - \varepsilon_b. \tag{7.28}$$

The positivity constraint is used in the HM algorithm. As said in refs. [46, 170] this constraint modifies the resulting image. For comparison purpose we have also developed a linearised Conjugate Gradient Method under positivity constraint (PCGM).

One of the main differences between the scalar two-dimensional and the vectorial three-dimensional configurations is that the three-dimensional near-field propagator $\bar{\mathcal{G}}$ presents a singularity (See for example Eq. (3.10)). As seen in Sec. 3.2.2, this leads to an alternative description of the scattering problem in terms of local field and sample polarisability α (instead of macroscopic field and permittivity contrast). In this case, Eq. (7.1) is replaced by

$$\mathbf{E}_{\text{local},l}(\mathbf{r}) = \mathbf{E}_{\text{inc},l}(\mathbf{r}) + \text{PV}\int_\Omega \bar{\mathcal{G}}(\mathbf{r},\mathbf{r}')\alpha(\mathbf{r}')\mathbf{E}_{\text{local},l}(\mathbf{r}')k_0^2 \mathrm{d}\mathbf{r}', \tag{7.29}$$

with $\mathbf{E}_{\text{local},l}(\mathbf{r}) = \mathbf{E}_l(\mathbf{r})[\varepsilon(\mathbf{r}) + 2]/3$ and

$$\alpha(\mathbf{r}) = 3\frac{\varepsilon(\mathbf{r}) - 1}{\varepsilon(\mathbf{r}) + 2}.$$

The second term of the right-hand part of this equation is generally lower than the second term of the right-hand part of Eq. (7.1). This is the reason why the renormalised Born approximation is usually better than the Born approximation and why the formulation in α reduces the computation time of the near-field equation [155]. This modification acts as a pre-conditioner that eases the inversion of Eq. (7.1).

It is thus tempting to use the description with the local field and polarisability α for reconstructing the sample. In this case, the polarisability can be seen as an auxiliary variable describing ε. Note that the positivity constraint can also be imposed to the polarisability. Indeed one can easily verifies that,

$$\begin{cases} \Re e(\chi) \geq 0 \\ \Im m(\chi) \geq 0 \end{cases} \Rightarrow \begin{cases} \Re e(\alpha) \geq 0 \\ \Im m(\alpha) \geq 0 \end{cases} \tag{7.30}$$

One can thus impose the positivity to α with the same type of auxiliary functions as that used for ε. Note however that Eq. (7.30) is an implication and not an equivalence. Reconstructions with positivity imposed on α can lead to reconstructed ε with strong negative values. We implemented the formulation in terms of local field and sample polarisability in HM, but, unfortunately did not observe any marked improvement, neither on the reconstruction quality nor in the computation time, for the examples studied. Hence, because of the interest of imposing the positivity on ε, the formulation in terms of ε seems then preferable.

7.3 Application to micro-wave data[1]

To investigate the performances of the different inversion methods sketched in the previous section, we applied them to experimental data stemming from the microwave imaging set-up described in the special section [171, 172]. In this imager, the targets are illuminated by an electromagnetic wave which can be assimilated to a plane wave. The scattered field is measured at 81 points on a sphere enclosing the targets (Imaging in the Fresnel-zone) with regular angular steps and with 36 incident directions taken in the (x, y) plane by rotating regularly over $[2\pi]$ the emitting antenna about the **z** axis. The background medium is homogeneous, $\varepsilon_b = 1$.

With this illumination and detection configuration, a single scattering analysis estimates the resolution of the reconstruction as $\lambda/4$ in the transverse (x, y) plane and $\lambda/1.8$ in the (x, z) and (y, z) planes. We considered two different targets, which are described in Fig. 7.3, and several incident frequencies from 3 GHz to 8 GHz.

Prior to presenting the reconstructions obtained with the four different inversion methods described in the first section, it is important to discuss their convergence behaviour and the stopping criterion. First, it is important to stress that the convergence of the three methods is not ensured mathematically. Yet, because of the minimisation process, the cost functional of CSI and HM are forced to decay at each iteration. Under some conditions, the CSI functional has even been shown to exhibit only one local minimum [173]. On the other hand, the decay of the cost functions of CGM and PCGM is not automatic as the total field inside Ω is estimated through a direct calculation, without minimising the cost-functional.

We observed that, in all the considered examples, the cost functions of CSI, CGM and PCGM had a similar behaviour. After a certain number of iterations, they would decay slowly and continuously without visible changes on the reconstructions. The HM cost function, on the contrary, would rapidly reach a constant value which depended on the accuracy with which the scalar coefficients b_n, $a^v_{l,n}$ and $a^w_{l,n}$ were optimized. We decided to stop the iterations of CGM, CSI and PCGM when the reconstruction did not evolve significantly any more, while we stopped the HM iteration when the cost function reached the plateau. Note that, the cost functions of these methods being normalised differently, we cannot use their values as a stopping criterion.

[1] Most of the text of this section was originally published in E. Mudry, P. C. Chaumet, K. Belkebir and A. Sentenac, *Electromagnetic wave imaging of three-dimensional targets using a hybrid iterative method*, Inverse Problems, **28**, 065007 (2012) [21]. My main contribution was the codes of the inversion algorithms.

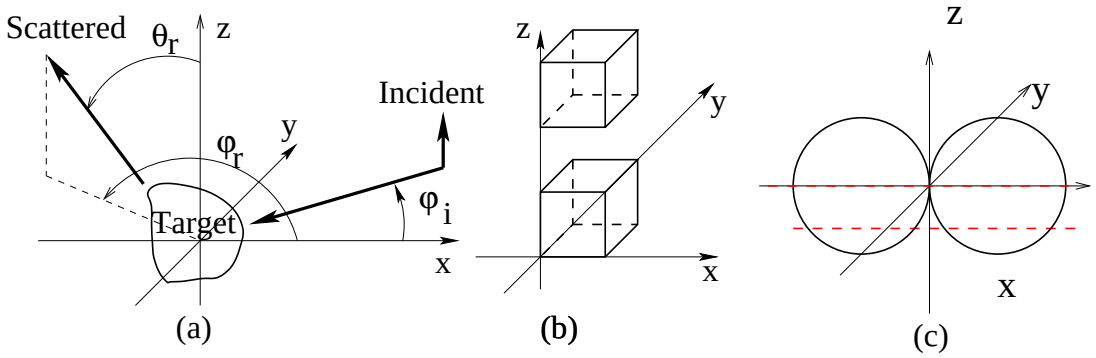

Figure 7.3: (a) Sketch of the experimental set-up. The illumination is done on the (x, y) plane with φ_i from 0° to 350° step 10°. The polarisation of the incident field is along the **z** direction. The receiver position angles varies φ_r from 20° to 340° step 40° and θ_r from -60° to 60° step 15°. (b-c) the two different targets under study. (b) two dielectric cubes of relative permittivity $\varepsilon = 2.4$ and side $a = 2.5$ cm located at $(a/2, a/2, a/2)$ and $(a/2, a/2, 5a/2)$. (c) Two spheres in contact with relative permittivity $\varepsilon = 2.6$ and radius $r = 2.5$ cm. The centres of the spheres are located at $(-r, 0, 0)$ and $(r, 0, 0)$.

7.3.1 Two cubes along the z direction

The first considered target is made of two small cubes placed along the **z** axis, as shown in Fig. 7.3 (b). This simple object permits to test and validate the Hybrid Method and to compare its performances to that of CGM, PCGM and CSI in terms of convergence and computation time.

At low frequency: 4 GHz We first inverted the data obtained at 4 GHz. At this frequency, the inter-distance between the cubes centres is about two third of the wavelength, which is above the single scattering resolution limit in the **z** direction. As expected, both CGM, PCGM, CSI and HM are able to resolve the two cubes, Fig. 7.4. Unsurprisingly, the results obtained with PCGM and HM using the permittivity positivity *a priori* information are better than that given by CGM and CSI without this *a priori* information. With these data with a high signal-to-noise ratio, it appears that PGCM is better than HM.

At high frequency: 8 GHz We now study the data obtained at 8 GHz which exhibits a lower signal-to-noise ratio than those obtained at 4 GHz [172, 170]. As expected, all four methods retrieve accurately the two cubes. PGCM and HM are once again slightly better than CGM and CSI. In this case, however, PGCM is not as good as HM as it reconstructs small ghosts objects outside the targets and exhibits high permittivity peaks whereas the HM reconstructed background is perfectly equal to one and its reconstructed permittivity close to the actual value. We have observed on many examples that, with data presenting a high signal-to-noise ratio, PGCM was the most efficient technique for retrieving the object smallest details but that, on the other hand, it was the least robust to noise.

Computation time The computation is carried on a single Intel Xeon processor with 3.2 GHz clock speed. For the two cubes target, we give in Tab. 7.1, the number of iterations, the computation time per iteration and the total computation time necessary to obtain the reconstructions

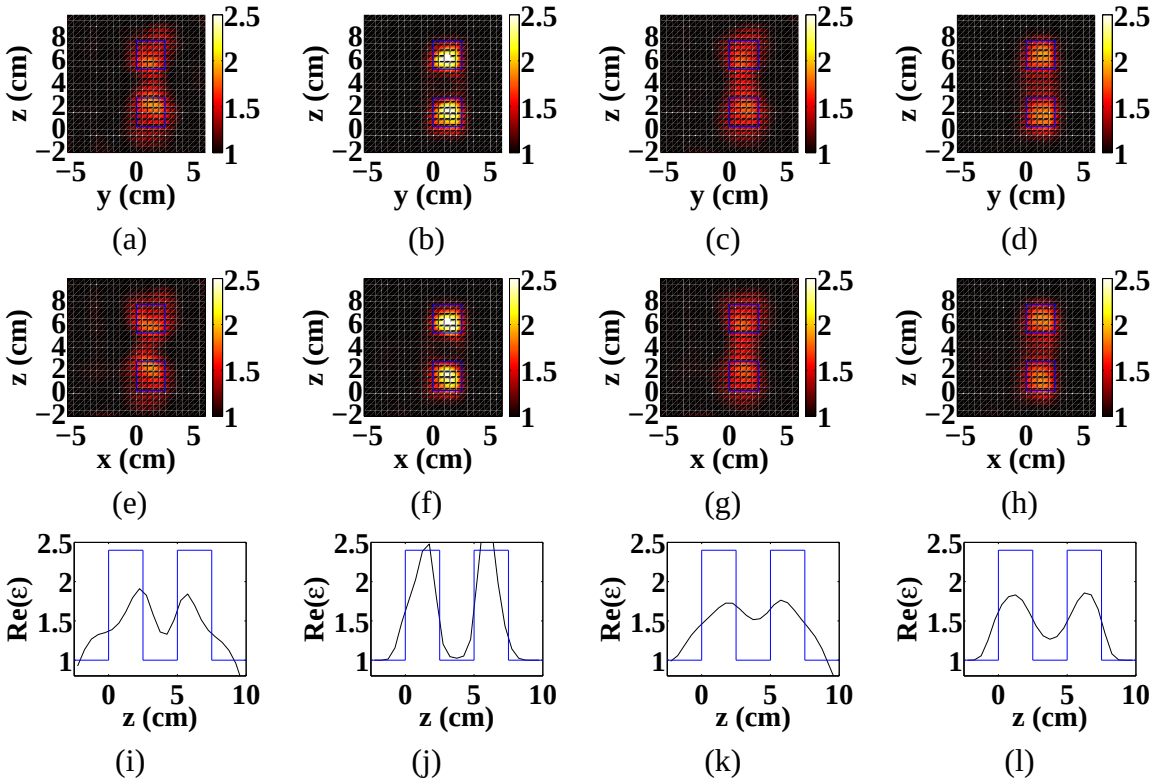

Figure 7.4: Reconstructed permittivity of the first target (two cubes along the **z** axis) presented in Fig. 7.3 obtained with the different inversion methods from data obtained at 4 GHz. The first column corresponds to CGM reconstruction; the second to PCGM, the third to CSI and the fourth to HM. The first line represents the relative permittivity in the plane (y, z) at $x = 0$; The second line represents the relative permittivity in the plane (x, z) at $x = 0$ and the third line the relative permittivity versus z for $x = y = 0$.

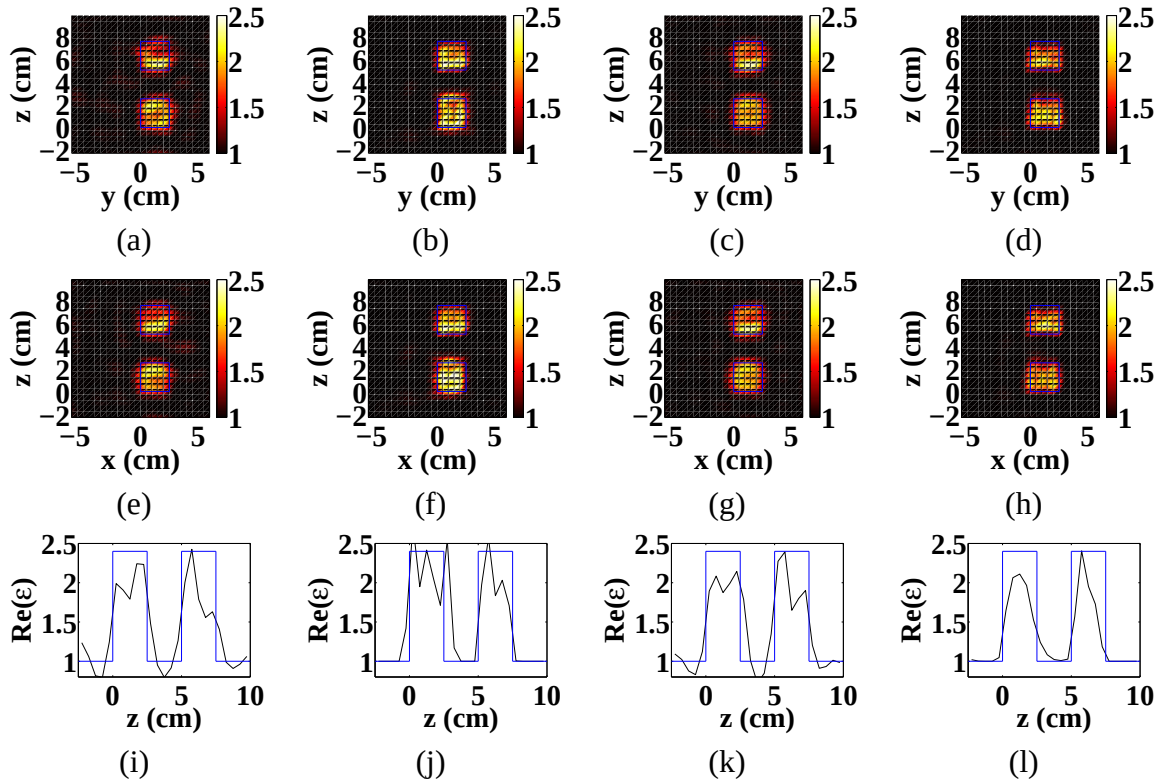

Figure 7.5: Same as in Fig. 7.4 but at 8 GHz.

plotted in Figs. (7.4) and (7.5). We observe that CSI is much slower than all the other approaches. Indeed, although its iteration computation time is the smallest, as one does not need to solve any forward problem, the number of iterations required for converged result is huge. On the other hand, CGM, PCGM and HM have a relatively long computation time for each iteration, but this issue is largely compensated by the small number of iterations required for getting a converged result. Actually, solving the forward problem, which used to be very time consuming, is now performed surprisingly fast thanks to the recent algorithmic progress [17, 18]. The CGM iteration is faster than PCGM and HM because it does not require to optimise iteratively the scalar coefficients β_n.

Note that for CGM, PCGM and HM the iteration computation time increases with the illu-

Frequency	Method	Iteration number	Time by iteration (min)	Total time (min)
4 GHz	HM	28	6.35	178
4 GHz	PCGM	25	3.2	80
4 GHz	CGM	200	0.91	182
4 GHz	CSI	3000	0.72	2146
8 GHz	HM	13	8.46	110
8 GHz	PCGM	25	7.68	192
8 GHz	CGM	200	1.2	240
8 GHz	CSI	3000	0.83	2493

Table 7.1: Time of computation necessary to get the final image and number of iterations needed for the four methods presented in this section.

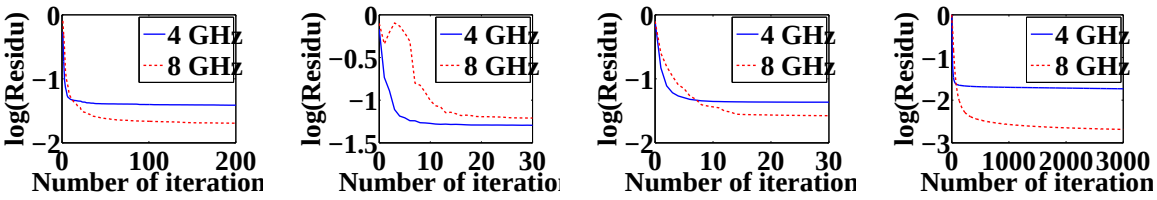

Figure 7.6: Behaviour of the cost functional for the four different methods at 4 GHz and 8 GHz. (a) CGM. (b) PCGM. (c) HM. (d) CSI.

mination frequency. Indeed, the time required to solve the direct problem depends directly on the object size with respect to the illumination wavelength. At 8 GHz, convergence of PCGM takes more iterations than at 4 GHz because of the lesser signal-to-noise ratio. At this frequency, HM is the fastest method.

The behaviour of the residual error versus the iteration is plotted for each method and for both frequencies in Fig. 7.6. We observe that, except for the PCGM which is most sensitive to noise, the high frequency data yields a better residue than the low frequency data. These curves are emblematic of the cost function behaviour of these methods. The HM residue reaches quickly a constant value plateau while the three other methods decrease monotonically and slowly after a few iterations. We recall that one cannot compare the value of the residues as each method has its own normalisation.

We now turn to another target which is more difficult to invert as it is larger than the wavelength of illumination or have a complex structure. It permits to investigate the performances of the techniques in terms of reconstruction accuracy and robustness to noise.

7.3.2 Two spheres in contact

At low frequency: 5 GHz In this section we study two spheres in contact. This configuration is particularly difficult as the contact is punctual and the two spheres form an object larger than the wavelength of illumination for the frequency of 5 GHz. The CGM and PCGM fail to converge and the reconstructions presented in Fig. 7.7 correspond to those obtained for the best residue, *i. e.* the 43-th iteration and 2-th iteration, respectively. This example points out the main problem of the CGM and PCGM in which the cost function is not forced to decrease.

On the other hand, the CSI method, third line of Fig. 7.7, converges and it retrieves the shape of the two spheres. Yet, the reconstructed relative permittivity is too high, especially close to the contact point. Similarly, HM gives a map of permittivity which roughly fits the actual shape of the spheres while the permittivity at the contact point is not overestimated.

We have observed that if the frequency is increased up to 6 GHz, HM fails to find the object and sole the CSI gives a meaningful result. For frequencies above 7 GHz all methods fail.

Frequency hopping To ameliorate the reconstruction, one can use the data obtained at different frequencies and perform a frequency hopping procedure. At each frequency, the object initial estimate introduced in the inversion algorithm is given by the reconstruction obtained at the preceding (lower) frequency. Figure 7.8 presents the results obtained using frequency

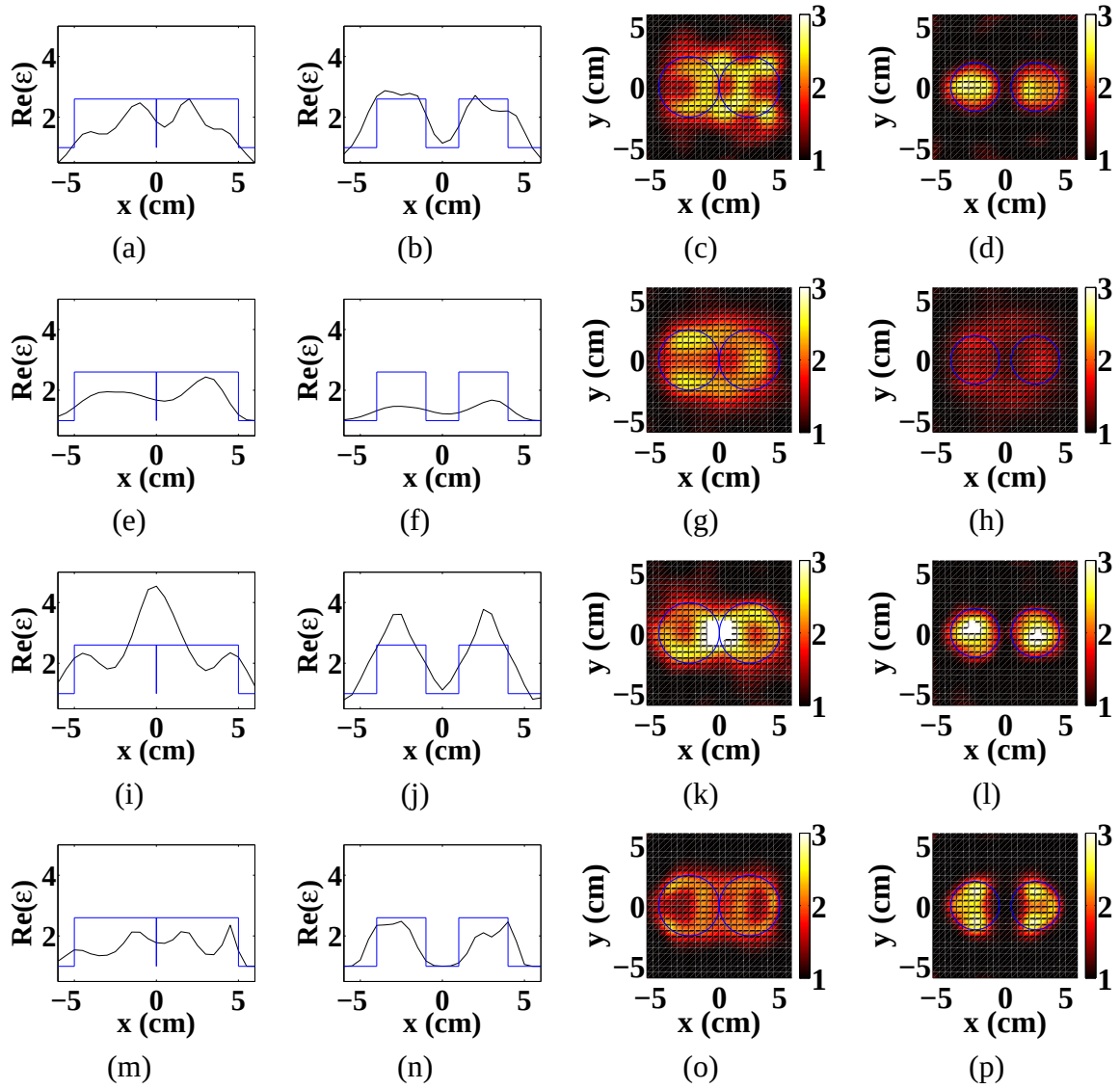

Figure 7.7: Reconstructed permittivity map of the second target (two spheres in contact) depicted in Fig. 7.3 (c) obtained with the four inversion methods from data obtained at 5 GHz. First line CGM; second line PCGM; third line CSI; Fourth line HM. First and second column: cut of the relative permittivity versus x for $y = z = 0$ and for $y = 0$ and $z = a/2$, respectively. Third and fourth column map of relative permittivity in the (x, y) plane for $z = 0$ and $z = a/2$, respectively.

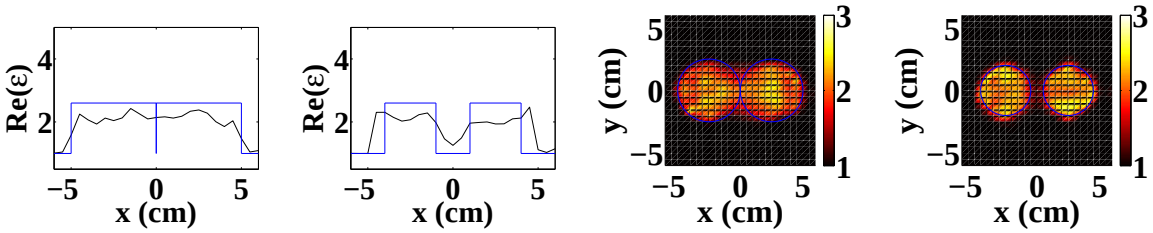

(a) (b) (c) (d)

Figure 7.8: Same as Fig. 7.7 but the reconstruction is obtained with HM *via* a frequency hopping procedure applied to the data measured at 3-4-5-6-7-8 GHz. (a) Relative permittivity versus x for $y = z = 0$ and (b) for $y = 0$ and $z = a/2$. (c) Map of relative permittivity in (x, y) plane for (c) $z = 0$ and (d) $z = a/2$.

hopping HM for the sequence 3-4-5-6-7-8 GHz. We considered only HM because CGM and PCGM failed to converge at 5 GHz and because CSI was much too long. It took 22 hours for HM to reconstruct the spheres and we had estimated the CSI time to 9 days.

We observe in Figure 7.8 that HM combined with frequency hopping gives an accurate reconstruction of the two spheres. With the good initial estimates, the convergence issue for frequencies above 6 GHz has disappeared. This example stresses the interest (in particular with respect to computation time) and the robustness of HM. Note that at 8 GHz the object size is about three wavelengths.

These two examples illustrate the results of our proposed reconstruction algorithms. This study shows that the Hybrid Gradient Method (HM) has a stability comparable to other reconstruction algorithms but that it is far quicker. This is why one can consider to apply it to optical TDM measurements, where the data-sets are huge because of the many observation directions that are obtained with the microscope objective and the camera.

7.4 Application to optical data[2]

7.4.1 Configuration and experimental set-up

Our TDM set-up is based on a reflection microscope, as seen in Fig. 7.9, in which the camera has been replaced by a wave-front sensor. A collimated laser beam (He-Ne 633 nm), controlled by a mirror mounted on step motors (Newport NSA12), illuminates the sample through an objective with $\mathrm{NA} = 0.95$ (Zeiss Epiplan-Apochromat 50$\times$) under various angles of incidence. The back-scattered field is imaged with a 290$\times$ magnification on a high-resolution wave-front sensor (Phasics SID4-HR, 400$\times$300 pixels) based on quadri-wave lateral shearing interferometry [83]. No reference path is needed and both the phase and intensity of the imaged field are retrieved with a single shot measurement.

To demonstrate the potential of our set-up for reconstructing the permittivity map of three-dimensional samples, we consider a test object made of four resin cylinders ($\varepsilon = 2$) deposited on a reflective silicon substrate $\varepsilon_1 = 15.07 + 0.18i$. This geometry corresponds to the second

[2]Images and parts of the text of this section was originally published in Y. Ruan *et al. Tomographic diffractive microscopy with a wavefront sensor*, Optics Letters, **37**, 1631-1633 (2012) [22]. My main contribution was the code of the inversion algorithm.

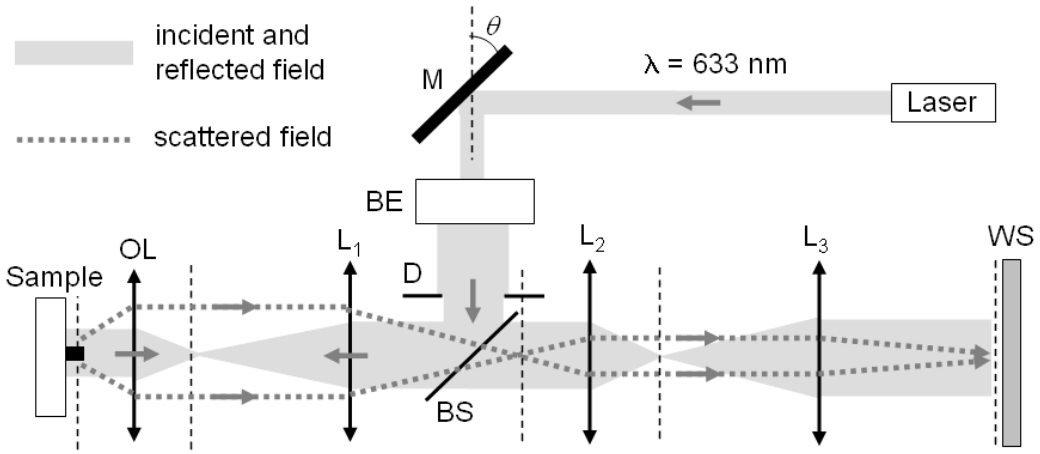

Figure 7.9: Schematic of the TDM set-up. M, rotative mirror. BE, beam expander. D, diaphragm. BS, beam-splitter. OL, objective lens. L1, tube lens. L2, L3, relay lenses ($f' = 3.5$ and 20 cm). WS, wave-front sensor.

configuration defined in Sec. 7.1. Note that Chapter 4 suggests that this configuration can have an improved axial resolution. The cylinders have a diameter close to 1 μm, a height of 120 nm, and their axes are placed at the corners of a square with 2 μm side.

A phase reference is measured on the bare substrate for each incidence prior to imaging the sample with a pixel size of 105 nm, and a single shot measurement is performed. This reference further diminishes speckle noise. We have used 6 incidences in the plane (x, z) with the electric field orthogonal to the plane of incidence (s polarisation), and 6 incidences in the plane (y, z) with the electric field parallel to the plane of incidence (p polarisation), with polar angles varying in the $[-30, 30]$ degrees range. The data have been restricted to about 2,000 scattering angles centred on the specular reflection on the substrate.

7.4.2 Results

Figure 7.10 shows the relative permittivity map reconstructed from the measured diffracted fields. (a-b) is obtained with the Hybrid gradient Method with positivity constraint. Moreover, the absorption of the resin being negligible, the permittivity is assumed positive ($\eta = 0$ in Eq. (7.28)). Fig. (7.10) (c-d) is obtained with a linear inversion technique under the renormalised Born approximation (code provided by Laurent Milord) and assuming that the sample is placed in vacuum. A vertical phase variation renders uninterpretable the real and imaginary parts of the reconstruction, so we decided to plot the modulus of the permittivity map. This implies that these images cannot be interpreted as a measure of permittivity. Figure 7.10 (a) and (d) show a longitudinal cut (y, z) in the middle of two of the cylinders, and (b) and (c) show a transverse cut (x, y) at the height where the reconstructed permittivity reaches a maximum, *i. e.* $z = 125$ nm for the non-linear inversion and $z = 53$ nm for the linear inversion.

We observe that, with the non-linear reconstruction, the transverse and axial dimensions of the resin cylinders have been correctly retrieved. The convergence of the iterative process was obtained after four iterations with a computational time of about 3 hours. The maximum reconstructed permittivity is smaller than the actual value $\varepsilon = 2$.

On the contrary, the linear reconstruction technique provides a far less accurate reconstruc-

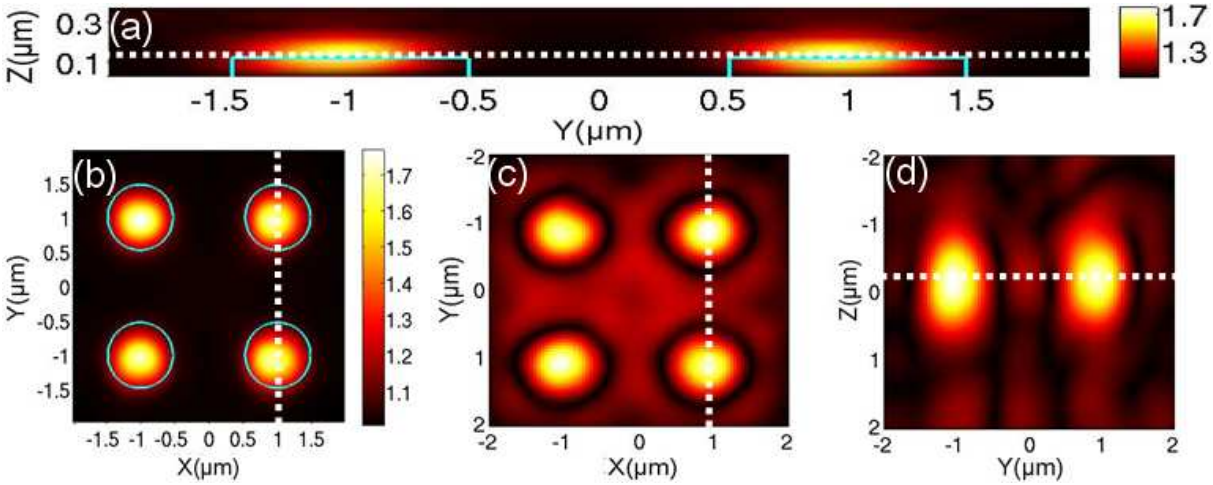

Figure 7.10: Comparison of the permittivity map retrieved with the iterative inversion algorithm (a-b) and the modulus of the 3D inverse Fourier transform of the data set (c-d). (a) longitudinal cut at $y = 1$ μm, (b) transverse cut at $z = 125$ nm (plain blue line: actual geometry of the sample). (c) transverse cut at $z = 53$ nm, (d) longitudinal cut at $y = 1$ μm. Cuts are along dashed lines.

tion, especially along the **z** axis. Indeed, the presence of the reflective surface is interpreted as a mirror object symmetrically placed along this axis. The lateral resolution is also lower, partly due to the absence of the positivity constraint and partly due to the assumption of single scattering. Moreover, reconstruction shows speckle patterns in the background due to noise in the measurements and errors on the positioning of the measured frequencies in the Fourier space. Indeed linear reconstruction implies usually several hundred of measurements [76]. Despite its lack of accuracy, linear inversion appears to be quite helpful in particular for estimating the initial size of Ω in our inversion algorithm.

This experimental result demonstrates the interest of our reconstruction technique for TDM. It can be used for various configurations and is stable for highly refracting samples. It allows the use of *a priori* constraints, like the positivity of the permittivity and the restriction of the reconstruction volume Ω. It is also more robust to noise than linear reconstructions and requires less incidences.

7.5 Conclusion

When the permittivity contrast is not small in comparison to 1, reconstructions of permittivity maps from TDM data necessitate non-linear inversion techniques that account for multiple scattering. This chapter presents the different algorithms that have been developed in the team to address this issue. They are all based on a rigorous modelling of the diffraction process.

These algorithms have been applied to data issued from the Fresnel data base, a base of micro-wave tomographic data. This study shows that the Contrast Source Inversion algorithm is the most stable for highly refracting samples, but that its computation time is prohibitive. Conversely, the Hybrid Method is slightly less stable but far quicker, allowing reconstructions from measurements taken at several wavelength.

The Hybrid Method has then been applied successfully to TDM experimental data where

the dielectric sample is deposited on a highly reflecting dioptre. This demonstrates the validity of this approach for permittivity map reconstruction in complex configurations. It also shows that a correct permittivity map can be obtained with a limited number of incidences. Further experiments are in progress for imaging more complex samples and studying the limit of resolution.

We believe that this work underlines the interest of the Hybrid Method in non-linear tomography. A possible extent would be to build a hybrid from the Contrast Source Inversion as the resulting method could be more stable for the highest diffracting samples. Another perspective is to build an algorithm inspired from the previous chapter that estimates jointly the permittivity map ε and the incident fields $\mathbf{E}_{\mathrm{inc},l}$.

Conclusion

This Ph. D. thesis was devoted to the amelioration of the resolution of stainless and fluorescence microscopies using spatially inhomogeneous illuminations. More precisely, we studied Tomographic Diffraction Microscopy (TDM), in which the sample varying permittivity diffracts the field of tilted incident plane waves, and structured illumination fluorescence microscopy, in which the sample fluorescence is excited by non-inhomogeneous light intensities.

We demonstrated numerically and experimentally that, in both cases, the axial resolution can be made equivalent to the transverse resolution just by placing the sample on a mirror. The mirror allows a quasi-isotropic observation and illumination of the sample in a much simpler way than the classical 4Pi configuration using two facing objectives. On the other hand, it requires a technique to separate the reflected waves of those reaching directly the objective. In TDM, we derived a specific numerical inversion scheme for treating the stack of holograms. We showed that, under the Born approximation, one could get a one-to-one correspondence between the object spatial frequencies within a ball of radius $4\pi/\lambda$ and the data. In confocal fluorescence microscopy, we developed a specific phase-shaping of the incident beam so that it focuses into a quasi-isotropic spot before the mirror. We believe that our approach may be useful in many microscopy configurations, like classical incoherent illumination microscopy or in techniques using non-linear light-matter interactions, such as high harmonic generation, STimulated Emission Depletion (STED) or even STochastic Optical Reconstruction Microscopy (STORM) and Photo-Activated fluorescence Light Microscopy (PALM), but also for three-dimensional patterning and reading.

The improved resolution obtained when the illumination is spatially inhomogeneous stems from the frequency mixing between the object and the probing field. The super-resolved map of the sample is numerically reconstructed from the many images obtained under different illuminations. Most of the reconstruction algorithms assume that the probing field is perfectly known. In this work, we developed inversion methods that reconstruct both the sample and the probing fields with the least possible *a priori* information on the latter. We used iterative techniques that minimise a functional over all possible sample and probe functions, measuring the distance between the actual measurements and a model. In structured illumination fluorescence microscopy, our reconstruction method (named blind-SIM) allows the use of uncontrolled or even random illumination patterns. It permits a dramatic simplification of the experimental implementation. In TDM, our reconstruction method permits to handle highly contrasted samples in which the internal field departs significantly from the incident field because of multiple scattering. Interesting perspectives opened by our algorithms are, among others, the combination of TDM with random illuminations, the adaptation to non-linear wave-matter interaction such as saturated fluorescence [142] or the development of sub-diffraction surface imaging using high frequency near-field patterns [174, 117, 175]. This last point has been initiated for grating-assisted fluorescence imaging and requires additional work for being totally operational.

In conclusion, I think that combining an accurate image-formation model to sophisticated reconstruction procedures is a promising path for improving the performances of microscopes while simplifying the experimental set-ups. With the increasing computing and algorithmic performances, this approach will certainly gain in popularity and, hopefully, attract researchers from the Inverse Problem and Signal Processing community.

Appendices

Appendix A

Demonstration of the results cited in Sec. 4.1.1.2

Et l'unique cordeau des trompettes marines
Guillaume Appolinaire

The goal of this appendix is to prove results cited in Sec. 4.1.1.2.

This starts with the system

$$\beta_{\text{inc}} - \beta = A \tag{A.1}$$
$$|\gamma_{\text{inc}} - \gamma| = B \tag{A.2}$$
$$\beta_{\text{inc}} - \beta = C \tag{A.3}$$
$$|\gamma_{\text{inc}} + \gamma| = D \tag{A.4}$$

There are bounds on the values that β, β_{inc}, γ and γ_{inc} can take. Since the wavelength does not vary and since the considered plane waves are not evanescent, we have

$$\beta^2 + \gamma^2 = k_0^2 \tag{A.5}$$
$$\beta_{\text{inc}}^2 + \gamma_{\text{inc}}^2 = k_0^2. \tag{A.6}$$

With the chosen sign convention (see Fig. 4.1), this means that

$$\gamma = \sqrt{k_0^2 - \beta^2} \tag{A.7}$$
$$\gamma_{\text{inc}} = -\sqrt{k_0^2 - \beta_{\text{inc}}^2}. \tag{A.8}$$

From Eqs. (A.1) and (A.3), one finds immediately $\boxed{A = C}$. From Eqs. (A.2) and (A.4), one has $B \geq 0$ and $D \geq 0$

Inserting Eqs. (A.7) and (A.8) in Eq. (A.2) one gets successively

$$\begin{aligned}
\sqrt{k_0^2-\beta^2}+\sqrt{k_0^2-\beta_{\rm inc}^2} &= \pm B \\
\sqrt{k_0^2-\beta_{\rm inc}^2} &= \pm B-\sqrt{k_0^2-\beta^2} \\
k_0^2-\beta_{\rm inc}^2 &= \left(\pm B-\sqrt{k_0^2-\beta^2}\right)^2 \\
k_0^2-\beta_{\rm inc}^2 &= B^2+k_0^2-\beta^2 \mp 2B\sqrt{k_0^2-\beta^2} \\
\pm 2B\sqrt{k_0^2-\beta^2} &= B^2+\beta_{\rm inc}^2-\beta^2
\end{aligned} \tag{A.9}$$

Equation (A.1) leads to $\beta_{\rm inc}^2 = (A+\beta)^2 = \beta^2+A^2+2A\beta$. Inserting this equality in Eq. (A.9), one obtains successively

$$\begin{aligned}
\pm 2B\sqrt{k_0^2-\beta^2} &= A^2+B^2+2A\beta \\
4B^2(k_0^2-\beta^2) &= (A^2+B^2+2A\beta)^2 \\
4B^2(k_0^2-\beta^2) &= (A^2+B^2)^2+4A(A^2+B^2)\beta+4A^2\beta^2
\end{aligned}$$

That means that β is a root of the second-degree equation

$$4\beta^2(A^2+B^2)-4\beta A(A^2+B^2)+(A^2+B^2)^2-4B^2k_0^2=0, \tag{A.10}$$

Its discriminant is

$$\begin{aligned}
\Delta &= 16A^2(A^2+B^2)^2-16(A^2+B^2)[(A^2+B^2)^2-4B^2k_0^2] \\
&= 16A^2(A^2+B^2)^2-16(A^2+B^2)(A^2+B^2)^2+64(A^2+B^2)B^2k_0^2 \\
&= -16B^2(A^2+B^2)^2+64(A^2+B^2)B^2k_0^2 \\
&= 16B^2(A^2+B^2)[4k_0^2-(A^2+B^2)]
\end{aligned}$$

Equation (A.10) has a solution if and only if $\Delta \geq 0$ that is equivalent to

$$\boxed{4k_0^2 \geq A^2+B^2} \tag{A.11}$$

that defines the $2k_0$-radius $z \geq 0$ half-ball.

Solutions of Eq. (A.10) are

$$\beta = -\frac{1}{2}A \pm \frac{1}{2}B\sqrt{\frac{4k_0^2}{A^2+B^2}-1}. \tag{A.12}$$

Using Eq. (A.1), we have immediately

$$\beta_{\rm inc} = \frac{1}{2}A \pm \frac{1}{2}B\sqrt{\frac{4k_0^2}{A^2+B^2}-1}. \tag{A.13}$$

The previous reasoning proves that the system composed of Eqs. (A.1) and (A.2) implies Eqs. (A.12) and (A.13). One need now to check that Eqs. (A.12) and (A.13) are solutions of

Eqs. (A.1) and (A.2). They are obviously solutions of Eq. (A.1). To prove that they are solutions of Eq. (A.2), one need to calculate γ and $\gamma_{\rm inc}$.

Equation (A.7) leads to

$$\gamma = \sqrt{k_0^2 - \beta^2} \tag{A.14}$$

$$= \sqrt{k_0^2 - \left(-\frac{1}{2}A \pm \frac{1}{2}B\sqrt{\frac{4k_0^2}{A^2+B^2} - 1}\right)^2} \tag{A.15}$$

$$= \sqrt{k_0^2 - \frac{A^2}{4} - \frac{B^2}{4}\left(\frac{4k_0^2}{A^2+B^2} - 1\right) \mp \frac{AB}{2}\sqrt{\frac{4k_0^2}{A^2+B^2} - 1}} \tag{A.16}$$

$$= \sqrt{\frac{(A^2+B^2)k_0^2}{A^2+B^2} - \frac{A^2}{4} - \frac{B^2k_0^2}{A^2+B^2} + \frac{B^2}{4} \mp \frac{AB}{2}\sqrt{\frac{4k_0^2}{A^2+B^2} - 1}} \tag{A.17}$$

$$= \sqrt{\frac{B^2}{4} - \frac{A^2}{4} + \frac{A^2k_0^2}{A^2+B^2} \mp \frac{AB}{2}\sqrt{\frac{4k_0^2}{A^2+B^2} - 1}} \tag{A.18}$$

$$= \sqrt{\frac{B^2}{4} + \frac{A^2}{4}\left(\frac{4k_0^2}{A^2+B^2} - 1\right) \mp \frac{AB}{2}\sqrt{\frac{4k_0^2}{A^2+B^2} - 1}} \tag{A.19}$$

$$= \sqrt{\left(\frac{1}{2}B \mp \frac{1}{2}|A|\sqrt{\frac{4k_0^2}{A^2+B^2} - 1}\right)^2} \tag{A.20}$$

$$= \left|\frac{1}{2}B \mp \frac{1}{2}|A|\sqrt{\frac{4k_0^2}{A^2+B^2} - 1}\right|. \tag{A.21}$$

In the same way, Eq. (A.8) leads to

$$\gamma_{\rm inc} = -\left|\frac{1}{2}B \pm \frac{1}{2}|A|\sqrt{\frac{4k_0^2}{A^2+B^2} - 1}\right|. \tag{A.22}$$

One gets Eq. (A.2), $|\gamma_{\rm inc} - \gamma| = B$ only if the formulae in the absolute values of γ and $\gamma_{\rm inc}$ have the same sign. That means

$$|A|\sqrt{\frac{4k_0^2}{A^2+B^2} - 1} \leq B \tag{A.23}$$

$$A^2\left(\frac{4k_0^2}{A^2+B^2} - 1\right) \leq B^2 \tag{A.24}$$

$$A^2\frac{4k_0^2}{A^2+B^2} \leq A^2 + B^2 \tag{A.25}$$

$$4A^2k_0^2 \leq (A^2+B^2)^2 \tag{A.26}$$

$$2k_0|A| \leq A^2 + B^2 \tag{A.27}$$

Equation $2k_0|A| = A^2 + B^2$ describes the two k_0-radius circles centred in $(k_0, 0)$ and $(-k_0, 0)$. This and Eq. (A.11) proves that (A, B) has to be in zone (1) of Fig. 4.1.

If $2k_0|A| \leq A^2 + B^2$, we get

$$\gamma = \frac{1}{2}B \mp \frac{1}{2}|A|\sqrt{\frac{4k_0^2}{A^2+B^2} - 1} \tag{A.28}$$

$$\gamma_{\text{inc}} = -\frac{1}{2}B \mp \frac{1}{2}|A|\sqrt{\frac{4k_0^2}{A^2+B^2} - 1}, \tag{A.29}$$

that verifies Eq. (A.2).

Equation (A.4) leads then to

$$\boxed{D = |A|\sqrt{\frac{4k_0^2}{A^2+B^2} - 1.}} \tag{A.30}$$

This implies that

$$D^2 = A^2\left(\frac{4k_0^2}{A^2+B^2} - 1\right) \tag{A.31}$$

$$A^2 + D^2 = A^2\frac{4k_0^2}{A^2+B^2}. \tag{A.32}$$

From Eq. (A.27),

$$\frac{1}{A^2+B^2} \leq \frac{1}{2k_0|A|} \tag{A.33}$$

$$\frac{4k_0^2A^2}{A^2+B^2} \leq \frac{4k_0^2A^2}{2k_0|A|}, \qquad \text{multiplying by } 4k_0^2A^2 \tag{A.34}$$

$$\frac{4k_0^2A^2}{A^2+B^2} \leq 2k_0|A| \tag{A.35}$$

$$A^2 + D^2 \leq 2k_0|A|, \qquad \text{using Eq. (A.32).} \tag{A.36}$$

This proves that (A, D) is in two k_0-radius circles centred in $(k_0, 0)$ and $(-k_0, 0)$, that means in zone (2) of Fig. 4.1.

Summarising, we have $C = A$, $D = |A|\sqrt{\frac{4k_0^2}{A^2+B^2} - 1}$,
(A, B) is in zone (1) ($B \geq 0$ and $2k_0|A| \leq A^2 + B^2 \leq 4k_0^2$)
and (C, D) is in zone (2) ($D \geq 0$ and $C^2 + D^2 \leq 2k_0|A|$).

Appendix B

Gradient calculation

Bergère ô tour Eiffel le troupeau des ponts bêle ce matin
Guillaume Appolinaire

B.1 Definition of a functional gradient and basic examples

This section gives the mathematical definition of a functional gradient. Deriving an example it expounds calculation rules for least-square functionals.

B.1.1 Definition

To define the gradient of a functional, one need first to define the directional derivative. F is a functional of the variable x, a function defined of the set Ω. For any function u of Ω, $\mathrm{D}_x F(u)$ the directional derivative of F along the direction u is defined as

$$\mathrm{D}_x F(u) = \lim_{t \to 0} \frac{F(x+tu) - F(x)}{t}. \tag{B.1}$$

Then g_x the gradient of F is defined as

$$g_x = \arg\max_u (\mathrm{D}_x F(u) | \|u\| = 1), \tag{B.2}$$

thus the direction were the directional derivative is the highest.

According to this definition, gradients are normalised such as $\|g_x\| = 1$. However, since in gradient type algorithms their value is always multiplied by a constant that is optimised, we most of time neglects it in the following.

B.1.2 First example

As a first example, we detail here the calculation of the gradient of the functional Eq. (6.18) defined in Sec. 6.2.3

$$F(\rho) = W \|M - (\rho I_0) * h\|_\Gamma^2. \tag{B.3}$$

$F(\rho + tu)$ is written

$$\begin{aligned} F(\rho + tu) &= W\|M - [(\rho + tu)I_0] * h\|_\Gamma^2 \\ &= W\|M - (\rho I_0) * h - t(uI_0) * h\|_\Gamma^2. \end{aligned} \tag{B.4}$$

For the sake of simplicity, one notes

$$P_0 = M - (\rho I_0) * h. \tag{B.5}$$

$F(\rho + tu)$ is then

$$\begin{aligned} F(\rho + tu) &= W\|P_0 - t(uI_0) * h\|_\Gamma^2 \\ &= W\langle P_0 - t(uI_0) * h | P_0 - t(uI_0) * h\rangle_\Gamma \\ &= W\|P_0\|_\Gamma^2 - 2tW\langle P_0 | (uI_0) * h\rangle_\Gamma + t^2 W\|(uI_0) * h\|_\Gamma^2 \\ &= F(\rho) - 2tW\langle P_0 | (uI_0) * h\rangle_\Gamma + O(t^2) \end{aligned} \tag{B.6}$$

Finally,

$$\mathrm{D}_\rho F(u) = \lim_{t\to 0} \frac{F(\rho + tu) - F(\rho)}{t} \tag{B.7}$$

$$= -2W\langle P_0 | (uI_0) * h\rangle_\Gamma \tag{B.8}$$

Assuming h as even: $\forall x \in \Omega, h(-x) = h(x)$, one has successively

$$\langle P_0 | (uI_0) * h\rangle_\Gamma = \langle P_0 * h | uI_0\rangle_\Omega \tag{B.9}$$

$$= \langle I_0(P_0 * h) | u\rangle_\Omega \tag{B.10}$$

that leads to

$$\mathrm{D}_\rho F(u) = -2W\langle I_0(P_0 * h) | u\rangle_\Omega \tag{B.11}$$

$$= \langle -2W I_0(P_0 * h) | u\rangle_\Omega \tag{B.12}$$

To find the gradient $g_\rho = \arg\max_u(\mathrm{D}_\rho F(u) | \|u\| = 1)$, one uses a theorem that states that $u = \frac{a}{\|a\|}$ maximises $(\langle a|u\rangle | \|u\| = 1)$. Thus from Eq. (B.12), one gets

$$g_\rho = \frac{-2W I_0(P_0 * h)}{\|2W I_0(P_0 * h)\|_\Omega}. \tag{B.13}$$

The normalisation factor does not matter in the Conjugate Gradient algorithm. We finally have

$$\boxed{g_\rho = -2W I_0(P_0 * h)} \tag{B.14}$$

B.1.3 Second example, functional with an auxiliary function variable

In Sec. 6.2.3 the functional Eq. (6.18) is modified for imposing the positivity of ρ. This is done in optimising an auxiliary function ξ such that $\rho = \xi^2$. The new functional is

$$F(\xi) = W\|M - (\xi^2 I_0) * h\|_\Gamma^2.$$

Of course, g^ξ can be derived using the reasoning of the previous section. However, one can avoid these tedious calculations using the chain rule

$$g_\xi = \frac{\partial \rho}{\partial \xi} g_\rho. \tag{B.15}$$

Using this relation and the definition of $\rho(\xi)$ we find

$$g_\xi = 2\xi g_\rho \tag{B.16}$$

and with Eq. (B.14) one finally gets

$$\boxed{g_\xi = -4W\xi I_0(P_0 * h).} \tag{B.17}$$

B.2 Gradients for Chap. 6

We gives here some details for the derivation of the gradients used in Chap 6.

B.2.1 Gradients for the blind-SIM algorithm without positivity

The gradients for the blind-SIM algorithm described in Sec. 6.2 derives from the functional Eq. (6.7)

$$F(\rho, (I_l)_{l=1,\dots,L-1}) = W \sum_{l=1}^{L-1} \|M_l - (\rho I_l) * h\|_\Gamma^2 + W \left\| M_L - \left[\rho \left(L I_0 - \sum_{l=1}^{L-1} I_l \right) \right] * h \right\|_\Gamma^2.$$

g_ρ is the gradient of F when the I_l are assumed constant. It is by definition

$$g_\rho = \arg\max_u (\mathrm{D}_\rho F(u) | \|u\| = 1) \quad \text{for} \tag{B.18}$$

$$\mathrm{D}_\rho F(u) = \lim_{t \to 0} \frac{F(\rho + tu, (I_l)_{l=1,\dots,L}) - F(\rho, (I_l)_{l=1,\dots,L})}{t}. \tag{B.19}$$

For the sake of simplicity, one notes

$$I_L = L I_0 - \sum_{l=1}^{L-1} I_l \tag{B.20}$$

and, for $l = 1, \dots, L$,

$$P_{0,l} = M_l - (\rho I_l) * h, \tag{B.21}$$

called the l-th residue.

$F(\rho + tu, (I_l)_{l=1,\dots,L})$ is written

$$\begin{aligned} F(\rho + tu, (I_l)_{l=1,\dots,L}) &= W \sum_{l=1}^{L} \|M_l - [(\rho + tu) I_l] * h\|_\Gamma^2 \\ &= W \sum_{l=1}^{L} \|M_l - (\rho I_l) * h - t(u I_l) * h\|_\Gamma^2. \end{aligned} \tag{B.22}$$

$F(\rho + tu)$ is then

$$\begin{aligned} F(\rho + tu, (I_l)_{l=1,\dots,L}) &= W \sum_{l=1}^{L} \|P_{0,l} - t(uI_l) * h\|_\Gamma^2 \\ &= W \sum_{l=1}^{L} \left(\|P_{0,l}\|_\Gamma^2 - 2t\langle P_{0,l} | (uI_l) * h \rangle_\Gamma + t^2 \|(uI_l) * h\|_\Gamma^2 \right) \qquad \text{(B.23)} \\ &= F(\rho) - 2tW \sum_{l=1}^{L} \langle P_{0,l} | (uI_l) * h \rangle_\Gamma + O(t^2) \qquad \text{(B.24)} \end{aligned}$$

Finally,

$$\mathrm{D}_\rho F(u) = -2W \sum_{l=1}^{L} \langle P_{0,l} | (uI_l) * h \rangle_\Gamma \qquad \text{(B.25)}$$

Assuming h as even: $\forall x \in \Omega, h(-x) = h(x)$, one has successively

$$\begin{aligned} \mathrm{D}_\rho F(u) &= -2W \sum_{l=1}^{L} \langle P_{0,l} * h | uI_l \rangle_\Omega \\ &= -2W \sum_{l=1}^{L} \langle I_l (P_{0,l} * h) | u \rangle_\Omega \\ &= \left\langle -2W \sum_{l=1}^{L} I_l (P_{0,l} * h) \middle| u \right\rangle_\Omega \qquad \text{(B.26)} \end{aligned}$$

Using the theorem of maximality cited in the previous section, one finally has

$$\boxed{g_\rho = -2W \sum_{l=1}^{L} I_l (P_{0,l} * h)} \qquad \text{(B.27)}$$

$g_{l;I}$ is the gradient of F when ρ and the $(L-2)$ other I_m are assumed constant. It is by definition

$$g_{l;I} = \arg\max_u (\mathrm{D}_{l;I} F(u) | \|u\| = 1) \quad \text{for} \qquad \text{(B.28)}$$

$$\mathrm{D}_{l;I} F(u) = \lim_{t \to 0} \frac{F(\rho, I_l + tu, (I_m)_{m=1,\dots,L-1, m \neq l}) - F(\rho, (I_m)_{m=1,\dots,L-1})}{t}. \qquad \text{(B.29)}$$

Expanding $F(\rho, I_l + tu, (I_m)_{m=1,\dots,L-1,m\neq l})$, one gets

$$\begin{aligned}
F(\rho, I_l + tu, (I_m)_{m=1,\dots,L-1,m\neq l}) &= W \sum_{m=1,m\neq l}^{L-1} \|P_{0,m}\|_\Gamma^2 + W\|M_l - (\rho(I_l + tu)) * h\|_\Gamma^2 \\
&+ W \left\| M_L - \left[\rho\left(LI_0 - \sum_{m=1,m\neq l}^{L-1} I_m - (I_l + tu)\right)\right] * h \right\|_\Gamma^2 \\
&= W \sum_{m=1,m\neq l}^{L-1} \|P_{0,m}\|_\Gamma^2 + W\|P_{0,l} - t(\rho u) * h\|_\Gamma^2 \\
&+ W\|M_L - [\rho\,(I_L - tu)] * h\|_\Gamma^2 \\
&= W \sum_{m=1,m\neq l}^{L-1} \|P_{0,m}\|_\Gamma^2 + W\|P_{0,l} - t(\rho u) * h\|_\Gamma^2 \\
&+ W\|P_{0,L} + t(\rho u) * h\|_\Gamma^2 \\
&= W \sum_{m=1}^{L} \|P_{0,m}\|_\Gamma^2 - 2tW\langle P_{0,l}|(\rho u) * h\rangle_\Gamma \\
&+ 2tW\langle P_{0,L}|(\rho u) * h\rangle_\Gamma + O(t^2) \\
&= F(\rho, (I_l)_{l=1,\dots,L-1}) - 2tW\langle P_{0,l} - P_{0,L}|(\rho u) * h\rangle_\Gamma + O(t^2).
\end{aligned}$$

This leads to

$$\begin{aligned}
\mathrm{D}_{l;I}F(u) &= -2W\langle P_{0,l} - P_{0,L}|(\rho u) * h\rangle_\Gamma \\
&= -2W\langle (P_{0,l} - P_{0,L}) * h|\rho u\rangle_\Omega \\
&= \langle -2W\rho[(P_{0,l} - P_{0,L}) * h]|u\rangle_\Omega
\end{aligned} \tag{B.30}$$

that implies

$$\boxed{g_{l;I} = -2W\rho[(P_{0,l} - P_{0,L}) * h].} \tag{B.31}$$

B.2.2 Gradients for the blind-SIM algorithm with positivity

In Sec. 6.2.2.1 the functional is modified to impose a positivity constraint using the auxiliary functions i_l and ξ defined by Eq. (6.14)

$$\begin{aligned}
I_l &= i_l^2, \\
\rho &= \xi^2.
\end{aligned}$$

The new functional is given by Eq. (6.15)

$$F(\xi, (i_l)_{l=1,\dots,L-1}) = W \sum_{l=1}^{L-1} \|M_l - (\xi^2 i_l^2) * h\|_\Gamma^2 + W \left\| M_L - \left[\xi^2\left(LI_0 - \sum_{l=1}^{L-1} i_l^2\right)\right] * h \right\|_\Gamma^2.$$

The gradients can be immediately derived from the previous section using the chain rule

$$g^{\xi} = -4W \sum_{l=1}^{L} \xi i_l^2 (P_{0,l} * h) \tag{B.32}$$

$$g_l^i = -4W\xi^2 i_l [(P_{0,l} - P_{0,L}) * h]. \tag{B.33}$$

B.2.3 Gradients for the filtered blind-SIM

In Sec. 6.4.3 an algorithm is described, minimising the functional Eq. (6.7)

$$F(\rho, (I_l)_{l=1,\ldots,L-1}) = W \sum_{l=1}^{L-1} \|M_l - (\rho I_l) * h\|_\Gamma^2 + W \left\| M_L - \left[\rho \left(L I_0 - \sum_{l=1}^{L-1} I_l \right) \right] * h \right\|_\Gamma^2$$

for $\rho \in \Omega$ and $I_l \in \tilde{\mathcal{S}}$, $\tilde{\mathcal{S}}$ being the set of real functions with value in Ω whose Fourier transform has its support included in $\mathcal{S}$, a sub-set of $\mathbb{R}^2$.

This functional is the same as the one of Sec. B.2.1. The only modification is the set in which I_l are estimated. This does not modify the calculations leading to g_ρ in Eq. (B.27). However, this changes the gradients $g_{l;I}$. As the functional is unchanged, Eq. (B.30) still holds

$$\mathrm{D}_{l;I} F(u) = \langle -2W\rho[(P_{0,l} - P_{0,L}) * h] | u \rangle_\Omega.$$

$g_{l;I}$ is the direction that minimises $\mathrm{D}_{l;I} F(u)$ inside $\tilde{\mathcal{S}}$. Formally it is defined, noting $v = -2W\rho[(P_{0,l} - P_{0,L}) * h]$, by

$$\begin{aligned} g_{l;I} &= \arg\max_u (\mathrm{D}_{l;I} F(u) | \|u\|_\Omega = 1, u \in \tilde{\mathcal{S}}) \\ &= \arg\max_u (\langle v | u \rangle_\Omega | \|u\|_\Omega = 1, u \in \tilde{\mathcal{S}}). \end{aligned} \tag{B.34}$$

The condition of membership of $\tilde{\mathcal{S}}$ hinders the use of the maximality theorem. One has to find an expression of $\mathrm{D}_{l;I} F(u)$ that includes this condition.

Defining f the function whose Fourier transform verifies

$$\tilde{f}(\mathbf{k}) \begin{cases} 1 & \text{if } \mathbf{k} \in \mathcal{S} \\ 0 & \text{otherwise,} \end{cases} \tag{B.35}$$

one has $\forall u \in \tilde{\mathcal{S}}, \tilde{f}\tilde{u} = \tilde{u}$ thus $\forall u \in \tilde{\mathcal{S}}, u * f = u$ and $\forall u \in \Omega, f * u \in \tilde{\mathcal{S}}$. Then, assuming f as even, since $u \in \tilde{\mathcal{S}}$,

$$\mathrm{D}_{l;I} F(u) = \langle v | u * f \rangle_\Omega \tag{B.36}$$

$$= \langle v * f | u \rangle_\Omega. \tag{B.37}$$

$\dfrac{v * f}{\|v * f\|}$ maximises $(\langle v * f | u \rangle) | \|u\| = 1)$ and $v * f \in \tilde{\mathcal{S}}$, thus

$$\frac{v * f}{\|v * f\|} = \arg\max_u (\mathrm{D}_{l;I} F(u) | \|u\|_\Omega = 1, u \in \tilde{\mathcal{S}}).$$

This proves that

$$\boxed{g_{l;I} = -2W \Big(\rho[(P_{0,l} - P_{0,L}) * h] \Big) * f.} \tag{B.38}$$

B.3 Gradients for Chap. 7

We give here some details for the derivation of the gradients used in Chap 7. The calculation techniques expounded in the previous section still applies. One need, however, to keep in mind that now the variables are complex numbers and the fields $\mathbf{E}_l$ and the sources $\mathbf{P}_l$ are vectorial functions of space.

B.3.1 Gradients for the Hybrid Gradient Method

The gradients used in the Hybrid Gradient Method described in Sec. 7.2.2.2 derives from the functional Eq. (7.18)

$$F_n(\chi,(\mathbf{E}_l)_{l=1,\dots,L}) = W_\Gamma \sum_{l=1}^{L} \|\mathbf{E}_{\mathrm{d},l} - \bar{\mathbf{B}}\chi\mathbf{E}_l\|_\Gamma^2 + W_\Omega \sum_{l=1}^{L} \|\mathbf{E}_l - \mathbf{E}_{\mathrm{inc},l} - \bar{\mathbf{A}}\chi\mathbf{E}_l\|_\Omega^2.$$

g_χ is the gradient of F when the $\mathbf{E}_l$ are constant. It is by definition

$$g_\chi = \arg\max_u (\mathrm{D}_\chi F(u) | \|u\| = 1) \quad \text{for} \tag{B.39}$$

$$\mathrm{D}_\chi F(u) = \lim_{t\to 0} \frac{F(\chi+tu,(\mathbf{E}_l)_{l=1,\dots,L}) - F(\chi,(\mathbf{E}_l)_{l=1,\dots,L})}{t}. \tag{B.40}$$

Expansion of $F(\chi+tu,(\mathbf{E}_l)_{l=1,\dots,L})$ gives

$$F(\chi+tu,(\mathbf{E}_l)_{l=1,\dots,L}) = W_\Gamma \sum_{l=1}^{L} \|\mathbf{E}_{\mathrm{d},l} - \bar{\mathbf{B}}(\chi+tu)\mathbf{E}_l\|_\Gamma^2 + W_\Omega \sum_{l=1}^{L} \|\mathbf{E}_l - \mathbf{E}_{\mathrm{inc},l} - \bar{\mathbf{A}}(\chi+tu)\mathbf{E}_l\|_\Omega^2.$$

For the sake of simplicity, one notes

$$\mathbf{P}_{0,l} = \mathbf{E}_{\mathrm{d},l} - \bar{\mathbf{B}}\chi\mathbf{E}_l \tag{B.41}$$

$$\mathbf{Q}_{0,l} = \mathbf{E}_l - \mathbf{E}_{\mathrm{inc},l} - \bar{\mathbf{A}}\chi\mathbf{E}_l \tag{B.42}$$

called the l-th residues.

$F(\chi+tu,(\mathbf{E}_l)_{l=1,\dots,L})$ can then be written

$$\begin{aligned} F(\chi+tu,(\mathbf{E}_l)_{l=1,\dots,L}) &= W_\Gamma \sum_{l=1}^{L} \|\mathbf{P}_{0,l} - t\bar{\mathbf{B}}u\mathbf{E}_l\|_\Gamma^2 + W_\Omega \sum_{l=1}^{L} \|\mathbf{Q}_{0,l} - t\bar{\mathbf{A}}u\mathbf{E}_l\|_\Omega^2 \\ &= F(\chi,(\mathbf{E}_l)_{l=1,\dots,L}) + \sum_{l=1}^{L} [-2tW_\Gamma \Re e\langle \mathbf{P}_{0,l} | \bar{\mathbf{B}}u\mathbf{E}_l\rangle_\Gamma \\ &\quad - 2tW_\Omega \Re e\langle \mathbf{Q}_{0,l} | \bar{\mathbf{A}}u\mathbf{E}_l\rangle_\Omega] + O(t^2). \end{aligned}$$

Thus the functional derivative $\mathrm{D}_\chi F(u)$ is

$$\mathrm{D}_\chi F(u) = -2\sum_{l=1}^{L} \big(W_\Gamma \Re e\langle \mathbf{P}_{0,l} | \bar{\mathbf{B}}u\mathbf{E}_l\rangle_\Gamma + W_\Omega \Re e\langle \mathbf{Q}_{0,l} | \bar{\mathbf{A}}u\mathbf{E}_l\rangle_\Omega \big).$$

$\bar{\mathbf{B}}^\dagger$ and $\bar{\mathbf{A}}^\dagger$ being the adjoint of respectively $\bar{\mathbf{B}}$ and $\bar{\mathbf{A}}$, this becomes

$$\mathrm{D}_\chi F(u) = -2\sum_{l=1}^{L}\big(W_\Gamma \Re e\langle \bar{\mathbf{B}}^\dagger \mathbf{P}_{0,l}|u\mathbf{E}_l\rangle_\Omega + W_\Omega \Re e\langle \bar{\mathbf{A}}^\dagger \mathbf{Q}_{0,l}|u\mathbf{E}_l\rangle_\Omega\big).$$

u is scalar when $\mathbf{E}_l$ is vectorial. A specific care is needed at this step. Indeed

$$\begin{aligned}\langle \bar{\mathbf{B}}^\dagger \mathbf{P}_{0,l}|u\mathbf{E}_l\rangle_\Omega &= \int_\Omega \left(\bar{\mathbf{B}}^\dagger \mathbf{P}_{0,l}\right)^* .(u\mathbf{E}_l)\mathrm{d}\mathbf{r} \\ &= \int_\Omega \left(\mathbf{E}_l^* .\bar{\mathbf{B}}^\dagger \mathbf{P}_{0,l}\right)^* u\mathrm{d}\mathbf{r} \\ &= \langle \mathbf{E}_l^* .\bar{\mathbf{B}}^\dagger \mathbf{P}_{0,l}|u\rangle_\Omega.\end{aligned}$$

This leads to

$$\begin{aligned}\mathrm{D}_\chi F(u) &= -2\sum_{l=1}^{L}\big(W_\Gamma \Re e\langle \mathbf{E}_l^* .\bar{\mathbf{B}}^\dagger \mathbf{P}_{0,l}|u\rangle_\Omega + W_\Omega \Re e\langle \mathbf{E}_l^* .\bar{\mathbf{A}}^\dagger \mathbf{Q}_{0,l}|u\rangle_\Omega\big) \\ \mathrm{D}_\chi F(u) &= \Re e\left\langle -2\sum_{l=1}^{L}(W_\Gamma \mathbf{E}_l^* .\bar{\mathbf{B}}^\dagger \mathbf{P}_{0,l} + W_\Omega \mathbf{E}_l^* .\bar{\mathbf{A}}^\dagger \mathbf{Q}_{0,l})\middle| u\right\rangle_\Omega .\end{aligned}$$

We finally have

$$\boxed{g_\chi = -2\sum_{l=1}^{L}(W_\Gamma \mathbf{E}_l^* .\bar{\mathbf{B}}^\dagger \mathbf{P}_{0,l} + W_\Omega \mathbf{E}_l^* .\bar{\mathbf{A}}^\dagger \mathbf{Q}_{0,l}).} \tag{B.43}$$

The positivity constraint is imposed by using two real auxiliary functions such that, from Eq. (7.28)

$$\chi(\xi,\eta) = 1 + \xi^2 + i\eta^2 - \varepsilon_b$$

Gradients along these auxiliary functions can be found using the chain rule

$$g_\xi = \Re e\left(g_\chi \frac{\partial \chi}{\partial \xi}\right) \tag{B.44}$$

$$g_\eta = \Re e\left(g_\chi \frac{\partial \chi}{\partial \eta}\right) \tag{B.45}$$

This leads to

$$g_\xi = -4\xi \Re e\left(\sum_{l=1}^{L}(W_\Gamma \mathbf{E}_l^* .\bar{\mathbf{B}}^\dagger \mathbf{P}_{0,l} + W_\Omega \mathbf{E}_l^* .\bar{\mathbf{A}}^\dagger \mathbf{Q}_{0,l})\right) \tag{B.46}$$

$$g_\eta = 4\eta \Im m\left(\sum_{l=1}^{L}(W_\Gamma \mathbf{E}_l^* .\bar{\mathbf{B}}^\dagger \mathbf{P}_{0,l} + W_\Omega \mathbf{E}_l^* .\bar{\mathbf{A}}^\dagger \mathbf{Q}_{0,l})\right). \tag{B.47}$$

$\mathbf{g}_{l;\mathbf{E}}$ is the gradient of F assuming χ and the $L-1$ other fields $(\mathbf{E}_m)_{m=1,\ldots,L,m\neq l}$ as fixed. It is equal to

$$\mathbf{g}_{l;\mathbf{E}} = \arg\max_{\mathbf{u}}(\mathrm{D}_{l;\mathbf{E}} F(\mathbf{u})|\|\mathbf{u}\| = 1) \quad \text{for} \tag{B.48}$$

$$\mathrm{D}_{l;\mathbf{E}} F(\mathbf{u}) = \lim_{t\to 0}\frac{F(\rho, \mathbf{E}_l + t\mathbf{u}, (\mathbf{E}_m)_{m=1,\ldots,L,m\neq l}) - F(\rho,(\mathbf{E}_m)_{m=1,\ldots,L})}{t}. \tag{B.49}$$

Expansion of $F(\rho, \mathbf{E}_l + t\mathbf{u}, (\mathbf{E}_m)_{m=1,\dots,L,m\neq l})$ gives

$$\begin{aligned}
F(\rho, \mathbf{E}_l + t\mathbf{u}, (\mathbf{E}_m)_{m=1,\dots,L,m\neq l}) &= W_\Gamma \sum_{m=1,m\neq l}^{L} \|\mathbf{P}_{0,m}\|_\Gamma^2 + W_\Omega \sum_{m=1,m\neq l}^{L} \|\mathbf{Q}_{0,m}\|_\Omega^2 \\
&+ W_\Gamma \|\mathbf{E}_{\mathrm{d},l} - \bar{\mathbf{B}}\chi(\mathbf{E}_l + t\mathbf{u})\|_\Gamma^2 \\
&+ W_\Omega \|(\mathbf{E}_l + t\mathbf{u}) - \mathbf{E}_{\mathrm{inc},l} - \bar{\mathbf{A}}\chi(\mathbf{E}_l + t\mathbf{u})\|_\Omega^2 \\
&= W_\Gamma \sum_{m=1,m\neq l}^{L} \|\mathbf{P}_{0,m}\|_\Gamma^2 + W_\Omega \sum_{m=1,m\neq l}^{L} \|\mathbf{Q}_{0,m}\|_\Omega^2 \\
&+ W_\Gamma \|\mathbf{P}_{0,l} - t\bar{\mathbf{B}}\chi\mathbf{u}\|_\Gamma^2 + W_\Omega \|\mathbf{Q}_{0,l} + t(\mathbf{u} - \bar{\mathbf{A}}\chi\mathbf{u})\|_\Omega^2 \\
&= F(\rho, (\mathbf{E}_m)_{m=1,\dots,L}) - 2tW_\Gamma \Re e\langle \mathbf{P}_{0,l} | \bar{\mathbf{B}}\chi\mathbf{u}\rangle_\Gamma \\
&+ 2tW_\Omega \Re e\langle \mathbf{Q}_{0,l} | \mathbf{u} - \bar{\mathbf{A}}\chi\mathbf{u}\rangle_\Omega.
\end{aligned}$$

Thus the descent directions are successively

$$\begin{aligned}
\mathrm{D}_{l,\mathbf{E}} F(\mathbf{u}) &= -2W_\Gamma \Re e\langle \mathbf{P}_{0,l} | \bar{\mathbf{B}}\chi\mathbf{u}\rangle_\Gamma + 2W_\Omega \Re e\langle \mathbf{Q}_{0,l} | \mathbf{u} - \bar{\mathbf{A}}\chi\mathbf{u}\rangle_\Omega \\
&= -2W_\Gamma \Re e\langle \chi^* \bar{\mathbf{B}}^\dagger \mathbf{P}_{0,l} | \mathbf{u}\rangle_\Omega + 2W_\Omega \Re e\langle \mathbf{Q}_{0,l} | \mathbf{u}\rangle_\Omega - 2W_\Omega \Re e\langle \chi^* \bar{\mathbf{A}}^\dagger \mathbf{Q}_{0,l} | \mathbf{u}\rangle_\Omega \\
&= \Re e\langle -2W_\Gamma \chi^* \bar{\mathbf{B}}^\dagger \mathbf{P}_{0,l} + 2W_\Omega \left(\mathbf{Q}_{0,l} - \chi^* \bar{\mathbf{A}}^\dagger \mathbf{Q}_{0,l}\right) | \mathbf{u}\rangle_\Omega.
\end{aligned}$$

We finally have

$$\boxed{\mathbf{g}_{l;\mathbf{E}} = -2W_\Gamma \chi^* \bar{\mathbf{B}}^\dagger \mathbf{P}_{0,l} + 2W_\Omega \left(\mathbf{Q}_{0,l} - \chi^* \bar{\mathbf{A}}^\dagger \mathbf{Q}_{0,l}\right).} \tag{B.50}$$

B.3.2 Gradients for the Contrast Source Method

The gradients used in the Hybrid Gradient Method described in Sec. 7.2.2.3 derives from the functional Eq. (7.24)

$$F(\chi, (\mathbf{P}_l)_{l=1,\dots,L}) = W_\Gamma \sum_{l=1}^{L} \|\mathbf{E}_{\mathrm{d},l} - \bar{\mathbf{B}}\mathbf{P}_l\|_\Gamma^2 + W'_\Omega \sum_{l=1}^{L} \|\mathbf{P}_l - \chi\mathbf{E}_{\mathrm{inc},l} - \chi\bar{\mathbf{A}}\mathbf{P}_l\|_\Omega^2.$$

This functional is composed on two terms. The first one does not depend on χ and has thus no influence on g_χ.

The residues are redefined as

$$\mathbf{P}_{0,l} = \mathbf{E}_{\mathrm{d},l} - \bar{\mathbf{B}}\mathbf{P}_l \tag{B.51}$$

$$\mathbf{Q}_{0,l} = \mathbf{P}_l - \chi\mathbf{E}_{\mathrm{inc},l} - \chi\bar{\mathbf{A}}\mathbf{P}_l. \tag{B.52}$$

Derivation of g_χ starts with the expansion of

$$\begin{aligned}
F(\chi + tu, (\mathbf{P}_l)_{l=1,\dots,L}) &= W_\Gamma \sum_{l=1}^{L} \|\mathbf{P}_{0,l}\|_\Gamma^2 + W'_\Omega \sum_{l=1}^{L} \|\mathbf{P}_l - (\chi + tu)\mathbf{E}_{\mathrm{inc},l} - (\chi + tu)\bar{\mathbf{A}}\mathbf{P}_l\|_\Omega^2 \\
&= W_\Gamma \sum_{l=1}^{L} \|\mathbf{P}_{0,l}\|_\Gamma^2 + W'_\Omega \sum_{l=1}^{L} \|\mathbf{Q}_{0,l} - tu(\mathbf{E}_{\mathrm{inc},l} + \bar{\mathbf{A}}\mathbf{P}_l)\|_\Omega^2 \\
&= F(\chi, (\mathbf{P}_l)_{l=1,\dots,L}) - 2tW'_\Omega \Re e\langle \mathbf{Q}_{0,l} | u(\mathbf{E}_{\mathrm{inc},l} + \bar{\mathbf{A}}\mathbf{P}_l)\rangle_\Omega.
\end{aligned}$$

This leads to the direction derivative

$$\begin{aligned} \mathrm{D}_{\chi}F(u) &= -2W'_{\Omega}\Re e\langle \mathbf{Q}_{0,l}|u(\mathbf{E}_{\mathrm{inc},l}+\bar{\mathbf{A}}\mathbf{P}_l)\rangle_{\Omega} \\ &= -2W'_{\Omega}\Re e\langle (\mathbf{E}_{\mathrm{inc},l}+\bar{\mathbf{A}}\mathbf{P}_l)^*.\mathbf{Q}_{0,l}|u\rangle_{\Omega} \end{aligned}$$

that leads to the gradient

$$\boxed{g_{\chi} = -2W'_{\Omega}(\mathbf{E}_{\mathrm{inc},l}+\bar{\mathbf{A}}\mathbf{P}_l)^*.\mathbf{Q}_{0,l}.} \tag{B.53}$$

$\mathbf{g}_{l;\mathbf{P}}$ is the gradient of F assuming χ and the $L-1$ other fields $(\mathbf{P}_m)_{m=1,\ldots,L,m\neq l}$ as fixed. It is equal to

$$\mathbf{g}_{l;\mathbf{P}} = \arg\max_{\mathbf{u}}(\mathrm{D}_{l;\mathbf{P}}F(\mathbf{u})|\|\mathbf{u}\|=1) \quad \text{for} \tag{B.54}$$

$$\mathrm{D}_{l;\mathbf{P}}F(\mathbf{u}) = \lim_{t\to 0}\frac{F(\rho,\mathbf{P}_l+t\mathbf{u},(\mathbf{P}_m)_{m=1,\ldots,L,m\neq l})-F(\rho,(\mathbf{P}_m)_{m=1,\ldots,L})}{t}. \tag{B.55}$$

For obtaining the gradient along the source functions $\mathbf{g}_{l;\mathbf{P}}$, one need to expand

$$\begin{aligned} F(\rho,\mathbf{P}_l+t\mathbf{u},(\mathbf{P}_m)_{m=1,\ldots,L,m\neq l}) &= W_{\Gamma}\sum_{m=1,m\neq l}^{L}\|\mathbf{P}_{0,m}\|^2_{\Gamma}+W'_{\Omega}\sum_{m=1,m\neq l}^{L}\|\mathbf{Q}_{0,m}\|^2_{\Omega} \\ &+ W_{\Gamma}\|\mathbf{E}_{\mathrm{d},l}-\bar{\mathbf{B}}(\mathbf{P}_l+t\mathbf{u})\|^2_{\Gamma} \\ &+ W'_{\Omega}\|(\mathbf{P}_l+t\mathbf{u})-\chi\mathbf{E}_{\mathrm{inc},l}-\chi\bar{\mathbf{A}}(\mathbf{P}_l+t\mathbf{u})\|^2_{\Omega} \\ &= W_{\Gamma}\sum_{m=1,m\neq l}^{L}\|\mathbf{P}_{0,m}\|^2_{\Gamma}+W'_{\Omega}\sum_{m=1,m\neq l}^{L}\|\mathbf{Q}_{0,m}\|^2_{\Omega} \\ &+ W_{\Gamma}\|\mathbf{P}_{0,l}-t\bar{\mathbf{B}}\mathbf{u}\|^2_{\Gamma}+W'_{\Omega}\|\mathbf{Q}_{0,l}+t\mathbf{u}-t\chi\bar{\mathbf{A}}\mathbf{u}\|^2_{\Omega} \\ &= F(\chi,(\mathbf{P}_m)_{m=1,\ldots,L})-2tW_{\Gamma}\Re e\langle\mathbf{P}_{0,l}|\bar{\mathbf{B}}\mathbf{u}\rangle_{\Gamma} \\ &+ 2tW'_{\Omega}\Re e\langle\mathbf{Q}_{0,l}|\mathbf{u}-\chi\bar{\mathbf{A}}\mathbf{u}\rangle_{\Omega}. \end{aligned}$$

The directional derivatives are thus

$$\begin{aligned} \mathrm{D}_{l;\mathbf{P}}F(\mathbf{u}) &= -2W_{\Gamma}\Re e\langle\mathbf{P}_{0,l}|\bar{\mathbf{B}}\mathbf{u}\rangle_{\Gamma}+2W'_{\Omega}\Re e\langle\mathbf{Q}_{0,l}|\mathbf{u}\rangle_{\Omega}-2W'_{\Omega}\Re e\langle\mathbf{Q}_{0,l}|\chi\bar{\mathbf{A}}\mathbf{u}\rangle_{\Omega} \\ &= -2W_{\Gamma}\Re e\langle\bar{\mathbf{B}}^{\dagger}\mathbf{P}_{0,l}|\mathbf{u}\rangle_{\Omega}+2W'_{\Omega}\Re e\langle\mathbf{Q}_{0,l}|\mathbf{u}\rangle_{\Omega}-2W'_{\Omega}\Re e\langle\bar{\mathbf{A}}^{\dagger}(\chi^*\mathbf{Q}_{0,l})|\mathbf{u}\rangle_{\Omega} \end{aligned}$$

that leads to the gradients

$$\boxed{\mathbf{g}_{l;\mathbf{P}} = -2W_{\Gamma}\bar{\mathbf{B}}^{\dagger}\mathbf{P}_{0,l}+2W'_{\Omega}\left(\mathbf{Q}_{0,l}-\bar{\mathbf{A}}^{\dagger}(\chi^*\mathbf{Q}_{0,l})\right).} \tag{B.56}$$

Bibliography

[1] J. D. Jackson, *Classical Electrodynamics*, 2nd ed. (Wiley, 1975).

[2] M. Born and E. Wolf, *Principles of Optics (7th Expanded edition)* (Cambridge University Press, 2001).

[3] M. Minsky, "Microscopy Apparatus, US patent 3,013,467," (Dec. 19, 1961 (Filed Nov. 7, 1957)).

[4] E. Mudry, P. C. Chaumet, K. Belkebir, G. Maire, and A. Sentenac, "Mirror-assisted tomographic diffractive microscopy with isotropic resolution," Opt. Lett. **35**(11), 1857–1859 (2010).

[5] S. Hell and E. Stelzer, "Properties of a 4pi confocal microscope," J. Opt. Soc. Am. A **9**, 2159–2166 (1992).

[6] E. Mudry, E. Le Moal, P. Ferrand, P. C. Chaumet, and A. Sentenac, "Isotropic Diffraction-Limited Focusing Using a Single Objective Lens," Phys. Rev. Lett. **105**, 203,903 (2010).

[7] E. L. Moal, E. Mudry, P. C. Chaumet, P. Ferrand, and A. Sentenac, "Isotropic single-objective microscopy: theory and experiment," J. Opt. Soc. Am. A **28**(8), 1586–1594 (2011).

[8] E. L. Moal, E. Mudry, P. C. Chaumet, P. Ferrand, and A. Sentenac, "Two-photon fluorescence isotropic-single-objective microscopy," Opt. Lett. **37**(1), 85–87 (2012).

[9] A. Sentenac and P. C. Chaumet, "Subdiffraction Light Focusing on a Grating Substrate," Phys. Rev. Lett. **101**, 013,901 (2008).

[10] R. Carminati, R. Pierrat, J. de Rosny, and M. Fink, "Theory of the time reversal cavity for electromagnetic fields," Opt. Lett. **32**, 3107–3109 (2007).

[11] W. Lukosz, "Optical Systems with Resolving Powers Exceeding the Classical Limit," J. Opt. Soc. Am. **56**(11), 1463–1471 (1966).

[12] M. G. L. Gustafsson, "Surpassing the lateral resolution limit by a factor of two using structured illumination microscopy," J. Micr. **198**(2), 82–87 (2000).

[13] R. Heintzmann and C. G. Cremer, "Laterally modulated excitation microscopy: improvement of resolution by using a diffraction grating," in *Optical Biopsies and Microscopic Techniques III*, I. J. Bigio, H. Schneckenburger, J. Slavik, K. Svanberg, and P. M. Viallet, eds., vol. 3568, pp. 185–196 (SPIE, 1999).

[14] E. Mudry, K. Belkebir, J. Girard, J. Savatier, E. L. Moal, C. Nicoletti, M. Allain, and A. Sentenac, "Structured illumination microscopy using unknown speckle patterns," Nature Photon. **6**(5), 312–315 (2012).

[15] M. R. Hestenes and E. Stiefel, "Methods of Conjugate Gradients for Solving Linear Systems," J. Res. Nat. Bur. Stand. **49**(6), 409–436 (1952).

[16] W. H. Press, B. P. Flannery, S. A. Teukolski, and W. T. Vetterling, *Numerical recipes. The art of scientific computing* (Cambridge University Press, 1986).

[17] J. J. Goodman and P. J. Flatau, "Application of fast-Fourier-transform techniques to the discrete-dipole approximation," Opt. Lett. **16**, 1198–1200 (2002).

[18] P. C. Chaumet and A. Rahmani, "Efficient iterative solution of the discrete dipole approximation for magneto-dielectric scatterers ," Opt. Lett. **34**, 917–919 (2009).

[19] K. Belkebir and A. G. Tijhuis, "Modified^2 gradient method and modified Born method for solving a two-dimensional inverse scattering problem," Inverse Probl. **17**(6), 1671–1688 (2001).

[20] P. M. van den Berg and R. E. Kleinman, "A contrast source inversion method," Inverse Probl. **13**, 1607–1620 (1997).

[21] E. Mudry, P. C. Chaumet, K. Belkebir, and A. Sentenac, "Electromagnetic wave imaging of three-dimensional targets using a hybrid iterative inversion method," Inverse Probl. **28**(6), 065,007 (2012).

[22] Y. Ruan, P. Bon, E. Mudry, G. Maire, P. C. Chaumet, H. Giovannini, K. Belkebir, A. Talneau, B. Wattellier, S. Monneret, and A. Sentenac, "Tomographic diffractive microscopy with a wavefront sensor," Opt. Lett. **37**(10), 1631–1633 (2012).

[23] J. Gelles, B. Schnapp, and M. Sheetz, "Tracking kinesin-driven movements with nanometer-scale precision," Nature **331**(6155), 450–453 (1988).

[24] S. W. Hell and J. Wichmann, "Breaking the diffraction resolution limit by stimulated emission: stimulated-emission-depletion fluorescence microscopy," Opt. Lett. **19**(11), 780–782 (1994).

[25] K. Fujita, M. Kobayashi, S. Kawano, M. Yamanaka, and S. Kawata, "High-Resolution Confocal Microscopy by Saturated Excitation of Fluorescence," Phys. Rev. Lett. **99**, 228,105 (2007).

[26] E. H. Synge, "A suggested method for extending microscopic resolution into the ultramicroscopic region," Philosophical Magazine Series 7 **6**(35), 356–362 (1928).

[27] A. Lewis, M. Isaacson, A. Harootunian, and A. Muray, "Development of a 500 Å spatial resolution light microscope: I. light is efficiently transmitted through $\lambda/16$ diameter apertures," Ultramicroscopy **13**(3), 227 – 231 (1984).

[28] J. C. Maxwell, "On the general laws of optical instruments," Quart. J. Pure Appl. Maths. **2**, 233–246 (1858).

[29] A. Diaspro, *Confocal and two-photon microscopy* (Wiley-Liss, 2002).

[30] J. W. Goodman, *Introduction to Fourier Optics (3rd ed.)* (Roberts & Company Publishers, 2004).

[31] E. Botcherby, R. Juškaitis, M. Booth, and T. Wilson, "An optical technique for remote focusing in microscopy," Optics Communications **281**(4), 880 – 887 (2008).

[32] A. J. den Dekker and A. van den Bos, "Resolution: a survey," J. Opt. Soc. Am. A **14**(3), 547–557 (1997).

[33] M. A. A. Neil, R. Juškaitis, and T. Wilson, "Method of obtaining optical sectioning by using structured light in a conventional microscope," Opt. Lett. **22**(24), 1905–1907 (1997).

[34] A. A. Michelson, *Studies in Optics* (Univ. of Chicago Press, 1927).

[35] F. Zernike, "Phase contrast, a new method for the microscopic observation of transparent objects," Physica **9**(7), 686 – 698 (1942).

[36] F. Zernike, "Phase contrast, a new method for the microscopic observation of transparent objects part II," Physica **9**(10), 974 – 986 (1942).

[37] G. Nomarski, "Interferential polarizing device for study of phase objects, US patent 2,924,142," (Feb. 02, 1960 (Filed May 11, 1953)).

[38] E. Stelzer, "Contrast, resolution, pixelation, dynamic range and signal-to-noise ratio: fundamental limits to resolution in fluorescence light microscopy," J. Microsc. (Oxf.) **189**(Part 1), 15–24 (1998).

[39] A. Köhler, "Ein neues Beleuchtungsverfahren für mikrophotographische Zwecke," Z Wiss Mikrosk **10**(4), 433–440 (1893).

[40] G. T. D. Francia, "Degrees of Freedom of an Image," J. Opt. Soc. Am. **59**(7), 799–803 (1969).

[41] E. D. Micheli and G. A. Viano, "Inverse optical imaging viewed as a backward channel communication problem," J. Opt. Soc. Am. A **26**(6), 1393–1402 (2009).

[42] R. Pierri and F. Soldovieri, "On the information content of the radiated fields in the near zone over bounded domains," Inverse Probl. **14**(2), 321 (1998).

[43] R. Piestun and D. A. B. Miller, "Electromagnetic degrees of freedom of an optical system," J. Opt. Soc. Am. A **17**(5), 892–902 (2000).

[44] F. M. Huang and N. I. Zheludev, "Super-Resolution without Evanescent Waves," Nano Letters **9**(3), 1249–1254 (2009).

[45] H. J. Hyvärinen, S. Rehman, J. Tervo, J. Turunen, and C. J. R. Sheppard, "Limitations of superoscillation filters in microscopy applications," Opt. Lett. **37**(5), 903–905 (2012).

[46] P. J. Sementilli, B. R. Hunt, and M. S. Nadar, "Analysis of the limit to superresolution in incoherent imaging," J. Opt. Soc. Am. A **10**(11), 2265–2276 (1993).

[47] R. Heintzmann, "Estimating missing information by maximum likelihood deconvolution," Micron **38**(2), 136 – 144 (2007).

[48] A. Gur, D. Fixler, V. Micó, J. Garcia, and Z. Zalevsky, "Linear optics based nanoscopy," Opt. Express **18**(21), 22,222–22,231 (2010).

[49] B. Saleh, "A priori information and the degrees of freedom of noisy images," J. Opt. Soc. Am. **67**(1), 71–76 (1977).

[50] J. L. Harris, "Diffraction and Resolving Power," J. Opt. Soc. Am. **54**(7), 931–933 (1964).

[51] N. Sandeau, H. Giovannini, P. Lenne, and H. Rigneault, "Observation of the interferences between the emitted beams in a 4Pi microscope by partial coherence interferometry," Appl. Phys. Lett. **87**(18) (2005).

[52] K. Wicker and R. Heintzmann, "Interferometric resolution improvement for confocal microscopes," Opt. Express **15**(19), 12,206–12,216 (2007).

[53] N. Sandeau, L. Wawrezinieck, P. Ferrand, H. Giovannini, and H. Rigneault, "Increasing the lateral resolution of scanning microscopes by a factor of two using 2-Image microscopy," J. Eur. Opt. Soc, Rapid Publ. **4** (2009).

[54] R. Heintzmann, V. Sarafis, P. Munroe, J. Nailon, Q. Hanley, and T. Jovin, "Resolution enhancement by subtraction of confocal signals taken at different pinhole sizes," Micron **34**(6-7), 293–300 (2003).

[55] W. Zhao, J. Tan, L. Qiu, and P. Jin, "SABCMS, a new approach to higher lateral resolution of laser probe measurement system," Sens. Actuators, A-Phys. **120**(1), 17 – 25 (2005).

[56] C. Sheppard, "Super-resolution in Confocal Imaging," Optik **80**(2), 53–54 (1988).

[57] C. B. Müller and J. Enderlein, "Image Scanning Microscopy," Phys. Rev. Lett. **104**, 198,101 (2010).

[58] C. J. R. Sheppard and Z. S. Hegedus, "Axial behavior of pupil-plane filters," J. Opt. Soc. Am. A **5**(5), 643–647 (1988).

[59] R. Dorn, S. Quabis, and G. Leuchs, "Sharper focusing for a radially polarized light beam," Phys. Rev. Lett. **91**, 233,901 (2003).

[60] T. R. M. Sales, "Smallest Focal Spot," Phys. Rev. Lett. **81**, 3844–3847 (1998).

[61] F. Lemoult, G. Lerosey, J. de Rosny, and M. Fink, "Resonant Metalenses for Breaking the Diffraction Barrier," Phys. Rev. Lett. **104**, 203,901 (2010).

[62] E. G. van Putten, D. Akbulut, J. Bertolotti, W. L. Vos, A. Lagendijk, and A. P. Mosk, "Scattering Lens Resolves Sub-100 nm Structures with Visible Light," Phys. Rev. Lett. **106**, 193,905 (2011).

[63] Z. Wang, W. Guo, L. Li, B. Luk'yanchuk, A. Khan, Z. Liu, Z. Chen, and M. Hong, "Optical virtual imaging at 50 nm lateral resolution with a white-light nanoscope," Nature Comm. **2** (2011).

[64] S. J. Strickler and R. A. Berg, "Relationship between Absorption Intensity and Fluorescence Lifetime of Molecules," J. Chem. Phys. **37**(4), 814–822 (1962).

[65] L. Song, E. J. Hennink, I. Young, and H. J. Tanke, "Photobleaching kinetics of fluorescein in quantitative fluorescence microscopy," Biophysical Journal **68**(6), 2588–2600 (1995).

[66] T. Dertinger, R. Colyer, G. Iyer, S. Weiss, and J. Enderlein, "Fast, background-free, 3D super-resolution optical fluctuation imaging (SOFI)," P. N. A. S. **106**(52), 22,287–22,292 (2009).

[67] R. R. Chance, A. Prock, and R. Silbey, "Lifetime of an emitting molecule near a partially reflecting surface," J. Chem. Phys. **60**(7), 2744–2748 (1974).

[68] A. Rahmani, P. C. Chaumet, F. de Fornel, and C. Girard, "Field propagator of a dressed junction: Fluorescence lifetime calculations in a confined geometry," Phys. Rev. A **56**, 3245–3254 (1997).

[69] E. Wolf, "Three-dimensional structure determination of semi-transparent objects from holographic data," Opt. Commun. **1**(4), 153 – 156 (1969).

[70] F. Natterer, "An error bound for the Born approximation," Inverse Probl. **20**(2), 447 (2004).

[71] A. D. Yaghjian, "Electric Dyadic Green's Functions in the Source Region," P IEEE **68**(2), 248–263 (1980).

[72] K. Belkebir, P. C. Chaumet, and A. Sentenac, "Superresolution in total internal reflection tomography," J. Opt. Soc. Am. A **22**(9), 1889–1897 (2005).

[73] V. Lauer, "New approach to optical diffraction tomography yielding a vector equation of diffraction tomography and a novel tomographic microscope," J. Microsc. **205**, 165–176 (2002).

[74] F. Charriere, A. Marian, F. Montfort, J. Kuehn, T. Colomb, E. Cuche, P. Marquet, and C. Depeursinge, "Cell refractive index tomography by digital holographic microscopy," Opt. Lett. **31**(2), 178–180 (2006).

[75] O. Haeberlé, K. Belkebir, H. Giovaninni, and A. Sentenac, "Tomographic diffractive microscopy: basics, techniques and perspectives," J. Mod. Opt. **57**(9), 686–699 (2010).

[76] M. Debailleul, B. Simon, V. Georges, O. Haeberlé, and V. Lauer, "Holographic microscopy and diffractive microtomography of transparent samples," Meas. Sci. Technol. **19**(7), 074,009 (2008).

[77] J. H. Bruning, D. R. Herriott, J. E. Gallagher, D. P. Rosenfeld, A. D. White, and D. J. Brangaccio, "Digital Wavefront Measuring Interferometer for Testing Optical Surfaces and Lenses," Appl. Opt. **13**(11), 2693–2703 (1974).

[78] I. Yamaguchi and T. Zhang, "Phase-shifting digital holography," Opt. Lett. **22**(16), 1268–1270 (1997).

[79] U. Schnars and W. Jüptner, "Direct recording of holograms by a CCD target and numerical reconstruction," Appl. Opt. **33**(2), 179–181 (1994).

[80] E. Cuche, F. Bevilacqua, and C. Depeursinge, "Digital holography for quantitative phase-contrast imaging," Opt. Lett. **24**(5), 291–293 (1999).

[81] A. Barty, K. A. Nugent, D. Paganin, and A. Roberts, "Quantitative optical phase microscopy," Opt. Lett. **23**(11), 817–819 (1998).

[82] J. Primot and L. Sogno, "Achromatic three-wave (or more) lateral shearing interferometer," J. Opt. Soc. Am. A **12**(12), 2679–2685 (1995).

[83] P. Bon, G. Maucort, B. Wattellier, and S. Monneret, "Quadriwave lateral shearing interferometry for quantitative phase microscopy of living cells," Opt. Express **17**(15), 13,080–13,094 (2009).

[84] S. S. Kou and C. J. R. Sheppard, "Image formation in holographic tomography: high-aperture imaging conditions," Appl. Opt. **48**(34), H168–H175 (2009).

[85] S. S. Kou and C. J. R. Sheppard, "Image formation in holographic tomography," Opt. Lett. **33**(20), 2362–2364 (2008).

[86] Y. Sung, W. Choi, C. Fang-Yen, K. Badizadegan, R. R. Dasari, and M. S. Feld, "Optical diffraction tomography for high resolution live cell imaging," Opt. Express **17**(1), 266–277 (2009).

[87] P. Mora, "Inversion = migration + tomography," Geophysics **54**(12), 1575–1586 (1989).

[88] T. Hutt and F. Simonetti, "Reconstructing the shape of an object from its mirror image," J. Appl. Phys. **108**(6), 064,909 (2010).

[89] C. Nolan, M. Cheney, T. Dowling, and R. Gaburro, "Enhanced angular resolution from multiply scattered waves," Inverse Probl. **22**, 1817–1834 (2006).

[90] F. Natterer, "Reflectors in wave equation imaging," Wave Motion **45**, 776–784 (2008).

[91] J.-J. Greffet, "Scattering of s-polarized electromagnetic waves by a 2d obstacle near an interface," Opt. Comm. **72**(5), 274 – 278 (1989).

[92] F. Pincemin, A. Sentenac, and J.-J. Greffet, "Near field scattered by a dielectric rod below a metallic surface," J. Opt. Soc. Am. A **11**(3), 1117–1127 (1994).

[93] J.-J. Greffet and R. Carminati, "Image formation in near-field optics," Prog. Surf. Sci. **56**, 133–237 (1997).

[94] G. Leuchs and M. Sondermann, "Time-reversal symmetry in optics," Phys. Scr. **85**(5), 058,101 (2012).

[95] M. Martinez-Corral and G. Saavedra, "The Resolution Challenge in 3D Optical Microscopy," in *Progress in Optics*, E. Wolf, ed., vol. 53 of *Prog. Opt.*, pp. 1 – 67 (Elsevier, 2009).

[96] A. S. van de Nes, J. J. M. Braat, and S. F. Pereira, "High-density optical data storage," Rep. Prog. Phys. **69**(8), 2323 (2006).

[97] E. Walker, A. Dvornikov, K. Coblentz, S. Esener, and P. Rentzepis, "Toward terabyte two-photon 3D disk," Opt. Express **15**(19), 12,264–12,276 (2007).

[98] P. C. Chaumet, B. Pouligny, R. Dimova, and N. Sojic, "Optical tweezers in interaction with an apertureless probe," J. Appl. Phys. **102**, 024,915–8 (2007).

[99] C. Selhuber-Unkel, I. Zins, O. Schubert, C. Sönnichsen, and L. B. Oddershede, "Quantitative Optical Trapping of Single Gold Nanorods," Nano Letters **8**(9), 2998–3003 (2008).

[100] M. Dienerowitz, M. Mazilu, and K. Dholakia, "Optical manipulation of nanoparticles: a review," J. Nanophotonics **2**(23), 021,875–32 (2008).

[101] M. Martinez-Corral, P. Andrés, C. J. Zapata-Rodriguez, and M. Kowalczyk, "Three-dimensional superresolution by annular binary filters," Opt. Comm. **165**(4–6), 267 – 278 (1999).

[102] M. Martinez-Corral, M. Caballero, E. H. K. Stelzer, and J. Swoger, "Tailoring the axial shape of the point spread function using the Toraldo concept," Opt. Express **10**(1), 98–103 (2002).

[103] G. Boyer, "New class of axially apodizing filters for confocal scanning microscopy," J. Opt. Soc. Am. A **19**(3), 584–589 (2002).

[104] M. Martinez-Corral, C. Ibáñez-López, G. Saavedra, and M. Caballero, "Axial gain resolution in optical sectioning fluorescence microscopy by shaded-ring filters," Opt. Express **11**(15), 1740–1745 (2003).

[105] N. Lindlein, S. Quabis, U. Peschel, and G. Leuchs, "High numerical aperture imaging with different polarization patterns," Opt. Express **15**(9), 5827–5842 (2007).

[106] W. Chen and Q. Zhan, "Diffraction limited focusing with controllable arbitrary three-dimensional polarization," J. Opt. **12**(4), 045,707 (2010).

[107] B. Davis, W. Karl, A. Swan, M. Unlu, and B. Goldberg, "Capabilities and limitations of pupil-plane filters for superresolution and image enhancement," Opt. Express **12**(17), 4150–4156 (2004).

[108] L. Melton, "Imaging: The big picture," Nature **437**(7059), 775–779 (2005).

[109] S. W. Hell, "Microscopy and its focal switch," Nature Meth. **6**(1), 24–32 (2009).

[110] M. Nagorni and S. W. Hell, "Coherent use of opposing lenses for axial resolution increase in fluorescence microscopy. I. Comparative study of concepts," J. Opt. Soc. Am. A **18**(1), 36–48 (2001).

[111] J. Bewersdorf, R. Schmidt, and S. W. Hell, "Comparison of I5M and 4Pi-microscopy," J. Microsc. (Oxf.) **222**, 105 (2006).

[112] C. J. R. Sheppard and K. G. Larkin, "Effect of numerical aperture on interference fringe spacing," Appl. Opt. **34**(22), 4731–4734 (1995).

[113] C. Sheppard and P. Torok, "Electromagnetic field in the focal region of an electric dipole wave," Optik **104**(4), 175–177 (1997).

[114] M. Schrader, M. Kozubek, S. W. Hell, and T. Wilson, "Optical transfer functions of 4Pi confocal microscopes: theory and experiment," Opt. Lett. **22**(7), 436–438 (1997).

[115] H. Matthews, D. Hamilton, and C. Sheppard, "Aberration Measurement by Confocal Interferometry," J. Modern Optics **36**(2), 233–250 (1989).

[116] M. Lang, T. Müller, J. Engelhardt, and S. W. Hell, "4Pi microscopy of type A with 1-photon excitation in biological fluorescence imaging," Opt. Express **15**(5), 2459–2467 (2007).

[117] A. Sentenac, K. Belkebir, H. Giovannini, and P. C. Chaumet, "Subdiffraction resolution in total internal reflection fluorescence microscopy with a grating substrate," Opt. Lett. **33**(3), 255–257 (2008).

[118] J. García, Z. Zalevsky, and D. Fixler, "Synthetic aperture superresolution by speckle pattern projection," Opt. Express **13**(16), 6073–6078 (2005).

[119] D. Sylman, V. Micó, J. García, and Z. Zalevsky, "Random angular coding for superresolved imaging," Appl. Opt. **49**(26), 4874–4882 (2010).

[120] R. Heintzmann and M. G. L. Gustafsson, "Subdiffraction resolution in continuous samples," Nature Photon. **3**(7), 362–364 (2009).

[121] P. Kner, B. B. Chhun, E. R. Griffis, L. Winoto, and M. G. L. Gustafsson, "Superresolution video microscopy of live cells by structured illumination," Nature Meth. **6**(5), 339–342 (2009).

[122] C. Bouman and K. Sauer, "A unified approach to statistical tomography using coordinate descent optimization," IEEE Trans. Image Process. **5**(3), 480–492 (1996).

[123] M. Allain and J.-P. Roques, "Imaging techniques for gamma-ray diffuse emission: application to INTEGRAL/SPI," A&A **447**(3), 1175–1187 (2006).

[124] E. Polak and G. Ribière, "Note sur la convergence de méthodes de directions conjuguées," Rev. Française Informat. Recherche Opérationnelle **3**(16), 35–43 (1969).

[125] M. Bertero and P. Boccacci, "A simple method for the reduction of boundary effects in the Richardson-Lucy approach to image deconvolution," A&A **437**(1), 369–374 (2005).

[126] R. Vio, J. Bardsley, M. Donatelli, and W. Wamsteker, "Dealing with edge effects in least-squares image deconvolution problems," A&A **442**(1), 397–403 (2005).

[127] A. Tikhonov and V. Arsénine, *Méthodes de résolution de problèmes mal posés* (Edition Mir, Moscou, 1974).

[128] P. Hansen, *Rank-deficient and Discrete Ill-posed Problems: Numerical Aspects of Linear Inversion.* (SIAM, Philadelphia, 1998).

[129] G. H. Golub, M. Heath, and G. Wahba, "Generalized cross-validation as a method for choosing a good ridge parameter," Technometrics **21**(2), 215–223 (1979).

[130] M. Bertero and P. Boccacci, *Introduction to inverse problems in imaging* (Institute of Physics Pub., London, 1998).

[131] J. W. Goodman, *Speckle Phenomena in Optics: Theory and Applications* (Roberts and Company Publishers, 2007).

[132] O. Mandula, "Patterned Excitation Microscopy," Master's thesis, King's College London (2008).

[133] K. Wicker, "Increasing resolution and light efficiency in fluorescence microscopy," Ph.D. thesis, King's College London (2010).

[134] A. Sentenac, K. Belkebir, H. Giovannini, and P. C. Chaumet, "High-resolution total-internal-reflection fluorescence microscopy using periodically nanostructured glass slides," J. Opt. Soc. Am. A **26**(12), 2550–2557 (2009).

[135] J. B. Pawley, *Handbook Of Biological Confocal Microscopy* (Springer US, 2006).

[136] T. Q. Pham, M. Bezuijen, L. J. van Vliet, K. Schutte, and C. L. L. Hendriks, "Performance of optimal registration estimators," Proc. SPIE **5817**, 133 (2005).

[137] C. Ventalon and J. Mertz, "Quasi-confocal fluorescence sectioning with dynamic speckle illumination," Opt. Lett. **30**(24), 3350–3352 (2005).

[138] J. Turunen, A. Vasara, and A. T. Friberg, "Propagation invariance and self-imaging in variable-coherence optics," J. Opt. Soc. Am. A **8**(2), 282–289 (1991).

[139] D. M. Cottrell, J. M. Craven, and J. A. Davis, "Nondiffracting random intensity patterns," Opt. Lett. **32**(3), 298–300 (2007).

[140] A. Dudley, R. Vasilyeu, V. Belyi, N. Khilo, P. Ropot, and A. Forbes, "Controlling the evolution of nondiffracting speckle by complex amplitude modulation on a phase-only spatial light modulator," Opt. Comm. **285**(1), 5 – 12 (2012).

[141] J. Idier, private communication (2012).

[142] R. Heintzmann, T. M. Jovin, and C. Cremer, "Saturated patterned excitation microscopy—a concept for optical resolution improvement," J. Opt. Soc. Am. A **19**(8), 1599–1609 (2002).

[143] M. Gustafsson, "Nonlinear structured-illumination microscopy: Wide-field fluorescence imaging with theoretically unlimited resolution," P. N. A. S. **102**, 13,081–13,086 (2005).

[144] L. Hirvonen, O. Mandula, K. Wicker, and R. Heintzmann, "Structured illumination microscopy using photoswitchable fluorescent proteins," in *Three-Dimensional and Multi-dimensional Microscopy: Image Acquisition and Processing XV*, J.-A. Conchello, C. J. Cogswell, T. Wilson, and T. G. Brown, eds., vol. 6861, p. 68610L (SPIE, 2008).

[145] D. Toomre and D. J. Manstein, "Lighting up the cell surface with evanescent wave microscope," Trends Cell Biol. **11**, 298–303 (2001).

[146] E. Chung, D. Kim, and P. So, "Extended resolution wide-field optical imaging objective-launched standing-wave total internal reflection fluorescence microscopy," Opt. Lett. **31**, 945–947 (2006).

[147] A.-L. Fehrembach, "Réseaux résonnants à bande interdite photonique: nouveaux filtres pour le DWDM," Ph.D. thesis, Université d'Aix-Marseille III (2003).

[148] J. Girard, "Microscopie de fluorescence et de diffraction super-résolues par éclairement multiple," Ph.D. thesis, Université d'Aix-Marseille III (2011).

[149] J. R. Fienup, "Reconstruction of an object from the modulus of its Fourier transform," Opt. Lett. **3**(1), 27–29 (1978).

[150] C.-A. Guérin and A. Sentenac, "Second-order perturbation theory for scattering from heterogeneous rough surfaces," J. Opt. Soc. Am. A **21**(7), 1251–1260 (2004).

[151] G. Maire, F. Drsek, J. Girard, H. Giovannini, A. Talneau, D. Konan, K. Belkebir, P. C. Chaumet, and A. Sentenac, "Experimental Demonstration of Quantitative Imaging beyond Abbe's Limit with Optical Diffraction Tomography," Phys. Rev. Lett. **102**(21), 213,905 (2009).

[152] J. Girard, G. Maire, H. Giovannini, A. Talneau, K. Belkebir, P. C. Chaumet, and A. Sentenac, "Nanometric resolution using far-field optical tomographic microscopy in the multiple scattering regime," Phys. Rev. A **82**, 061,801 (2010).

[153] J. Hadamard, *Lectures on Cauchy's Problem in Linear Partial Differential Equation* (Yale University Press, New Haven, 1923).

[154] A. Dubois, "Étude de l'interaction d'une onde électromagnétique avec une structure matérielle en régime temporel: problèmes directs et inverses." Ph.D. thesis, Université d'Aix-Marseille III (2005).

[155] E. M. Purcell and C. R. Pennypacker, "Scattering and absorption of light by nonspherical dielectric grains," Astrophys. J. **186**, 705–714 (1973).

[156] M. A. Yurkin, V. P. Maltsev, and A. G. Hoekstra, "Convergence of the discrete dipole approximation. I. Theoretical analysis," J. Opt. Soc. Am. A **23**(10), 2578–2591 (2006).

[157] P. C. Chaumet, "Modélisation électromagnétique: Applications à l'imagerie optique et aux forces optiques," Mémoire d'habilitation, Université d'Aix-Marseille III (2007).

[158] P. C. Chaumet, A. Sentenac, and A. Rahmani, "Coupled dipole method for scatterers with large permittivity," Phys. Rev. E **70**, 036,606–6 (2004).

[159] J. Tang, Y. Shen, Y. Zheng, and D. Qiu, "An efficient and flexible computational model for solving the mild slope equation," Coastal Engineering **51**, 143–154 (2004).

[160] S.-L. Zhang, "GPBi-CG: Generalized Product-type Methods Based on Bi-CG for Solving Nonsymmetric Linear Systems," SIAM J. Sci. Comput. **18**, 537–551 (1997).

[161] P. C. Chaumet and K. Belkebir, "Three-dimensional reconstruction from real data using a conjugate gradient-coupled dipole method," Inverse Probl. **25**, 024,003–17 (2009).

[162] C. Gilmore, P. Mojabi, and J. LoVetri, "Comparison of an Enhanced Distorted Born Iterative Method and the Multiplicative-Regularized Contrast Source Inversion method," IEEE Trans. Antennas Propag. **57**(8), 2341–2351 (2009).

[163] L. Pan, X. Chen, Y. Zhong, and S. P. Yeo, "Comparison among the variants of subspace-based optimization method for addressing inverse scattering problems: transverse electric case," J. Opt. Soc. Am. A **27**(10), 2208–2215 (2010).

[164] R. E. Kleinman and P. M. van den Berg, "A modified gradient method for two-dimensional problems in tomography," J. Comput. Appl. Math. **42**, 17–35 (1992).

[165] R. E. Kleinman and P. M. van den Berg, "Two-dimensional location and shape reconstruction," Radio Sci. **29**(4), 1157–1169 (1994).

[166] A. Dubois, K. Belkebir, and M. Saillard, "Retrieval of inhomogeneous targets from experimental frequency diversity data," Inverse probl. **21**(16), S65–S79 (2005).

[167] T. M. Habashy, M. L. Oristaglio, and A. T. de Hoop, "Simultaneous nonlinear reconstruction of two-dimensional permittivity and conductivity," Radio Sci. **29**(4), 1101–1118 (1994).

[168] P. C. Chaumet, A. Sentenac, K. Belkebir, G. Maire, and H. Giovannini, "Improving the resolution of grating-assisted optical diffraction tomography using a priori information in the reconstruction procedure," J. Mod. Opt. **57**, 798–808 (2010).

[169] K. Belkebir, S. Bonnard, F. Pezin, P. Sabouroux, and M. Saillard, "Validation of 2D inverse scattering algorithms from multi-frequency experimental data," J. Electromag. Waves Appl. **14**, 1637–1667 (2000).

[170] P. C. Chaumet, K. Belkebir, and A. Sentenac, "Experimental microwave imaging of three-dimensional targets with different inversion procedures," J. Appl. Phys. **106**, 034,901–8 (2009).

[171] A. Litman and L. Crocco, "Testing inversion algorithms against experimental data: 3D targets," Inverse Probl. **25**, 020,201–5 (2009).

[172] J. M. Geffrin and P. Sabouroux, "Continuing with the Fresnel database: experimental setup and improvements in 3D scattering measurements," Inverse Probl. **25**(2), 024,001 (2009).

[173] P. M. van den Berg and A. Abubakar, "Contrast source inversion method: state of art," Prog. Electromagn. Res. **34**, 189–218 (2001).

[174] A. Sentenac, P. C. Chaumet, and K. Belkebir, "Beyond the Rayleigh Criterion: Grating Assisted Far-Field Optical Diffraction Tomography," Phys. Rev. Lett. **97**, 243,901 (2006).

[175] E. G. van Putten, D. Akbulut, J. Bertolotti, W. L. Vos, A. Lagendijk, and A. P. Mosk, "Scattering Lens Resolves Sub-100 nm Structures with Visible Light," Phys. Rev. Lett. **106**, 193,905 (2011).

Abstract

Various fields of experimental science are constantly requiring smaller resolution for optical microscopy. In this thesis are presented several works for improving resolution in fluorescence microscopy and in Tomographic Diffraction Microscopy (TDM), an emerging phase microscopy technique. In the first part it is shown that one can improve the axial resolution in depositing the sample on a mirror. In confocal fluorescence microscopy, this is done by shaping the illumination beam with a Spatial Light Modulator. In TDM this is done by adapting the reconstruction method. Then algorithms are proposed for reconstructing high-resolution images from structured illumination measurements with unknown illumination fields, both in fluorescence imaging (blind-SIM algorithm) and in TDM. This allows a dramatical simplification of the experimental set-ups in fluorescence structured illumination and the image reconstruction of high optical index samples in TDM.

keyword: optical microscopy, resolution, fluorescence, phase microscopy, structured illumination, inverse problems.

Résumé

La microscopie optique est une technique essentielle pour de nombreuses disciplines des sciences expérimentales qui nécessitent des résolutions sans cesse plus petites. Dans ce travail de thèse sont présentés plusieurs travaux pour l'amélioration de la résolution en microscopie de fluorescence et en microscopie tomographique par diffraction (MTD), une récente technique de microscopie de phase. Dans un premier temps, il est montré que déposer l'échantillon sur un miroir permet d'augmenter la résolution axiale en MTD et en microscopie confocale de fluorescence. En microscopie confocale, il faut pour cela mettre en forme le faisceau incident grâce à un modulateur spatial de lumière. En MTD, il suffit d'adapter le programme de reconstruction. La deuxième partie présente des algorithmes pour reconstruire des images haute résolution à partir de mesures en éclairement structuré avec de champs d'illumination inconnus, à la fois en microscopie de fluorescence (algorithme blind-SIM) et en MTD. En microscopie de fluorescence, ces algorithmes permettent de simplifier drastiquement les montages expérimentaux produisant l'éclairement structuré et en MTD, d'obtenir des images d'échantillons à fort indice.

mots-clés : microscopie optique, résolution, fluorescence, microscopie de phase, éclairement structuré, problèmes inverses.